AIRCRAFT AND TECHNOLOGY CONCEPTS FOR AN N+3 SUBSONIC TRANSPORT, PHASE 2 FINAL REPORT

by

A. Uranga, M. Drela, E.M. Greitzer,
C. Casses, D.G. DiOrio, A.E. Espitia, A.D. Grasch, D.K. Hall,
A.C. Huang, M.K. Lieu, S. Sato, N.M. Siu, C.S. Tan, N.A. Titchener, E. van Dam
Massachusetts Institute of Technology, Cambridge, Massachusetts

J.S. Hollman, D. Kordonowy, R.A. Opperman, J.T. Chambers, B.D. Smith,
E. Pliakas, A. Cardona, S. Giblin, D.S. Campbell
Aurora Flight Sciences, Cambridge, Massachusetts

W.K. Lord, G.L. Suciu
Pratt & Whitney, East Hartford, Connecticut

GTL Report Series 2

Report # 2-001

May 2018

Gas Turbine Laboratory
Massachusetts Institute of Technology
Cambridge, Massachusetts

Abstract

This report describes the results from investigations of an advanced design civil aircraft, the D8 double-bubble, carried out from 2010 to 2015 by a team from MIT, Aurora Flight Sciences, and Pratt & Whitney, as part of a NASA N+3 Phase 2 Project. The project goal was to further develop the future subsonic transport concept with the goal of achieving step reductions in fuel and emissions for a 2030-2035 service-entry timeframe. The aerodynamic benefit of boundary layer ingestion (BLI) at cruise was quantified to be 8.6% at fixed nozzle area, through a back-to-back comparison of non-BLI and BLI versions of the D8, which included low-speed tests of 1:11 scale powered models in the NASA Langley 14– by 22–Foot Subsonic Tunnel. This represents the first measurement of BLI performance improvements for a realistic aircraft configuration. A novel engine architecture with a nonconcentric, reverse-flow arrangement of the core and fan sections was conceived to satisfy the FAA 1-in-20 engine failure rule for the D8 aircraft's integrated propulsion system with side-by-side engines. The BLI benefit results, coupled with the innovative engine design, give evidence that aircraft using BLI can provide a viable path for step improvements in fuel efficiency of subsonic transports.

Acknowledgments

This work was supported by the NASA Fundamental Aeronautics program, Fixed Wing Project, through Cooperative Agreement Number NNX11AB35A.

From NASA Langley we thank Scott Anders for his guidance and valuable suggestions, as well as Greg Gatlin and Judith Hannon who actively participated in the wind tunnel tests and data analysis. We are indebted to the staff of the NASA Langley 14– by 22–Foot Subsonic Tunnel for the high level of enthusiasm and expertise shown during this experimental campaign, in particular Jim Byrd and Les Yeh who served as Test Engineers. We would also like to acknowledge Shishir Pandya from NASA Ames for his work on the numerical simulations, as well as Randall Chriss and Michael Hathaway for their feedback on the small-cores work. We are most appreciative of the strong interest, support, and useful input contributed by the NASA Fixed Wing Project management, especially Rubén del Rosario, Richard Wahls, and Kim Pham.

We thank Harold Youngren of Aerocraft Inc. who was instrumental in performing the CFD analyses during the model design phase. We also wish to thank the many people who offered technical feedback, in particular N. Cumpsty, Y. Dong, A. Epstein, E. Gallagher, R. Liebeck, A. Murphy, J. Sabnis, and G. Tillman.

Contents

1 Summary

Significant improvements in fuel efficiency are required to address the challenges posed by the projected increase in aviation demand and the growing environmental concerns. The NASA N+3 program is aimed at the development of commercial transports three generations ahead of the current fleet that could enter service in the 2020-2035 timeframe and provide step improvements in performance. A team from MIT, Aurora Flight Science, and Pratt & Whitney, together with NASA personnel, has pursued a research effort in response to these challenges.

In Phase 1 of the N+3 program (2008–2010), the MIT-led team examined a number of technologies and aircraft concepts, including a 180-passenger D8 "double bubble" aircraft in the Boeing 737-800 or Airbus 320 class. This D8 concept was selected by NASA for further development in a Phase 2 project centered on the two tasks summarized below. The work was performed between 2010 and 2015 in close collaboration with NASA and is summarized in the present final report.

A major conclusion from this Phase 2 program is that, at the level of details to which it was studied, BLI is a viable technology for reducing fuel burn and emissions of commercial subsonic transports. The D8 configuration in particular was shown to be a feasible candidate for future fuel-efficient aircraft. Furthermore, the alternative architecture engines conceptually designed for the D8 hold considerable promise for future transport aircraft of all types. Finally, the quantitative data gathered on BLI-induced distortion and propulsion system response will help better model and design engines that operate in distorted flow throughout the whole flight envelope.

1.1 Task 1: Airframe Propulsion System Integration

This task, performed primarily by MIT and Aurora, focused on the D8 aircraft performance, particularly on the integration between the fuselage and the boundary layer ingesting (BLI) propulsion system. The effort centered on the aerodynamic design of the D8 airframe and BLI systems, and on the design, construction, and low-speed (roughly Mach 0.1) tests of a 1:11 powered wind tunnel model at MIT and at the NASA Langley 14– by 22–Foot Subsonic Tunnel. Test rigs were also built and used in supporting experiments at MIT to characterize the electrically-driven propulsors, which were used in the wind tunnel model. Appropriate flow survey equipment was also designed, built, and used in the wind tunnel tests.

Both non-BLI and BLI versions of the D8 model were tested, providing the first experimental back-to-back comparison of non-BLI and BLI propulsion for a transport aircraft, and thus a measure of the benefit that BLI provides. Work on BLI analysis theory and the development of suitable BLI performance metrics was also carried out in parallel with the experimental work.

The experimental and theoretical program was supported by 3D RANS computational work performed by NASA personnel. The computations were important to interpret the experimental results, particularly the physical origins of the BLI power-saving benefit.

The project objectives for Task 1 have been achieved. Well-defined BLI performance metrics have been developed and successfully applied. The aerodynamic characteristics and performance of the D8 aircraft's BLI system have been experimentally and computationally assessed via the back-to-back comparison of BLI versus non-BLI propulsion systems. The aerodynamic-only BLI benefit has been measured to be 8.6% at fixed nozzle area. On an actual aircraft this would be augmented by system-level benefits, primarily via weight reduction, for an estimated overall benefit of 19% for the BLI aircraft versus a conventional non-BLI aircraft designed for the same mission. The BLI system was also shown to function at high angles of attack up to 12°, sideslip up to ±15°, and with one engine out.

1.2 Task 2: High Efficiency, High Pressure Ratio Small Core Engines

This task, performed primarily by MIT and Pratt & Whitney, focused on advancing highly efficient, high pressure ratio small core (1.5 to 2 lbm/s exit corrected flows) engine and compressor technology for advanced civil aircraft. It also included the development of novel architectures for small-core high pressure ratio turbofan engines, which are anticipated to be needed for future aircraft such as the D8. One challenge is the fact that the shaft connecting the front fan with its driving low-pressure turbine in the rear must have a minimum diameter for structural reasons. On the very high bypass ratio engines toward which the industry is moving, this shaft forces the relatively small core to have unacceptably large hub to tip ratios, and very small blade heights. These have poor performance due to the low chord Reynolds numbers, poor manufacturing relative tolerances, and primarily large tip-gap ratios. Another challenge is the risk of fratricide in closely-spaced twin engine installations, where a possible turbine disk burst in one engine could also destroy the neighboring core.

Both of these problems were addressed with the development of an innovative conceptual engine architecture with a nonconcentric, reverse-flow arrangement of the engine core and propulsion-fan sections. This arrangement allows the core to have a smaller diameter, giving larger blade sizes and smaller nondimensional tip clearances. This has considerable promise of allowing high pressure ratios and high core efficiencies to be maintained down to small core sizes. Furthermore, the nonconcentric core can be oriented to place its disk-burst zone away from neighboring cores or critical airframe structure, thus addressing the engine fratricide problem on BLI propulsion systems with adjacent engines and meeting the FAA 1-in-20 rule with the D8.

1.3 Report Scope and Organization

This final report for the NASA N+3 Phase 2 project "Aircraft and Technology Concepts for an N+3 Subsonic Transport", NASA-MIT Cooperative agreement NNX11AB35A, presents the research work that was carried out from November 2010 to May 2015 by a team from MIT, Aurora Flight Sciences, and Pratt & Whitney. It serves primarily as a project introduction and summary document. The results presented are preliminary in nature, and are likely to be refined as further analysis is performed. They are however representative of the performance predictions and the overall conclusions presented in this report are not expected to change.

Final and definitive results of this Phase 2 work will be published in the coming months. Most of the project details are documented in separate reports, theses, and papers, which are attached here in appendices. Several of the sections in this report are adapted from these previous documents.

2 Phase 2 Project

2.1 Motivation

In 2008, NASA put forward a solicitation for aircraft concepts targeted for three generations ahead of the current flying fleet. This "N+3" program aims to develop advanced concepts, plus enabling technologies, to provide step improvements in fuel efficiency and lowering the environmental impact of commercial aircraft entering service in the 2030-2035 timeframe.

A team led by MIT, in partnership with Aurora Flight Sciences and Pratt & Whitney, responded to this solicitation and is now starting a 3rd phase. The Phase 1 was awarded from September 2008 through March 2010, and was documented in its own final NASA Contractor Report [1]. The Phase 2 started in November 2010 and ended in May 2015. The present document is the final report for this second phase. A Phase 3 will run for a little more than a year starting in July 2015.

The Phase 2 aimed at advancing the maturation of concepts and technologies needed for achieving the fuel and emission reductions that the D8 advanced aircraft concept promises. Of major importance to the performance gains are (1) the use of boundary layer ingestion, and (2) the availability of highly efficient small core engines with high pressure ratios. These two aspects were the focus of the two tasks under the Phase 2 program.

2.2 Objectives

All of the objectives of the Phase 2 project were achieved. The work was divided into two research thrusts. Task 1 focused on the airframe-propulsion system integration for the D8 aircraft. The main goal was to quantify the aerodynamic benefit of boundary layer ingestion (BLI) for the D8 aircraft, and thus prove the feasibility of using BLI for fuel burn reduction of subsonic commercial transports. The specific objectives were:

- Design and define the aft-section of the D8 where the propulsion system blends with the fuselage
- Quantify the aerodynamic benefit of BLI for the D8
- Develop the methodology for studying aircraft configurations with BLI
- Formulate a technology road map for the D8

Task 2 revolved around high-efficiency, high-OPR small cores, and had the following objectives:

- Determine the viability for high component efficiency at exit compressor corrected flows of the order of 1.5 lbm/s (efficiency limits and scaling with size, efficiency loss mitigation)
- Propose and define a conceptual engine design to meet the N+3 requirements
- Formulate a technology road map to realize the benefits of small core engines

2.3 Team

A government-industry-university collaboration was put together, and the team was able to leverage the different skills of each organization: MIT, Aurora Flight Sciences, Pratt & Whitney, and NASA. In addition to achieving the project's technical goals, the project provided important educational benefits: at MIT, a total of 8 graduate students (2 doctoral, 6 masters) and 13 undergraduate students participated in the Phase 2 project throughout its five-year duration.

The Phase 2 team was composed of the following individuals from industry and university:

Daniel Campbell [‡]	Michael Lieu [§*]
Angelica Cardona [‡]	Wesley Lord [¶]
Cécile Casses [§*]	Jeremy Hollman [‡]
Jeffrey Chambers [‡]	Roedolph Opperman [‡]
Austin DiOrio [§*]	Elena Pliakas [‡]
Mark Drela [§] (Chief Engineer)	Sho Sato [§*]
Alex Espitia [§*]	Nina Siu [§*]
Sydney Giblin [‡]	Benjamin Smith [‡]
Adam Grasch [§*]	Gabriel Suciu [¶]
Edward Greitzer [§] (Principal Investigator)	Choon Tan [§]
David Hall [§*]	Neil Titchener [§]
Arthur Huang [§]	Alejandra Uranga [§] (Technology Lead)
David Kordonowy [‡]	Elise van Dam [§+]

Affiliations:

[‡] Aurora Flight Sciences
[§] MIT
[§*] MIT graduate student
[§+] MIT visiting graduate student from TU Delft
[¶] Pratt & Whitney

In addition, the following MIT undergraduate students interned with the project at some point or another as part of MIT's Undergraduate Research Opportunity Program (UROP):

Michael Basara	Ian Fischer	Giulia Pantalone
Jamie Byron	Grace Krusell	Jason Pier
Nate Colgan	Zhaoming (Tommy) Li	Peter Williams
Trang Dang	Jordan Lopez	
Alex Feldstein	Chris Maynor	

3 Task 1: Airframe Propulsion System Integration

Nomenclature

Roman Symbols

A_{nozzle}	Propulsor nozzle exit area
A_{fan}	Fan area, as covered by fan blades (*i.e.* hub area subtracted), $A_{\text{fan}} = 0.0159\,\text{m}^2$
AR	Aspect ratio
b	Model wing span, $b = 161.3\,\text{in} = 4.097\,\text{m}$
c	Model reference chord, $c = 10.75\,\text{in} = 0.273\,\text{m}$
C_D	Drag coefficient of unpowered configuration
C_{D_i}	Induced drag coefficient
C_L	Vertical aerodynamic force (lift) coefficient, $C_L = F_Z \,/\, (q_\infty\, S_{\text{ref}})$
C_m	Overall pitching moment coefficient, $C_m = \mathcal{M}_Y \,/\, (q_\infty\, S_{\text{ref}}\, c)$
C_{P_E}	Electrical power coefficient, $C_{P_E} = P_E \,/\, (q_\infty\, S_{\text{ref}}\, V_\infty)$
C_{P_K}	Mechanical flow power coefficient, $C_{P_K} = P_K \,/\, (q_\infty\, S_{\text{ref}}\, V_\infty)$
$C_{P_{\text{Shaft}}}$	Shaft power coefficient, $C_{P_{\text{Shaft}}} = P_{\text{Shaft}} \,/\, (q_\infty\, S_{\text{ref}}\, V_\infty)$
C_p	Static pressure coefficient, $C_p = (p - p_\infty) \,/\, q_\infty$
C_{p_t}	Total pressure coefficient, $C_{p_t} = (p_t - p_{t_\infty}) \,/\, q_\infty$
C_W	Normalized aircraft weight, $C_W = W \,/\, (q_\infty\, S_{\text{ref}})$
C_X	Streamwise force coefficient, $C_X = F_X \,/\, (q_\infty\, S_{\text{ref}})$ ($= C_D$ for unpowered configuration)
C_Φ	Dissipation coefficient, $C_\Phi = \Phi \,/\, (q_\infty\, S_{\text{ref}}\, V_\infty)$
CI	95% confidence interval
d_{fan}	Model propulsor fan diameter, $d_{\text{fan}} = 5.65\,\text{in} = 0.144\,\text{m}$
e	Span efficiency
F_A	Net axial aerodynamic force on entire model, along model and balance longitudinal axis x
F_N	Net normal aerodynamic force on entire model, along model and balance normal axis z
F_X	Net streamwise aerodynamic force on entire model; negative values indicate net forward force
F_Z	Net vertical aerodynamic force (lift) on entire model, normal to tunnel freestream direction
$\dot{m}$	Propulsor mass flow
M	Mach number
M_∞	Freestream (tunnel) Mach number
$\mathcal{M}_Y$	Pitching moment
$\hat{\mathbf{n}}$	Unit normal vector
p	Static pressure
p_∞	Freestream (tunnel) static pressure
p_t	Total pressure
p_{t_∞}	Freestream (tunnel) total pressure
P_E	Electrical power supplied to propulsors
P_K	Mechanical flow power
P_{Shaft}	Propulsor shaft power
PSC	Power saving coefficient, $PSC = (P_{K\,\text{non-BLI}} - P_{K\,\text{BLI}})/P_{K\,\text{non-BLI}}$
q_∞	Freestream (tunnel) dynamic pressure, $q_\infty = \frac{1}{2}\,\rho_\infty\, V_\infty^2$
R	Gas constant
Re_c	Reynolds number based on reference chord and freestream (tunnel) conditions
$\mathcal{R}_{P_K}$	Power ratio, $\mathcal{R}_{P_K} = P_{K\,\text{BLI}}/P_{K\,\text{non-BLI}} = 1 - PSC$
S_{ref}	Model reference area, $S_{\text{ref}} = 1686\,\text{in}^2 = 1.088\,\text{m}^2$
SM	Static margin
U_{tip}	Fan blade tip speed, $U_{\text{tip}} = \Omega\, d_{\text{fan}}\,/2$

V	Velocity magnitude (speed)
V_∞	Freestream (tunnel) speed
$\mathbf{V}$	Velocity vector
W	Aircraft weight
x, y, z	Model axes: x is longitudinal, y is spanwise
X, Y, Z	Tunnel axes: X is streamwise (horizontal) and Z is vertical pointing up
$x_{\text{ref}}, z_{\text{ref}}$	Moment-reference location

Greek Symbols

α	Model angle of attack
β	Sideslip angle
Δ	Difference quantity
η_f	Fan efficiency, $\eta_f = P_K \,/\, P_{\text{Shaft}}$
η_m	Motor efficiency, $\eta_m = P_{\text{Shaft}} \,/\, P_E$
η_o	Overall efficiency, $\eta_o = \eta_m \, \eta_f$
η_p	Propulsive efficiency, $\eta_p = (P_K - \Phi_{\text{jet}}) \,/\, P_K$
γ	Heat capacity ratio
ϕ	Flow coefficient
Φ	Dissipation quantity
Φ_{airframe}	Airframe dissipation, $\Phi_{\text{airframe}} = \Phi_{\text{surf}} + \Phi_{\text{wake}} + \Phi_{\text{vortex}}$
Φ_{jet}	Jet dissipation
Φ_{surf}	Surface dissipation
Φ_{vortex}	Vortex dissipation
Φ_{wake}	Wake dissipation
Φ_{wing}	Wing viscous dissipation
Ω	Propulsor fan angular velocity, or wheel speed
ρ	Density
ρ_∞	Freestream (tunnel) density

Subscripts

t	Total (stagnation) quantity
∞	Freestream (tunnel) quantity
LaRC	NASA Langley 14– by 22–Foot Subsonic Tunnel quantity
GTL	MIT GTL 1×1 wind tunnel quantity
cg	Center of gravity
np	Neutral point
ref	Reference quantity
spec	Specified quantity
trim	Change in parameter needed to achieved pitch trim

Acronyms and Abbreviations

BLI	Boundary layer ingestion
BPR	Engine bypass ratio
CFD	Computational Fluid Dynamics
FAA	Federal Aviation Administration
FHP	Five-hole probe
FPR	Fan pressure ratio
GTL	Gas Turbine Laboratory

MIT	Massachusetts Institute of Technology
NASA	National Aeronautics and Space Administration
OPR	Overall pressure ratio
PFEI	Payload fuel energy intensity (fuel energy burned divided by payload and range)
RANS	Reynolds Averaged Navier-Stokes
RPM	Revolutions per minute
SOC	Start-of-climb
TASOPT	Transport Aircraft System OPTimization
TO	Take-off
TOC	Top-of-climb

3.1 Overview

Part of the contents of this Section 3.1 is adapted from [2].

In 2008, NASA put forward a solicitation for aircraft concepts targeted for three generations ahead of the current flying fleet. This "N+3" program aims to develop advanced concepts, plus enabling technologies, to provide step improvements in fuel efficiency and lowering the environmental impact of commercial aircraft entering service in the 2030-2035 timeframe.

During Phase 1 of the N+3 program[1], a team led by MIT, in partnership with Aurora Flight Sciences and Pratt & Whitney, developed a conceptual design for a 180-passenger, 3 000 nm range transport, in the Boeing 737 or Airbus A320 aircraft class. This so-called D8.5 *double-bubble* aircraft (named for its characteristic double bubble fuselage cross-section) was estimated to require 71% less fuel while generating 76% fewer emissions (LTO NOx) than the 737-800 used as the basis for comparison [1].

In Phase 2 of the program[2], the team advanced the D8 concept through wind tunnel experiments and high-fidelity computations. This involved the detailed aerodynamic design of the integrated fuselage and propulsion system, as well as development of suitable scaling arguments, metrics, and baselines for experimental BLI evaluation. A major component of this work was a series of low-speed (roughly Mach 0.1) experiments in NASA Langley 14– by 22–Foot Subsonic Tunnel using 1:11 scale, 13.4 ft span, powered models to evaluate the aerodynamic performance both with and without BLI. A picture taken during the first set of tests undertaken in August–September 2013 is shown in Figure 3.1. The performance metric used to quantify the aerodynamic BLI benefit is the mechanical flow power required to produce a given net stream-wise force on the aircraft. A second wind tunnel entry in August–September 2014 was undertaken to obtain additional and repeat measurements, the latter reducing uncertainty in the measured BLI benefit measurements.

Figure 3.1: D8 model in its BLI integrated configuration in NASA Langley 14– by 22–Foot Subsonic Tunnel during the August–September 2013 experiments (Photo credit: NASA/George Homich).

Three configurations of the D8 were tested in the wind tunnel program: (i) an unpowered model to characterize the airframe alone, (ii) a model powered by podded propulsors that ingest freestream flow to serve as the baseline, referred to as the non-BLI configuration, and (iii) a BLI model configuration, also called integrated, whose propulsors are flush-mounted above the rear of the fuselage and ingest part of the fuselage boundary layer. To remove extraneous variability and facilitate comparison between configurations, the three versions share components and propulsion units to a high degree. The focus of the tests were to measure the aerodynamic BLI benefit over a range of flight conditions, including climb, level flight (cruise), and descent. Limited tests at high angle of attack, high yaw, and with single engine-out were also performed to verify acceptable operating characteristics at these more extreme points of the operating envelope.

The experimental measurements demonstrated an aerodynamic BLI benefit at the simulated cruise condition of $(8.6 \pm 1.8)\%$ in propulsive power at fixed nozzle area. The benefit at climb and

[1] September 2008 through March 2010
[2] November 2010 through May 2015

descent conditions was comparable. The BLI system also exhibited no adverse or unusual behavior at high angle of attack up to $\alpha = 12°$, large sideslip angles up to $\beta = \pm 15°$, and with single engine-out.

It must be stressed that the D8 wind tunnel tests are *not* conventional propulsion tests. The goal was *not* to determine the propulsor performance (*e.g.* thrust) under different installations, but rather to evaluate the *aircraft configuration overall performance*. Boundary layer ingestion (BLI) tightly couples the propulsion system with the body (airframe), and it was a deliberate choice not to separate the force contributions from each of these subsystems. The model is seen as a system, the components of which are not independent. The benefit of BLI is simply determined by the total power required to maintain flight, *e.g.*, zero net overall force for cruise at steady level flight.

For all the force data that was gathered during the tests, and the complementary numerical simulations that were performed, one could *in principle* decompose the measured overall forces into a number of contributions like gross thrust, ram drag, installation drag, powered lift, etc. However, doing so would require introducing assumptions and approximations that are extraneous to the core experimental measurements and the goal of the experiments, and therefore *reduce*, rather than strengthen, the value of the reported experimental results.

The Phase 2 experiments have advanced the technology-readiness level of the full-size D8 aircraft concept for the following reasons. First, the non-dimensional fan disk loadings and propulsive efficiencies in the experiments were representative of full-size aircraft. Second, the combination of large model size and appropriate boundary layer trips on all surfaces ensured turbulent flow, so that the results can be scaled to full-size aircraft Reynolds numbers. Third, the model was large enough to allow detailed flow-field measurements of propulsor inflows and outflows. Fourth, the use of electric motors allowed direct measurement of the flow power input for use as a surrogate for fuel burn. Finally, the high quality of the flow and force measurements in the 14×22 tunnel ensured accurate resolution of the aerodynamic differences between non-BLI and BLI configurations.

A computational effort was carried out in parallel and as a complement to the wind tunnel experiments. The entire wind tunnel test section with the powered model were simulated to allow a direct comparison with the measurements without wind tunnel corrections, thus increasing confidence in the experimental validation of the computational results.

3.2 Introduction

The contents of this Section 3.2 is adapted from [2].

3.2.1 The D8 Aircraft Concept

The D8 configuration [3] is characterized by a wide twin-aisle lifting fuselage producing close to 19% of the aircraft's total lift (compared to 13% for a 737-800). The wider fuselage enables the use of smaller and lighter wings and a pi-tail with a two-point structural support. The fuselage nose shape provides a positive nose-up pitching moment of roughly +0.084 in C_m, which reduces the required horizontal tail size. It also reduces the trimming tail down-force in cruise by +0.03 in C_L, thus shrinking the wing area. A low-sweep wing, which contributes to a lighter structure, is made possible by a cruise speed of Mach 0.72, compared to Mach 0.80 for the 737-800 aircraft. Numerous additional features contribute to the significant overall fuel-burn reduction as discussed in Section 3.8.1.

For the present work, the most important feature of the D8 configuration is that it allows the engines to be flush-mounted on the top rear of the fuselage, and to ingest roughly 40% of the fuselage boundary layer[3]. The engines are located near the fuselage's rear stagnation point, so

[3] as computed based on fuselage boundary layer kinetic energy defect

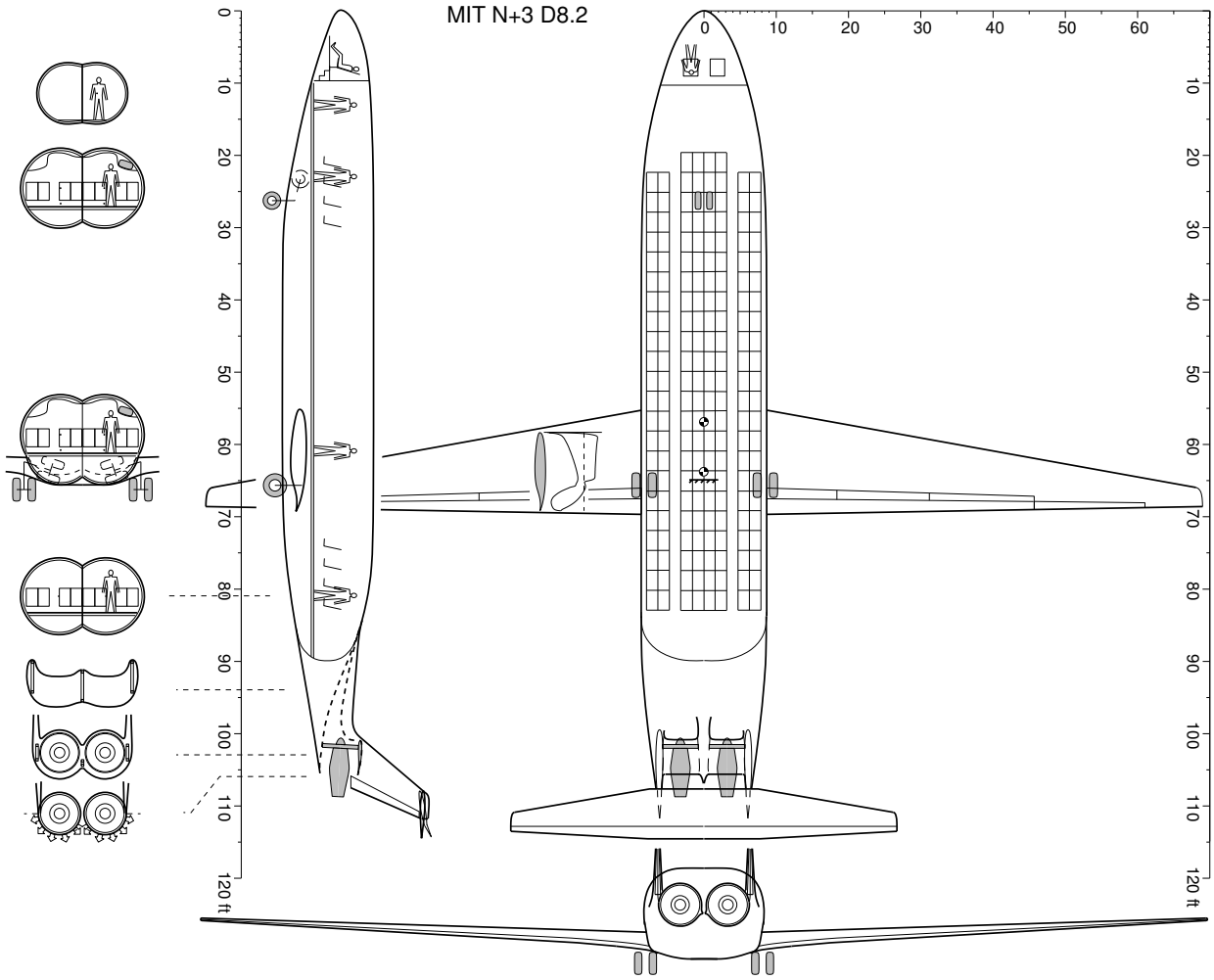

Figure 3.2: Three-view of D8.2 transport aircraft concept.

the fuselage performs much of the diffusion and flow alignment into the fans normally achieved by the nacelle of an isolated podded engine. As a result, the D8 nacelles are smaller, saving weight and reducing external wetted-area losses. The engine placement also enables a shorter and lighter landing gear, and allows the fuselage to provide noise shielding.

The design features described above are the key characteristics of the D8.2 aircraft concept shown in Figure 3.2. Compared to the equivalent 737-800, the D8.2 achieves a 36% reduction in fuel burn from the configuration alone, without the use of either advanced materials or advanced engine-core technology. During Phase 1 of the N+3 effort, additional technological advances expected to occur in the next 20–30 years were estimated to have the potential to yield fuel burn savings close to 65% relative to the 737-800 [1], as exemplified by the D8.6 aircraft concept. The focus of Phase 2 and this document is on BLI, one of the enabling technologies for the D8.2 aircraft, which could enter service in a shorter term.

During the Phase 1 study, the D8 BLI engine installation was designed at the conceptual level only. Because the geometry near the engines is complex, and includes integration with the rear fuselage and the twin vertical tails, there was a possibility for unexpected interference losses. A major goal of the Phase 2 effort, therefore, was to perform a detailed aerodynamic design of this

installation, and evaluate its performance experimentally and computationally to demonstrate that the configuration can be realized in an efficient and effective manner.

3.2.2 Boundary Layer Ingestion (BLI)

The theoretical benefit of boundary layer ingestion (BLI) on propulsive efficiency is well established, and has been analyzed using a number of different frameworks. The classical explanation dating back to Betz [4] is that a reduced inflow velocity of the propulsive stream-tube results in less power being required to impart a given momentum flow to the stream-tube. This approach was used by Smith [5], whose analysis suggested that power savings as large as 50% were possible for some combinations of inflow wake profiles and high propulsor disk loadings. For more practical disk loadings the savings were estimated to be a more modest 10% – 20%.

An alternative view of BLI as analyzed by Drela [6] is that it reduces the power dissipation in the overall flowfield, primarily by reducing the streamwise velocities and associated wasted kinetic energy left by the aircraft by "filling-in" the wake with the propulsor, as sketched in Figure 3.3. One advantage of this power balance approach is that it unifies all the power losses on the aircraft, both the surface boundary layer losses of the airframe and the propulsive losses of the power plant, without the need to resort to separate drag and thrust estimates. Indeed, one practical complication of BLI is that although the net streamwise force is well-defined, its decomposition into "drag" and "thrust" components is ambiguous. This is true even for non-BLI configurations where the airframe and propulsor pressure fields interact, although the ambiguity is especially severe in the case of BLI. In the power-balance framework, the design objective is then not to minimize engine power for a required thrust (equal to airframe drag), but rather to minimize engine power needed to produce a zero net streamwise force on the overall integrated airframe-propulsion system configuration. The latter is equivalent to minimizing the overall dissipation in the flowfield, specifically the airframe boundary layers and the propulsive jets. The engine thrust force and the airframe drag force do not need to be treated separately or even defined in this framework.

The theoretical benefit of BLI is likely to be mitigated to some extent by the unfavorable effect of the distorted propulsor inflow on the fan performance, with the effect depending on fan-blade Mach number, and also on the fan-blade Reynolds number to some extent. Since the N+3 experiments do not match the Mach or Reynolds numbers, it is necessary here to separate out the fan-efficiency effect from the propulsive-efficiency effect, which is also conveniently done using the power-balance framework.

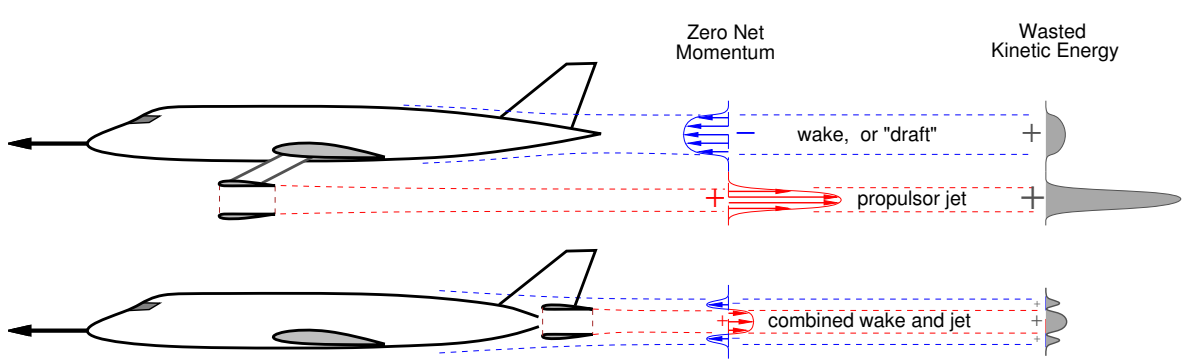

Figure 3.3: Illustration of power-saving benefit of boundary layer ingestion (bottom) compared to a conventional aircraft (top): reduction in axial velocities of combined wake and jet results in a reduction in wasted kinetic energy deposited in the flow.

The three types of mechanical power sources within a flowfield are net mechanical flow power P_K across propulsor inflow and outflow planes, power from moving surfaces, and volumetric "p dV" work within the flowfield, as described by Drela [6]. For the control volume chosen here, which fully envelops the propulsor, and in the low speed case, the sole remaining flowfield power source P_K is given by the volume flux of total pressure, *i.e.*,

$$P_K \;\equiv\; \oiint \left[p_\infty - p + \tfrac{1}{2}\rho \left(V_\infty^2 - V^2 \right) \right] \mathbf{V} \cdot \hat{\mathbf{n}} \; \mathrm{d}S \;=\; \oiint \left(p_{t_\infty} - p_t \right) \mathbf{V} \cdot \hat{\mathbf{n}} \; \mathrm{d}S \; . \tag{3.1}$$

The area integral is taken over the inflow and outflow planes of the propulsor with $\hat{\mathbf{n}}$ pointing into the propulsor, so that P_K is a measure of net engine flow power, and any losses internal to the propulsor are immaterial. This then separates the issue of fan efficiency from the aerodynamics of the BLI configuration, and the fan blading losses due to BLI can then be accounted for separately.

3.2.3 Wind Tunnel Testing Approach

The distinction between thrust and drag, and between (vectored) powerplant lift and airframe lift, are ambiguous for a configuration with integrated propulsors. The ambiguity is most obvious when the forces are defined in terms of surface pressure and shear forces, since the surface cannot be meaningfully subdivided into powerplant and airframe portions. Some ambiguity also appears when the forces are alternatively defined in terms of pressures and momentum flux changes on an outer control volume surface, since the streamtube passing through the propulsor has also interacted with the airframe and thus has both "thrust" and "drag" contributions. Extracting these contributions requires introduction of *hypothetical* expansions of the streamtube flow to ambient pressure at various points along the streamtube, and also requires assuming the amount of total pressure loss (if any) that would occur due to any mixing during these expansions.

To avoid all these force decomposition complications and uncertainties, in the present tests we chose *not* to make any such decomposition. Instead, we only consider the net streamwise and vertical forces, F_X and F_Z, and match their nondimensional values to those of the full-size aircraft. Specifically, in steady level cruise, F_X is exactly zero and F_Z is exactly equal to the aircraft weight, and the propulsor power needed to achieve these force values is the energy cost needed to fly. Any split of these forces into airframe and propulsor contributions would be immaterial in this relatively simple net-force and propulsor-power framework.

3.2.4 BLI Performance Parameters

As motivated by the preceding discussion, the appropriate power metric to compare BLI and non-BLI configurations is the mechanical flow power, P_K, defined in the power-balance framework. This section defines and discusses the various parameters used to quantify and evaluate performance.

Net Force Coefficients

The nondimensional forms of the streamwise and normal aerodynamic forces that are used here to define level flight cruise are

$$C_X \;\equiv\; \frac{F_X}{q_\infty \, S_{\mathrm{ref}}} \; , \tag{3.2}$$

$$C_L \;\equiv\; \frac{F_Z}{q_\infty \, S_{\mathrm{ref}}} \; . \tag{3.3}$$

Net Propulsor Power Coefficient

One method of P_K measurement was via surveys of the propulsor inflow and outflow planes. In this incompressible flow, the pressure fields and velocity magnitudes, together with flow directions, are used to calculate P_K from its definition (3.1) by appropriate numerical integration. This method of obtaining P_K is referred to as the *direct method*. The result is then nondimensionalized into the corresponding flow power coefficient

$$C_{P_K} \equiv \frac{P_K}{q_\infty V_\infty S_{\text{ref}}} . \tag{3.4}$$

Electrical Power Coefficient

An alternative way used to obtain the propulsor power P_K was via the measured electrical power P_E supplied to the motor, together with motor and fan efficiencies, η_m and η_f respectively, which were measured in separate off-line experiments using a motor dynamometer and a fan flow rig at MIT. The electrical power coefficient is defined as

$$C_{P_E} \equiv \frac{P_E}{q_\infty V_\infty S_{\text{ref}}} , \tag{3.5}$$

and the two power coefficients are related through

$$C_{P_K} = \eta_f \, \eta_m \, C_{P_E} , \tag{3.6}$$

which is the relation used in the *indirect method* to obtain P_K. The advantage of this method is that electrical motor power can be measured reliably and instantly, in contrast to the flow survey method that is relatively time consuming. The disadvantage of using (3.6) is that uncertainties in the off-line measurements of the motor and fan efficiencies introduce additional uncertainties in the resulting C_{P_K} values.

BLI Benefit

The primary objective of BLI is to reduce the propulsor flow power required to achieve a net streamwise force on the aircraft. Following Smith [5], we quantify the aerodynamic BLI benefit via the power saving coefficient PSC, which in terms of mechanical flow power is

$$PSC \equiv \frac{(P_K)_{\text{non-BLI}} - (P_K)_{\text{BLI}}}{(P_K)_{\text{non-BLI}}} \tag{3.7}$$

or in terms of the BLI to non-BLI flow power ratio

$$\mathcal{R}_{P_K} \equiv \frac{(P_K)_{\text{BLI}}}{(P_K)_{\text{non-BLI}}} = 1 - PSC . \tag{3.8}$$

Note that the BLI benefit is a function of the aircraft operating parameters C_L and C_X. In the experiments, these parameters were systematically varied by specifying the model angle of attack α, and the motor wheel speed, Ω. The BLI benefit value of most interest is the one corresponding to the simulated cruise condition, *i.e.*, when $C_L = 0.64$ and $C_X = 0$.

Propulsive Efficiency

A useful metric is the propulsive efficiency, which quantifies how efficient the propulsion system is at converting input energy into useful output. We define the propulsive efficiency to be the ratio

of net propulsive power delivered to the vehicle to the total power added to the flow. Thus,

$$\eta_p \equiv \frac{P_K - \Phi\text{jet}}{P_K} , \tag{3.9}$$

in which the jet dissipation Φjet is a measure of wasted kinetic energy in the jet flow [6]. With conventional, non-BLI, propulsion, the above definition of propulsive efficiency is equivalent to the traditional one, in that the numerator becomes equal to the thrust power and the denominator becomes equal to the kinetic energy rate deposited in the flow [7].

3.2.5 Bases of Comparison of BLI and Non-BLI Configurations

Given a non-BLI propulsor with some jet velocity, mass flow, and nozzle area, there is no unique way to choose an "equivalent" BLI propulsor as a basis for comparison. One rational constraint is that the net force (added momentum flow) be the same. However, this is not sufficient: the mass flow must also be constrained in some manner, typically via the nozzle area which can be thought of as a surrogate for propulsive efficiency—as nozzle area increases, jet velocity decreases, and hence propulsive efficiency increases. Each different nozzle area therefore results in a different BLI propulsor mass flow and performance, and a different BLI benefit value.

Specific choices are to make the comparison at equal mass flow, equal nozzle area, equal jet velocity, or equal power[4]. The BLI benefit is manifested differently for each of these comparisons as illustrated in Figure 3.4. For example, at constant nozzle area, the BLI configuration requires roughly 7% less propulsive power. At the other extreme, a BLI propulsor that requires the same amount of power has a smaller nozzle with 40% less area, which would certainly produce a system-level weight benefit. Since the BLI and non-BLI wind tunnel models of the Phase 2 program shared the same physical propulsor units, the comparison was performed at the same nozzle areas, which is expected to give roughly a 7% BLI benefit as indicated in Figure 3.4.

[4] The equations that define an equivalent BLI propulsor are presented in Section 3.10.2 and used to generate Figure 3.4

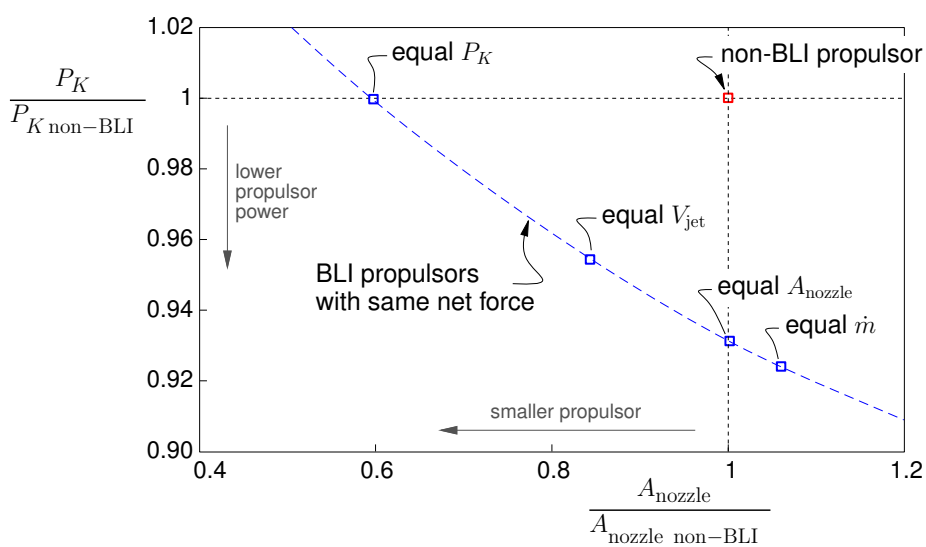

Figure 3.4: Range of D8 BLI propulsor power versus nozzle area, relative to values of a baseline non-BLI propulsor.

Another benefit of BLI, which is not represented in Figure 3.4, is the reduction of external nacelle losses. On conventional engine installations the nacelle aligns the inflow with the engine axis, and also diffuses the inflow to approximately Mach 0.6, which is required for maximum efficiency with a typical front fan. The nacelle's diffusion into the fan produces supervelocities on the nacelle exterior, resulting in additional nacelle viscous dissipation losses (or additional nacelle drag in the conventional thrust-and-drag framework). On the D8 installation these flow-alignment and flow-diffusion functions are performed mainly by the rear fuselage, allowing the D8 nacelles to be minimal in thickness (see Figure 3.7) and have lower external velocities compared to a conventional nacelle. Furthermore, the D8 nacelles also cover only the upper half of each fan and thus have a fraction of the wetted area. Consequently their viscous losses are only about a quarter of those for a conventional nacelle [3]. This is then expected to increase the aerodynamic BLI benefit above the 7% value indicated in Figure 3.4. A major goal of this study is to quantify this aerodynamic benefit, which is the combination of (i) the propulsive benefits of reducing jet and wake losses, and (ii) the reduction of the external nacelle surface friction losses.

Finally, it is worthwhile to note that these aerodynamic benefits of BLI are not the only ones that can be realized in practice. To put the results of the present study in the overall airplane-design context, additional system-level benefits, which are enabled by adopting a BLI propulsion system, must also be considered. The estimation of system-level benefits was not part of the Phase 2 effort, but they are estimated and discussed in some detail in Section 3.8.1 and Reference [2].

3.3 Approach

3.3.1 D8 Model Configurations

The contents of this Section 3.3.1 is adapted and expanded based on [2].

The wind tunnel experiments seek to measure the aerodynamic benefit of BLI for the D8 aircraft, by comparing the performance of two 1:11 scale[5] powered wind tunnel models representative of the full-size D8. The *non-BLI, or podded, configuration* model, shown in Figure 3.9, has propulsors on rear-mounted pods that ingest uniform freestream flow, and serves as the baseline. The *BLI, or integrated, configuration* model, shown in Figure 3.10, has the same physical propulsors but they are embedded into the aft top fuselage to ingest part of the fuselage's boundary layer. A third *unpowered configuration* model, shown in Figure 3.6, was also tested. It is the same as the non-BLI configuration, except the propulsor pods are removed. It was used to measure the aerodynamic characteristics of the airframe to allow a more complete aerodynamic characterization of the aircraft. Drawings of the model parts can be found in Section 3.10.

Common Geometry

The unpowered, non-BLI (podded), and BLI (integrated) models share the same physical components, except for the removable aft 20% of the fuselage and attached vertical tails—the horizontal tail is common. The front fuselage and wing geometry were defined during the Phase 1 work [1,3]. CFD evaluations showed no substantive reasons for altering the design, and hence the front fuselage and wing were used unchanged for the 1:11 scale model experimental investigation. The rear 20% of the fuselage and propulsion sections were designed as part of the present Phase 2 work. The schematic in Figure 3.5 illustrates the model's fuselage cut location aft of which the tails of the non-BLI and BLI configurations differ. Table 3.1 gives size characteristics of the 1:11 scale models.

Following usual procedures in sub-scale testing, all the model components are tripped to obtain turbulent boundary layers—wings, fuselage, tail surfaces, and propulsor nacelles. The surface trips

[5] 1:11 scale nominally. The actual scale is 1:11.16.

Table 3.1: Reference dimensions of the 1:11 D8 models.

Dimension	Value	
Reference area, S_{ref}	1.088 m^2	1686.00 in^2
Reference chord, c	0.273 m	10.75 in
Span, b	4.097 m	161.3 in
Overall length of non-BLI configuration	3.218 m	126.7 in
Overall length of BLI configuration	3.138 m	123.6 in
Propulsor fan diameter	0.144 m	5.65 in

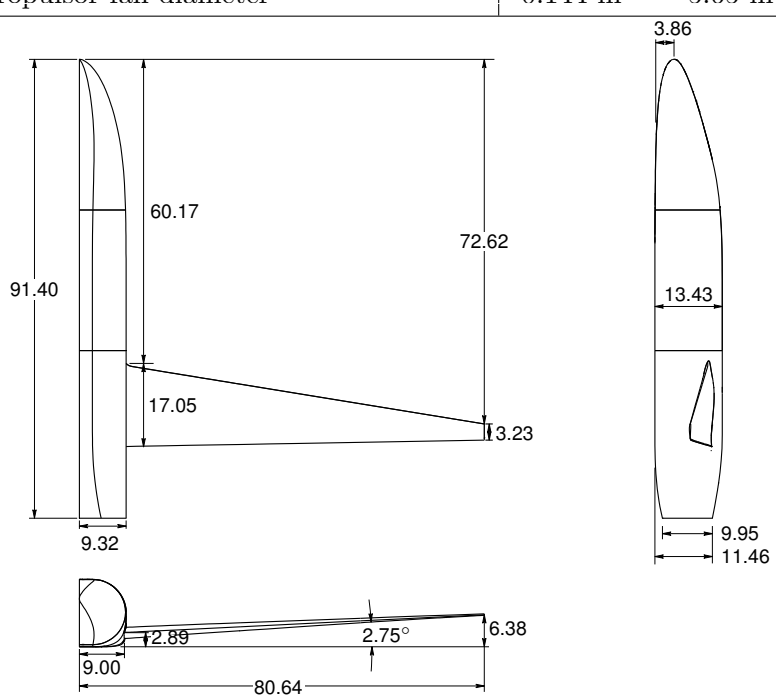

Figure 3.5: Model geometry common to all configurations. Units: inches.

consisted of 0.125 in wide masking tape in several layers, for a total thickness of 0.013 in on all surfaces, except for the fuselage bottom surface which has two trip arcs at 0.013 in and 0.015 in thickness each. Adequacy of the trips was determined by tracking the drag of the unpowered configuration as the thickness of the trip strips was gradually increased by adding successive layers of tape. As thickness was increased, the initial drag coefficient changes were significant, and the process was stopped once these changes became negligible. Further confirmation of the adequacy of the trips was obtained by comparing drag at different tunnel speeds: decreasing drag coefficient is observed with increasing Reynolds number over most of the range of angles of attack studied, as expected when boundary layers are turbulent.

Unpowered Configuration

The unpowered configuration, shown in Figure 3.6, consists of the D8 common-body and the tail utilized by the podded configuration without pylons or propulsors. The tail section was designed to minimize flow acceleration under the pi-tail (between the verticals) and to keep the rear of the fuselage unloaded in order to preserve the overall configuration spanwise loading and pitching

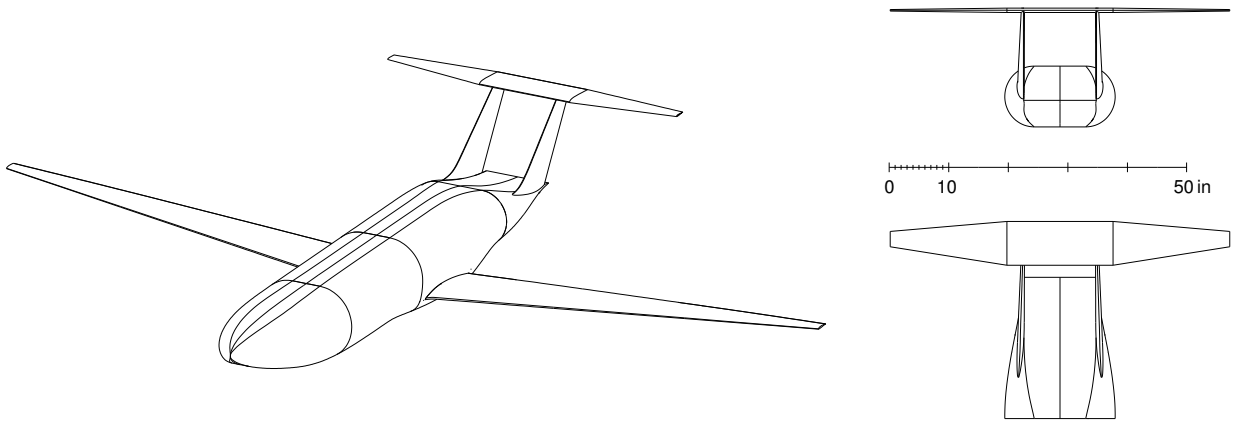

Figure 3.6: Unpowered configuration model geometry.

moment. Care was also taken to ensure the vertical tails were unloaded in zero-yaw flow conditions. This was achieved by toeing out[6] the lower (root) profile of the vertical tails by 3° and toeing out the upper (tip) profile by 1.5°.

Electric Propulsors

Both podded and integrated model configurations are powered by the same two propulsor units, each consisting of a fan stage (rotor and stator), motor, center-body, aluminum housing, nozzle, and power electronics. Using the same propulsor units largely removes variability of the propulsion elements between the two configurations, and thus gives the best possible evaluation of the benefits of BLI alone, separate from any extraneous effects.

Commercially available off-the-shelf fan stages were used in the propulsors. These were carbon-fiber composite TF8000 ducted fans manufactured by Aeronaut primarily for use on RC airplanes. The 5.65 in diameter rotor has 5 blades, and the stator 4 blades. Each propulsor has a 2 kW Lehner Motors 3040-27 brushless DC electric motor. Each motor and its controller is powered by a Sorenson 2 kW DC power supply with a 240 V, 3-phase input.

The propulsors were designed such that the rotor, stator, internal ducting, center-body, nozzle, and motor comprise a removable piece separate from the outer nacelle, thus allowing them to be interchanged between the non-BLI and the BLI configurations. Each physical propulsor unit had a designated side (on the model's left or right side) and was utilized exclusively on that side throughout the investigation. Figure 3.7 shows the propulsors with the podded or integrated support nacelle structure indicated in gray.

In order to be able to change nozzle area (and therefore propulsive efficiency), three plugs of different sizes were manufactured. They were designed to provide minimum losses [8], and are shown in Figure 3.8. The corresponding nozzle areas are given in Table 3.2.

[6] angle between fuselage longitudinal direction and airfoil chord

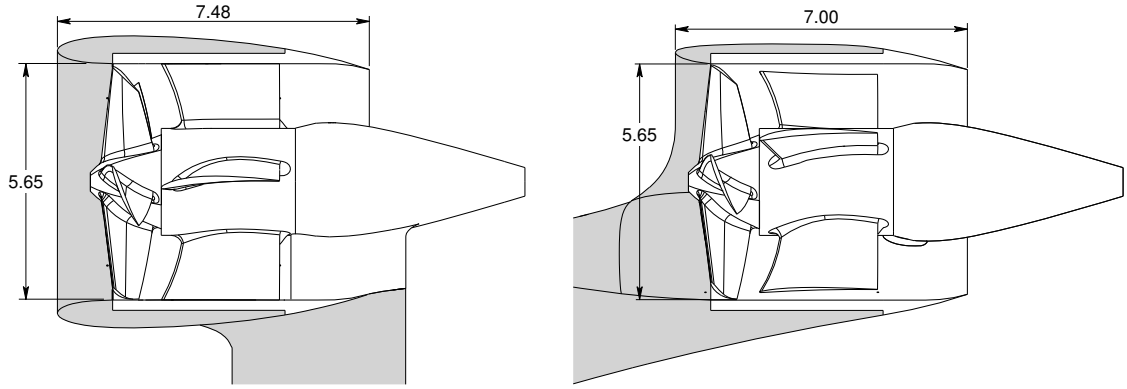

Figure 3.7: Non-BLI (left) and BLI (right) model propulsors. The unshaded parts are common to both configurations, and the grayed regions show the nacelles and support structures specific to each configuration. Units: inches.

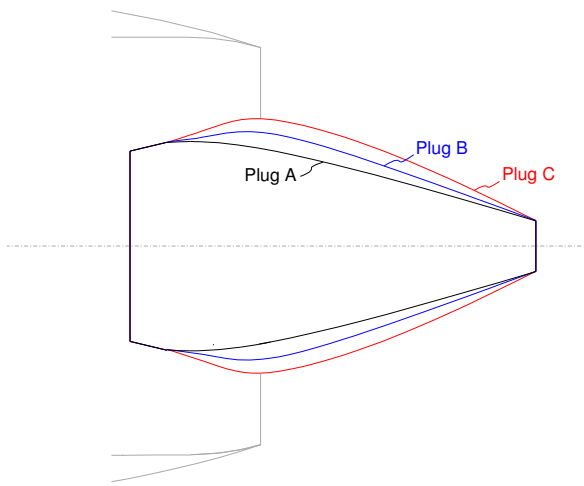

Figure 3.8: Propulsor plugs used to change nozzle areas.

Table 3.2: Nozzle area to fan area ratios; $A_{\text{fan}} = 0.0159\,\text{m}^2$.

Plug	Ratio of nozzle area to fan area $A_{\text{nozzle}}/A_{\text{fan}}$
A	0.679
B	0.604
C	0.535

Non-BLI (Podded) Configuration

The non-BLI, or podded, configuration has the propulsor units embedded in axisymmetric nacelles, mounted on pylons at the rear of the aircraft as shown in Figure 3.9. The length of the pylon and angle at which it intersects the fuselage were chosen to give a very small static pressure field interaction between the propulsor and the body. The intent is to make this installation represent an "isolated" propulsion system to serve as a control case to which the BLI installation can be compared. The pylon airfoil cross-section was made as small as the installation and structure allowed. The intent was to make the non-BLI configuration as efficient as possible, so that the BLI benefits would not be artificially inflated in the comparison with the BLI configuration.

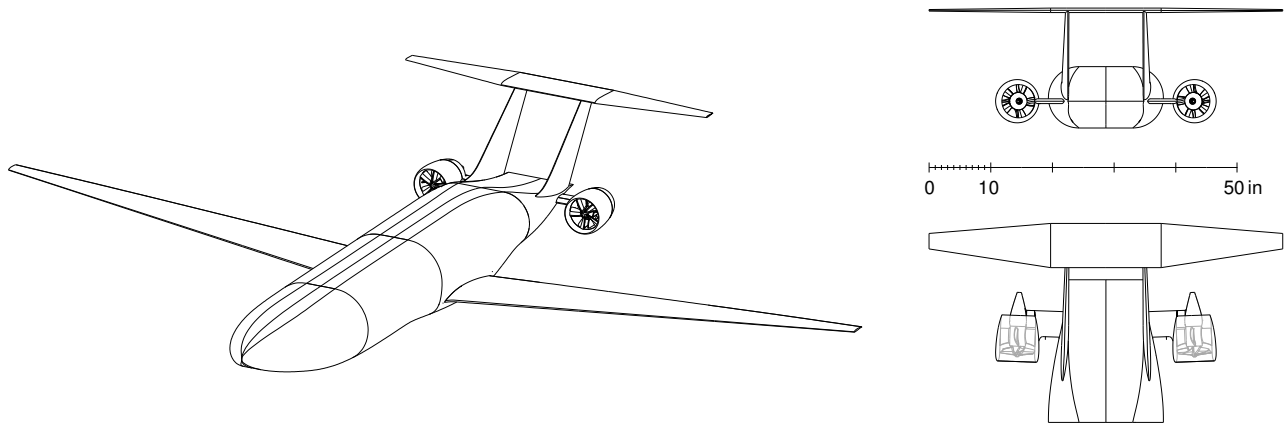

Figure 3.9: Non-BLI, or podded, configuration model geometry.

BLI (Integrated) Configuration

The BLI, or integrated, configuration has the propulsor units embedded in the rear fuselage with added upper-half nacelles, as in Figure 3.10. The whole fuselage rear (upper and lower surfaces), vertical tails, and propulsor nacelles were designed together as an aerodynamically integrated geometry that provides the required diffusion upstream of the fan, while avoiding any obvious aerodynamic interference between the upper-half nacelles and the tail surfaces. It must be emphasized that this aerodynamic design is considered only "good enough", in that the only design objectives were the necessary diffusion and the elimination of any obvious problems such as unnecessary local overspeeds and flow separations. It is not "optimal" in any sense, and could likely be improved with more extensive design work in the future, possibly using multidisciplinary design and optimization methods. Hence, the BLI benefit values measured in this program are considered lower bounds, and could possibly be increased with additional aerodynamic design work.

The vertical tails differ slightly in twist distribution from the non-BLI configuration, to align them with the local flowfield of the rear fuselage-propulsion system combination. The half-nacelles over the BLI propulsors were designed with a smaller thickness and leading edge overhang than the podded nacelles as can be seen in Figure 3.7. The specific aerodynamic design objective for shaping the half-nacelles was to have an acceptable overspeed inside the nacelle lip at high engine power, to obtain a positive pressure coefficient, and zero, or weak, streamwise pressure gradients over the outside nacelle surfaces. Positive pressures and weak pressure gradients minimize skin friction losses, and also eliminate the need for fillets in the relatively tight inside corners between the two nacelles and between each nacelle and the adjoining vertical tail.

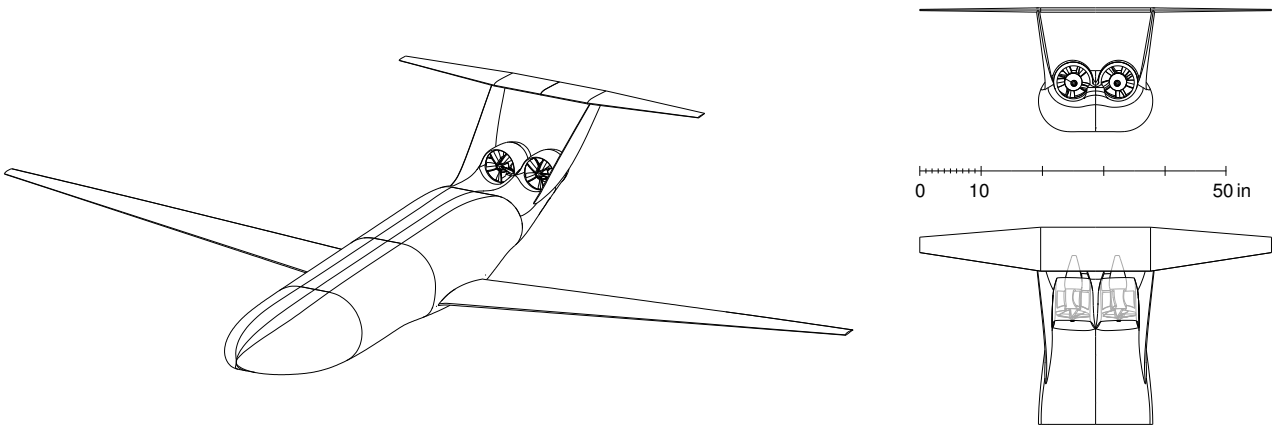

Figure 3.10: BLI, or integrated, configuration model geometry.

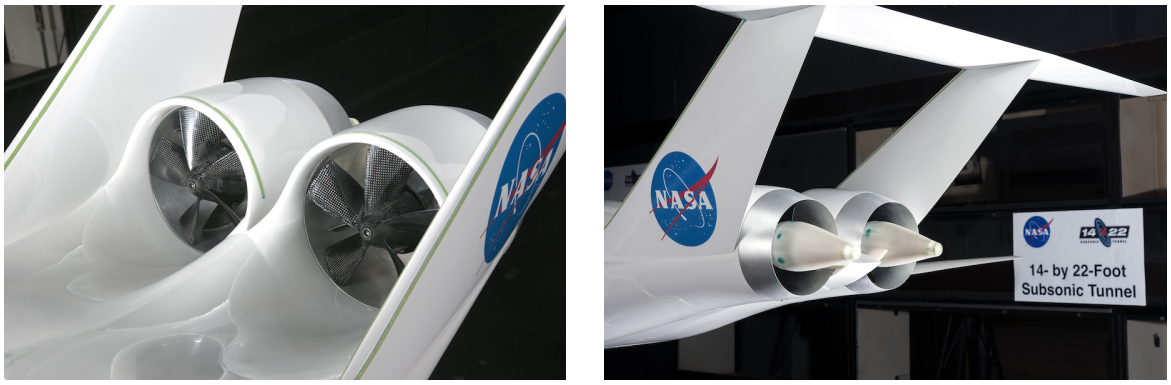

Figure 3.11: Close view on the BLI configuration model tail in NASA Langley 14–by 22–Foot Subsonic Tunnel during the August-September 2013 experiments (Photo credits: NASA/George Homich).

3.3.2 Experimental Approach

The contents of this Section 3.3.2 is adapted and expanded based on [2].

Model and Tunnel Axes

Figure 3.12 shows the two axes systems considered in this investigation.

- The *model (or body) axes* referred to by the lower case letters (x, y, z) are linked to the aircraft: the x-direction is aligned with the fuselage's longitudinal direction, and the y-direction is defined spanwise (from fuselage's symmetry plane towards the right wing tip). The model force balance reports forces in these same axes.

- The *tunnel (or wind) axes* referred to by upper case letters (X, Y, Z) are set by the tunnel: the X-direction is aligned with the tunnel's horizontal streamwise direction (pointing downstream), and the Z-direction is vertical pointing up.

Note that with a zero sideslip angle the y and Y directions are the same, while (x, z) and (X, Z) are related by a rotation (along the y or Y axis) by the angle of attack α.

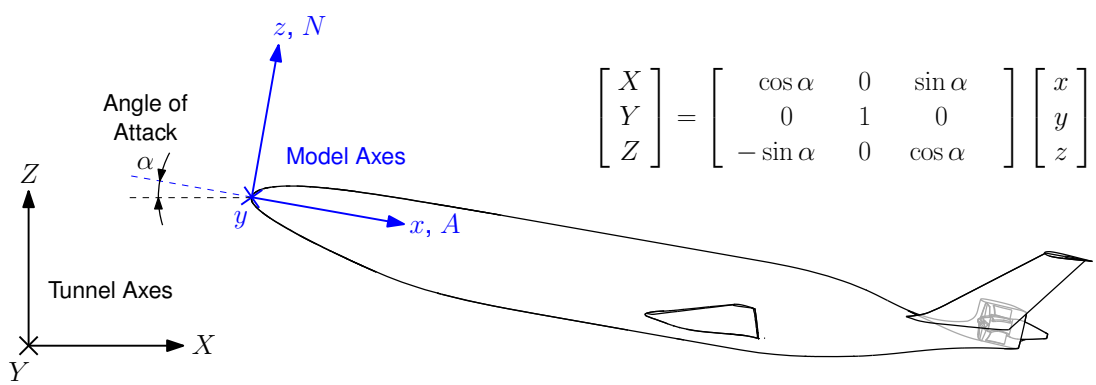

$$\begin{bmatrix} X \\ Y \\ Z \end{bmatrix} = \begin{bmatrix} \cos\alpha & 0 & \sin\alpha \\ 0 & 1 & 0 \\ -\sin\alpha & 0 & \cos\alpha \end{bmatrix} \begin{bmatrix} x \\ y \\ z \end{bmatrix}$$

Figure 3.12: Model and tunnel axes. The x, z model axes are alternatively denoted by A, N.

Wind Tunnel

Measurements were conducted in the 14– by 22–Foot Subsonic Tunnel at the NASA Langley Research Center operating in closed test section mode. The test section has a rectangular cross-section of 14.5×21.75 ft[7]. Figure 3.13 shows a schematic of the model inside the tunnel. The model is attached near the wing's quarter chord to a pitch-head and trunnion mounting system that controls angle of attack as well as model height.

The model is vertically positioned so that a reference point near the wing root is held at the center of the tunnel as the angle of attack is changed. The uncertainty on model position within the test section (vertically and spanwise) is ±1 in. At zero angle-of-attack, the 1:11 scale D8 model has a wind-tunnel blockage[8] of approximately 0.5%.

[7] The tunnel sidewalls slightly diverge, resulting in a width of 21.98 ft at the test section exit 50 ft downstream.
[8] ratio of model to test section cross-sectional areas

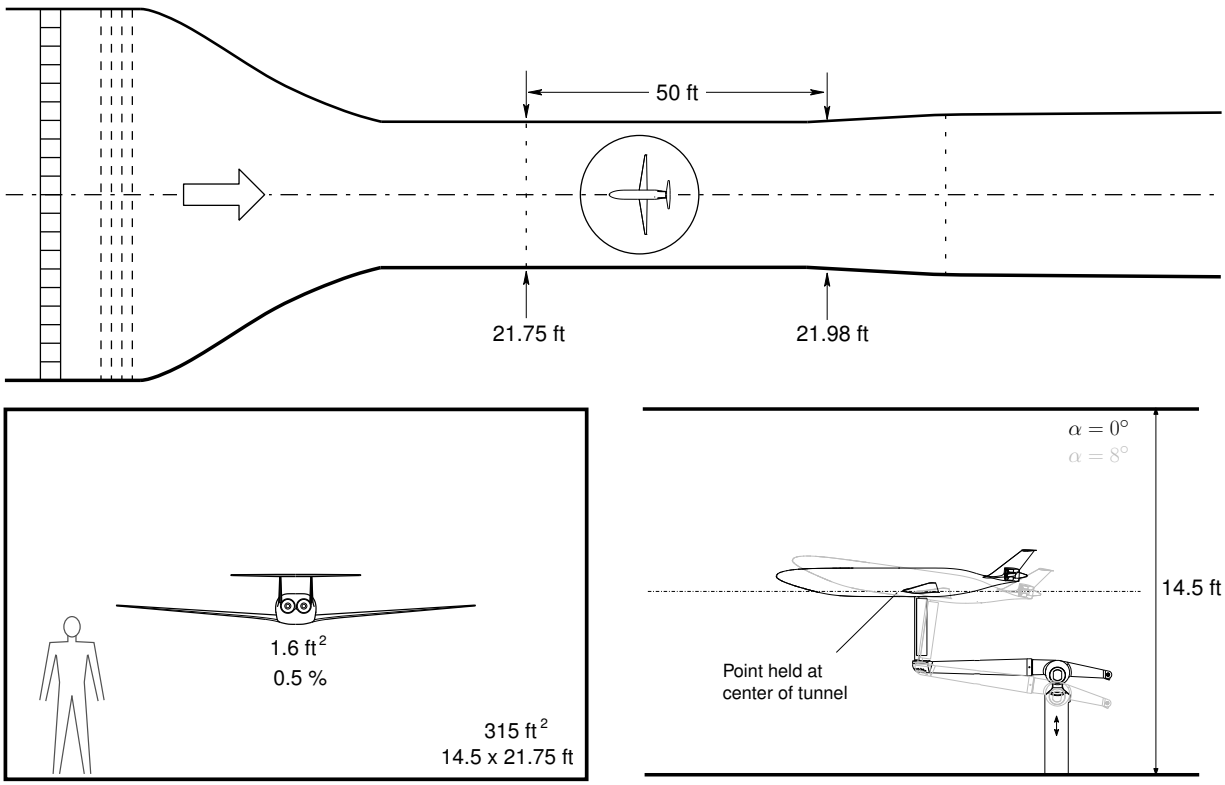

Figure 3.13: Schematic views (top, rear, side) of the D8 model in the test section of NASA Langley 14– by 22–Foot Subsonic Tunnel (top view adapted from [9]).

Test Procedures

In the first wind tunnel entry in 2013, the majority of the tests were performed at the tunnel speed of 70 mph, or Mach 0.092. Two other speeds were used to evaluate Reynolds numbers effects: 42 mph and 56 mph. In the second tunnel entry in 2014, tests were also performed at 84 mph, or Mach 0.110. The reference quantities for these speeds are listed in Table 3.3. Throughout this document, the terms freestream, or tunnel, velocity are used to refer to the uncorrected test section velocity provided by the facility's system.

The common body of the D8 was mounted on the pitch head and trunnion via an internal force

Table 3.3: Tunnel nominal operating conditions: freestream velocity V_∞, dynamic pressure q_∞, Mach number M_∞, and Reynolds number based on reference chord Re_c, assuming standard sea level operation.

V_∞		q_∞		M_∞	Re_c
(mph)	(m/s)	(psf)	(Pa)		
42	18.8	4.5	216	0.055	3.6×10^5
56	25.0	8.0	382	0.074	4.6×10^5
70	31.3	12.5	598	0.092	5.7×10^5
84	37.5	18.0	861	0.110	6.8×10^5

Table 3.4: Propulsor fan wheel speeds for power-sweep runs.

Ω (RPM)	5 250	8 000	10 600	12 250	13 500	14 500
U_{tip}/V_∞ at $V_\infty = 42\,\text{mph}$	2.11	3.21	4.26	4.92	5.42	5.82
U_{tip}/V_∞ at $V_\infty = 56\,\text{mph}$	1.58	2.41	3.19	3.67	4.07	4.37
U_{tip}/V_∞ at $V_\infty = 70\,\text{mph}$	1.26	1.93	2.55	2.95	3.25	3.49
U_{tip}/V_∞ at $V_\infty = 84\,\text{mph}$	1.05	1.61	2.13	2.46	2.71	2.91

balance at the beginning of each test campaign and was not removed until the conclusion of the tests—changes between the unpowered, podded, and integrated configurations were undertaken in situ. When in a powered configuration, the center of gravity of the model is located approximately 5 in aft of the force balance reference center.

After any configuration change, a load check was performed to verify the model instrumentation, and in particular to rule-out any fouling between metric and nonmetric components. Weight tares, or wind-off force readings, were obtained before and after every set of runs.

The unpowered configuration was tested first: angle of attack sweeps were performed from 0° to 8° at each tunnel speed. For the podded and integrated configurations, the angle of attack was held constant while the propulsor power was varied by setting the fan wheel speed to the values specified in Table 3.4. In addition to these power sweeps, a number of pressure rake and five-hole-probe surveys were performed, each at fixed angle of attack and fan wheel speed.

Force Measurements

The forces and moments on the model were measured using the NASA 843A six-component internal force balance, calibrated at NASA Langley specifically for this test. They are reported in the balance axes system, and rotated to the freestream axes using the angle of attack measured by a NASA Q-flex accelerometer mounted on the model near the balance location. The force balance data is taken at 50 Hz over 8 seconds, and each data point is thus an average of 400 samples. Since we are interested in relative changes between non-BLI and BLI configurations, and given the small model blockage, no wind tunnel corrections are applied and forces are reported as uncorrected values.

The force balance measures the axial and normal forces, F_A and F_N, defined in the body axes. These are converted to tunnel-axes forces through rotation by the angle of attack, α, namely

$$F_X = F_A \cos\alpha + F_N \sin\alpha \ , \tag{3.10}$$

$$F_Z = -F_A \sin\alpha + F_N \cos\alpha \ . \tag{3.11}$$

The forces have the model weight contributions removed using wind-off weight tare measurements, so that F_X and F_Z are the aerodynamic forces on the entire model, including its propulsors, and these depend on the propulsor power setting P_K, and the model's angle of attack α. Hence, the measured forces are of the form

$$F_X(P_K, \alpha) \ , \quad F_Z(P_K, \alpha) \ ,$$

which after the nondimensionalizations (3.2)–(3.4) become

$$C_X(C_{P_K}, \alpha) \ , \quad C_L(C_{P_K}, \alpha) \ .$$

The steady level cruise condition is defined by

$$C_X(C_{P_K}, \alpha) = 0 \,, \tag{3.12}$$

$$C_L(C_{P_K}, \alpha) = C_W \,, \tag{3.13}$$

where $C_W \equiv W/(q_\infty S_{\text{ref}})$ is the normalized weight of the aircraft in question. The present experiments used $C_W = 0.64$, which is the design cruise value for the full-scale D8 aircraft.

The wind tunnel models had fixed solid horizontal tails, so there was no provision to adjust the model's pitching moment during the experiments, and no correction was made to the data in order to bring it to a zero pitching moment condition. This is justified by the fact that such trimming would have a negligible effect on the main quantity of interest, namely the BLI benefit at cruise, as analyzed and discussed in Section 3.5.6.

Electrical Power Measurements

The electrical power drawn by the propulsors is calculated from the continuous reading of voltage, v, and current, i, out of the power supply: $P_E = i\,v$. The electrical power coefficient is then given by its definition (3.5). The fan wheel speed is determined from the motor controller voltage frequency.

Flow Surveys

For the 2013 tunnel tests, a rotating rake of 22 total pressure tubes was constructed and used to survey the flow just upstream of the BLI fan and just downstream of the nacelle exit plane, as shown in Figure 3.14. The rake is driven by a small stepper motor via a timing belt, and the entire rake mechanism is mounted on a strut attached to the pitch-head behind the model. The foot of the rake contacts the model surface to precisely index its position relative to the model. Since the rake indexing foot applies an unknown force to the model, force data is not collected while the rake system is in place. Another rake of static tubes was also used in a separate survey to measure the static pressure field at the same survey plane. A detailed description of both the total-pressure and static-pressure rakes, as well as the rake mounting and driving system can be found in References [10] and [11].

One useful feature of the rake system is that because all 22 tubes are sampled simultaneously, the required survey test time is correspondingly shorter by this same factor than if a single probe were used. The main disadvantage is that the rakes provide only the total pressure p_t and the speed $V = |\mathbf{V}| = \sqrt{2(p_t - p)/\rho}$ via total and static pressures. They do not provide the direction of the velocity vector $\mathbf{V}$, which is needed to evaluate the direction cosine of the $\mathbf{V} \cdot \hat{\mathbf{n}}$ product in the P_K definition (3.1). The distribution of this direction cosine over the survey plane must instead be assumed known or estimated from computations.

To eliminate the uncertainty in P_K from the assumed flow direction, the 2014 tests included surveys using a single Five Hole Probe (FHP), which simultaneously measures p_t, p, and all three components of the velocity vector $\mathbf{V}$. The greater survey times required by the FHP were considered to be worthwhile.

A "theta–theta" traverse system was designed and built to move the FHP over the propulsor inlet and exit survey planes. It was composed of two arms each linked to a stepper motor that rotates them independently in order to reach any desired point along a plane. Like the earlier rotating-rake system, the theta–theta system could be indexed directly to the model near the measurement plane, and thus permit more accurate probe positioning than would be possible with conventional X–Y traverse frame systems. More details on the FHP survey system can be found in Reference [12].

Although the FHP did provide the necessary flow data over most of the survey planes, it was

found to have unacceptable errors in p and $\mathbf{V}$ inside the shear layers. The problem was due to the p_t gradient, or equivalently the transverse vorticity components inside the shear layer. Every FHP is calibrated in uniform flow, and pressure differences reported by a pair of opposing side ports on the probe are attributed to the flow being angled relative to the probe axis, and <u>not</u> to any transverse p_t gradient. This is equivalent to assuming the transverse vorticity is sufficiently small. More precisely, the transverse vorticity parameters

$$\bar{\Omega}_y \equiv \frac{R}{V}\frac{\partial V}{\partial z} \quad , \qquad \bar{\Omega}_z \equiv -\frac{R}{V}\frac{\partial V}{\partial y}$$

where R is the probe diameter and y, z are the two directions transverse to the flow, are assumed to be negligibly small,

$$\bar{\Omega}_y \ll 1 \, , \, \bar{\Omega}_z \ll 1 \, .$$

In the propulsor-exit flows in our wind tunnel models, the shear layer thicknesses were comparable

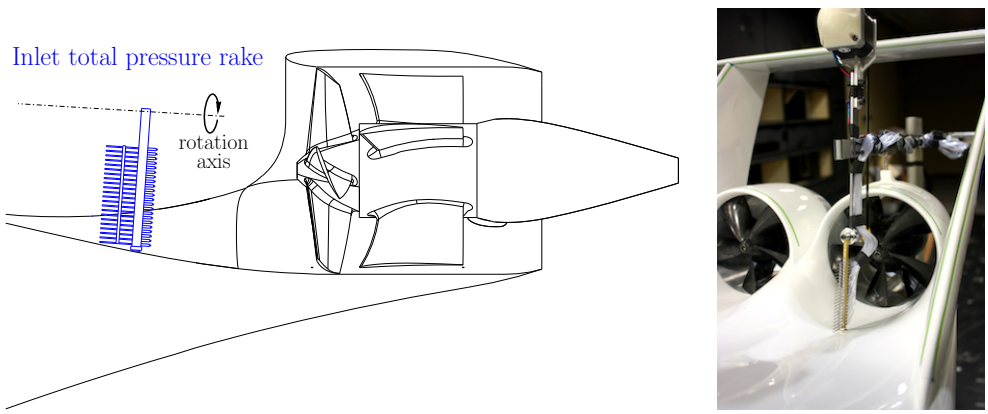

Figure 3.14: Schematic (left) and picture (right) of total pressure rotating rake system for surveying the flow ingested by the BLI configuration propulsor.

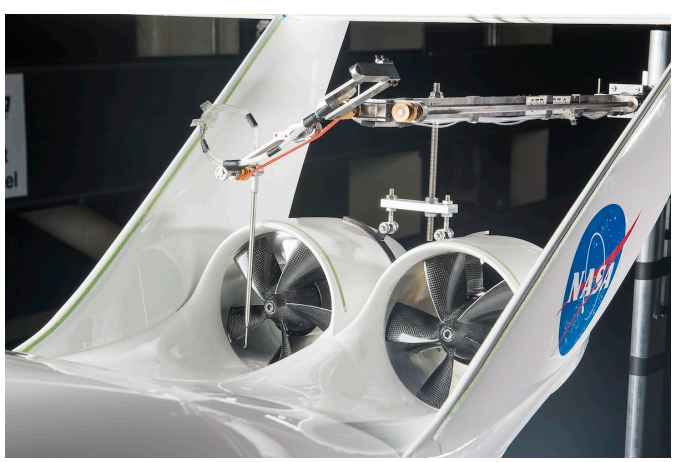

Figure 3.15: Picture of five-hole-probe survey system installed on the integrated configuration for surveying the flow ingested by the BLI propulsors (Photo credit: NASA/George Homich).

to R, and the change in V across each layer comparable to V itself, so that $\bar{\Omega}_y$ or $\bar{\Omega}_z$ were not small. As a result, the FHP calibration tables reported obviously incorrect flow angles inside the shear layer, sometimes 40° away from the propulsor axis. However, inside and outside the propulsive jet, where $\bar{\Omega} \ll 1$ did hold, the data from the FHP was quite smooth. Since the flow angles across the jet shear layer must be smooth and continuous, the flow angles reported by the FHP over the shear layer were interpolated across the shear layer from inside and outside the jet. The P_K could then be computed from (3.1) using numerical integration with some confidence. Similarly, regions with nonphysical flow angles were reported by the FHP at the propulsor inlet plane in some of the off-design conditions; however, the cruise inlet flow was appropriately resolved and thus integrated to obtain P_K without the need for FHP angle corrections.

3.3.3 Post-Processing of Experimental Data

This section details the processing that was done on the raw data collected during the wind tunnel tests in order to compute the quantities pertaining to the D8 model performance.

Run Types

Three types of runs were performed during the wind tunnel tests at NASA Langley:

(i) Angle of Attack Sweeps: This type of run was performed for the unpowered configuration. It is taken by setting the freestream conditions to the desired uncorrected tunnel velocity V_∞. The model angle of attack, α, is then varied and the forces on the model recorded at each angle. The angle is increased from 0° up to 8°, and then brought back down to 0°, in increments of 1°. Thus, one angle-of-attack sweep run is made of 18 points, two at each of the nine angles $\{0°, 1°, 2°, 3°, 4°, 5°, 6°, 7°, 8°\}$.

(ii) Power Sweeps: This type of run was performed for the powered configurations (non-BLI and BLI). It is taken by setting the freestream velocity, V_∞, and the model angle of attack, α. The power input to the propulsors is then varied by setting the wheel speed to a series of values (those in Table 3.4 plus that giving $C_X = 0$), and recording the forces at each power level.

(iii) Flow Surveys: This type of run was performed for the powered configurations. The survey system is installed (attached to the model support system and indexed on the model), and then the tunnel brought to the desired velocity, V_∞. The model angle of attack, α, and the propulsor wheel speed, Ω are set. The survey is then started and the survey system moves the probe (either pressure rakes or five-hole-probe) to the desired locations, where a data point is taken to record the pressures. Each survey at a set angle of attack and power level constitutes one run.

A full set of data is recorded at each point on all the types of runs, including freestream conditions, forces and moments, electrical power input to the motors (via current and voltage), fan wheel speed, differential pressures at all the pressure ports (on the fuselage and propulsor inner walls). Note however that the forces and moments recorded during flow survey runs are not used, since the survey system rests on the model and generates nonaerodynamic forces (fouling).

Table 3.5 lists the most important variables recorded by the data acquisition system. A comprehensive list of the recorded quantities is provided in Section 3.10.1, together with the equations used to compute all quantities of interest.

Table 3.5: Quantities directly recorded during the tests at NASA Langley 14– by 22–Foot Subsonic Tunnel.

Quantity	Description
α	Model angle of attack, and angle of balance's A axis relative to tunnel's X axis
q_∞	Freestream (tunnel) dynamic pressure[9]
V_∞	Freestream (tunnel) velocity[10]
F_A	Axial aerodynamic force in balance frame (wind-off weight tare removed)
F_N	Normal aerodynamic force in balance frame (wind-off weight tare removed)
F_X	Net aerodynamic streamwise force, $F_X = F_A \cos\alpha + F_N \sin\alpha$
F_Z	Net aerodynamic vertical force, $F_Z = -F_A \sin\alpha + F_N \cos\alpha$
P_E	Electrical power supplied to propulsor motors[11]
Ω	Fan (or motor) wheel speed

Data Acquisition

All data pertaining to the propulsors, to pressure ports on the model and propulsors, and to pressures recorded by the survey instrumentation is recorded by a desktop computer specifically brought by the MIT team to Langley for data-acquisition. It is linked to the propulsor electronic boxes and to the model pressure sensors. The 14– by 22–Foot Subsonic Tunnel data acquisition system records the freestream conditions, the model angle of attack, and the forces and moments from the internal model balance. The two data-acquisition systems are synchronized, and the Langley system is triggered by the MIT desktop to record data as needed. We will refer to these two linked computers as the data acquisition system.

Correction to Match C_L

To evaluate the aerodynamic benefit of BLI at cruise condition (zero net streamwise force), it is appropriate to compare the power required by BLI and non-BLI configurations *at the same overall vertical force coefficient* C_L. However, it was found during testing that for a fixed support-system angle of attack, varying propulsor power by an amount ΔC_{P_E} caused the model's angle of attack to change slightly by an amount $\Delta\alpha$, due to the compliance of the model's force balance. This angle change, together with the propulsor inflow-induced added lift on the rear fuselage, then also caused the lift coefficient to change by an amount ΔC_L. These sensitivities of $\Delta\alpha$ and ΔC_L to ΔC_{P_E} are shown in Figure 3.16. Note that the sensitivities are greater for the BLI configuration, mainly due to the reduced pressure on the top aft fuselage from the propulsors at high power, which increases the lift and induces a pitch-down moment.

A typical data run consisted of fixed tunnel speed V_∞, and a fixed α (set when the propulsors were at idle power, roughly 5 000 RPM wheel speed), and during the run the propulsor power was then varied in power across its full range. This power sweep produced the small $\Delta\alpha$ changes occurring during the run, as described above. Although this $\Delta\alpha$ could have been removed by adjusting the model support-system angle for each power setting to maintain exactly the desired value of either α or C_L, this was deemed impractical to do due to the large number of runs and data

[9] Computed from tunnel's reference total pressure (PTOT), and calibration between PTOT and empty test section static pressure (DPINF); see Sections 3.6 and 3.10.1

[10] Computed from tunnel's reference total pressure (PTOT), total temperature (TTOT), and calibration between PTOT and empty test section static pressure (DPINF); see Section 3.6 and 3.10.1

[11] Measured as the product of voltage and current on the power supply, one power measurement for each propulsor

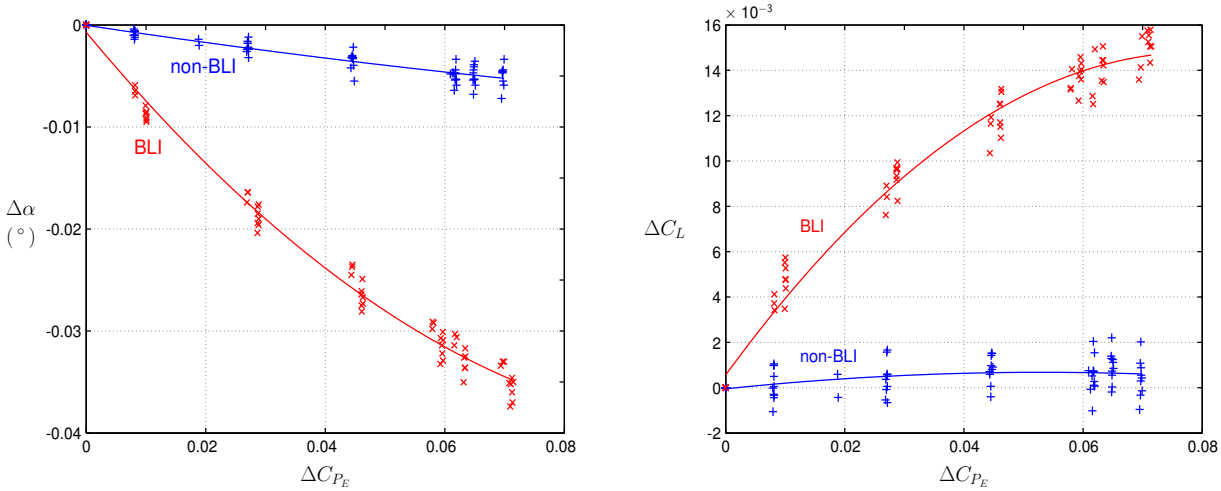

Figure 3.16: Example of changes in angle of attack (left) and lift coefficient (right) versus variations in power level to the propulsors: data points and curve fits for 84 mph, Plug B, Entry 2, at nominally 2° angle of attack.

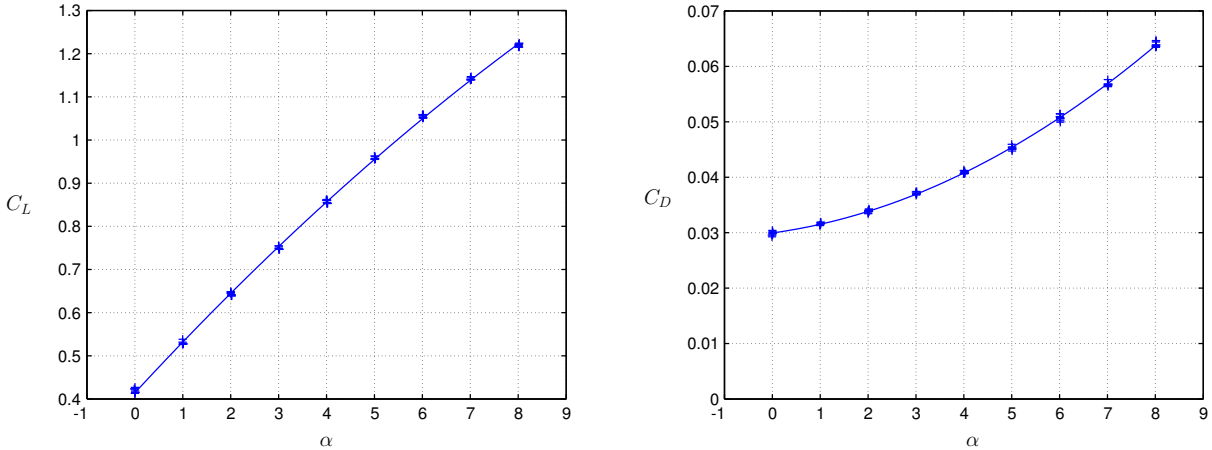

Figure 3.17: Lift and drag coefficients versus angle of attack for the unpowered configuration; data from both tunnel entries.

points taken during the entire testing campaign[12]. Instead, the undesirable $\Delta\alpha$ and corresponding ΔC_L changes were accounted for by correcting the measured streamwise coefficient, $\widetilde{C}_X$, as follows.

For a given measured $\widetilde{C}_L$, the angle of attack change $\delta\alpha$ that would be needed to attain the desired value of $(C_L)_{\text{spec}} = 0.64$, which is the cruise value of the full-size D8 concept, is such that

$$(C_L)_{\text{spec}} = \widetilde{C}_L + \frac{\partial C_L}{\partial \alpha}\delta\alpha \tag{3.14}$$

and therefore we have

[12] A run is a set of data points taken at fixed nominal V_∞ and α, while either power level or survey probe location is varied. A total of 343 runs where taken during Entry 1 in the summer of 2013, and 444 during Entry 2 in the summer of 2014.

$$\delta\alpha \;=\; \frac{(C_L)_{\rm spec} - \widetilde{C}_L}{\partial C_L/\partial\alpha}\,. \tag{3.15}$$

The value of C_X corrected for the effect of power-level changes on angle of attack to produce the specified $(C_L)_{\rm spec}$ is thus

$$C_X \;=\; \widetilde{C}_X + \delta C_X \;=\; \widetilde{C}_X + \frac{\partial C_X}{\partial\alpha}\delta\alpha \;=\; \widetilde{C}_X + \frac{\partial C_X/\partial\alpha}{\partial C_L/\partial\alpha}\left[(C_L)_{\rm spec} - \widetilde{C}_L\right]\,. \tag{3.16}$$

The slopes $\partial C_X/\partial\alpha \simeq 0.2\,{\rm rad}^{-1}$ and $\partial C_L/\partial\alpha \simeq 5.8\,{\rm rad}^{-1}$ are obtained from the unpowered configuration measurements shown in Figure 3.17. Note that only the slopes of the C_L versus α and C_X versus α curves are important for the correction, and they are taken at the angle of attack of interest, namely $\alpha = 2°$. At cruise, the resulting δC_X corrections for the non-BLI and BLI configurations are -1×10^{-4} and 6×10^{-4}, respectively, and are small compared to the streamwise force measurement uncertainty values derived in Section 3.6. The effect of correcting forces to match C_L is discussed in Section 3.5.2.

Conversion of Electrical Power into Mechanical Flow Power

The conversion between electrical power, P_E, and mechanical flow power, P_K, for the indirect method is done as follows. A series of fan characteristics was measured in MIT GTL's 1×1 ft wind tunnel, at different wheel speeds, in clean flow and with a distortion representative of the fuselage boundary layer that is ingested when the propulsors are installed on the BLI configuration. Data was taken with the propulsor at three wheel speeds (Ω = 8000, 10600, 13500 RPM), and for varying inlet velocity to span a range of electrical power inputs. At each condition, a five-hole-probe survey was performed at the inlet and exit planes to determine the mass flow (or flow coefficient ϕ) and the mechanical flow power P_K. This supplementary experiment is discussed in detail in References [13, 14]. It provides a set of $(\Omega\,, P_E\,, \phi\,, P_K)$ data used to convert electrical power into mechanical flow power. The characteristics are shown in Figure 3.18.

Under the same inlet flow, the propulsor operating point is uniquely determined by the couple (Ω, P_E) of fan wheel speed and electrical power input. We can therefore calculate the mechanical flow power for each point at which the propulsors were operating during the Langley Wind Tunnel tests. The process is illustrated in Figure 3.19: given that we know the electrical power input P_E, we find the flow coefficient from the P_E versus ϕ curve at the set wheel speed Ω. Knowing ϕ, we can get the overall efficiency from the η_o versus ϕ curve, and therefore also $P_K = \eta_o P_E$. Finally, the fan efficiency can be obtained as $\eta_f = \eta_o/\eta_m$ given that the motor efficiency, η_m, is only a function of Ω and is known for each motor from its calibration (see [15] for details).

When a characteristic is not available at the required wheel speed, η_o is obtained by linear interpolation between the other characteristics. A determination of the sensitivity of results to this interpolation is discussed in Section 3.5.4.

Curve Fits to Data Points

During the wind tunnel experiments, data was taken for at least 10 repeated runs[13], by which we mean that at least 10 measurements were taken at any given condition as defined by V_∞, α, and Ω (or power level). Each measurement yields values C_{X_i} and $C_{P_{K_i}}$ at that condition, where i spans from 1 to N, and N is the number of repeated runs at that condition. Figure 3.20 shows the

[13] For the non-BLI configuration with Plug B, 15 and 12 runs were taken at 70 mph and at 84 mph respectively. For the BLI configuration, at 70 mph and 84 mph respectively, 13 and 13 runs were taken with Plug A, 17 and 16 with Plug B, and 12 and 13 with Plug C.

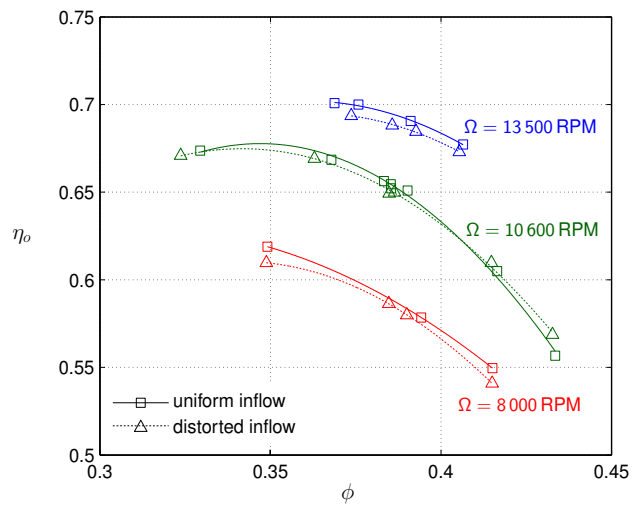

Figure 3.18: Propulsor characteristic in uniform and distorted inflow for the left propulsor unit: overall efficiency versus flow coefficient.

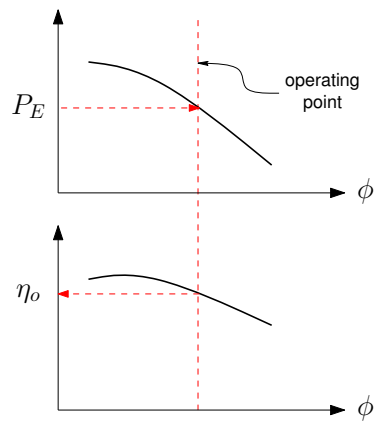

Figure 3.19: Schematic of conversion between electrical and flow power: the $P_E(\phi)$ characteristic at the desired wheel speed is used to determine ϕ at the measured value of P_E; the $\eta_o(\phi)$ characteristic is then used to determine the conversion factor between P_E and P_K.

points $(C_{P_{K_i}}, C_{X_i})$ for all the data taken in the Langley tunnel entries at $V_\infty = 84\,\text{mph}$, and $\alpha = 2°$ corrected to $C_L = 0.64$. Each cluster of points in the Figure represent a set of repeated runs, and the scatter of the cluster is a measure of the experimental repeatability.

A second-order polynomial curve is fit through the points $(C_{X_i}, C_{P_{K_i}})$ that have a C_X value between -0.026 and $+0.026$ (or correspondingly a C_{P_K} value between 0.01 and 0.09) for any given configuration. This curve-fit polynomial, p, is taken to be the $C_{P_K}(C_X)$ curve measured experimentally, such that the power at any given streamwise force is given by $C_{P_K} = p(C_X)$. This curve is shown as a solid line in Figure 3.20. The BLI benefit at cruise is then

$$PSC = \frac{p_{\text{non-BLI}}(C_X = 0) - p_{\text{BLI}}(C_X = 0)}{p_{\text{non-BLI}}(C_X = 0)} \,. \tag{3.17}$$

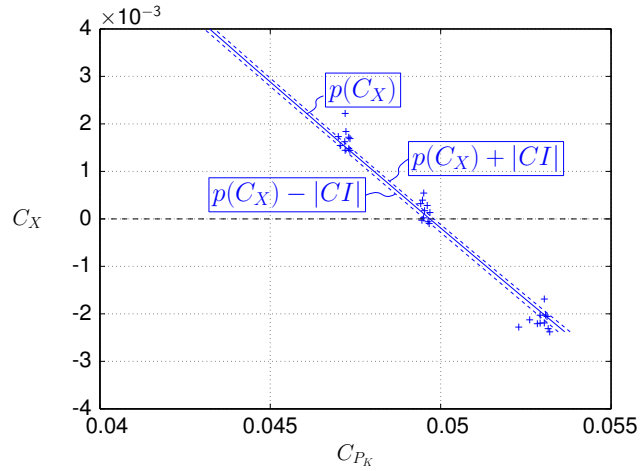

Figure 3.20: Example of streamwise force versus power data, showing experimentally measured points $(C_{P_{K_i}}, C_{X_i})$ (+ symbols), polynomial curve fit (solid line), and confidence interval (dashed lines), for the non-BLI configuration at 84 mph, Plug 3, Entry 2.

and is the difference between the curve fits for BLI and non-BLI configurations at zero net force.

The range of $(C_{X_i}, C_{P_{K_i}})$ points used for the curve-fitting is limited because we are mostly interested in the results at the cruise condition. Given that we know the force versus power dependence is not a polynomial relation[14], we want to minimize the extraneous errors at cruise that would result from a polynomial fit that includes experimental points far from cruise.

Note that these curve fits of $C_{P_K}(C_X)$ for the non-BLI and BLI configurations are a major result of the N+3 Phase 2 program, and constitute the experimentally measured aerodynamic performance curves with and without BLI.

Confidence Intervals

The value of the benefit is important, but also of importance is the confidence we have in that result. We thus also quantify and plot the 95% confidence interval of the repeated runs.

The 95% confidence interval is the bounds about the estimated mean that encompass the true mean value within 95% confidence. Note that the confidence interval quantifies the repeatability (or uncertainty) of a mean of measurements, and is not to be confused with the prediction interval which is the bounds within which any single future measurement will fall. Following the procedure of Wahls *et al.* [16], we use regression statistical analysis to estimate this confidence interval as

$$\mathrm{CI} \;=\; \pm\, t \times \mathrm{SE} \times Q(X_0) \tag{3.18}$$

in which t is the cumulative distribution function for a 95% confidence using N samples and a polynomial fit of order $K = 2$. The standard error is given by

$$\mathrm{SE} \;=\; \sqrt{\frac{1}{N-K-1}\sum_{i=1}^{N}\left(Y_i - \hat{Y}_i\right)^2} \tag{3.19}$$

where $\hat{Y}_i$ is the value from the curve fit corresponding to the measured point Y_i, and Q is obtained

[14] A physically-accurate relation can be derived using the power balance method, and will be presented in a future publication. However, differences in curve-fitted results at cruise between those using such a relation and the polynomial-based ones are not significant when the latter is restricted to fitting data near cruise as is done here.

from the covariance matrix as

$$Q(X_0) \;=\; \sqrt{X_0^T \left(X^T X\right)^{-1} X_0} \tag{3.20}$$

which uses the measurements X (*i.e.*, the $(C_{X_i}, C_{P_{K_i}})$ data points) and the polynomial curve-fit evaluation at the points of interest $X_0 = [1\,,\, X_0\,,\, X_0^2]$ (see [16] for more details).

This confidence interval for the non-BLI configuration data is shown in the C_X versus C_{P_K} plot as dashed lines in Figure 3.20. The band between the dashed lines has a width of $\Delta C_{P_K} = 2\,\mathrm{CI}$ and is located a distance of CI on each side of the $C_{P_K}(C_X)$ curve.

The confidence interval on the BLI benefit can then be calculated by propagating the CI values for each configuration, and is given by

$$\mathrm{CI}_{PSC} \;=\; \sqrt{\frac{1}{C^2_{P_{K_{0\,\mathrm{non-BLI}}}}} \left[\left(\frac{C_{P_{K_{0\,\mathrm{BLI}}}}}{C_{P_{K_{0\,\mathrm{non-BLI}}}}} \right)^2 \mathrm{CI}^2_{0\,\mathrm{non-BLI}} + \mathrm{CI}^2_{0\,\mathrm{BLI}} \right]} \tag{3.21}$$

where

$$\begin{aligned}
C_{P_{K_{0\,\mathrm{non-BLI}}}} &= C_{P_{K_{\mathrm{non-BLI}}}}(C_X = 0)\ , \\
C_{P_{K_{0\,\mathrm{BLI}}}} &= C_{P_{K_{\mathrm{BLI}}}}(C_X = 0)\ , \\
\mathrm{CI}_{0\,\mathrm{non-BLI}} &= \mathrm{CI}_{\mathrm{non-BLI}}(C_X = 0)\ , \\
\mathrm{CI}_{0\,\mathrm{BLI}} &= \mathrm{CI}_{\mathrm{BLI}}(C_X = 0)\ .
\end{aligned}$$

The BLI benefit at cruise is then written as $PSC \pm \mathrm{CI}_{PSC}$.

3.3.4 Computational Approach

The numerical simulations of the experimental tests were performed under the lead of S. Pandya from NASA Ames. The contents of this Section 3.3.4 is adapted from [17].

The Overflow code [18] was used to obtain viscous solutions to the Reynolds-Averaged Navier-Stokes equations on the configurations of the D8 aircraft inside the wind tunnel with an actuator disk model to represent the fan. A methodology for structured overset mesh computations of the D8 airframe using Overflow was defined and validated in a previous study [19]. Following that study, and using the overset best practices [20], a baseline mesh was developed. A study of solution sensitivity to various meshing parameters was carried out in the previous study to determine the best parameters for a mesh. Four major parameters were tested independently: the wall spacing (target y^+), the surface spacing (wing leading edge spacing, trailing edge spacing, and global spacing parameters on the surface), the near-wall stretching ratio, and the off-body spacing. The study led to use of a y^+ of 1, a fine-mesh reference value of 0.5, a stretching ratio of 1.07, and an off-body spacing corresponding to 2.4% of the chord. The surface spacing of 0.5 corresponds to a spacing of 0.016 times the chord at midspan. The leading edge spacing is 0.1% the chord, and the trailing edge spacing is half that at the leading edge. All other surfaces (*e.g.*, fuselage, pi-tail) follow similar surface mesh spacing rules and utilize the same reference value. These choices result in a surface mesh that has approximately 550 points defining the root airfoil and 300 points defining the tip airfoil with the mesh stretching to coarser spacing in flatter regions.

The Chimera Grid Tools (CGT) package was used to generate surface and volume meshes [21, 22]. Because of symmetry, only the right half of the airplane and wind tunnel is modeled in all CFD simulations, thus roughly halving the computational cost compared to full-span simulations. First, overlapping surface grids are generated from reference surface triangulations or structured

patches. The surface meshes are then used to generate body-fitted near-body volume meshes with spacing set to capture a turbulent boundary layer. Another set of body-fitted grids cover the region near the wind tunnel walls with a grid spacing more appropriate for an inviscid wall. Additionally, a set of Cartesian box grids covers the space between the near-body grids and the test section wall grid. Finally, the volumes upstream and downstream of the test section are covered with a core grid that follows the shape of the outer shell of the wind tunnel grid. Figure 3.21 shows a depiction of the overset meshes in the wind tunnel test section with blue regions indicating areas of mesh to mesh communication.

The baseline mesh for the unpowered configuration consists of 36 overset volume meshes containing approximately 113 million points for the D8, wind tunnel walls, and mounting strut. The nacelle, pylon and hub add another 13 grids and approximately 15 million points to the mesh for the podded nacelle configuration. The integrated nacelles have a more complex geometry that necessitates 28 additional grids, which add 24 million grid points over the unpowered configuration.

Best practices obtained from the previous study were also used for selecting flow solver options. The right-hand side is discretized using second-order central differencing. On the left-hand side, the Pulliam-Chausee diagonalized approximate-factorization scheme [23] is used with a grid sequencing startup and multi-grid to lower the cost of converging the computations. The solver was run in steady-state mode with the low-Mach number pre-conditioner turned on. Both SA and SST turbulence models [24] are used with the assumption that the flow is fully turbulent. Matrix dissipation was used in all the computations to mitigate spurious total pressure errors.

Wind Tunnel Modeling

For simplicity, the model support structure in the Langley wind tunnel tests was not modeled in the CFD calculations. Because the focus is on the relative BLI benefits between the different configurations, the effects of the mounting support, which is common for all configurations, is less important than if absolute results were the focus. All other aspects of the wind tunnel geometry, including the settling chamber, contraction section, test section, and diffuser are modeled with slip walls. The tunnel total-to-static pressure ratio and Reynolds number are specified to match the observed conditions in the wind tunnel. Contours of total pressure loss in Figure 3.22 show that the total pressure loss is zero everywhere except in the wake of the test article.

Engine Fan Modeling

The propulsor fan was modeled as an actuator disk placed at the approximate fan location, with a uniform pressure rise imposed across it. Since the fluid velocity is unchanged by the actuator disk, the pressure rise across the actuator disk is also the total pressure rise. The computation is carried

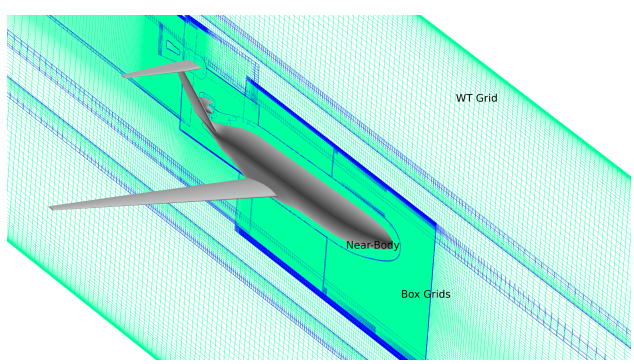

Figure 3.21: A cut through the overset mesh in the wind tunnel test section showing areas of mesh-to-mesh communication in blue.

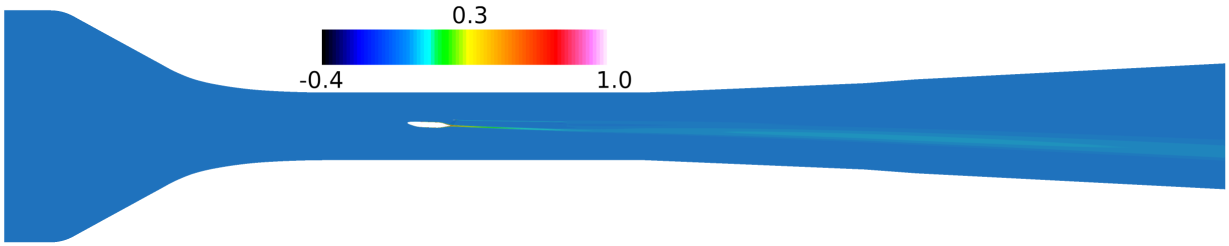

Figure 3.22: Contours of total pressure loss coefficient along the wind tunnel centerplane for the unpowered configuration. The wind tunnel's settling chamber, contraction, test section, and diffuser are modeled as part of the CFD simulations. The persistence of the wake to the exit indicates low numerical dissipation.

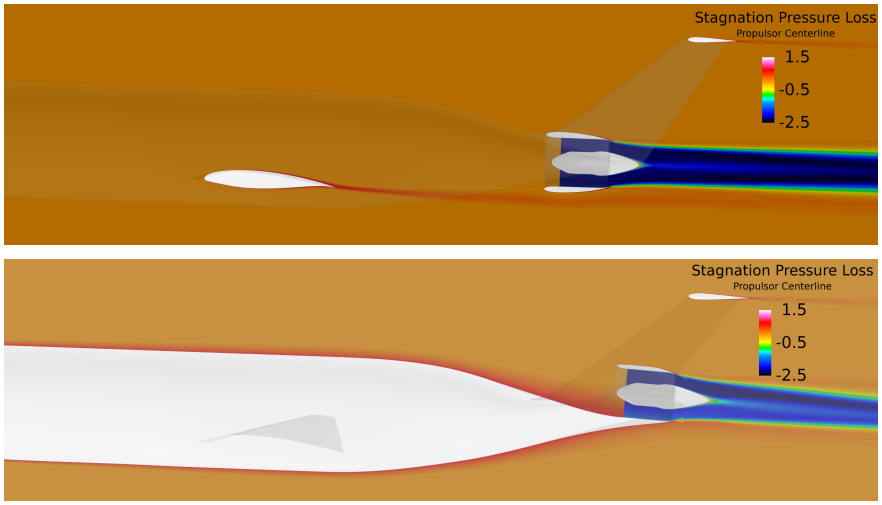

Figure 3.23: Contours of total pressure loss coefficient in a plane through the centerline of the propulsor for the non-BLI (top) and BLI (bottom) configurations.

out with four different pressure rise values spanning the expected total pressure rise at cruise.

Figure 3.23 shows the total pressure loss coefficient, $(p_{t_\infty} - p_t)/q_\infty$, in a cutting plane located approximately at the centerline of the propulsor for the non-BLI and BLI configurations. Since the actuator disks are set at the same static pressure rise (and hence total pressure rise) for both configurations, the main difference in propulsor performance comes from differences in mass flow.

3.3.5 Approach Summary

Three independent methods were used to obtain the mechanical flow power, P_K, for both the BLI and non-BLI configurations, and thus quantify the BLI benefit:

(i) the *indirect method* for which electrical power is recorded during the wind tunnel tests and converted to flow power, while an internal balance measures the corresponding model loads;

(ii) the *direct method*, which integrates flowfield quantities to compute P_K from its definition (3.1), and of which there are two variants: one using the pressure rake measurements taken during the first tunnel entry, and one using the FHP data of the second entry;

(iii) the use of *numerical simulations* to obtain and integrate the flowfield.

3.4 BLI Benefit Results

This section provides a preview of the major results of the quantification of the BLI benefit for the D8. More complete and final results will be published in future journal articles.

In particular, at the time this report was submitted in the Fall of 2015, the data obtained with the five-hole-probe was still being processed, due to delays linked to probe calibration and the difficulties related to using such a probe in a shear flow. Furthermore, the simulations of the wind tunnel tests led by S. Pandya from NASA Ames were still being refined. We therefore only present here the indirect method results and the direct method results based on the rake system.

3.4.1 Force versus Power

Figure 3.24 compares the measured net streamwise force coefficient, C_X, of the BLI and non-BLI configurations over a range of power levels, C_{P_K}, at $C_L = 0.64$ (nominally $\alpha = 2°$). It includes the data taken during the two wind tunnel entries at both 70 mph and 84 mph freestream velocities, and processed using the indirect method, *i.e.*, via conversion of electrical power into flow power. At each condition (α, V_∞, power setting) of interest, a minimum of 10 repeat measurements were taken over the two Langley tunnel entries: these are shown as + symbols in the figures. Also shown are the results from the direct method for data taken with pressure rakes during the first entry at 70 mph, as described in detail in [10]. Finally, we have included the results of the unpowered configuration, whose net-streamwise force is representative of the drag of the non-BLI configuration airframe, *i.e.*, propulsors removed.

The lines in the upper plot with the full measured range correspond to a data fit (as described in Section 3.3.3) through the values of C_{P_K} obtained with the indirect method. On the bottom plot is a zoom-in view of the same data near the simulated cruise condition of $C_X = 0$, and includes dashed lines indicating the 95% confidence interval for each configuration calculated as described in Section 3.3.3. The confidence interval region provides a measure of the repeatability and hence uncertainty of the experimental measurements. A more detailed uncertainty analysis is given in Section 3.6.

There are no statistically significant differences between data points taken at different speeds. This is evident by looking closely at the clouds of points in the figure, in which the spread between points at the same speed is comparable to the differences between speeds. This proves that the Reynolds number effects are negligible, thanks to the proper boundary layer tripping of the model surfaces, and that these low-speed results can be confidently scaled up to flight Reynolds numbers.

Figure 3.24 summarizes the major finding of this investigation. The horizontal offset between the BLI and the non-BLI curves represents the difference in power required by their respective propulsors, and hence represents the power-reduction benefit of BLI as defined by equation (3.7) at equal nozzle area (same propulsor in both configurations). At the cruise condition of $C_X = 0$, this aerodynamic BLI benefit is measured to be $PSC = 8.6\%$, with a confidence interval $\mathrm{CI}_{PSC} = \pm\, 0.3\%$, *i.e.*, $PSC = (8.6 \pm 0.3)\%$. This would translate to the same percentage reduction in fuel burn for a full-size aircraft. Furthermore, the data indicates that the BLI benefit exists over a wide range of C_{P_K} settings and corresponding C_X values, from descent to climb.

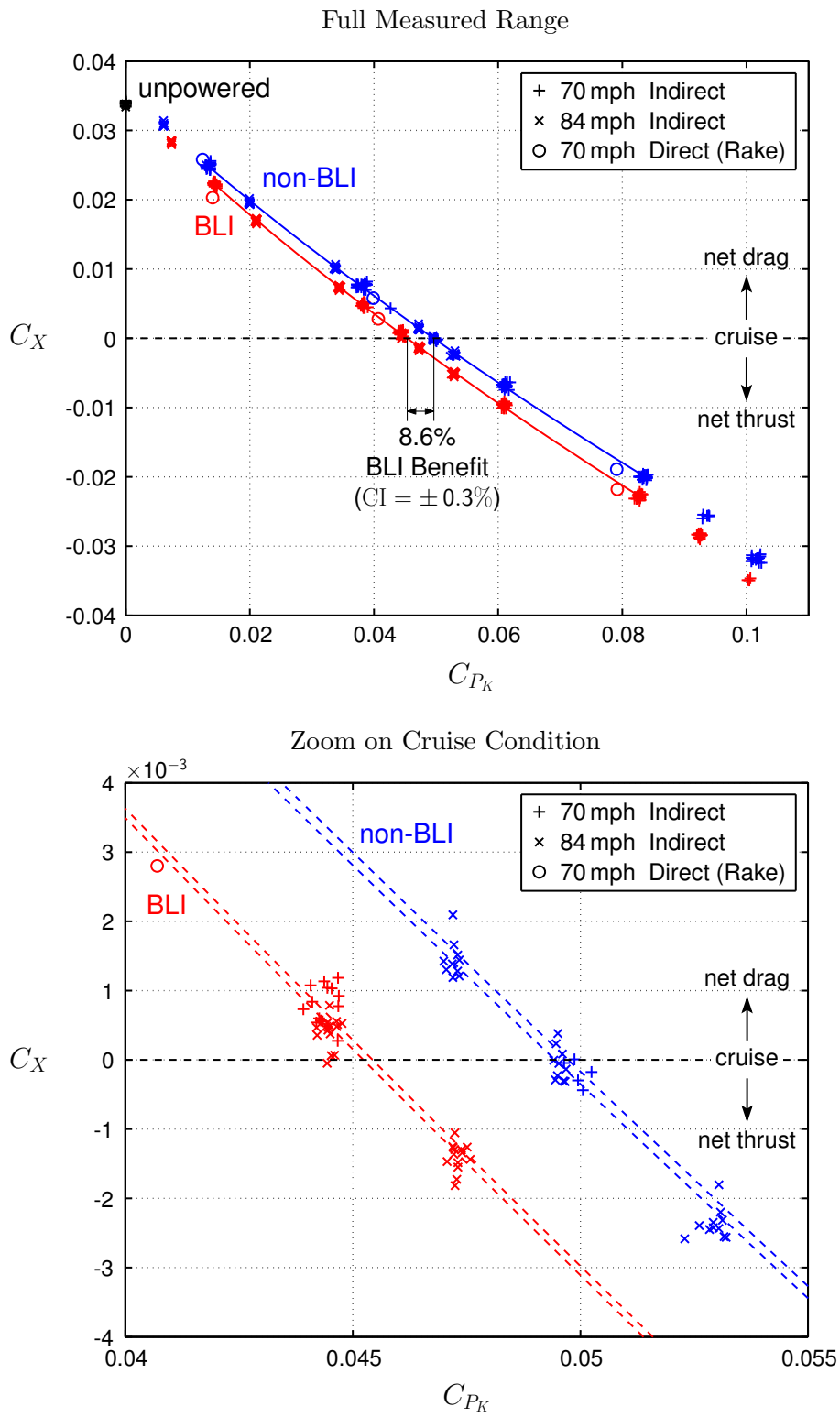

Figure 3.24: Net streamwise force coefficient versus mechanical flow power coefficient with Plug B, at nominal $\alpha = 2°$ corrected to $C_L = 0.64$: full measured range (top), and zoom in on cruise condition (bottom). For each of the non-BLI and the BLI configurations, solid lines on the top plot show curve fits to data points and dashed lines on the bottom plot show the confidence interval, while the symbols are experimental measurements.

3.4.2 Propulsive Efficiency

The propulsive power for any propulsor, BLI or non-BLI, in general depends on its diameter or mass flow, on fan pressure ratio, and other parameters. Therefore, when comparing BLI and non-BLI propulsors, we must specify what is being held fixed between the two configurations. As mentioned in Section 3.2.5, possible choices for the comparison are at the same power, same propulsive efficiency, same nozzle area, same mass flow, or some combination of these.

In the experiments, a range of possible comparisons was spanned by varying the nozzle area via the installation of nozzle plugs of different sizes. Plug B, used to generate the results in Figure 3.24 corresponds to a nominal nozzle area. Measurements were also performed with Plugs A and C, which gave larger and smaller nozzle areas, respectively, and thus larger and smaller propulsive efficiencies relative to nominal. The effects of the varying nozzle area are summarized in Figure 3.25, which is the equivalent of Figure 3.4 except that propulsive efficiency rather than nozzle area is on the horizontal axis.

The dashed lines in Figure 3.25 show curve fits of $1/\eta_p$ to reflect the analytical scaling[15]. The good match between analytical predictions and measured propulsor power for the three nozzle plugs and both configurations indicates that the theory is reliable for general BLI propulsor prediction performance.

[15] In the power balance framework, $\eta_p P_K = P_K - \Phi_{\text{jet}} = \Phi_{\text{surf}} + \Phi_{\text{wake}} + \Phi_{\text{vortex}} = \Phi_{\text{airframe}}$, and therefore $P_K = \Phi_{\text{airframe}}/\eta_p$.

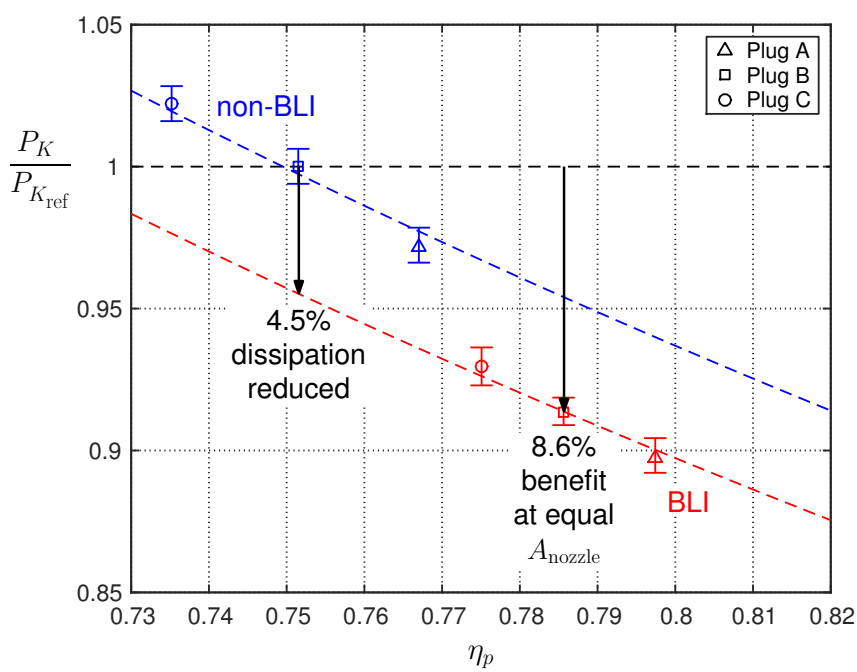

Figure 3.25: Mechanical flow power ratio versus propulsive efficiency at simulated cruise ($C_L = 0.64$, $C_X = 0$). Symbols are experimental measurements (mean of all repeated runs), dashed lines are analytical predictions, and $P_{K_{\text{ref}}}$ is the power of the non-BLI configuration at simulated cruise with Plug B (blue square). The error bars on the symbols give the confidence intervals of each point. Vertical offset between the lines is the difference in airframe dissipation between the two configurations.

Since the overall flow power can be written as $P_K = \Phi_{\text{airframe}}/\eta_p$, the vertical offset between the BLI and non-BLI curves in Figure 3.25 is the difference in airframe dissipation between the two configurations. We see that the BLI airframe has 4% less dissipation, which must be mostly due to its smaller nacelles and smaller velocities on the nacelle surfaces.

It is useful to restate here the physical origins of the BLI benefit. About half of the benefit is the result of an increased propulsive efficiency, or equivalently decreased jet velocity for the same added streamwise force. The lower jet velocity in the BLI case is in part due to the fact that the ingested flow is slower, so for a given velocity change the final jet velocity is slower as well. The slower jet constitutes less kinetic energy deposited into the flow, and ultimately lost via jet dissipation.

Because the BLI system partially eliminates the fuselage viscous wake, there is also an additional benefit due to the reduction of the wake dissipation. Also, since the BLI configuration has smaller nacelles (see Figure 3.7) with lower surface velocities, the surface dissipation is reduced as well. These two additional BLI benefits correspond to the vertical offset between the non-BLI and BLI analytical curves, as indicated in Figure 3.25, and account for about half the total aerodynamic BLI benefit. Since this benefit does not depend on propulsor area or propulsive efficiency, the line offset is constant.

Note that in this analysis we have assumed that the propulsors do not significantly affect the aircraft's spanwise load distribution (primarily the result of flow around the wings), so that BLI and non-BLI configurations have the same vortex dissipation and equivalent induced drag for any given lift coefficient. This assumption is analyzed in Section 3.5.5, which show that the two configurations have nearly the same overall spanwise loads and vortex kinetic energies.

3.4.3 Data Summary

Presented in the following table are the overall results at the simulated cruise condition ($C_L = 0.64$, $C_X = 0$). These are from curve-fits over data points from both tunnel entries and all runs at 70 mph and 84 mph tunnel speeds.

Table 3.6: Summary of experimental results at simulated cruise ($C_L = 0.64$, $C_X = 0$): power coefficients, propulsor operating points, efficiencies, and BLI benefit. The non-BLI configuration with Plug B is used as the reference case and sets $P_{K_{\text{ref}}}$, both for $P_K/P_{K_{\text{ref}}}$ and $PSC = 1 - P_K/P_{K_{\text{ref}}}$.

	Non-BLI			BLI		
	Plug A	Plug B	Plug C	Plug A	Plug B	Plug C
C_{P_E}	0.0707	0.0707	0.0742	0.0645	0.0655	0.0664
$C_{P_{\text{Shaft}}}$	0.0564	0.0568	0.0577	0.0521	0.0526	0.0536
C_{P_K}	0.0482	0.0496	0.0507	0.0445	0.0453	0.0461
V_{jet}/V_∞	1.61	1.66	1.72	1.55	1.60	1.65
U_{tip}/V_∞	2.81	2.79	2.73	2.73	2.71	2.69
ϕ	0.377	0.361	0.342	0.370	0.354	0.335
η_f	0.858	0.878	0.879	0.856	0.863	0.862
η_p	0.767	0.752	0.735	0.797	0.786	0.775
$P_K/P_{K_{\text{ref}}}$	0.972	1	1.022	0.897	0.913	0.929
PSC	2.8%	0	-2.2%	10.3%	8.6%	7.1%

3.5 Sensitivity of Results to Analysis and Modeling Assumptions

We present here the sensitivity of the BLI benefit as computed via the indirect method to the various uncertainties in the recorded data or the post-processing methods. The BLI benefit proved to be insensitive to the details of how flow power was computed, with differences in benefit values always smaller than repeatability and uncertainty.

3.5.1 Comparison Between Wind Tunnel Entries

The BLI benefit result is based on data acquired during two tunnel entries in the NASA Langley 14–by 22–Foot Subsonic Tunnel a full a calendar year apart. Entry 1 spanned four consecutive weeks of tunnel time from August 8 through September 16, 2013, and Entry 2 spanned five consecutive weeks from August 1 through September 8, 2014. The NASA internal balance used to measure forces and moments was calibrated shortly before Entry 1, and then again shortly before Entry 2.

In order to determine how force measurements changed between tunnel entries, we can look at data taken at a tunnel speed of 70 mph that was used during both entries (while 84 mph was only considered during Entry 2), and with the nominal Plug B, which is also the plug for which the largest number of repeated runs was taken.

Figures 3.26 and 3.27 show the lift and drag coefficients measured for the unpowered configuration for each of the two tunnel entries, with separate fit curves for each entry. It shows an average difference in C_L at the cruise angle of attack of 2° of 1.4%, and a difference in C_X of less than 0.2%. Those differences are within the instrument precision quoted on the NASA force balance calibration (see Section 3.6). Furthermore, the spread among data points from one entry overlaps with the spread for the other entry. In other words, the repeatability between entries is within the repeatability for a single entry, in particular for the net streamwise force, which is one of the two major quantities of interest (the other one being power).

The same conclusion can be made by looking at the forces on the powered configurations at fixed wheel speed shown in Figure 3.28. Note also that the BLI and non-BLI configurations have nearly the same C_L versus α curve, especially near the $\alpha = 2°$ of the simulated cruise point, which indicates that the different propulsor installations do not significantly affect the airframe's lift characteristics. The BLI and non-BLI configurations also have nearly the same C_X versus α slopes, which indicates that the different propulsor installations have little effect on the airframe's induced drag characteristics.

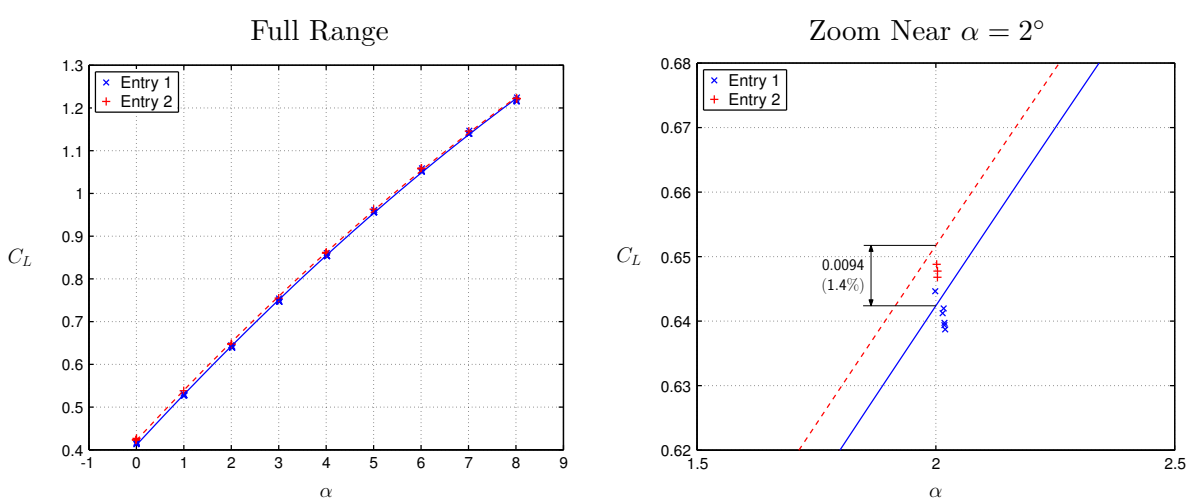

Figure 3.26: Comparison of lift coefficient measured on the unpowered configuration during the two tunnel entries at 70 mph.

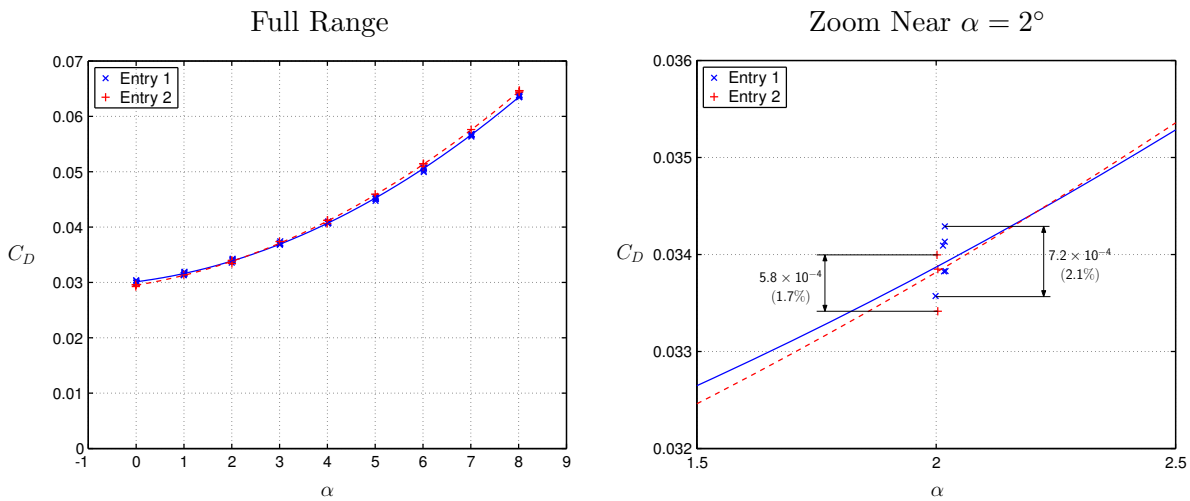

Figure 3.27: Comparison of drag (or streamwise force) coefficient measured on the unpowered configuration during the two tunnel entries at 70 mph.

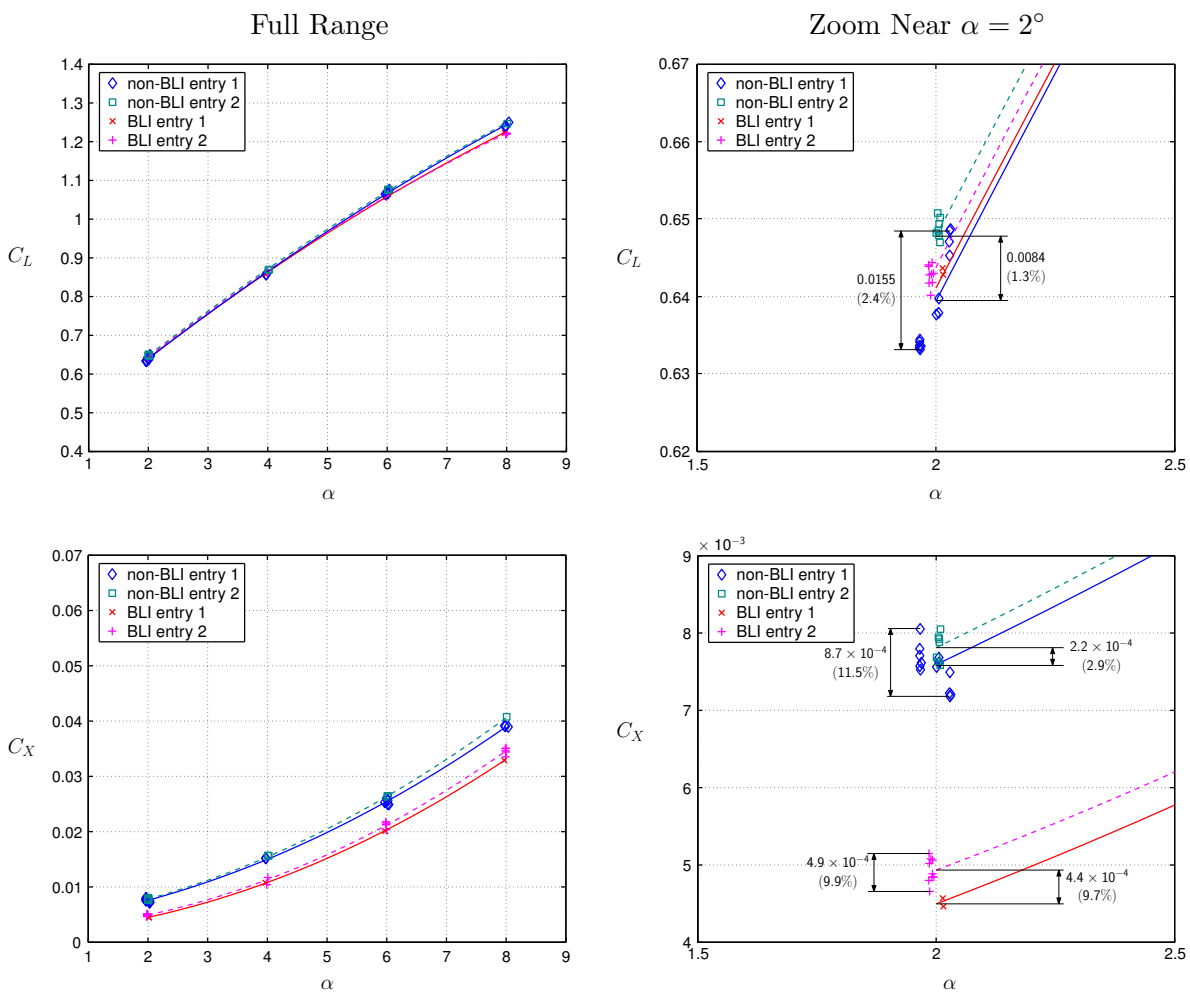

Figure 3.28: Comparison of lift coefficient (top) and streamwise force coefficient (bottom) measured on the powered configurations at fixed wheel speed of $\Omega = 10\,600$ during the two tunnel entries at 70 mph with Plug B.

3.5.2 Effect of Correction to Match C_L

As discussed in Section 3.3.3, we have presented the BLI benefit when the two configurations have the same vertical force coefficient. For this, we introduced a C_L-correction, and we show here how the benefit is insensitive to this and similar corrections.

Figure 3.29 shows the C_X versus C_{P_K} plot with (i) data with corrections to match C_L, (ii) data with corrections to match α, and (iii) data uncorrected for effect of power level on angle of attack. The dashed black lines on the right-hand-side plot that zooms in on the cruise condition indicate the confidence interval for the uncorrected data. The way the data is corrected to match C_L was explained in Section 3.3.3. The correction to match α here is as follows: $\delta C_X = (\partial C_X/\partial\alpha)\,\delta\alpha$, where $\delta\alpha = \alpha - \alpha_0$ is the difference between the measured angle of attack and its nominal value of $\alpha_0 = 2°$.

As can be seen in Figure 3.29, the difference between $C_X(C_{P_K})$ curve fits for the various corrections is within the experimental repeatability and within the confidence interval of the curve-fits. The BLI benefit for uncorrected data is 8.7%, that with matching C_L is 8.6%, and that with matching α is 8.5%, and all three have a confidence interval of 0.3%. The corresponding differences in BLI benefit at cruise are two orders of magnitude smaller than the benefit value itself, *e.g.*, $(PSC_{\text{uncorrected}} - PSC_{C_L\text{-match}})/PSC_{\text{uncorrected}} \approx 0.01$.

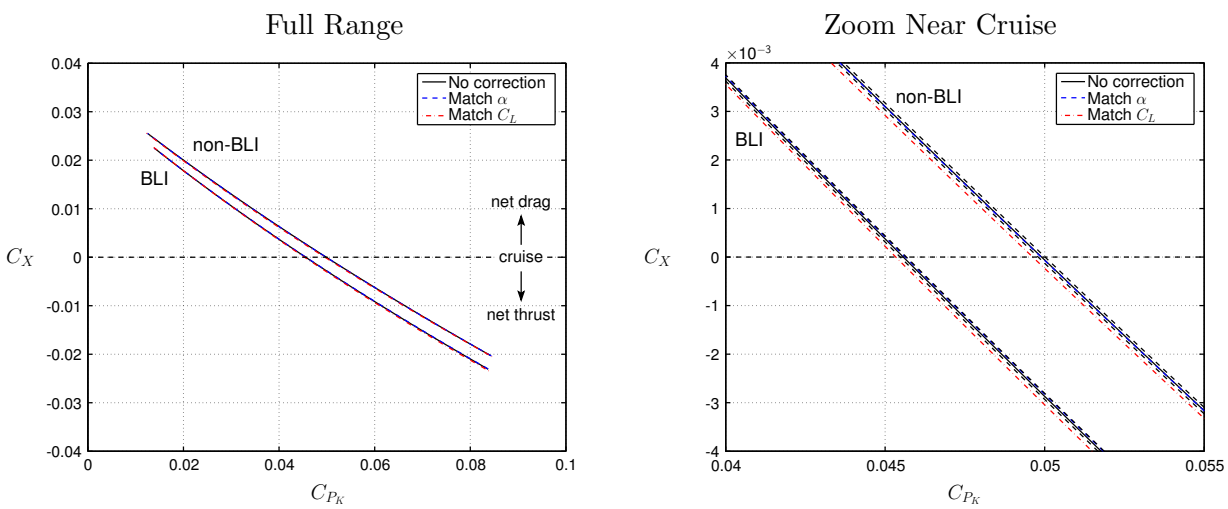

Figure 3.29: Effect of corrections to account for the effect of power level on model angle of attack on the C_X versus C_{P_K} curve fits with Plug B at $C_L = 0.64$.

3.5.3 Effect of Motor Efficiency

Three sets of motors were used in the Langley tests: set 1 is comprised of motors numbered 6 and 7 on the left and right propulsors, respectively, and was used for Entry 1; set 2 with motors 16 and 13 was used for the majority of the runs in Entry 2; set 3 with motors 9 and 15 was used during the last day of testing in Entry 2. The change to set 3 during the second tunnel entry was done in order to acquire data with two sets of motors to discern any spurious effects from motor variability.

Each motor was calibrated at MIT on a dynamometer measuring torque to determine its efficiency through the range of wheel speeds and power levels representative of the operation during

the Langley tests. Sample results of these calibration tests are shown in Figure 3.30. Note that different motors differ by as much as 4% in their efficiency η_m at any given wheel speed and power combination, although this was of course accounted for by the indirect flow power measurement relation $C_{P_K} = \eta_f \, \eta_m \, C_{P_E}$. Nevertheless, there was some concern that a specific motor might drift off its calibration curve in Figure 3.30, and thus corrupt the indirect C_{P_K} measurement.

To investigate this, we first note that the fan efficiency η_f measured in the flow rig at MIT was virtually unaffected by which motor was used, as shown in Figure 3.31. Hence, only motor variation remained as the main concern. Figure 3.32 shows that the results obtained with the different motors have no appreciable effect on the C_X versus C_{P_K} results, even at different tunnel speeds that imply different RPM and power levels and hence different points along the motor calibration curves. Therefore, motor changes and any uncertainties in motor efficiency have no significant impact on flow power and therefore on the measured BLI benefit.

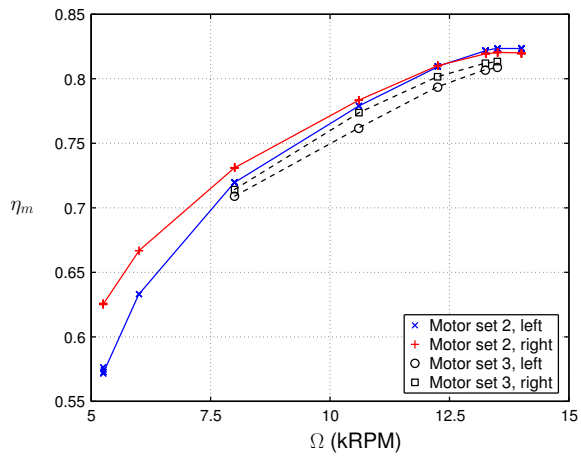

Figure 3.30: Motor efficiency versus wheel speed for motor sets 2 and 3.

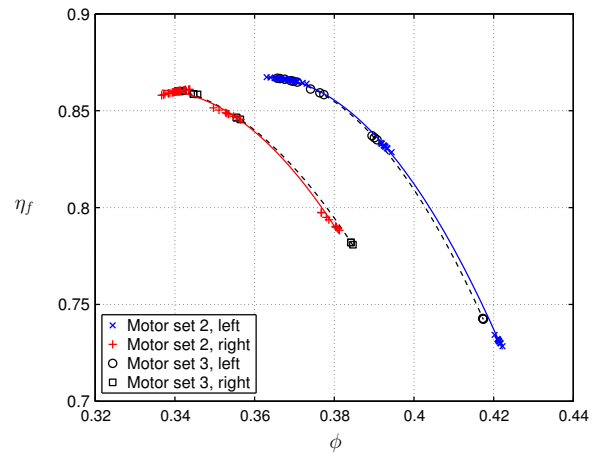

Figure 3.31: Fan efficiency versus flow coefficient with Plug B at 84 mph, $C_L = 0.64$ obtained from data acquired with motor sets 2 and 3.

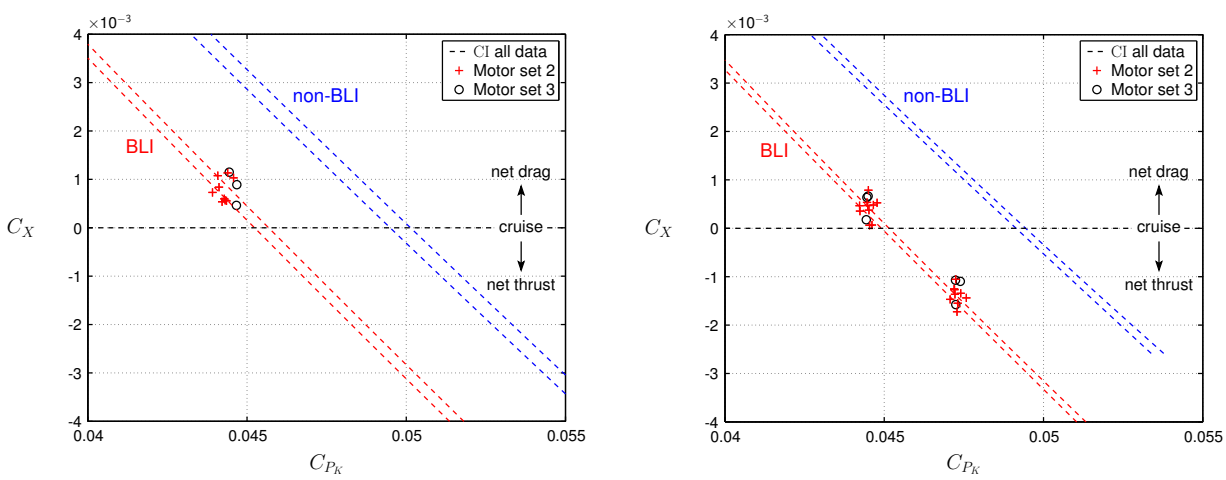

Figure 3.32: Effect of motor change on C_X versus C_{P_K} at 70 mph (left) and 84 mph (right) with Plug B at $C_L = 0.64$: curve fits (solid lines), confidence intervals (dashed lines), and data with different motors for BLI configuration (symbols).

3.5.4 Effect of Interpolation Between Propulsor Characteristics

One other possible source of uncertainty is the interpolation of fan efficiency curves, such as the ones shown in Figure 3.31. Because fan efficiency measurements in the flow rig at MIT were very time consuming, characteristics were only taken at three wheel speeds ($\Omega = 8\,000$, $10\,600$, $13\,500$ RPM). These were then linearly interpolated to the actual conditions in the Langley tests to obtain the necessary actual η_f values needed to obtain C_{P_K} from C_{P_E}. To gauge the errors that might result from this interpolation, we consider here the following four different possible interpolation approaches:

- No interpolation: if a characteristic at a given wheel speed is not available, then the data for that wheel speed is discarded. Note that in this case, the curve-fit for C_X versus C_{P_K} is then done without those data points.

- Nearest: the data from the characteristic at the nearest wheel speed is used. For instance, the characteristic at 10 600 is used for the cruise points taken at 11 100 RPM for Plug B, 70 mph.

- Linear (used for all other data presented in this report): if a characteristic at the desired wheel speed is not available, then the efficiency and flow coefficient are obtained by linear interpolation between the values from adjacent characteristics. For instance data at the cruise point of 11 100 RPM is converted by interpolating between the 10 600 and 13 500 characteristics.

- 13 500: the characteristic obtained at $\Omega = 13\,500$ RPM is used to determine the operating point and conversion factor, irrespective of the test Ω value.

As can be seen in Figure 3.33, the type of propulsor-characteristic interpolation used for conversion of C_{P_E} into C_{P_K} has only a negligible effect on the $C_X(C_{P_K})$ results, as long as a characteristic that is representative (close to) the actual one is used, *i.e.*, any of the above approaches except for the 13 500 fixed-characteristic one is valid. This lack of sensitivity is important given that the characteristics taken at different wheel speeds in the MIT supplementary experiments did not collapse exactly, probably due to Reynolds number effects.

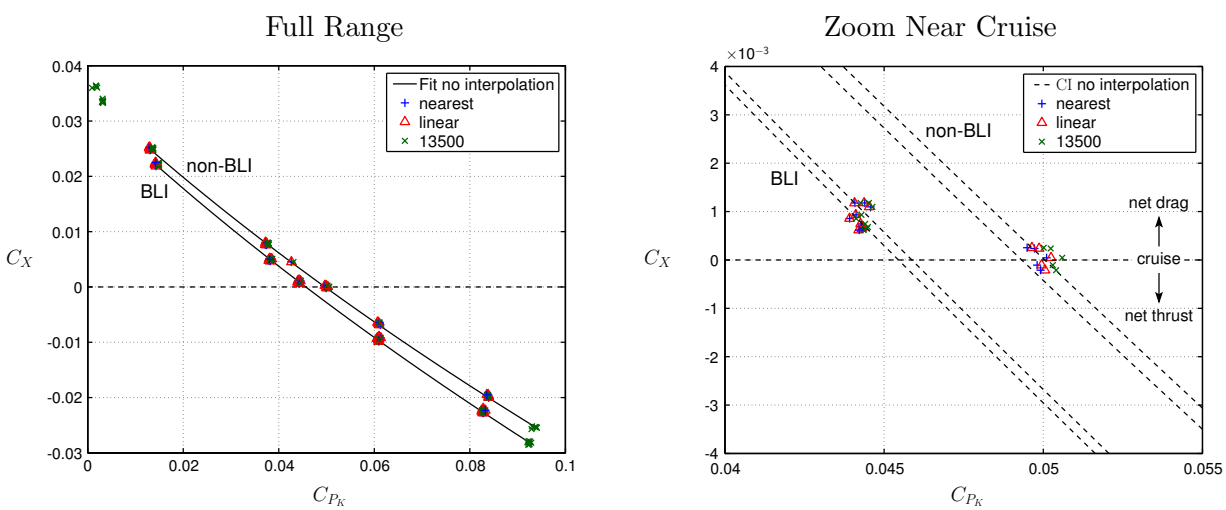

Figure 3.33: Effect of interpolating between propulsor characteristics on C_X versus C_{P_K} data from Entry 2 with Plug B, at 70 mph, $C_L = 0.64$. The dashed lines on the right-hand-side plot show the confidence interval on the fit with no interpolation.

3.5.5 Evaluation of Induced Drag

The design wingspan and spanwise loading distribution of a transport aircraft are typically determined via the optimum trade-off between structural weight and vortex dissipation (or the equivalent induced drag). Since this trade-off is not expected to be significantly influenced by the presence or absence of BLI, every effort was made to make the BLI and non-BLI configurations have the same vortex dissipation when the BLI benefit is measured, so that this benefit is associated with the *propulsion aerodynamics* alone.

Since the BLI and non-BLI configurations have the same wings, horizontal tail, and most of the fuselage, they are naturally expected to have nearly the same lift characteristics and spanwise load distributions. However, the different propulsor installations were observed to produce very slightly different lift characteristics at high angles of attack, as can be seen on the upper left of Figure 3.28. The lift was also slightly influenced by the power level, especially on the BLI configuration, as can be seen in Figure 3.16.

These small but unwanted effects of BLI on the overall lift were mostly removed via the C_L-mismatch correction procedure described in Section 3.3.3 via equations (3.15) and (3.16). However, since the motor power level influences the pressure field upstream of the propulsor thus having the potential to directly affect the lift distribution on the rear BLI-configuration fuselage, there is the possibility that the *span efficiency* was significantly changed as well. This then opens up the possibility that some of the measured BLI benefit in the experiment is partly due to unwanted changes in vortex dissipation. This possible effect is examined and estimated next.

The traditional Oswald span efficiency e_O is defined from the slope of the C_D versus C_L^2 curve, where

$$C_D \;\simeq\; C_{D_0} \;+\; \frac{C_L^2}{\pi\, AR\, e_O} \tag{3.22}$$

is the conventional overall drag coefficient assumed to be quadratic in C_L. One issue here is that the "parasite" drag coefficient, C_{D_0}, does not represent all the surface and wake (non-vortex) dissipation of the airframe. Any "profile drag creep" with increasing C_L would instead be lumped into the C_L^2 term, where it would masquerade as induced drag and thus modify the e_O value. Therefore the Oswald span efficiency e_O is not a true measure of the vortex dissipation of the configuration, and hence it will not be considered here.

A more accurate alternative to the oversimplified quadratic relation (3.22) is the expression for the overall streamwise force coefficient obtained from the nondimensional form of the power balance equation [6], namely

$$C_X \;=\; C_{\Phi_{\text{wing}}} + C_{\Phi_{\text{rest}}} + C_{\Phi_{\text{vortex}}} - \left(C_{P_K} - C_{\Phi_{\text{jet}}}\right) \;. \tag{3.23}$$

Here $C_{\Phi_{\text{wing}}}$ is the coefficient of dissipation in the wing's boundary layer and viscous wake, $C_{\Phi_{\text{rest}}}$ is the dissipation in the boundary layers and wakes of the remaining airframe components (specifically the fuselage, tails, and nacelles), $C_{\Phi_{\text{vortex}}}$ is the dissipation of the transverse kinetic energy of the potential flow about the trailing vortex system, and $C_{\Phi_{\text{jet}}}$ is the dissipation of the axial kinetic energy of the propulsive jets.

It is reasonable to assume that the wing viscous flow and the overall trailing vortex system do not significantly interact with the propulsors, and therefore to write

$$C_{\Phi_{\text{vortex}}} \;=\; C_{D_i}(C_L) \;=\; \frac{C_L^2}{\pi AR\, e} \tag{3.24}$$

$$C_{\Phi_{\text{wing}}} \;=\; C_{D_{\text{wing}}}(C_L) \tag{3.25}$$

where C_{D_i} is the conventional induced drag coefficient, and $C_{D_{\text{wing}}}$ is the wing's conventional profile drag coefficient as discussed by Drela [6]. As indicated above, C_{D_i} is related simply to C_L via the span efficiency e, which we are careful to distinguish from the Oswald span efficiency e_O in equation (3.22). The $C_{D_{\text{wing}}}(C_L)$ relation is not so simple, but for a moderately high aspect ratio low-sweep wing such as the one on the D8 model, it can be approximated as the chord-weighted average of the values of the two-dimensional airfoil drag coefficient c_d across the span. These can be obtained from two-dimensional viscous airfoil calculations using XFOIL [25] for the five airfoil sections across the span which define the wing geometry (shown in Section 3.10.4), and with tripped boundary layers to reflect the trips on the model wing. The computed polars are shown in Figure 3.34 at the Reynolds number for each airfoil corresponding to the 70 mph tunnel speed. The wing's overall profile drag polar implied by these section polars is closely approximated by the curve-fit function

$$C_{D_{\text{wing}}}(C_L) \;\simeq\; 0.0114 + 0.0005\,C_L + 0.0022\,C_L^2 + 0.0002\,C_L^{12}\ , \tag{3.26}$$

which is also shown on the plot.

The power balance relation (3.23) now becomes

$$C_X - C_{D_{\text{wing}}} \;=\; \frac{C_L^2}{\pi\,AR\,e} + \left[C_{\Phi_{\text{rest}}} - \left(C_{P_K} - C_{\Phi_{\text{jet}}}\right)\right] \tag{3.27}$$

where the last three terms in the brackets are expected to be nearly independent of C_L over the modest angle of attack range between 2° and 6°. The reason why $C_{\Phi_{\text{rest}}}$ is fixed is because it consists of the viscous dissipation of the fuselage and the nearly non-lifting tail, whose tripped turbulent boundary layers see only weak adverse pressure gradients with modest α changes. Furthermore, if the wind tunnel speed, the propulsor wheel speed, and the propulsor nozzle area are all held fixed over the α range, then the propulsor flow will not change significantly and the combination $\left(C_{P_K} - C_{\Phi_{\text{jet}}}\right)$ is expected to also remain fixed and is equal to the conventional thrust coefficient for the non-BLI case.

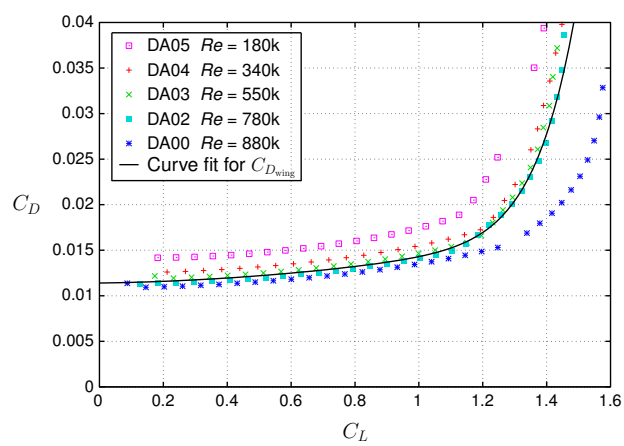

Figure 3.34: Drag polars for model wing airfoils at Reynolds numbers corresponding to 70 mph tunnel speed, together with the resulting curve fit equation (3.26) for the overall wing profile drag polar.

We can now examine a series of wind tunnel operating points for all three configurations (unpowered, non-BLI, BLI) for which the angle of attack is varied but the tunnel speed is set to 70 mph. For the powered configurations, the propulsor wheel speed is held fixed at 10 600 RPM, and the same nozzle area is used (Plug B). For each point, we estimate $C_{D_{\text{wing}}}$ from the curve-fit (3.26) using the measured C_L. The resulting plots of $C_X - C_{D_{\text{wing}}}$ versus C_L^2 are shown in Figure 3.35, together with lines with slopes $1/(\pi AR)$ along the points for each configuration, where here $AR = 15.4$. With the previously-discussed assumption that the three terms in the brackets in equation (3.27) stay fixed, any variation in the data points in Figure 3.35 for any one configuration must be entirely due to the remaining C_L^2 term, for which we have

$$\frac{\partial(C_X - C_{D_{\text{wing}}})}{\partial(C_L^2)} = \frac{1}{\pi\, AR\, e} \,. \tag{3.28}$$

Thus, any deviation of the data points from the straight lines can be attributed to a non-unity span efficiency.

The close fit of the data to the straight lines indicates that all three configurations have very nearly $e = 1$, which seems surprisingly high. However, we should note that the assumed $C_{D_{\text{wing}}}(C_L)$ function (3.26) is an estimate at best, and also that the C_X data is uncorrected for tunnel wall effects, which partially act as "ground effect", and in theory can increase e above unity. Regardless, the main conclusion from Figure 3.35 is that all three configurations exhibit very nearly the same span efficiency over the operating range of α between 2° and 6°, so that variation in vortex dissipation (or induced drag) is <u>not</u> a factor in the measured BLI benefit results. The BLI benefits are therefore attributable only to propulsion aerodynamic effects as intended.

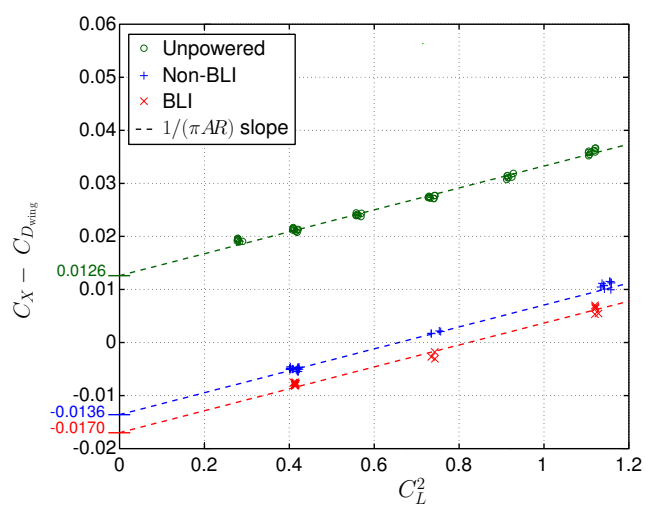

Figure 3.35: Polar plots of $C_X - C_{D_{\text{wing}}}$ versus C_L^2 as measured experimentally at 70 mph (symbols), compared against lines with ideal induced drag slope $1/(\pi AR)$. Data for the BLI and non-BLI models is for fixed wheel speed of $\Omega = 10\,600$ RPM with Plug B. The close fit between points and lines imply same span efficiency $e \simeq 1$ for all three configurations.

3.5.6 Evaluation of Trim Drag

The wind tunnel models had fixed solid horizontal tails, so there was no provision to adjust the model's pitching moment during the experiments. Here we show that trimming each configuration would have a negligible effect on the quantities of interest, namely net streamwise force and BLI benefit at cruise.

Figure 3.36 shows the measured C_m vs. α for the unpowered, non-BLI, and BLI configurations, each defined about the model's moment reference location $(x_{\text{ref}}, z_{\text{ref}}) = (66.532\,\text{in}, -2.527\,\text{in})$. Note that the pitching moment of the unpowered and non-BLI configurations, which share the tail section, saw a significant change in magnitude between Entries 1 and 2, most likely due to the horizontal tail having been assembled differently. However, this does not impact the trim drag as the stability derivative of the moment with respect to angle of attack remained essentially unchanged.

The different configurations have somewhat different pitching moments, and also different sensitivities to power as seen from the measurements shown in Figure 3.37. This raises the possibility of a significant difference in trim drag appearing in an actual aircraft implementation of either configuration, which would affect the realizable BLI benefit. This potential trim drag penalty will be examined next.

For trim we must examine the pitching moment about the aircraft's center of gravity location, which is given by

$$C_{m_{\text{cg}}} \;=\; C_m \;+\; \frac{x_{\text{cg}} - x_{\text{ref}}}{c}\, C_N \;-\; \frac{z_{\text{cg}} - z_{\text{ref}}}{c}\, C_A \;, \tag{3.29}$$

where the subscript cg refers to coordinates of the center of gravity and the subscript ref indicates the moment reference center coordinates, with x and z along the aircraft longitudinal and transverse directions respectively. For small angles of attack and when the normal (or lift) forces dominate

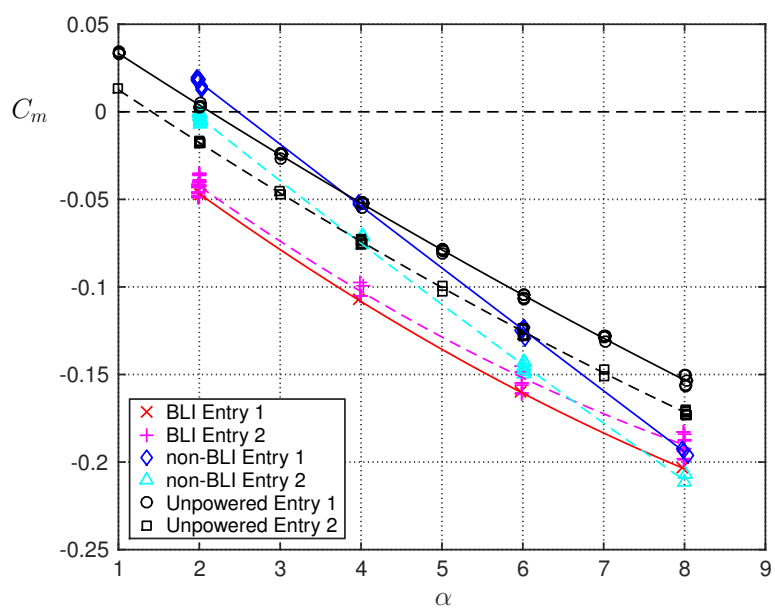

Figure 3.36: Pitching moment coefficient versus angle of attack. The curves for the power configurations (non-BLI and BLI) are for a set wheel speed of 10600 RPM with Plug B.

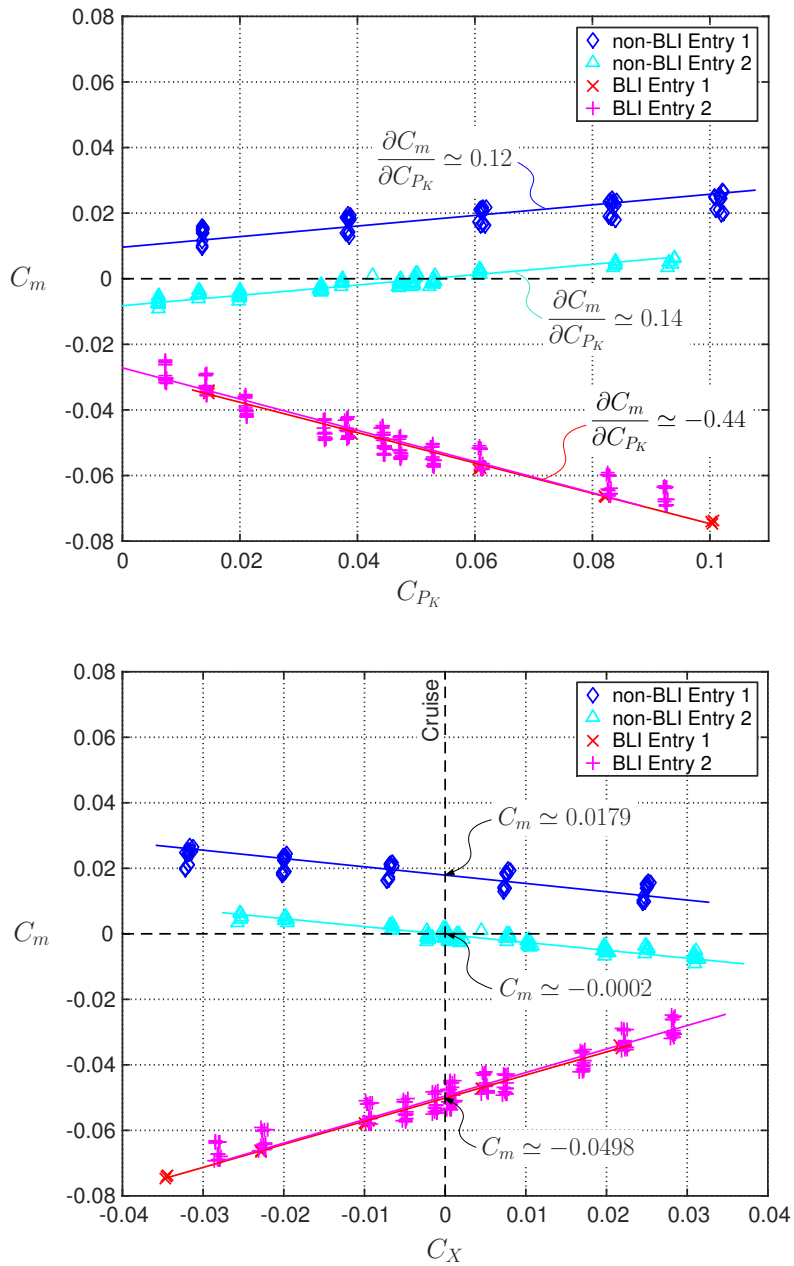

Figure 3.37: Pitching moment coefficient versus flow power coefficient (top) and versus net streamwise force coefficient (bottom) at fixed angle of attack of $\alpha = 2°$ with Plug B. The bottom plot gives the C_m values at the cruise point $C_X = 0$.

the pitching moment,

$$C_{m_{\rm cg}} \simeq C_m + \frac{x_{\rm cg} - x_{\rm ref}}{c} C_L \ , \tag{3.30}$$

and this is a good approximation for this estimation study.

The neutral-point location is the particular $x_{\rm cg}$ value for which $C_{m_{\rm cg}}$ is stationary with respect

to α, and is defined by

$$\left.\frac{\partial C_{m_{\rm cg}}}{\partial \alpha}\right|_{x_{\rm cg}=x_{\rm np}} = \frac{\partial C_m}{\partial \alpha} + \frac{x_{\rm np}-x_{\rm ref}}{c}\,\frac{\partial C_L}{\partial \alpha} = 0 \ , \tag{3.31}$$

from which we obtain

$$\frac{x_{\rm np}-x_{\rm ref}}{c} = -\frac{\partial C_m/\partial \alpha}{\partial C_L/\partial \alpha} \ . \tag{3.32}$$

Any other $x_{\rm cg}$ location can then be conveniently specified via the static margin, SM, as

$$\frac{x_{\rm cg}-x_{\rm ref}}{c} = \frac{x_{\rm np}-x_{\rm ref}}{c} - SM \ , \tag{3.33}$$

while the pitching moment derivative with respect to C_L is given by

$$SM = -\frac{\partial C_{m_{\rm cg}}/\partial \alpha}{\partial C_L/\partial \alpha} = -\frac{\partial C_{m_{\rm cg}}}{\partial C_L} \tag{3.34}$$

Table 3.7 gives the neutral point locations determined from the measured $C_m(\alpha)$ and using the vertical force slope value $\partial C_L/\partial \alpha$ obtained from the measured $C_L(\alpha)$ curves shown in Figure 3.28.

For an operational aircraft, the pitching moment about its center of gravity has the dependencies $C_{m_{\rm cg}}(\delta_e, \alpha\,;\, SM)$, where δ_e is the elevator deflection or the overall horizontal-tail trim setting. Starting with the nonzero $C_{m_{\rm cg}}$ from the measurements, we now consider the change $\Delta C_{m_{\rm cg}}(\Delta\delta_e)$ which is needed to obtain $C_{m_{\rm cg}} + \Delta C_{m_{\rm cg}} = 0$, which is another level cruise requirement for an actual aircraft, while also adjusting α to maintain the specified C_L value.

Table 3.7: Pitching moment coefficient about moment reference center, stability derivatives in units of 1/rad, neutral point location, and elevator control derivatives in units of 1/deg, for the non-BLI and BLI configurations at the cruise condition $C_L = 0.64$, $C_X = 0$. The computed values were obtained from the AVL vortex-lattice model [26].

	C_m	$\partial C_m/\partial \alpha$	$\partial C_L/\partial \alpha$	$(x_{\rm np}-x_{\rm ref})/c$	$\partial C_m/\partial \delta_e$	$\partial C_L/\partial \delta_e$
Non-BLI	-0.0002	-2.00	6.59	0.303	—	—
BLI	-0.0498	-1.87	6.59	0.284	—	—
Computed	0.0219	-2.06	6.77	0.304	-0.0823	0.0175

Conceptually, these trim changes are determined by the 2×2 linear system

$$\begin{bmatrix} \frac{\partial C_{m_{\rm cg}}}{\partial \alpha} & \frac{\partial C_{m_{\rm cg}}}{\partial \delta_e} \\ \frac{\partial C_L}{\partial \alpha} & \frac{\partial C_L}{\partial \delta_e} \end{bmatrix} \begin{bmatrix} \Delta\alpha \\ \Delta\delta_e \end{bmatrix} = \begin{bmatrix} (C_{m_{\rm cg}})_{\rm spec} - C_{m_{\rm cg}} \\ (C_L)_{\rm spec} - C_L \end{bmatrix} \tag{3.35}$$

where the first row above is seen to be equivalent to $\Delta C_{m_{\rm cg}} + C_{m_{\rm cg}} = (C_{m_{\rm cg}})_{\rm spec}$. The trim drag is defined as the change in C_X resulting from these $\Delta\delta_e$ and $\Delta\alpha$. Specifically, we obtain

$$\Delta C_{X_{\rm trim}} = C_X(\alpha+\Delta\alpha, \delta_e+\Delta\delta_e) - C_X(\alpha, \delta_e) \tag{3.36}$$

$$\simeq C_{D_i}(\alpha+\Delta\alpha, \delta_e+\Delta\delta_e) - C_{D_i}(\alpha, \delta_e) \tag{3.37}$$

where the approximate form (3.37) assumes that the changes in streamwise force from the trim change are predominantly due to vortex dissipation, or the equivalent conventional induced drag C_{D_i}. The corresponding required change in C_{P_K} can then be estimated by

$$\Delta C_{P_{K\,\rm trim}} = -\frac{\partial C_{P_K}}{\partial C_X}\,\Delta C_{X_{\rm trim}} \simeq 1.5\,\Delta C_{X_{\rm trim}} \tag{3.38}$$

where the slope value of $\partial C_{P_K}/\partial C_X \simeq -1.5$ is obtained from the measured $C_{P_K}(C_X)$ data shown in Figure 3.24.

Here, the two C_{D_i} values in (3.37) are computed for the entire wing+tail+fuselage configuration using the Trefftz-Plane analysis implemented in the AVL vortex-lattice code [26]. The modeled geometry and a sample Trefftz-Plane analysis solution are shown in Figure 3.38. AVL can also impose any specified trim condition by iteratively using its own stability and control derivatives, thus in effect implementing the 2×2 trim system (3.35).

The AVL solution does not model the propulsors, and specifically does not capture the propulsor effects on the measured pitching moment coefficient C_m, or the corresponding $C_{m_{\rm cg}}$ for the chosen *SM*. To correct the measured C_X values to get pitch trim, we perform two AVL calculations for each of the following chosen *SM* values:

1. Specify $(C_L)_{\rm spec} = 0.64$, $(C_{m_{\rm cg}})_{\rm spec} = 0$, and
2. Specify $(C_L)_{\rm spec} = 0.64$, $(C_{m_{\rm cg}})_{\rm spec} = (C_{m_{\rm cg}})_{\rm non\text{-}BLI} - (C_{m_{\rm cg}})_{\rm BLI} = 0.0496$.

The $(C_{m_{\rm cg}})_{\rm spec}$ value in the second case is the negative of the C_m change from non-BLI to BLI, and thus is the C_m change which must be imparted by the elevator to restore pitch trim. The difference in the two C_{D_i} values given by the AVL solutions with and without this C_m change is $\Delta C_{X_{\rm trim}}$ as given by (3.37), and are plotted in Figure 3.39.

The differences in $\Delta C_{P_{K\,\rm trim}}$ values between BLI and non-BLI configurations, which are obtained from the differences in $\Delta C_{X_{\rm trim}}$ values, are listed in Table 3.8, together with the change in the BLI benefit due to trim

$$\Delta PSC_{\rm trim} = \frac{-\,\Delta C_{P_{K\,\rm trim}}\big|^{\rm BLI}_{\rm non\text{-}BLI}}{C_{P_{K\,\rm non\text{-}BLI}}}\,. \tag{3.39}$$

Interestingly, the BLI case actually shows a pitch-trim *benefit* for small static margins, and a penalty for large static margins, although both the $\Delta C_{X_{\rm trim}}$ and $\Delta C_{P_{K\,\rm trim}}$ changes due to trim, and their differences between the two configurations, are extremely small. One reason for this is that the D8 fuselage has a substantial nose-up pitching moment compared to more conventional fuselages. This results in very small trim tail loads for the optimized configuration, as described in Drela [3]. For

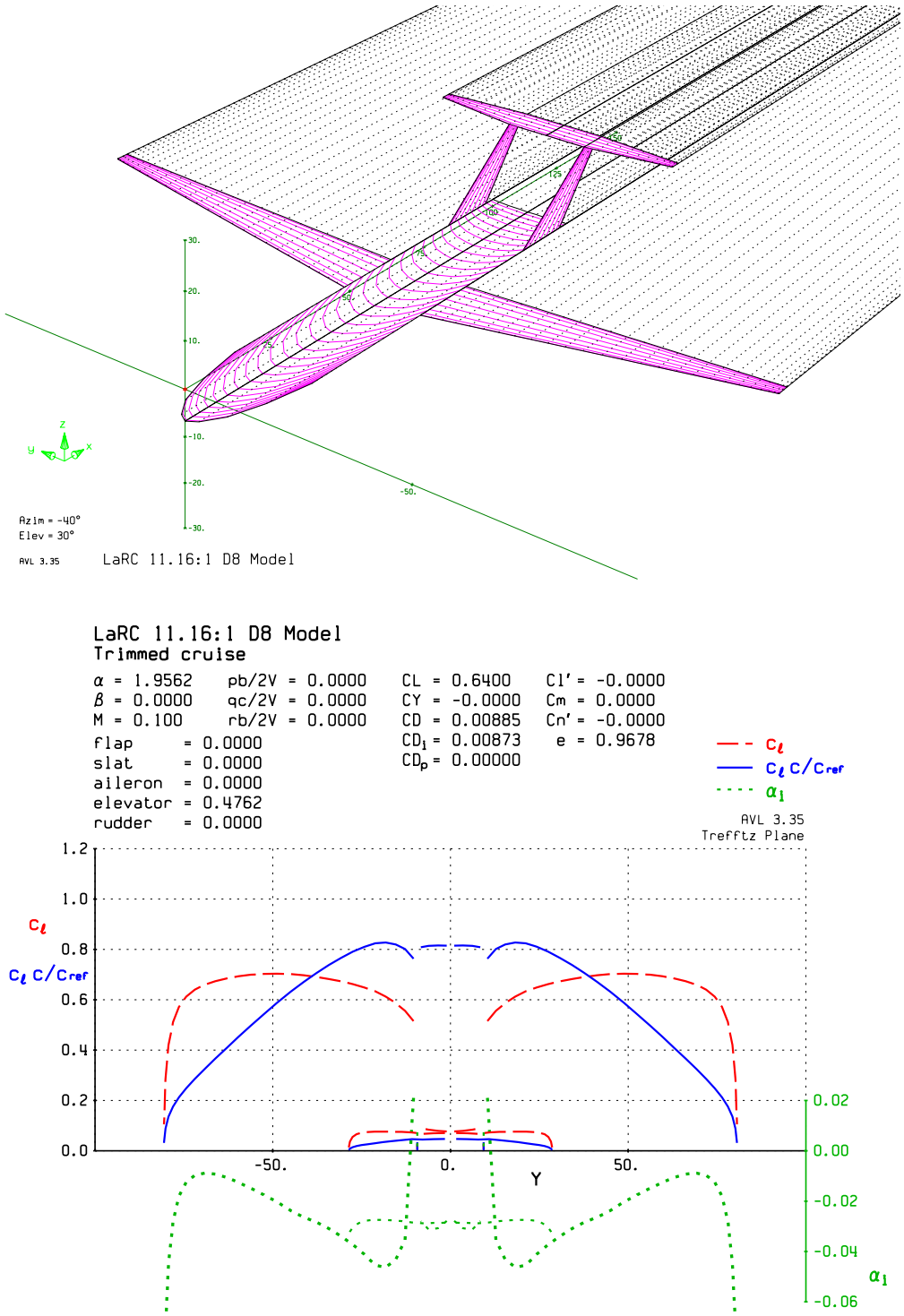

Figure 3.38: AVL vortex lattice model and sample solution used to evaluate trim drag differences between BLI and non-BLI configurations.

the present experiments, the pitch-trim benefit or penalty values are seen to be smaller than the uncertainty in the C_{P_K} measurements, and hence are neglected.

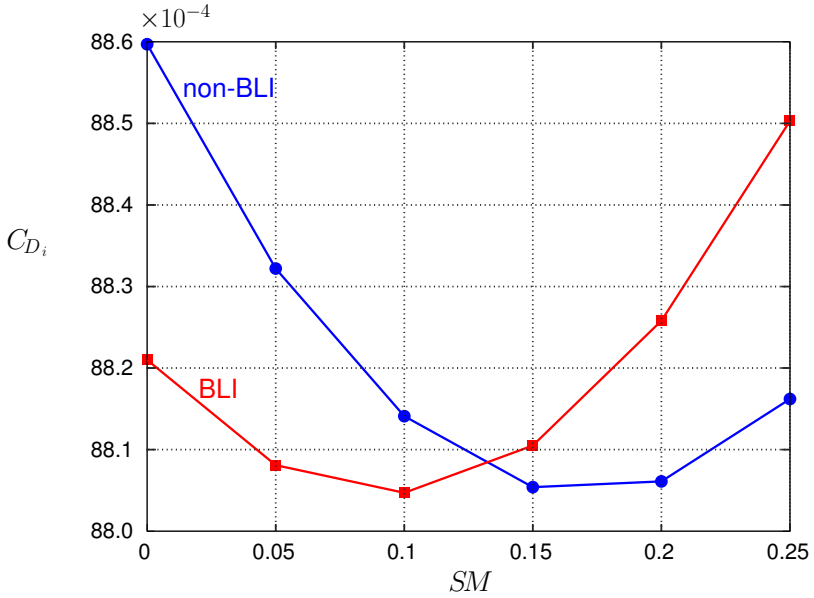

Figure 3.39: Pitch-trimmed C_{D_i} values computed by AVL versus the specified static margin. The change from the non-BLI to the BLI values represents the pitch-trim penalty (or benefit) of the BLI configuration.

Table 3.8: Differences (between BLI and non-BLI cases) of trim corrections to measured C_X and C_{P_K}, and the resulting change in the BLI benefit, ΔPSC_{trim}, which would result from imposing pitch trim on an actual aircraft in level cruise, for a range of static margins.

SM	$\Delta C_{X_{\text{trim}}}\|^{\text{BLI}}_{\text{non-BLI}}$	$\Delta C_{P_{K\,\text{trim}}}\|^{\text{BLI}}_{\text{non-BLI}}$	ΔPSC_{trim}
0.00	-0.387×10^{-4}	-0.580×10^{-4}	$+0.13\%$
0.05	-0.241×10^{-4}	-0.362×10^{-4}	$+0.08\%$
0.10	-0.094×10^{-4}	-0.141×10^{-4}	$+0.03\%$
0.15	0.051×10^{-4}	0.077×10^{-4}	-0.02%
0.20	0.197×10^{-4}	0.296×10^{-4}	-0.07%
0.25	0.341×10^{-4}	0.512×10^{-4}	-0.11%

3.6 Uncertainty Analysis

In this section we analyze the precision (random) and bias (systematic) errors associated with the D8 powered model experiments in the NASA Langley 14– by 22–Foot Subsonic Tunnel . The uncertainty in the BLI benefit in terms of mechanical flow power measured during the wind tunnel tests is found to be ±1.8% in *PSC*.

This analysis is performed on the data obtained using Plug B, and spans from directly measured quantities all the way to the BLI benefit. We detail the precision errors associated with each direct measurement and then provide a step-by-step account of the uncertainty propagation to the final quantities of interest, such as mechanical flow power and aerodynamic BLI benefit. Sources of bias errors are also briefly discussed.

Uncertainty-Specific Variables

B_a	Bias, or systematic error, in variable a
I_a	Instrumentation precision error in variable a related to instrumentation limitations
K	Polynomial order for curve fit, $K = 2$
N	Number of samples
P_a	Precision (random) error in variable a
R_a	Repeatability in variable a, measured at 95% confidence
U_a	Uncertainty (total error) in variable a accounting for bias and precision, $U_a = \sqrt{B_a^2 + P_a^2}$
Y_i	Sample value of Y that corresponds to sample point a_i
$\hat{Y}_i$	Value of Y based on curve fit that corresponds to sample point a_i

3.6.1 Methodology

The definitions used in this uncertainty analysis are briefly presented here. Background on the statistical approach, as well as a detailed account of uncertainty analysis for wind tunnel measurements can be found in References [27] and [16].

Uncertainty: Total Error

The total error or *uncertainty* in a quantity a, denoted by U_a, is defined as the difference between the experimentally determined value of a quantity and its true value. It is composed of two parts: a bias (systematic) error B_a, and a precision (random) error P_a. The uncertainty in a is defined as

$$U_a = \sqrt{B_a^2 + P_a^2} \ . \tag{3.40}$$

Bias: Systematic Error

The *bias*, or *systematic error*, denoted by B_a, accounts for any effect or process that results in a constant deviation or shift of a measured quantity a from its true value. For example, drift or calibration error in a pitot-static manometer will result in an incorrect measurement of tunnel dynamic pressure and corresponding tunnel velocity. Drift or calibration error in a force balance will produce an incorrect offset or scale factor in its measured forces.

Estimation or even detection of bias errors typically requires an independent means of measurement of the quantities of interest, such as a second pitot-static system or force balance being operated in parallel. Frequently these are impractical, in which case the bias errors cannot be determined with certainty. However, they can be minimized by calibration, taring, and zeroing of the instruments using good experimental practices. In the present wind tunnel test program

every effort was made to either minimize or quantify these types of errors (see Section 3.3.2), and corrections have been made to the data to account for all known systematic errors. Throughout the majority of the analysis that follows, bias errors will thus be neglected, and we will assume

$$U_a \simeq P_a \tag{3.41}$$

This is further justified by the fact that we are interested in the BLI benefit, which is a relative measure. We compare the BLI configuration performance to the non-BLI configuration, with both sharing the majority of the hardware and all the instrumentation (in particular tunnel instrumentation, force measurement system, and propulsors), and are thus subject to the same biases.

Precision: Random Error

The *precision error*, denoted by P_a, is the estimate of random variation or scatter in a measured quantity a. The scatter can be caused by electrical noise, vibrations, or by uncompensated variations in temperature, moisture, *etc.*, of the sensor elements or associated electronics. Where possible we will consider two alternative estimates of precision error, either $P_a = I_a$ or $P_a = R_a$, described as follows.

The *instrumentation precision* error, I_a, assumes that the scatter is the result of the limited precision and accuracy of all the instruments employed to measure quantity a. The value of I_a is either specified by the manufacturer via a precision tolerance, or estimated from the instrument calibration.

The *repeatability* error, R_a, is determined by performing multiple measurements of the same quantity (preferably at different times), to get N samples a_i of the (true) quantity a. Following standard practice, we take R_a to be the 95% confidence interval on the mean for the measured variable x. This confidence interval is defined using regression statistical analysis[16] through the procedure of Wahls *et al.* [16], and we write

$$R_a = \mathrm{CI} = \pm\, t \times \mathrm{SE} \times Q(X_0) \tag{3.42}$$

in which t is the cumulative distribution function for a 95% confidence using N samples and a polynomial fit of order $K = 2$. The standard error is given by

$$\mathrm{SE} = \sqrt{\frac{1}{N-K-1}\sum_{i=1}^{2}\left(Y_i - \hat{Y}_i\right)^2}\ , \tag{3.43}$$

and Q is obtained from the covariance matrix $\left(X^T X\right)^{-1}\mathrm{SE}^2$ as

$$Q(X_0) = \sqrt{X_0^T\left(X^T X\right)^{-1} X_0}\ , \tag{3.44}$$

which uses the measurements X (*i.e.*, the $(C_{X_i}, C_{P_{K_i}})$ data points) and the polynomial curve-fit evaluation at the points of interest $X_0 = [1\,,\, X_0\,,\, X_0^2]$ (see [16] for more details).

In most cases we have found that $R_a < I_a$, indicating that manufacturer-quoted precision of the instrumentation is overly conservative and hence unnecessarily pessimistic. For this reason we will in general choose

$$U_a \simeq P_a = \min(\, I_a\,,\, R_a\,) \tag{3.45}$$

where it is understood that I_a is chosen if R_a is not available.

[16] Mathematically, this assumes a large N, as well as a Gaussian error distribution, which is often a good approximation and is adopted by convention [28]. We will show the probability density function of some of the quantities to justify the Gaussian assumption.

Uncertainty Propagation
The uncertainty on a dependent variable, *i.e.*, one that is calculated as a function of independently measured variables, can be evaluated by propagating the uncertainties of the independent variables upon which it depends. This is known as uncertainty propagation.

Let b be a function of n independent variables a_1, a_2, ..., a_n, which have independent random (precision) errors, *i.e.*, the variables upon which b depends are statistically independent of each other. The combined uncertainty on b can then be computed as

$$U_b = \sqrt{\left(\frac{\partial b}{\partial a_1} U_{a_1}\right)^2 + \ldots + \left(\frac{\partial b}{\partial a_n} U_{a_n}\right)^2} = \sqrt{\sum_{j=1}^{n} \left(\frac{\partial b}{\partial a_j} U_{a_j}\right)^2} \ . \tag{3.46}$$

Note that in the case where b is only made of products or quotients, *i.e.*, $b = a_1 a_2 \ldots / a_k \ldots$, the above can be written as

$$\frac{U_b}{b} = \sqrt{\left(\frac{U_{a_1}}{a_1}\right)^2 + \left(\frac{U_{a_2}}{a_2}\right)^2 + \ldots + \left(\frac{U_{a_n}}{a_n}\right)^2} = \sqrt{\sum_{j=1}^{n} \left(\frac{U_{a_j}}{a_j}\right)^2} \ . \tag{3.47}$$

A derivation of the uncertainty propagation equations can be found in Reference [29].

3.6.2 Freestream Condition Uncertainty

Tunnel Instrumentation
The quantities that are directly measured by the NASA Langley 14– by 22–Foot Subsonic Tunnel instrumentation [9] and which are used to determine the freestream conditions are

$$\mathrm{DPI} = p_{t_\infty} - p_s \ , \tag{3.48}$$

$$\mathrm{PTOT} = p_{t_\infty} \ , \tag{3.49}$$

$$\mathrm{TTOT} = T_{t_\infty} \ , \tag{3.50}$$

where p_s is the static pressure measured at a reference location inside the contraction (12 ft upstream of the test section reference location).

One quantity of interest is the difference between total and static pressures in the test section, $p_{t_\infty} - p_\infty$, but this cannot be directly measured during the testing since it would be disturbed by the presence of the model. Instead, the pressure difference DPINF is measured with a Pitot-static probe placed in the empty tunnel test section, and is calibrated against the simultaneously-measured DPI by the relation

$$\mathrm{DPINF} = (p_{t_\infty} - p_\infty)_{\mathrm{empty}} = 0.998 \ \mathrm{DPI} \ C' \simeq p_{t_\infty} - p_\infty \ , \tag{3.51}$$

where

$$C' = 1.1381 + 0.000172 \, \mathrm{DPI} + 0.0000051 \, \mathrm{DPI}^2 \ . \tag{3.52}$$

The constant 0.998 is a probe entrance calibration factor, and C' is a calibration factor which as indicated depends on DPI (in units of psf). This calibration for DPINF in terms of DPI was performed independently of the N+3 experiments and is implemented in the tunnel's data acquisition system which provides the freestream conditions from the measured DPI, PTOT, and TTOT.

The wind tunnel freestream condition is uniquely defined by the freestream Mach number, dynamic pressure, and velocity, via the isentropic compressible flow relations

$$M_\infty = \left\{ \frac{2}{\gamma-1} \left[\left(\frac{p_\infty}{p_{t_\infty}} \right)^{-(\gamma-1)/\gamma} - 1 \right] \right\}^{1/2} , \tag{3.53}$$

$$q_\infty = \frac{\gamma}{2} p_\infty M_\infty^2 , \tag{3.54}$$

$$V_\infty = \sqrt{\gamma R T_{t_\infty}}\, M_\infty \left(1 + \frac{\gamma-1}{2} M_\infty^2 \right)^{-1/2} , \tag{3.55}$$

where $\gamma = 1.4$ is the ratio of specific heats for air, and $R = 287\,\mathrm{J/(kg\,K)}$ is the air specific gas constant [30]. These freestream variables need to be expressed in terms of quantities that are directly measured during the experiments, namely the independent variables DPI, PTOT, TTOT.

Introducing the measured quantities (3.48) through (3.51) into the above relations we get

$$\mathcal{P}(\mathrm{DPI}, \mathrm{PTOT}) \equiv \frac{p_\infty}{p_{t_\infty}} = 1 - \frac{0.998\,\mathrm{DPI}\,C'}{\mathrm{PTOT}} \tag{3.56}$$

$$M_\infty(\mathrm{DPI}, \mathrm{PTOT}) = \left[\frac{2}{\gamma-1} \left(\mathcal{P}^{-(\gamma-1)/\gamma} - 1 \right) \right]^{1/2} \tag{3.57}$$

$$q_\infty(\mathrm{DPI}, \mathrm{PTOT}) = \frac{\gamma}{\gamma-1} \mathrm{PTOT} \left(\mathcal{P}^{1/\gamma} - \mathcal{P} \right) \tag{3.58}$$

$$V_\infty(\mathrm{TTOT}, \mathrm{DPI}, \mathrm{PTOT}) = \sqrt{\gamma R\, \mathrm{TTOT}} \left[\frac{2}{\gamma-1} \left(1 - \mathcal{P}^{(\gamma-1)/\gamma} \right) \right]^{1/2} . \tag{3.59}$$

We use these expressions to define the freestream conditions without any wind tunnel wall corrections, since we are only interested in the relative changes between BLI and non-BLI configurations[17]. The wind tunnel operating point for both series of wind tunnel tests (Entry 1 in 2013 and Entry 2 in 2014) was thus set by holding the (uncorrected) freestream velocity, V_∞, constant.

Another quantity that is of interest is the product $q_\infty V_\infty$, used in the nondimensionalization of power. We can multiply equations (3.58) and (3.59) together to get an expression for $(qV)_\infty$ as a function of the tunnel variables DPI, PTOT, and TTOT, namely

$$\begin{aligned} (qV)_\infty(\mathrm{TTOT}, \mathrm{DPI}, \mathrm{PTOT}) = {} & \frac{\gamma}{\gamma-1} \mathrm{PTOT} \left(\mathcal{P}^{1/\gamma} - \mathcal{P} \right) \\ & \times \sqrt{\gamma R\, \mathrm{TTOT}} \left[\frac{2}{\gamma-1} \left(1 - \mathcal{P}^{(\gamma-1)/\gamma} \right) \right]^{1/2} . \end{aligned} \tag{3.60}$$

Tunnel Instrumentation Precision

The precision errors in the three independently measured quantities DPI, PTOT, TTOT are only due to instrumentation limitations[18], primarily electronic noise. They are given in Table 3.9.

We can now use the expressions (3.56) through (3.60) to propagate the instrumentation errors in DPI, PTOT, and TTOT (which are statistically independent) to the freestream conditions following the root-sum-square rule (3.46). For instance, the instrument error in the dynamic pressure is

$$I_{q_\infty} = \sqrt{ \left(\frac{\partial q_\infty}{\partial \mathrm{DPI}}\, I_{\mathrm{DPI}} \right)^2 + \left(\frac{\partial q_\infty}{\partial \mathrm{PTOT}}\, I_{\mathrm{PTOT}} \right)^2 + \left(\frac{\partial q_\infty}{\partial \mathrm{TTOT}}\, I_{\mathrm{TTOT}} \right)^2 } , \tag{3.61}$$

where the derivatives are most conveniently computed via $\mathcal{P}$ using the chain rule.

[17] The 1:11 scale D8 model blockage is only 0.5% and therefore the wall correction would be small in any case.

[18] We assume the facility calibrations are effectively exact.

Table 3.9: Instrumentation precision from wind tunnel freestream instrumentation.

	Instrument Precision	Instrument
I_{DPI}	0.7 Pa	0–144 psfd Mensor
I_{PTOT}	14 Pa	0–20 psia Mensor
I_{TTOT}	0.2 K	*unknown*

Table 3.10: Instrumentation precision in measured wind tunnel conditions. The values in parentheses are fractional values given in percent, *e.g.*, $I_{q_\infty}/q_\infty \times 100\%$.

V_∞	42 mph	56 mph	70 mph	84 mph
I_{q_∞} (Pa)	0.80 (0.37%)	0.80 (0.21%)	0.80 (0.13%)	0.80 (0.09%)
I_{V_∞} (m/s)	0.036 (0.19%)	0.028 (0.11%)	0.024 (0.08%)	0.022 (0.06%)
$I_{(qV)_\infty}$ (kg/s^3)	23 (0.56%)	30 (0.32%)	38 (0.20%)	47 (0.14%)

The instrument precision in q_∞, V_∞, and $(qV)_\infty$ at the four freestream velocities examined for the D8 tests at NASA Langley are given in Table 3.10. Note that $I_{(qV)_\infty}/(qV)_\infty = I_{q_\infty}/q_\infty + I_{V_\infty}/V_\infty$ since the q_∞ and V_∞ measurements come from the same signals and are hence perfectly correlated.

The relative uncertainties in the Table 3.10 parameters decrease with increasing freestream speed, especially I_{q_∞}. The reason is that, in the low speed flow limit, equation (3.58) asymptotes to

$$q_\infty \simeq 0.998\ \mathrm{DPI}\ C' \simeq 1.15\ \mathrm{DPI}\ , \tag{3.62}$$

which does not depend on PTOT. Consequently, $I_{q_\infty} \simeq 1.15\, I_{\mathrm{DPI}}$ is nearly constant, and therefore the relative uncertainty of q_∞ decreases as $I_{q_\infty}/q_\infty \sim 1/q_\infty \sim 1/V_\infty^2$, and is only 0.09% at 84 mph.

Tunnel Instrumentation Repeatability

The wind tunnel does not have independent additional instruments to measure DPI, PTOT, TTOT, so we cannot measure repeatability of the wind tunnel conditions themselves. However, the main quantities of interest are nondimensional coefficients like C_X and C_{P_K}, which are computed from the dimensional quantities F_X, P_K, q_∞, V_∞. All these are measured, computed, and logged simultaneously. Hence, if the set tunnel condition differs slightly from its intended value, the corresponding data point will merely be shifted slightly along the C_X versus C_{P_K} curve, which itself is unchanged. Any residual effects from the difference in Reynolds number or model elastic deformation are deemed insignificant, as indicated by the insensitivity of the C_X versus C_{P_K} curve across the used tunnel speed range between 42 mph and 84 mph, and one full-year between entries 1 and 2. We therefore neglect any uncertainties in the setting of the wind tunnel flow at a precise operating condition, and only have to consider instrumentation errors on the precision in wind tunnel conditions.

Tunnel Instrumentation Bias Errors

Calibration of the Langley wind tunnel instruments performed after the D8 experiments took place determined[19] there was a +12.3 Pa (+0.256 psf) bias in PTOT and a −13.4 Pa (−0.279 psf) bias in

[19] personal communication with J. Hannon from NASA Langley Research Center

the tunnel's reference pressure PA. These biases have been corrected in the post-processing of the experimental data, and are therefore not accounted for in the present uncertainty calculations.

3.6.3 Force Measurement Uncertainty

Force Instrumentation Precision

The NASA internal force balance 843A was used during both wind tunnel entries, and was calibrated at NASA Langley. The main quantities of interest it measures in regard to our investigation are the balance axial force F_A, and the balance normal force F_N. The NASA Q-flex accelerometer was used to measure the angle of attack α of the model and balance. The precision limits of these instruments were provided by the NASA Langley force balance department and are presented in Table 3.11.

The measured axial and normal forces in the balance axes, F_A and F_N respectively, are converted into the net streamwise and lift forces on the D8 model in wind tunnel axes via the standard axis rotation relations

$$F_X = F_A \cos\alpha + F_N \sin\alpha \,, \tag{3.63}$$

$$F_Z = -F_A \sin\alpha + F_N \cos\alpha \,. \tag{3.64}$$

Using the standard rule (3.46) for error propagation yields the instrumentation precision in these rotated force components, namely

$$I_{F_X} = \sqrt{(I_{F_A}\cos\alpha)^2 + (I_{F_N}\sin\alpha)^2 + \left[I_\alpha(F_N\cos\alpha - F_A\sin\alpha)\right]^2} \,, \tag{3.65}$$

$$I_{F_Z} = \sqrt{(I_{F_A}\sin\alpha)^2 + (I_{F_N}\cos\alpha)^2 + \left[I_\alpha(F_N\sin\alpha + F_A\cos\alpha)\right]^2} \,. \tag{3.66}$$

The magnitudes of instrument precision in Table 3.11 are such that the uncertainty terms due to the imprecision in the angle of attack, I_α, are over an order-of-magnitude smaller than those due to the force balance. Equations (3.65) and (3.66) can therefore be simplified to

$$I_{F_X} \simeq \sqrt{(I_{F_A}\cos\alpha)^2 + (I_{F_N}\sin\alpha)^2} \,, \tag{3.67}$$

$$I_{F_Z} \simeq \sqrt{(I_{F_A}\sin\alpha)^2 + (I_{F_N}\cos\alpha)^2} \,. \tag{3.68}$$

The final step is to nondimensionalize the forces to get the net streamwise force coefficient and lift coefficient instrument precision errors. Using equation (3.47) gives

$$I_{C_X} = \sqrt{\left(\frac{I_{F_X}}{q_\infty S_{\text{ref}}}\right)^2 + \left(\frac{I_{q_\infty}}{q_\infty}C_X\right)^2} \,, \tag{3.69}$$

$$I_{C_L} = \sqrt{\left(\frac{I_{F_Z}}{q_\infty S_{\text{ref}}}\right)^2 + \left(\frac{I_{q_\infty}}{q_\infty}C_L\right)^2} \,. \tag{3.70}$$

Using the instrument precision I_{F_A} and I_{F_N} from Table 3.11, the instrument precision I_{q_∞} from Table 3.10, and the model lift curve $C_L(\alpha)$, the above two equations give I_{C_X} and I_{C_L} as functions of V_∞ and α. These are shown in Figures 3.40 and 3.41, and illustrate the decrease in instrument precision error with increasing freestream velocity. The main cause is the increasing q_∞ in the denominator of equations (3.69) and (3.70), which in effect "dilutes" the nearly fixed instrument precisions I_{F_X}, I_{F_Z}, I_{q_∞}. The α dependence of I_{C_L} is mainly via the C_L term in (3.70) that is a function of α.

Table 3.11: Instrument precision in force balance instrumentation.

	Instrument Precision	Instrument
I_{F_A}	0.434 N (0.0975 lb)	NASA 843A force balance
I_{F_N}	1.346 N (0.3025 lb)	NASA 843A force balance
I_α	0.00009 rad (0.005°)	NASA Q-flex

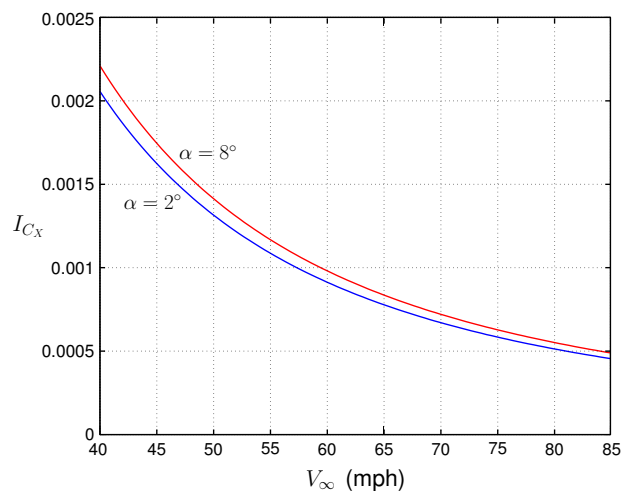

Figure 3.40: Instrument precision in C_X as a function of V_∞ and α.

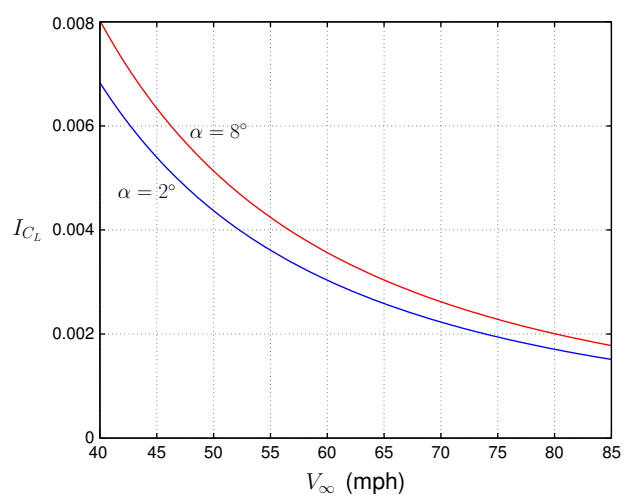

Figure 3.41: Instrument precision in C_L as a function of V_∞ and α.

Force Instrumentation Repeatability

To supplement the above instrument precision analysis, we can assess the repeatability of the force measurements obtained from the NASA 843A force balance by using multiple measurements at nominally constant conditions.

An example histogram of measured C_X with $N = 10$ samples is presented in Figure 3.42, plotted as a probability density function. All samples are from Entry 2, for the BLI configuration with $V_\infty = 70$ mph, $\Omega = 10600$ RPM, using Plug B, and at the simulated cruise angle of attack of $\alpha = 2°$. The samples span the entire calendar time span of the second wind tunnel entry, before and after various model changes, and therefore give a realistic representation of the variations due to the inability to repeat conditions and measurements exactly.

A normal distribution fit has been made to the data, as shown in Figure 3.42, to quantify the repeatability in terms of the sample standard deviation and hence a 95% confidence interval, R_{C_X}, via equation (3.42). The data scatter is close to Gaussian, and the repeatability is quantified for C_X and C_L at 70 mph and 84 mph using normal distribution fits. Table 3.12 compares the resulting repeatability numbers R_{C_X} and R_{C_L} with the instrument precision numbers I_{C_X} and I_{C_L} determined in the previous section. The R_{C_X} values are seen to be somewhat lower than I_{C_X}, while R_{C_L} is somewhat larger than I_{C_L}. However, the fact that the precision and the repeatability agree to within a factor of 2 so closely gives some confidence that these represent the true uncertainty in the measured C_X and C_L.

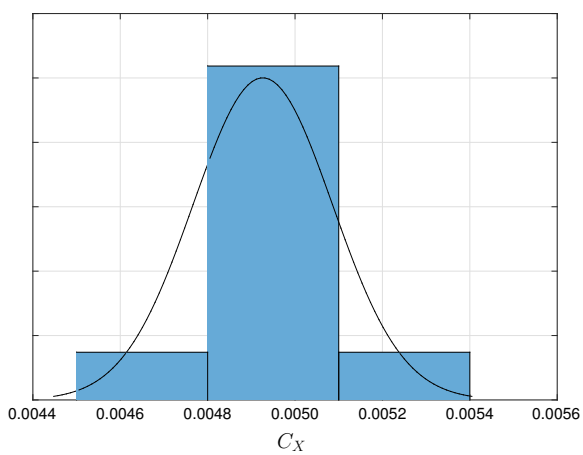

Figure 3.42: Probability density function of C_X at nominally identical conditions.

Table 3.12: Comparison of instrument precision and repeatability for $N = 10$ samples in force coefficients for the BLI configuration, $\alpha = 2$, Plug B, Entry 2.

V_∞	70 mph	84 mph
I_{C_X}	0.00067	0.00047
R_{C_X}	0.00032	0.00034
I_{C_L}	0.0023	0.0016
R_{C_L}	0.0027	0.0028

3.6.4 Electrical Power Uncertainty

Electrical Power Instrumentation Precision

Electrical power is computed as the product of voltage, v, and current, i, both measured at the electric motors' power supply: $P_E = v\,i$. Combining the instrument precision in v and i then gives the instrument precision in P_E as

$$I_{P_E} = \sqrt{\left(\frac{I_v}{v}\right)^2 + \left(\frac{I_i}{i}\right)^2}\, P_E \ . \tag{3.71}$$

The instrument precisions for voltage and current quoted by the instrument manufacturer are presented in Table 3.13. The precision in the power supply voltage is associated with the voltage readout from the National Instruments card. The precision in the current is dominated by uncertainty associated with the current monitor in the power supply.

The quantity of interest is the nondimensionalized electrical power coefficient and its instrument precision, given respectively by

$$C_{P_E} = \frac{P_E}{(qV)_\infty S_{\text{ref}}} \ , \tag{3.72}$$

$$I_{C_{P_E}} = \sqrt{\left(\frac{I_{P_E}}{P_E}\right)^2 + \left(\frac{I_{(qV)_\infty}}{(qV)_\infty}\right)^2}\, C_{P_E} \ , \tag{3.73}$$

and their values at 70 mph and 84 mph are given in Table 3.13. With the manufacturer's quoted precisions for I_v and I_i, the electrical measurement precision I_{P_E} dominates in (3.73), with the contribution of $I_{(qV)_\infty}$ being relatively minor.

Table 3.13: Instrument precision in electrical power quantities.

I_v	$0.0025\,v + 0.15625$	
I_i	$0.010\,i$	(1.0%)
I_{P_E}	$0.012\,P_E$	(1.2%)
$I_{C_{P_E}}$	$0.014\,C_{P_E}$	(1.4%)

Electrical Power Repeatability

To determine the repeatability of the electrical power measurements we consider multiple measurements for the non-BLI configuration at $V_\infty = 84$ mph, $\alpha = 2°$, at a propulsor wheel speed of $\Omega = 13500$ RPM with Plug B. The measured C_{P_E} for $N = 10$ samples taken throughout the Entry 2 tests are shown as the histogram of their probability density function in Figure 3.43. The Gaussian fit curve in the figure indicates that the variation in C_{P_E} closely follows the normal distribution, and we therefore quantify the repeatability as $R_{C_{P_E}} = K\,\bar{s}_{C_{P_E}}$, which is compared with $I_{C_{P_E}}$ in Table 3.14. The fact that $R_{C_{P_E}}$ is roughly ten times smaller than $I_{C_{P_E}}$ indicates that the manufacturers' quoted electrical instrument precisions I_v and I_i are very conservative compared to the actual precision obtained in practice.

Electrical Power Bias Errors

There are no known bias (systematic) errors in the measurements of electrical power, P_E, or the electrical power coefficient, C_{P_E}.

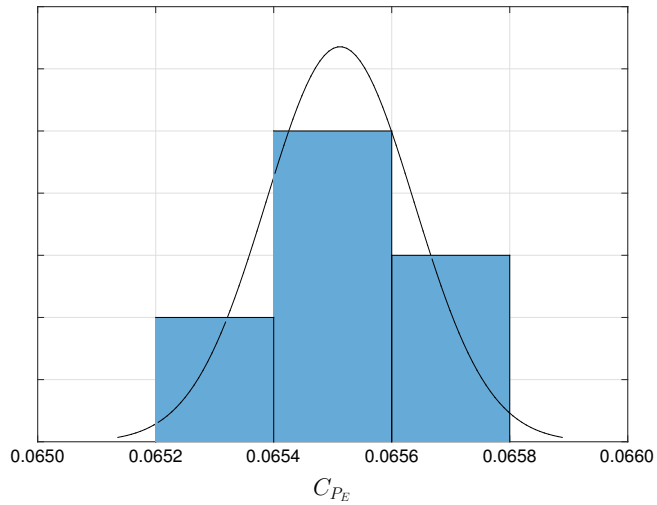

Figure 3.43: Probability density function of C_{P_E} at nominally identical conditions.

Table 3.14: Comparison of fractional C_{P_E} instrument precision and repeatability near simulated cruise for both configurations.

V_∞	70 mph	84 mph
$I_{C_{P_E}}/C_{P_E}$	1.21%	1.21%
$R_{C_{P_E}}/C_{P_E}$	0.16%	0.19%

3.6.5 Mechanical Flow Power Uncertainty (Based on the Indirect Method)

Mechanical Flow Power Instrumentation Precision

The indirect method calculates the mechanical flow power, P_K, as the product of electrical power, P_E, and overall efficiency, η_o, *i.e.*,

$$P_K = \eta_o \, P_E \ , \tag{3.74}$$

or, in terms of power coefficients,

$$C_{P_K} = \eta_o \, C_{P_E} \ . \tag{3.75}$$

The instrument precision on mechanical flow power is thus written using the product rule (3.47) as

$$\frac{I_{C_{P_K}}}{C_{P_K}} = \sqrt{\left(\frac{I_{\eta_o}}{\eta_o}\right)^2_{\text{GTL}} + \left(\frac{I_{C_{P_E}}}{C_{P_E}}\right)^2_{\text{LaRC}}} \ , \tag{3.76}$$

in which we added the subscripts GTL and LaRC to indicate where each of the quantities is measured. The value of η_o (product of motor and fan efficiencies) was measured in the complementary experiments performed in MIT's GTL 1×1 tunnel over the range of operating conditions seen in the NASA Langley tunnel. The C_{P_E} measurements were taken at Langley during the 14– by 22–Foot Subsonic Tunnel wind tunnel tests.

The uncertainty analysis of the complementary GTL tests is presented in Reference [13]. The relative instrument precision on the overall efficiency is $I_{\eta_o}/\eta_o \approx 0.012$, which covers the range of operating conditions seen at Langley for all the tunnel speeds. Typical efficiency values are $\eta_o \approx 0.65$ over most of the propulsor operating range.

Using these results, and the instrument precision values for C_{P_E}, the instrument precision on C_{P_K} from the indirect method can be computed from (3.76), the result of which is shown in Table 3.15.

Table 3.15: Fractional instrument precision in mechanical flow power variables computed using the indirect method.

I_{η_o}/η_o	1.2%
$I_{C_{P_K}}/C_{P_K}$	1.8%

Mechanical Flow Power Repeatability

The repeatability of the overall efficiency R_{η_o} was obtained in the complementary GTL tests [13] with $N = 4$ samples, This, together with $R_{C_{P_E}}$ obtained in the Langley tests, gives the repeatability of mechanical flow power via the product rule (3.47) as

$$\frac{R_{C_{P_K}}}{C_{P_K}} = \sqrt{\left(\frac{R_{\eta_o}}{\eta_o}\right)^2_{\text{GTL}} + \left(\frac{R_{C_{P_E}}}{C_{P_E}}\right)^2_{\text{LaRC}}}\,. \tag{3.77}$$

The values of these instrument precisions and repeatabilities are given and compared in Table 3.16. Note that R_{η_o} dominates the final $R_{C_{P_K}}$ value.

Table 3.16: Comparison of fractional instrument precisions and repeatabilities associated with power coefficients near simulated cruise for both speeds.

	BLI	Non-BLI
I_{η_o}/η_o	1.20%	1.20%
R_{η_o}/η_o	0.70%	0.70%
$I_{C_{P_E}}/C_{P_E}$	1.21%	1.21%
$R_{C_{P_E}}/C_{P_E}$	0.16%	0.19%
$I_{C_{P_K}}/C_{P_K}$	1.57%	1.56%
$R_{C_{P_K}}/C_{P_K}$	0.72%	0.73%

Mechanical Flow Power Bias Errors

There are no known bias (systematic) errors in the measurements of mechanical flow power.

3.6.6 BLI Benefit Uncertainty (Based on the Indirect Method)

Precision in Power at Cruise Condition

The most important results of this analysis are the total precision (and hence uncertainty) in the power requirement at simulated cruise, $C_X = 0$, and therefore the total precision in the aerodynamic BLI benefit at cruise. One further equation is required. There is uncertainty in the setting of the simulated cruise point and an additional term must be introduced when quantifying the error on the power coefficient at the cruise condition in terms of mechanical flow power. The equations for the propagated instrument precision and repeatability at simulated cruise are

$$I_{C_{P_K}|_{C_X=0}} = \sqrt{\left(I_{C_{P_K}}\right)^2 + \left(I_{C_X} \left.\frac{\mathrm{d}C_{P_K}}{\mathrm{d}C_X}\right|_{C_X=0}\right)^2}\,, \tag{3.78}$$

$$R_{C_{P_K}|_{C_X=0}} = \sqrt{\left(R_{C_{P_K}}\right)^2 + \left(R_{C_X} \left.\frac{\mathrm{d}C_{P_K}}{\mathrm{d}C_X}\right|_{C_X=0}\right)^2}\,, \tag{3.79}$$

where the second term in each equation accounts for the uncertainty in the streamwise force coefficient. Using the C_{P_K} versus C_X plot to estimate the derivative, we have then have

$$\left.\frac{\mathrm{d}C_{P_E}}{\mathrm{d}C_X}\right|_{C_X=0} \simeq 1.6\,, \tag{3.80}$$

and thus

$$\frac{I_{C_{P_K}|_{C_X=0}}}{C_{P_K}} = \sqrt{\left(\frac{I_{C_{P_K}}}{C_{P_K}}\right)^2 + \left(1.6\,\frac{I_{C_X}}{C_{P_K}}\right)^2}\,, \tag{3.81}$$

$$\frac{R_{C_{P_K}|_{C_X=0}}}{C_{P_K}} = \sqrt{\left(\frac{R_{C_{P_K}}}{C_{P_K}}\right)^2 + \left(1.6\,\frac{R_{C_X}}{C_{P_K}}\right)^2}\,. \tag{3.82}$$

The resulting final fractional precision and repeatability values for C_{P_K} at the simulated cruise condition are given in Table 3.17.

Precision in BLI Benefit

In quantifying the uncertainty in the aerodynamic BLI benefit, the precision in the mechanical flow power coefficient at cruise for *both* the BLI and non-BLI configurations must be taken into account.

Table 3.17: Comparison of instrument precision and repeatability in flow power coefficient at the simulated cruise condition.

	BLI		Non-BLI	
	70 mph	84 mph	70 mph	84 mph
$I_{C_{P_K}\|_{C_X=0}}/C_{P_K}$	2.85%	2.28%	2.67%	2.17%
$R_{C_{P_K}\|_{C_X=0}}/C_{P_K}$	1.34%	1.40%	1.26%	1.31%

The power saving coefficient definition (3.7) as specialized to the cruise condition case is

$$PSC_0 = \frac{C_{P_K}|_{C_X=0_{\text{non-BLI}}} - C_{P_K}|_{C_X=0_{\text{BLI}}}}{C_{P_K}|_{C_X=0_{\text{non-BLI}}}} . \tag{3.83}$$

Combining the instrument precision or the repeatability for the non-BLI and BLI configurations yields

$$I_{PSC_0} = \mathcal{R}_{P_K} \sqrt{\left(\frac{I_{C_{P_K}|_{C_X=0}}}{C_{P_K}}\right)^2_{\text{non-BLI}} + \left(\frac{I_{C_{P_K}|_{C_X=0}}}{C_{P_K}}\right)^2_{\text{BLI}}} , \tag{3.84}$$

$$R_{PSC_0} = \mathcal{R}_{P_K} \sqrt{\left(\frac{R_{C_{P_K}|_{C_X=0}}}{C_{P_K}}\right)^2_{\text{non-BLI}} + \left(\frac{R_{C_{P_K}|_{C_X=0}}}{C_{P_K}}\right)^2_{\text{BLI}}} . \tag{3.85}$$

These instrument precision and repeatability values are presented in Table 3.18. Since the instrument precision on the electrical power measurements were found to be extremely conservative, we take the repeatability value to be representative of the actual uncertainty in the measured BLI benefit.

Table 3.18: Instrument precision and repeatability in BLI benefit.

		70 mph	84 mph
Instrument Precision	I_{PSC_0}	3.65%	2.94%
Repeatability	R_{PSC_0}	1.70%	1.78%

BLI Benefit Uncertainty

We have quantified both the instrument precision and repeatability, and the latter has consistently been smaller for all quantities. This indicates that the manufacturer-quoted precision values are conservative. Furthermore, care was taken to perform a sufficient number of repeat runs during the tests at the NASA Langley 14– by 22–Foot Subsonic Tunnel, spread throughout the 4–6 weeks of tests in each entry, separated by model changes, and through two tunnel entries one year apart. Finally, the BLI benefit measured at cruise is the same *within repeatability* for the two cruise freestream velocities considered (70 mph and 84 mph). We therefore believe the repeatability of the experimental data is a better measure of the true uncertainty than the instrument precision.

The uncertainty on the BLI benefit is thus estimated to be 1.8% (the higher of the 70 mph and 84 mph R_{PSC_0} repeatability values) giving an average, experimentally measured, BLI benefit of 8.6% ± 1.8% at simulated cruise with fixed nozzle area.

3.7 Inlet Distortion Fields

As part of the experiments performed at the NASA Langley 14– by 22–Foot Subsonic Tunnel, a series of flow surveys were taken at the integrated propulsor inlet, approximately $0.08\,d_{\text{fan}}$ (11 mm) upstream of the nacelle leading edge (see [12, 15] for more details).

Here we present the inlet flowfields at the climb, cruise, and descent mission points whose conditions are given in Table 3.19. These mission points are illustrated in the C_X versus C_L envelope of Figure 3.44, which includes points of the full size D8.2 from TASOPT predictions, and also the ranges measured during the propulsor power sweeps in the NASA Langley tunnel. Note that the model envelope for the tests is a subset of the full-size D8.2 mission envelope: the model's power limitations and lack of takeoff flaps did not permit reaching the extreme full-size C_X values.

The fields of Figures 3.45 through 3.48 were taken using a five-hole-probe (FHP) during the second tunnel entry in the summer of 2014. Since the FHP was calibrated by the manufacturer in uniform flow, we present the pressure read by the probe's front center port in place of, and as an approximation to, the total pressure, since the latter is unaffected by the inaccuracy of the probe's calibration for use in shear flows. Shear-flow corrections to the calibration will be added in the future, and final inlet flow fields published.

Table 3.19: Conditions of mission points for wind tunnel tests: simulated points.

	Angle of Attack	Freestream	Fan Wheel Speed	
	α	V_∞	Ω	U_{tip}/V_∞
Start of climb (SOC)	8°	42 mph	14 000 RPM	5.62
Top of climb (TOC)	2°	70 mph	13 500 RPM	3.25
Cruise	2°	70 mph	11 100 RPM	2.67
Descent	8°	70 mph	5 250 RPM	1.27

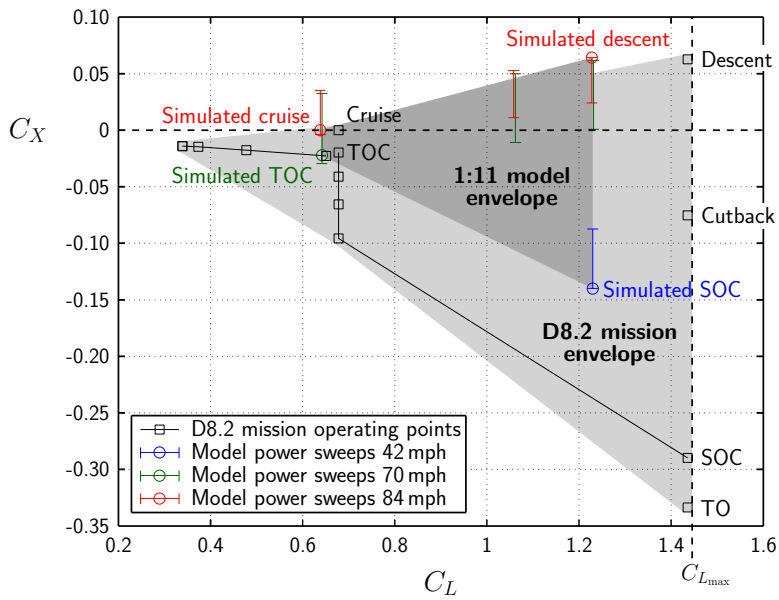

Figure 3.44: Mission envelope on plane of net streamwise force coefficient versus lift coefficient. The points designated as "simulated" correspond to wind tunnel tests, while the D8.2 envelope designates full-size transonic predictions from TASOPT.

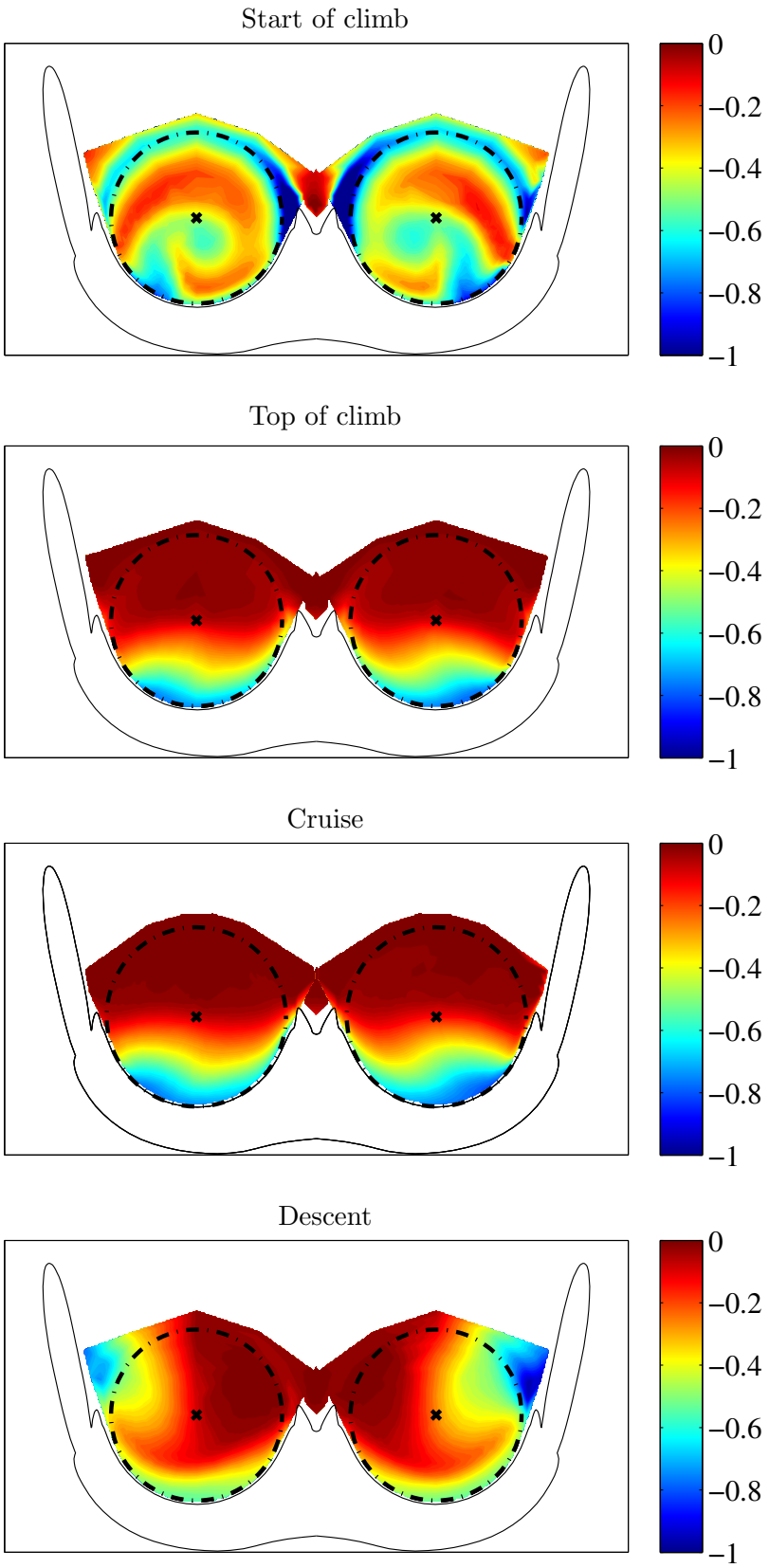

Figure 3.45: Contours of total pressure coefficient C_{p_t}, as approximated by probe's front center port, at the propulsor inlet of the BLI configuration, with Plug B, obtained from the FHP surveys at the simulated mission points. View is looking upstream.

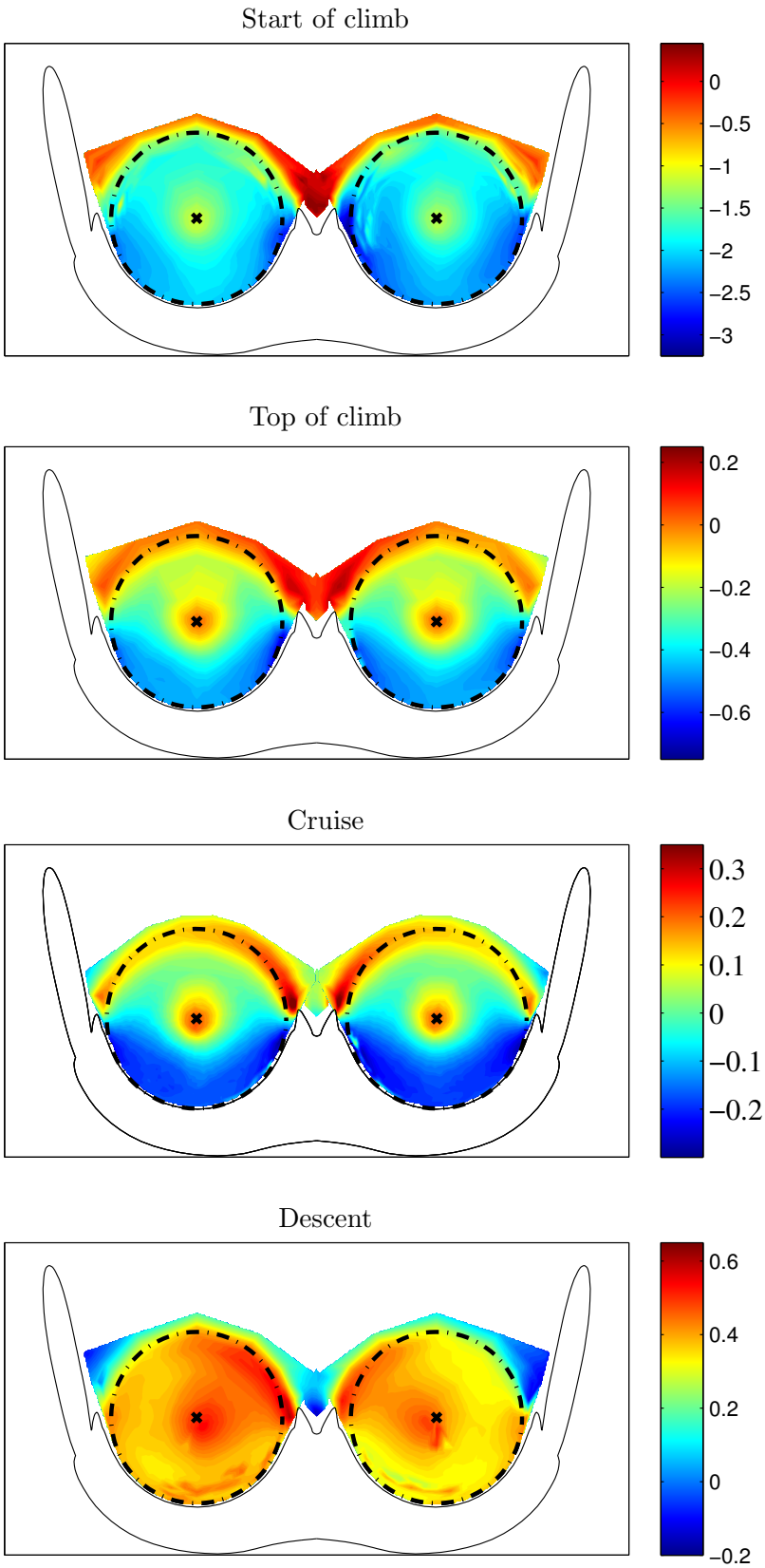

Figure 3.46: Contours of static pressure coefficient C_p at the propulsor inlet of the BLI configuration, with Plug B, obtained from the five-hole-probe surveys at the simulated mission points. View is looking upstream.

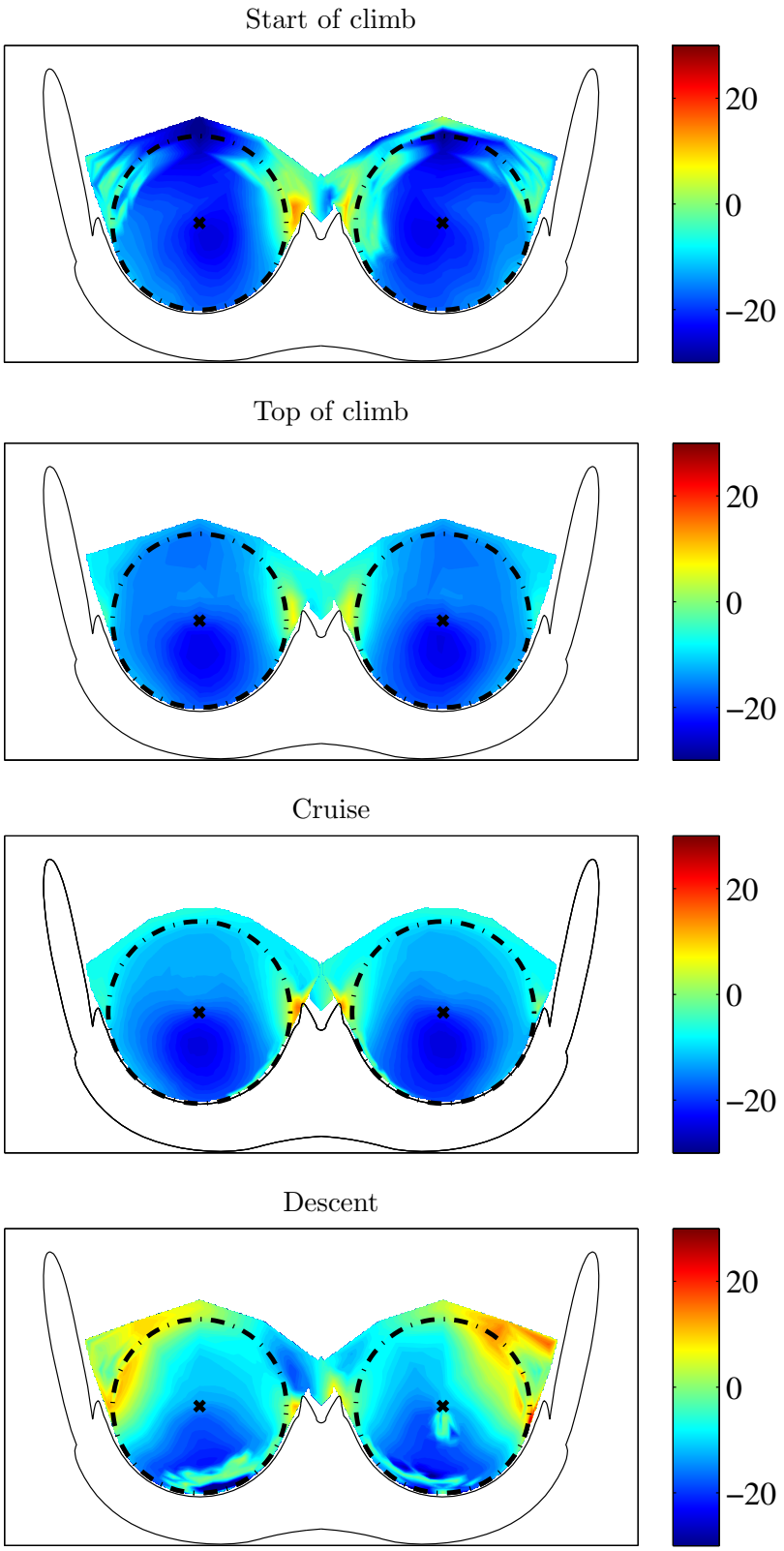

Figure 3.47: Contours of flow pitch angle (in degrees) at the propulsor inlet of the BLI configuration, with Plug B, obtained from the five-hole-probe surveys at the simulated mission points. The angle is taken with respect to the propulsor's axis, with positive values for flow directed upwards, and the view is looking upstream.

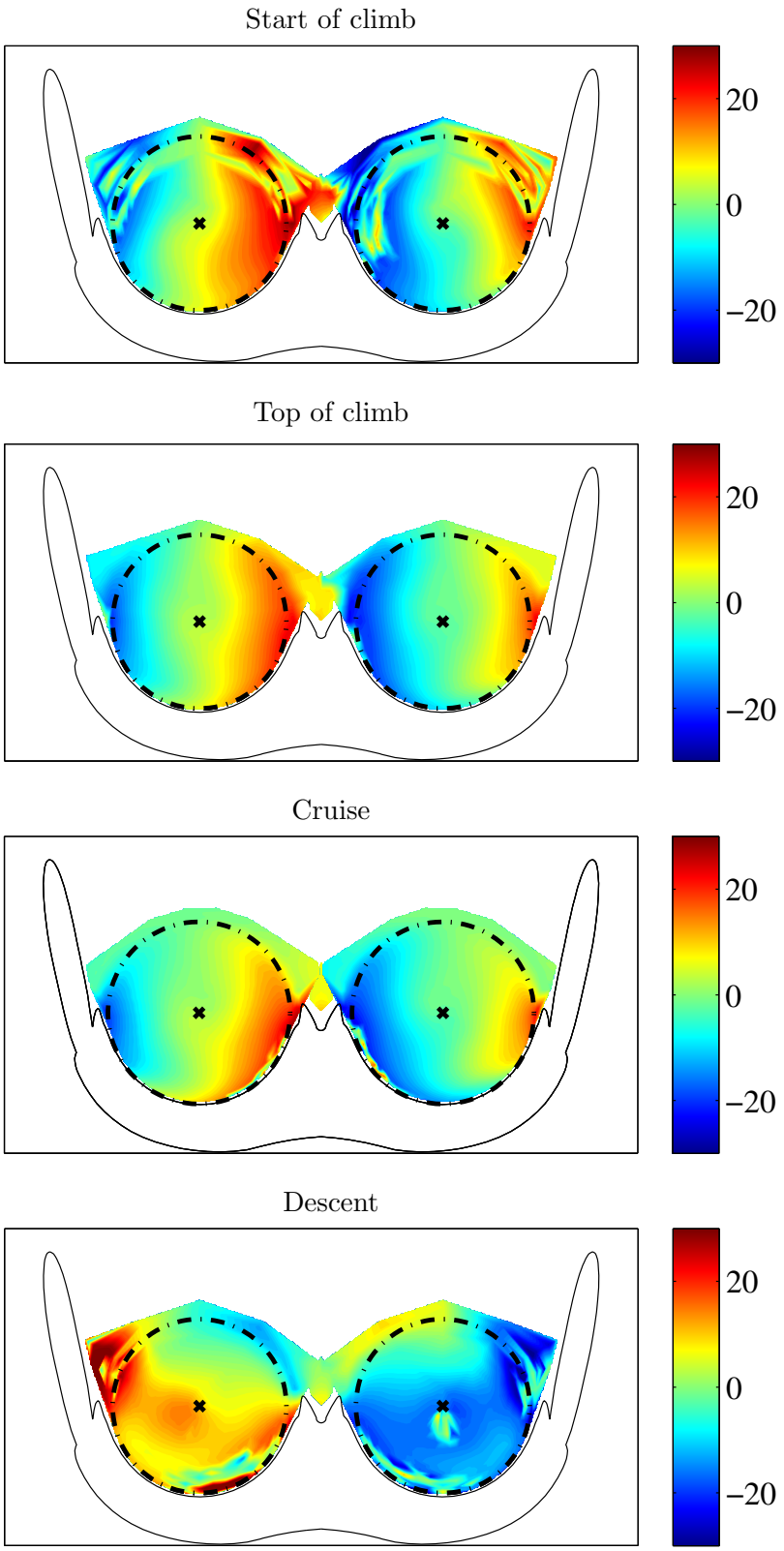

Figure 3.48: Contours of flow yaw angle (in degrees) at the propulsor inlet of the BLI configuration, with Plug B, obtained from the five-hole-probe surveys at the simulated mission points. The angle is taken with respect to the propulsor's axis, with positive values for flow going from right to left, and the view is looking upstream.

3.8 Additional Considerations for Full-Size Aircraft

3.8.1 System-Level Benefits of BLI and the D8 Configuration

The contents of this Section 3.8.1 is adapted and expanded based on [2].

The Phase 2 program focused almost entirely on the *aerodynamic* BLI benefit, which is mainly the result of improved propulsive efficiency and also reduced engine nacelle wetted-area losses and reduced fuselage wake dissipation. However, an actual aircraft BLI installation will produce additional benefits from the weight reductions enabled by BLI. The D8 concept aircraft has numerous features that give fuel benefits in addition to those attributable to its BLI system, as described by Drela [3] and summarized briefly in Section 3.2.1.

To quantify all the benefits of BLI, including those at the system level, and also to quantify the overall benefits of the D8 aircraft, a sequence of conceptual aircraft designs are defined and optimized using the TASOPT methodology [1, 3]. The mission is set for all steps at a 3 000 nm range with 180 passengers (enforced as a 38 700 lb payload), and all aircraft use two engines[20].

Starting with the baseline 737-800 aircraft, the distinctive design features of the D8 are introduced one at a time, and the aircraft is re-optimized at each step to minimize mission fuel burn. This results in a sequence through which the 737-800 "morphs" into the D8 aircraft, with the fuel burn for each design step shown in Figure 3.49. The changes that occur at each step can then be examined to determine the physical origin of fuel burn reductions, including system-level effects.

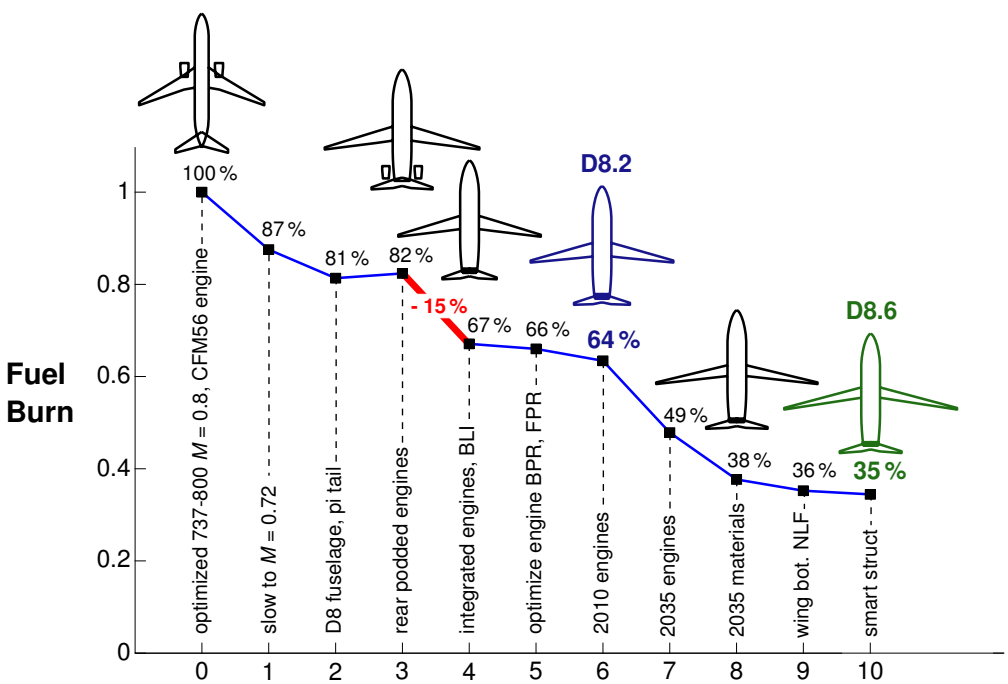

Figure 3.49: "Morphing" sequence of design changes from the optimized 737-800 baseline (step 0) to the D8 configuration. The vertical axis and percent numbers give the changes in fuel burn with respect to the step 0 baseline. BLI is introduced between steps 3 and 4 (red segment).

[20] At the end of MIT's Phase 1 work in 2010, three-engine D-series aircraft for this same mission were proposed, named D8.1 when using current technology assumptions, and D8.5 for the 2035 technology level. For Phase 2, two engines were adopted since the performance penalty is only about 0.5% in fuel burn, but the advantages in cost and maintenance are deemed important.

The main design variables optimized at each step are cruise C_L, wing aspect ratio AR, wing sweep angle, airfoil thickness-to-chord ratio at several spanwise stations, spanwise load distribution, turbofan combustor temperatures $T_{t\,4}$ at takeoff and cruise, and start-of-cruise altitude h_{cruise}. The key aircraft parameters as they evolve over the morphing sequence are listed in Table 3.20.

The morphing process starts from a version of the 737-800 optimized with TASOPT at step 0. The first morphing step is the result of slowing down the cruise speed from Mach 0.80 to 0.72, which reduces fuel burn mainly thanks to a larger aspect ratio and a larger cruise C_L, both enabled structurally and aerodynamically by a smaller sweep. The change to the D8 double-bubble fuselage from case 1 to 2 reduces fuel burn mainly from a reduced maximum weight, which is due to the larger fuselage lift fraction and nose-up pitching moment offset. The bypass ratio (*BPR*) and fan pressure ratio (*FPR*) are for now held fixed at the values of the CFM56 engine used on the 737-800.

The change from step 2 to step 3 is the movement of the engine nacelles from under the wing to the rear of the fuselage. The rearward weight shift increases the required tail size, but this is partly offset by the nacelles providing some pitch stability. The maximum engine-out yaw moments are reduced by the slightly smaller engine spacing, and the landing gear is shortened and lightened significantly. Overall, a 1% fuel burn increase is predicted, although this has some uncertainty due to the large degree of cancellation between the numerous competing effects.

BLI is introduced between steps 3 and 4, and consists of moving the rear podded engines to the top of the fuselage. The engine bypass ratio and fan pressure ratio are held fixed for now, but the entire aircraft is re-sized and re-optimized. This gives a fuel burn reduction of 19%, which is about twice the propulsion-only benefit of 8–10% predicted by analysis and the Phase 2 experiment. The extra benefit is due to the savings from reduced nacelle weight, reduced vertical tail size allowed by the smaller engine-out yaw moments, plus the compounding effect on the overall weight.

Additional benefits of about 1% are produced when the engines are optimized for BLI from step 4 to step 5. Finally, the 4% reduction between steps 5 and 6 is due to switching to 2010 engine technology[21] instead of the CFM56's 1975 technology. Specifically, overall pressure ratio (*OPR*) is increased from 30 to 40, and the engine weight model adjusted.

Steps 7 through 10 introduce technology levels that are expected to reach maturity in 2035, and are referred to as *N+3 technology*. The reader is referred to the Phase 1 report [1] for an explanation of what these N+3 technology characteristics are and how they were derived.

Between steps 6 and 7, the engine is upgraded to one with an *OPR* of 50, and which also has improved component efficiencies and improved engine materials, thus reducing turbine cooling flows and overall engine weight. Together with compounding weight reductions, the corresponding aircraft has a fuel burn reduction of 24%.

Between steps 7 and 8 the airframe materials have an increased allowable-stress to density ratio giving a lighter airframe. Between steps 8 and 9 the wing's lower surface is assumed to have natural laminar flow, which is modeled as a reduced wing profile drag (wing upper surface is assumed to remain turbulent). Finally, the use of smart structures at step 10 enables a further increase in the airframe allowable-stress to density. The final D8.6 aircraft is predicted to require 65% less fuel than the baseline optimized 737.

In the present Phase 2 study the BLI and non-BLI configurations have essentially the same geometry, so the measured BLI benefit of 8.6% at equal nozzle area is only due to direct propulsive and aerodynamic effects. However, the morphing study presented here indicates that this fuel burn reduction will be more than doubled to 19% when system-level benefits enabled by BLI are accounted for. Once all the D8 design features are incorporated, the benefit increases to 36%, all with current airframe and engine technology. Finally, incorporation of forecast 2035 technologies increases the benefit to 65%.

[21] What we call *current technology* per the 2010 year when Phase 1 was completed [1]

Table 3.20: Optimized aircraft parameters in "morphing" sequence. The reference area, S, is defined as the exposed wing area plus the wing carry-through area inside the fuselage. When BLI is present, 40% of the fuselage boundary layer kinetic energy defect is ingested. The reference values at Step 0 are $W_{\max 0} = 160\,858$ lb and $W_{\text{fuel}_0} = 35\,131$ lb. The relative step fuel weight values in the fifth column give the change relative to the previous step. The L/D values are evaluated as $C_L/C_{\Phi_{\text{airframe}}}$ for the BLI cases in steps 4–10.

Step	BLI?	Weights			Geometry			
		$W_{\max}$ frac	W_{fuel} frac	W_{fuel} step %	Span (ft)	S (ft^2)	AR	Sweep (°)
0	N	1.000	1.000		115.8	1240	10.8	26.7
1	N	0.990	0.873	−13%	148.9	1338	16.6	11.1
2	N	0.882	0.812	−7%	133.6	1123	15.9	12.0
3	N	0.897	0.823	+1%	143.2	1187	17.3	13.3
4	Y	0.801	0.669	−19%	131.6	1029	16.8	13.1
5	Y	0.811	0.663	−1%	131.0	1033	16.6	12.0
6 (D8.2)	Y	0.803	0.638	−4%	132.1	1060	16.5	11.8
7	Y	0.746	0.487	−24%	125.5	903	17.4	12.6
8	Y	0.644	0.383	−21%	149.4	935	23.9	10.7
9	Y	0.641	0.359	−6%	157.8	984	25.3	12.8
10(D8.6)	Y	0.630	0.350	−3%	160.0	953	26.9	12.5

Step	Cruise Condition							
	Mach	Alt. (ft)	C_L	L/D	T_{t4} (K)	BPR	FPR	OPR
0	0.80	34 784	0.564	16.16	1294	5.100	1.650	30
1	0.72	36 110	0.677	19.56	1233	5.100	1.650	30
2	0.72	36 037	0.717	18.71	1239	5.100	1.650	30
3	0.72	36 083	0.691	18.96	1263	5.100	1.650	30
4	0.72	35 795	0.705	19.52	1237	5.100	1.650	30
5	0.72	35 769	0.711	19.45	1419	7.136	1.625	30
6 (D8.2)	0.72	36 584	0.711	19.48	1451	7.704	1.600	40
7	0.72	35 049	0.727	19.08	1757	26.833	1.370	50
8	0.72	40 045	0.764	21.37	1745	26.639	1.375	50
9	0.72	40 778	0.748	22.86	1740	26.572	1.372	50
10(D8.6)	0.72	40 781	0.760	23.02	1682	25.074	1.371	50

3.8.2 Appropriate Comparisons in Defining Vehicle Fuel Burn Benefits

As discussed above, the context for making appropriate comparisons must include descriptions not only of propulsor and aircraft aerodynamics, but also of the other vehicle system aspects that impact fuel burn, such as aircraft weight. In this section we examine the BLI benefits appearing between steps 3 and 4 in more detail, again using the TASOPT conceptual design procedure [1].

Figure 3.50 gives the dependence of full-size propulsor flow power coefficient C_{P_K} on propulsive efficiency η_p, for both the BLI and non-BLI configurations at the cruise point. The BLI configuration has a lower C_{P_K} for a given η_p, primarily due to the additional BLI benefits of reduced wake losses and reduced nacelle wetted-area losses.

The BLI and non-BLI comparison in Figure 3.50 is in terms of the nondimensional coefficient C_{P_K}, and is therefore somewhat incomplete. In reality, what matters is the *dimensional* propulsor power and corresponding fuel burn, and this in turn requires that changes in the reference area S_{ref} used in the C_{P_K} definition (3.4) be accounted for. On an actual aircraft, either with or without BLI, as η_p increases there must be an increase in the propulsor diameter, and hence also an increase in the propulsor weight and in the nacelle losses.

These additional weight and nacelle losses will result in an increase in the required wing area and therefore S_{ref}. Thus, as the propulsor diameter is increased, the penalties for an increasing value of S_{ref} will eventually cancel out the decreasing power requirement that is gained from the higher propulsive efficiency, producing a minimum in the payload fuel energy intensity (PFEI) as shown in Figures 3.51 and 3.52. PFEI is the mission fuel energy divided by the product of payload mass and range [31], and is an appropriate dimensional metric for transportation energy requirements. The minimum fuel burn occurs at propulsive efficiencies of 74% and 78% for the non-BLI and BLI configurations, respectively, with a fuel savings from BLI of 15%.

Figure 3.52 shows the same fuel burn as in Figure 3.51, but as a function of fan diameter rather than propulsive efficiency. The optimized BLI fuel burn benefit occurs at nearly constant fan diameter, and also approximately constant fan mass flow (difference of less than 5%). Another interpretation of the BLI benefit, therefore, is that BLI allows for increased propulsive efficiency without the penalties caused by increasing the propulsor size.

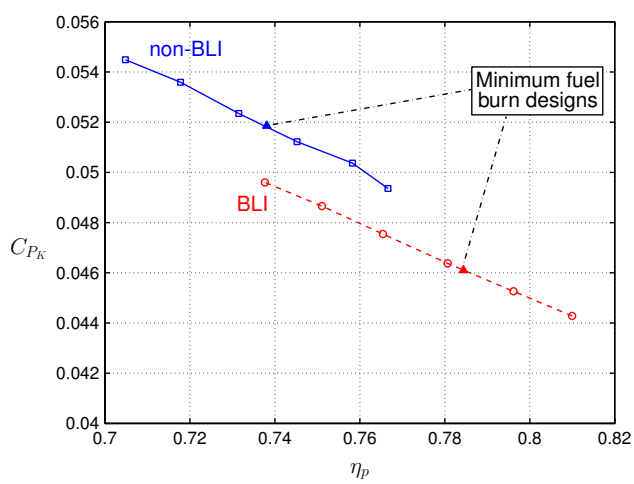

Figure 3.50: Flow power coefficient versus propulsive efficiency for the full-size D8 aircraft configuration; estimates based on airframe drag performance and calculated with TASOPT for different propulsor designs.

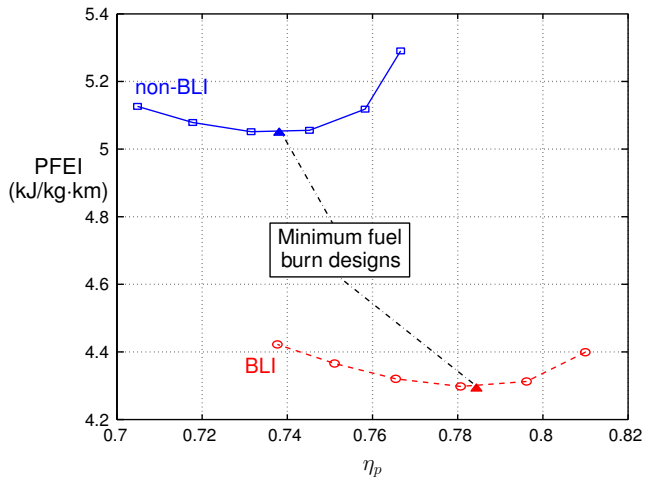

Figure 3.51: Payload fuel energy intensity (PFEI) versus propulsive efficiency for optimized D8 aircraft in BLI and non-BLI configurations.

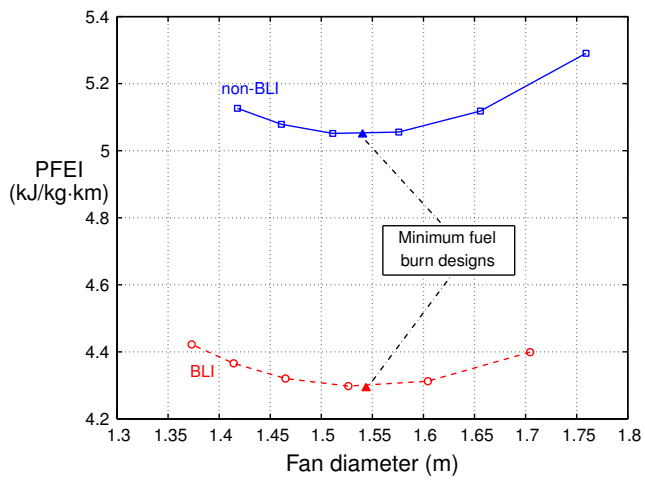

Figure 3.52: Payload fuel energy intensity (PFEI) versus fan diameter for optimized full-size D8 aircraft in BLI and non-BLI configurations.

3.8.3 Propulsor Design and Performance

Up to this point, because the focus was on the aerodynamic BLI benefit, we have treated the propulsor as a "black box" that adds mechanical energy to the flow. Let us briefly consider some of the implications of BLI for propulsion system design and performance.

Figure 3.53 shows propulsive efficiency as a function of fan pressure ratio (FPR) for the D8 designs considered in Figures 3.50 and 3.51. With BLI, a higher propulsive efficiency is achieved at any given FPR because the reduced inlet total pressure means lower jet velocity. Furthermore, the minimum fuel burn design with BLI has a lower FPR than the non-BLI minimum fuel burn design because of (i) the reduction in net propulsive power at fixed fan area and (ii) the propulsive efficiency increase associated with BLI. The implication is that BLI and non-BLI fans need to be similar in size for the same application, but the former will have a lower FPR and thus higher propulsive efficiency at the same diameter.

One consequence of fan operation with BLI is that there will be a decreased efficiency, because of the locally off-design operation that occurs. In Figure 3.54 we show the effect of cruise fan efficiency on fuel burn. The isolated symbol is for the non-BLI case, with fan efficiency assumed to be 92%. The solid line represents a fan with decreased maximum efficiency. For reference, fan efficiency decreases of 1 to 2% have been quoted in the open literature for distortions representative of an ingested fuselage boundary layer [32,33]. Exploration of methodologies to mitigate the effects of inlet distortion show there is potential for reducing the efficiency decrease through asymmetric geometry tailoring [34]. The mission fuel burn increases by approximately 0.8% per 1% decrease in cruise fan efficiency. Therefore, even with a cruise fan efficiency as much as 5% lower than for the baseline non-BLI fan, a fuel savings of more than 10% can be achieved with BLI. Of importance is also the fact that the optimized fan diameter is not sensitive to changes in fan efficiency, and the aerodynamic BLI benefit can be treated independently of the propulsor internal flow performance, an approach that was adapted during this Phase 2 research.

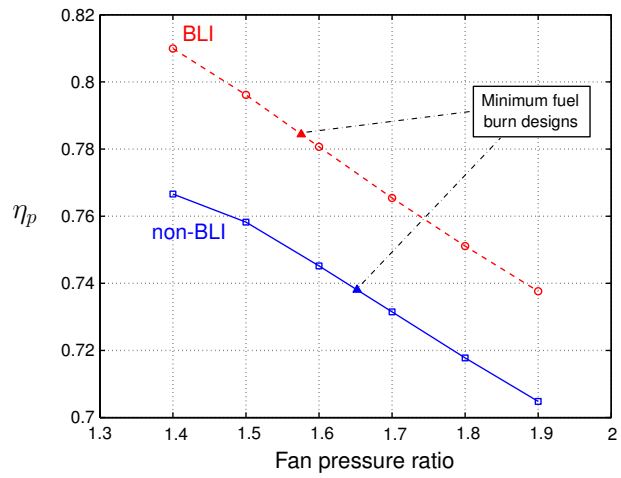

Figure 3.53: Propulsive efficiency versus fan total pressure ratio for optimized full-size D8 aircraft in BLI and non-BLI configurations.

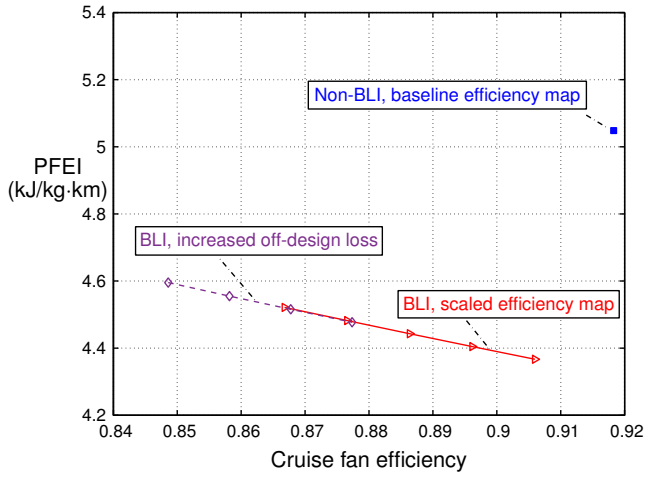

Figure 3.54: Fuel burn versus cruise fan efficiency for optimized full-size D8 aircraft; comparison of baseline non-BLI fan and BLI fan with reduced maximum efficiency.

3.9 Summary and Conclusions

Three configurations of the D8 aircraft were tested in the NASA Langley 14– by 22–Foot Subsonic Tunnel using a 1:11 scale powered model: (i) an unpowered version to characterize the airframe alone, (ii) a non-BLI configuration with podded propulsors which ingest freestream flow and which serves as the baseline, and (iii) a BLI configuration whose propulsors are flush-mounted above the rear of the fuselage and ingest part of the fuselage boundary layer. Following the power balance framework, the mechanical flow power required to produce a given net streamwise force on the aircraft is used as the performance metric. Power and force measurements on the BLI and non-BLI configurations provide the first experimental back-to-back comparison for the quantification of the aerodynamic benefit of BLI for a complete transport aircraft configuration.

The tests measured the aerodynamic BLI benefit over a range of flight conditions, including climb, cruise, and descent. Limited tests at high angle of attack, high yaw, and with single engine-out were also performed to verify acceptable operating characteristics at these more extreme points of the operating envelope. Detailed surveys of the flowfield at the propulsor inlet show the distortion that the propulsors see as a result of BLI. The exit planes were also surveyed to quantify the overall propulsor aerodynamic flow power.

The experimental measurements demonstrated an aerodynamic BLI benefit at the simulated cruise condition of 8.6% in propulsive power at fixed nozzle area, with an uncertainty of $\pm 1.8\%$. The benefit at climb and descent conditions was comparable. The BLI propulsion system also exhibited no adverse or unusual behavior at high angles of attack up to $\alpha = 12°$, large sideslip angles up to $\beta = \pm 15°$, and with single engine-out.

A complementary system-level conceptual study shows that roughly 19% fuel burn reduction from BLI can be achieved once the aircraft is redesigned to take full advantage of an integrated BLI propulsion system.

The interested reader is referred to publications [35], [36], [37] for analysis of BLI and the wind tunnel data that go beyond what is presented in this report.

3.10 Supplementary Material

3.10.1 Experimental Data Variables

The variables computed as part of the post-processing of experimental data are listed below, together with their defining equations.

Constants

Propulsor fan area	$A_{\text{fan}} = 0.0159\,\text{m}^2$
Nozzle area	A_{nozzle} (see values in Table 3.2)
Reference chord	$c = 0.2731\,\text{m}$
Reference area	$S_{\text{ref}} = 1.0878\,\text{m}^2$
Fan blade radius	$r_{\text{tip}} = 0.072\,\text{m}$

Tunnel Variables

Tunnel total pressure	$\text{PTOT} = p_{t_\infty}$
Tunnel static pressure	p_s
Reference pressure	$\text{PA} = p_a$ (tunnel control room ambient pressure)
Tunnel total temperature	$\text{TTOT} = T_{t_\infty}$
Differential pressures measured by tunnel instrumentation	
	$\text{DPI} = p_{t_\infty} - p_s$
	$\text{DPAT} = p_{t_\infty} - p_a$
Calibrated differential pressure	$\text{DPINF} = (p_{t_\infty} - p_\infty)_{\text{empty}} = 0.998\,\text{DPI}\,C' \simeq p_{t_\infty} - p_\infty$
Wind tunnel dynamic pressure calibration factor	
	$C' = 1.1381 + 0.000172\,\text{DPI} + 0.0000051\,\text{DPI}^2$

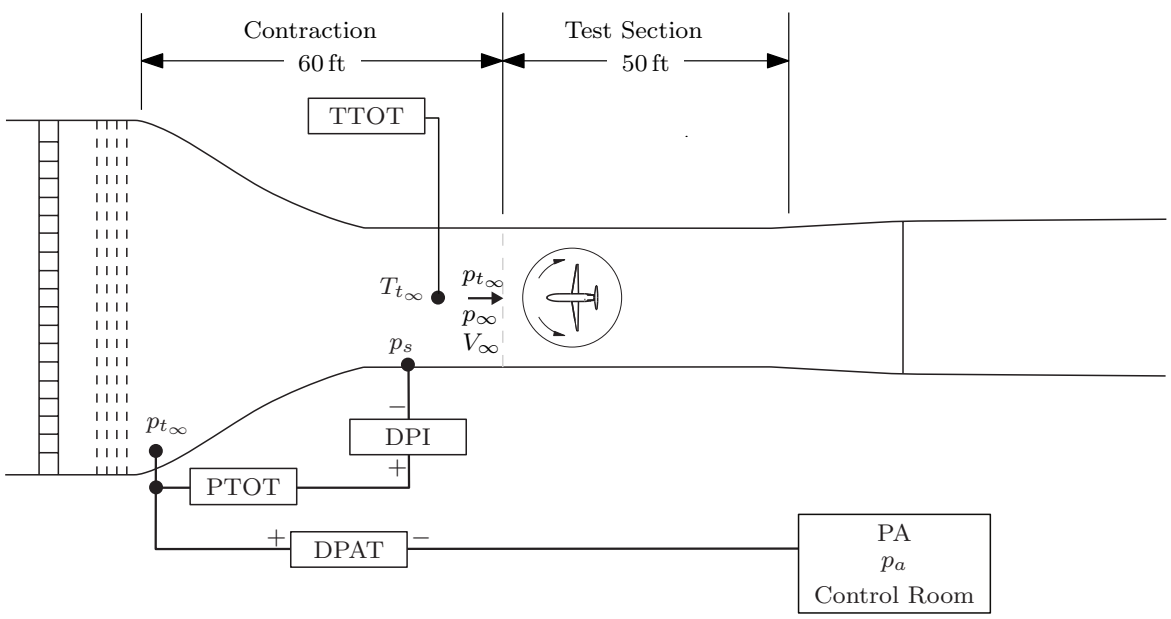

Figure 3.55: Schematic of NASA Langley 14– by 22–Foot Subsonic Tunnel instrumentation for measuring freestream tunnel conditions.

Freestream Conditions

Note that all freestream quantities are uncorrected for wind tunnel blockage, since we are only interested in relative differences between non-BLI and BLI configurations. Furthermore, the 1:11 scale D8 model blockage is only 0.5% and therefore the wall corrections would be small in any case.

Freestream static pressure	$p_\infty = \mathrm{PTOT} - \mathrm{DPINF}$
Freestream total pressure	$p_{t_\infty} = \mathrm{PTOT}$
Freestream total temperature	$T_{t_\infty} = \mathrm{TTOT}$
Freestream Mach number	$M_\infty = \left(\frac{2}{\gamma-1}\left[\left(\frac{p_\infty}{p_{t_\infty}}\right)^{-\frac{\gamma-1}{\gamma}} - 1\right]\right)^{1/2}$
Freestream velocity	$V_\infty = M_\infty\sqrt{\gamma R T_{t_\infty}}\left(1+\frac{\gamma-1}{2}M_\infty^2\right)^{-1/2}$
Freestream dynamic pressure	$q_\infty = \frac{\gamma}{2}p_\infty M_\infty^2$
Freestream temperature	$T_\infty = T_{t_\infty} - \dfrac{V_\infty^2}{2c_\mathsf{p}}$
Freestream density	$\rho_\infty = \dfrac{p_\infty}{R\,T_\infty}$
Freestream viscosity	$\mu_\infty = \mu_0\left(\dfrac{T}{T_0}\right)^{3/2}\dfrac{T_0+110.4}{T+110.4}$

from Sutherland's Law with $\mu_0 = 1.716\times10^{-5}\,\mathrm{kg/m\cdot s}$, $T_0 = 273.15\,\mathrm{K}$

Reynolds number	$Re_c = \dfrac{\rho_\infty V_\infty\, c}{\mu_\infty}$

Airframe Variables

Model and balance angle of attack	α
Balance axial force (model x-direction)	F_A
Balance side force (model y-direction)	F_Y
Balance normal force (model z-direction)	F_N
Balance pitching moment (about model y-direction)	$\mathcal{M}_Y$
Net aerodynamic streamwise force on model	$F_X = F_A\cos\alpha + F_N\sin\alpha$
Net aerodynamic side force on model	$F_Y = F_Y$
Net aerodynamic vertical force on model	$F_Z = -F_A\sin\alpha + F_N\cos\alpha$
Net streamwise force coefficient	$C_X = \dfrac{F_X}{q_\infty S_{\mathrm{ref}}}$
Net side force coefficient	$C_Y = \dfrac{F_Y}{q_\infty S_{\mathrm{ref}}}$
Net vertical force coefficient	$C_L = \dfrac{F_Z}{q_\infty S_{\mathrm{ref}}}$
Pitching moment coefficient	$C_m = \dfrac{\mathcal{M}_Y}{q_\infty S_{\mathrm{ref}}\, c}$

Propulsor Variables

Power supply voltage	v
Power supply current	i
Wheel speed	Ω
Rotor tip speed	$U_{\text{tip}} = \Omega\, d_{\text{fan}}/2$
Electrical motor efficiency	η_m
Fan efficiency	η_f
Overall efficiency	$\eta_o = \eta_f\, \eta_m$
Electrical power	$P_E = i\, v$
Electrical power coefficient	$C_{P_E} = \dfrac{P_E}{q_\infty V_\infty S_{\text{ref}}}$
Shaft power	$P_{\text{Shaft}} = \eta_m\, P_E$
Shaft power coefficient	$C_{P_{\text{Shaft}}} = \dfrac{P_{\text{Shaft}}}{q_\infty V_\infty S_{\text{ref}}}$
Alternative shaft power coefficient	$\widetilde{C}_{P_{\text{Shaft}}} = \dfrac{P_{\text{Shaft}}}{\rho\, U_{\text{tip}}^3\, A_{\text{fan}}}$
Mass flow through propulsor	$\dot{m}$
Jet velocity	$\overline{V}_{\text{jet}}$ (two-dimensional equivalent)
Fan face velocity	$\overline{V}_{\text{fan}}$ (two-dimensional equivalent)
Fan face total pressure	$\overline{p}_{t_{\text{fan}}}$ (two-dimensional equivalent)
Flow coefficient	$\phi = \dfrac{\overline{V}_{\text{fan}}}{U_{\text{tip}}}$
Total pressure rise coefficient	$\psi_{tt} = \dfrac{\Delta \overline{p}_t}{\rho U_{\text{tip}}^2} = \dfrac{C_{P_K}}{2\,\dfrac{A_{\text{fan}}}{S_{\text{ref}}}\left(\dfrac{U_{\text{tip}}}{V_\infty}\right)^3 \phi} = \dfrac{\widetilde{C}_{P_{\text{Shaft}}}}{\phi}$
Total enthalpy rise coefficient	$\psi = \dfrac{\Delta \overline{h}_t}{U_{\text{tip}}^2} = \dfrac{C_{P_{\text{Shaft}}}}{2\,\dfrac{A_{\text{fan}}}{S_{\text{ref}}}\left(\dfrac{U_{\text{tip}}}{V_\infty}\right)^3 \phi} = \dfrac{C_{P_K}}{2\,\dfrac{A_{\text{fan}}}{S_{\text{ref}}}\left(\dfrac{U_{\text{tip}}}{V_\infty}\right)^3 \phi\, \eta_f} = \dfrac{\widetilde{C}_{P_{\text{Shaft}}}}{2\,\phi}$
Fan face total pressure coefficient	$k = \dfrac{\overline{p}_{t_{\text{fan}}} - p_{t_\infty}}{q_\infty}$ ($k < 0$ with BLI)

Power Balance Variables

Mechanical flow power	$P_K = \eta_f \, \eta_m \, P_E$
Mechanical flow power coefficient	$C_{P_K} = \dfrac{P_K}{q_\infty V_\infty S_{\text{ref}}}$
Jet dissipation	$\Phi_{\text{jet}} = \dfrac{1}{2}\dot{m}\left(\overline{V}_{\text{jet}} - V_\infty\right)^2$
Jet dissipation coefficient	$C_{\Phi_{\text{jet}}} = \dfrac{\Phi_{\text{jet}}}{q_\infty V_\infty S_{\text{ref}}} = \dfrac{A_\infty}{S_{\text{ref}}}\left(\dfrac{\overline{V}_{\text{jet}}}{V_\infty} - 1\right)^2$
Specific propulsive power	$C_{P_p} = \dfrac{P_K - \Phi_{\text{jet}}}{q_\infty V_\infty S_{\text{ref}}}$
Propulsive efficiency	$\eta_p = \dfrac{P_K - \Phi_{\text{jet}}}{P_K} = 1 - \dfrac{\Phi_{\text{jet}}}{P_K}$
Non-dimensional jet velocity	$\dfrac{\overline{V}_{\text{jet}}}{V_\infty} = \sqrt{1 + \dfrac{1}{\phi}\left(\dfrac{S_{\text{ref}}}{A_{\text{fan}}}\right)\left(\dfrac{V_\infty}{U_{\text{tip}}}\right)C_{P_K} + k}$
Capture flow ratio	$\dfrac{A_\infty}{A_{\text{fan}}} = \dfrac{\overline{V}_{\text{fan}}}{V_\infty} = \dfrac{U_{\text{tip}}}{V_\infty}\,\phi$
	In a conventional engine installation, A_∞ is the area of the propulsor streamtube far upstream where the flow is at V_∞ and p_∞.

3.10.2 Derivation of BLI Configuration Equations

As stated in Section 3.2.5, there is more than one way to choose a BLI configuration to compare with a reference non-BLI configuration. Here we derive the equations that define an equivalent BLI configuration given a known non-BLI configuration.

Let us assume that the characteristics of a given reference non-BLI configuration are known, in particular its power requirement, $P_K^{\text{non-BLI}}$, and its dissipation terms (jet, surface, wake, and vortex) following the power balance framework. Our goal is to find the equivalent terms for a BLI configuration.

At the cruise condition, the power balance equation states that the input flow power is equal to the total dissipation, that is

$$P_K = \Phi_{\text{jet}} + \Phi_{\text{surf}} + \Phi_{\text{wake}} + \Phi_{\text{vortex}} \ . \tag{3.86}$$

or, equivalently,

$$P_K - \Phi_{\text{jet}} \ = \ \Phi_{\text{surf}} + \Phi_{\text{wake}} + \Phi_{\text{vortex}} \ . \tag{3.87}$$

where the left-hand side is the net propulsive power. Surface dissipation is not significantly changed with BLI, and therefore

$$\Phi_{\text{surf}} \ \approx \ \Phi_{\text{surf}}^{\text{non-BLI}} \ . \tag{3.88}$$

At the same lift coefficient, BLI and non-BLI configurations have the same induced drag (assuming no change in spanwise loading distribution, which is mainly determined by the common wings) and therefore the same vortex dissipation, such that

$$\Phi_{\text{vortex}} \ \approx \ \Phi_{\text{vortex}}^{\text{non-BLI}} \ . \tag{3.89}$$

The wake dissipation is reduced by re-energizing the boundary layer flow through BLI, and we can write

$$\Phi_{\text{wake}} \ = \ (1 - f_{\text{BLI}})\Phi_{\text{wake}}^{\text{non-BLI}} \ , \tag{3.90}$$

where f_{BLI} is the fraction of total kinetic energy defect being ingested by the BLI propulsors. The net propulsive power for a BLI configuration can be thus be written as

$$P_K - \Phi_{\text{jet}} \ = \ \Phi_{\text{surf}}^{\text{non-BLI}} + (1 - f_{\text{BLI}})\Phi_{\text{wake}}^{\text{non-BLI}} + \Phi_{\text{vortex}}^{\text{non-BLI}} \ , \tag{3.91}$$

and all the terms in the right-hand-side are known from the non-BLI configuration.

From the definition of flow power, we can write

$$P_K \ = \ \frac{1}{2}\dot{m}V_\infty^2 \left[\left(\frac{\overline{V}_{\text{jet}}}{V_\infty} \right)^2 - 1 \right] + f_{\text{BLI}}\Phi_{\text{surf}} \ , \tag{3.92}$$

The second term on the right-hand-side corresponds to the ingested dissipation energy, $\overline{V}_{\text{jet}}$ is the two-dimensional equivalent jet velocity at the propulsor nozzle plane, and

$$\dot{m} \ = \ \rho \overline{V}_{\text{jet}} A_{\text{nozzle}} \tag{3.93}$$

is the mass flow through the propulsor whose nozzle area is A_{nozzle}. Similarly, we can write the jet

dissipation as

$$\Phi_{\text{jet}} = \frac{1}{2}\dot{m}V_\infty^2\left[\frac{\overline{V}_{\text{jet}}}{V_\infty} - 1\right]^2 . \tag{3.94}$$

Equations (3.91), (3.92), (3.93), (3.94) constitute four equations with five unknowns (P_K, Φ_{jet}, $\overline{V}_{\text{jet}}$, $\dot{m}$, A_{nozzle}) that define an equivalent non-BLI configuration. One can add the definition of propulsive efficiency, $\eta_p = (P_K - \Phi_{\text{jet}})/P_K$, as another important characteristics of a configuration which provides one additional equation and one additional unknown. There is thus a range of solutions to this system of equations and corresponding equivalent BLI configurations for any given non-BLI aircraft, each one defined by an arbitrary choice.

In Figure 3.4 which is reproduced below, we varied the nozzle area A_{nozzle} to obtain the curve of equivalent BLI configurations, on which lie the particular cases that have the same mass flow, or the same nozzle area, or the same jet velocity, or the same flow power as the known non-BLI configuration used as reference.

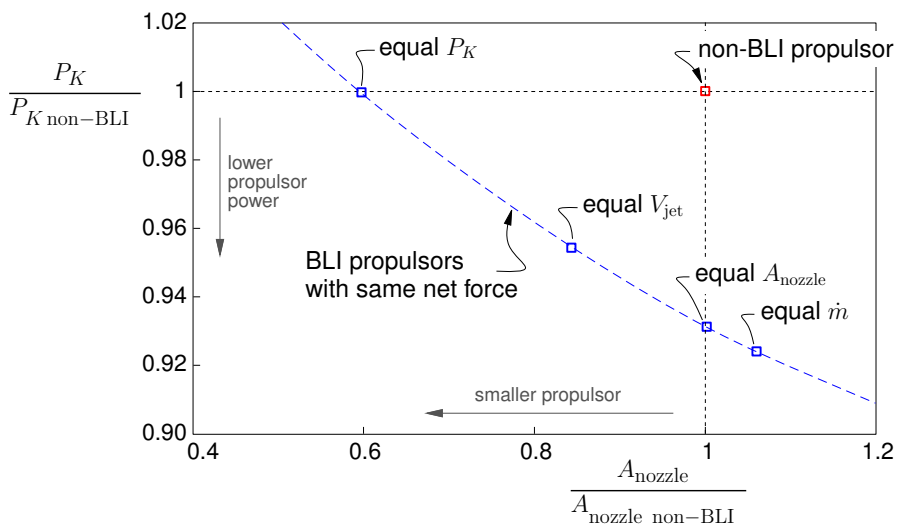

Figure 3.4 (duplicate): Range of D8 BLI propulsor power versus nozzle area, relative to values of a baseline non-BLI propulsor. For all cases the net aircraft streamwise force is held at the cruise value of zero.

3.10.3 Wind Tunnel Test Matrix

The following tables summarize the data acquired during the two entries into the NASA Langley 14– by 22–Foot Subsonic Tunnel. The freestream (tunnel) velocity is denoted by V_∞, the model angle of attack by α, and its sideslip angle by β. The numbers in the cells indicate run number as recorded by the tunnel data acquisition system.

All of the Entry 1 (2013) data was taken using the electrical motors numbered 6 and 7 on the left and right propulsors, respectively. During Entry 2 (2014), the motors used were 16 and 13 for left and right propulsors, respectively, unless otherwise specified. The note "new motors" designates data taken during Entry 2 with motors 9 and 15 on left and right propulsors, respectively.

Entry 1 – Power Sweeps

			$\alpha = 2°$	$\alpha = 4°$	$\alpha = 6°$	$\alpha = 8°$
BLI (Integrated)	Plug A	$V_\infty = 70$ mph	138 231 247	232	139 233	234
		$V_\infty = 56$ mph	141		140	
		$V_\infty = 42$ mph	142 239		143 240	241
	Plug B	$V_\infty = 70$ mph	100 108	101	102	103
		$V_\infty = 56$ mph	104		107	
		$V_\infty = 42$ mph	105		106	
	Plug C	$V_\infty = 70$ mph	113 128	114 127	115 126	116 125
		$V_\infty = 56$ mph	120	119	118	117
		$V_\infty = 42$ mph	121	122	123	124

			$\alpha = 2°$	$\alpha = 4°$	$\alpha = 6°$	$\alpha = 8°$
Non-BLI (Podded)	Plug A	$V_\infty = 70$ mph	041[a] 044[a] 064 264 270 283 284 285 316 318	065 265	067 266 317 319	066 267
		$V_\infty = 56$ mph	042[a]			
		$V_\infty = 42$ mph	043[a] 256	257	258	259
	Plug B	$V_\infty = 70$ mph	047[a] 051[a] 055 057 083 322 324 326	058 084	048[a] 059 085 323 325 327	052[a] 060 086
		$V_\infty = 56$ mph	049[a] 090	089	050[a] 088	087
		$V_\infty = 42$ mph	062 091	092	093	061 094
	Plug C	$V_\infty = 70$ mph	070	071	072	073
		$V_\infty = 56$ mph	074	81	080	079
		$V_\infty = 42$ mph	075	076	077	078

Unpowered	AoA Sweeps	$V_\infty = 70$ mph	032 033 036 334 337 338
		$V_\infty = 56$ mph	034 335
		$V_\infty = 42$ mph	035 336

[a] bad model pressure data

Entry 2 – Power Sweeps

Note: runs numbered 289 and below were taken without proper temperature compensation on ESPs; pressures may have drifted

			$\alpha = 2°$	$\alpha = 4°$	$\alpha = 6°$	$\alpha = 8°$
BLI (Integrated)	Plug A	$V_\infty = 84$ mph	066 074 076 260 262 266 267 358 361 362	067	068 077	069
		$V_\infty = 70$ mph	070 075 078 261 359 360 363	071	072	073
		$V_\infty = 56$ mph	079			
		$V_\infty = 42$ mph	080			
	Plug B	$V_\infty = 84$ mph	037 049 064 098 112 121 235 245 364 365 372	038 099	039 050 100 236 246	040 051 101 237 247
		$V_\infty = 70$ mph	041 052 063 102 113 122 238 248 366 373	042 103	043 053 104 239 249	044 054 105 240 250
		$V_\infty = 56$ mph	106 114		045 055 061 107 115 241	046 056 062 108 116 242
		$V_\infty = 42$ mph	109 117		047 057 059 110 118 243	048 058 060 111 119 244
	Plug C	$V_\infty = 84$ mph	083 093 095 254 256 263 265 352 355 356 368 371	084	085	086
		$V_\infty = 70$ mph	087 094 096 255 264 353 354 357 369 370	088	089	090
		$V_\infty = 56$ mph	091			
		$V_\infty = 42$ mph	092			
Non-BLI (Podded)	Plug A	$V_\infty = 84$ mph	186 188			
		$V_\infty = 70$ mph	187 189			
	Plug B	$V_\infty = 84$ mph	131 143 146 147 159 164 182 203 204 221 224 225	132 165	133 148 160	134
		$V_\infty = 70$ mph	135 144 145 149 161 166 181	136 167	150 162 168	169
		$V_\infty = 56$ mph	137 170		138 171 179	139 172 180
		$V_\infty = 42$ mph	140 173		141 174 177 222	142 175 178 223

New Motors [a]			
BLI (Integr.)	Plug A	$V_\infty = 84$ mph	394 398 399
		$V_\infty = 70$ mph	395 397 400
	Plug B	$V_\infty = 84$ mph	384 387 388 401 404
		$V_\infty = 70$ mph	385 386 389 402 403

Unpowered			
AoA Sweeps		$V_\infty = 84$ mph	019 020 024
		$V_\infty = 70$ mph	018 021 023
		$V_\infty = 56$ mph	022

[a] propulsor pressure ports not connected

Static Thrust ($\alpha = 2°$, $V_\infty = 0$)

Entry 1

	PLUG	BOTH MOTORS	LEFT MOTOR	RIGHT MOTOR
BLI (INTEGRATED)	A	144	145	146
	C	130	131	132
NON-BLI (PODDED)	A	250	251	252

Entry 2

	PLUG	BOTH MOTORS	LEFT MOTOR	RIGHT MOTOR
BLI (INTEGRATED)	A	257 391[b]	259 393[b]	258 392[b]
	B	032 232 275[a] 381[b] 405[b, c]	034 234 277[a] 383[b] 407[b, c]	033 233 276[a] 382[b] 406[b, c]
	C	251	253	252
NON-BLI (PODDED)	B	130	130	130

[a] FHP survey system installed and indexed off nacelles
[b] new motors
[c] mini-tufts in place

Entry 1 – Pressure Rake Surveys

All rake surveys done with Plug B

		V_∞	α	RPM	Left Total Pressure	Left Static Pressure	Right Total Pressure	Right Static Pressure
BLI (Integrated)	Inlet	70 mph	2°	5 250	216	204	187	193
				8 000	215	203	179	192
				11 000	214	202	180	191
				13 500	213	201	181	190
			4°	8 000	218	206	185	195
				13 000	217	205	186	194
			6°	8 000	212 221	209	182	198
				11 000	220	208	183	197
				13 000	219	207	184	196
		42 mph	6°	8 000	223	211	189	200
				13 000	222	210	188	199
	Exit	70 mph	2°	8 000	166	160	170	174
				11 000	167	162	171	175
				13 500	168	163	172	176
			6°	13 000	169	165	173	177
Non-BLI (Podded)	Exit	70 mph	2°	8 000	295	288	302	308
				11 000	294	287	301	307
				13 500	293	286	300	306
			6°	13 000	296	289	303	309
		42 mph	2°	8 100	299	292	305	311
			6°	7 800	297	291		
				13 000	298	290	304	310

Entry 2 – FHP Surveys

		Condition	Plug	V_∞	α	β	RPM	Grid	Left	Right	Center	Full
BLI (Integrated)	Inlet	Cruise	B	70 mph	2°	0°	11 100	fine	272[a, f]	273[a, f]	274[a, f]	
		Cruise	B	84 mph	2°	0°	13 250	fine	268[a] 297[b]	269[a] 298[b]	270[a] 299[b]	
		Cruise	A	84 mph	2°	0°	13 450	fine	290	291	292	
		Cruise	C	84 mph	2°	0°	13 200	fine	294[b]	295[b]	296[b]	
		TOC	B	70 mph	2°	0°	13 500	coarse				308
		Descent	B	70 mph	8°	0°	5 250	medium				280[a]
		Descent	B	70 mph	6°	0°	5 250	coarse				303
		Descent cross-wind	B	70 mph	6°	+15°	5 250	coarse				304
		Descent cross-wind	B	70 mph	6°	-15°	5 450	coarse				305[c]
		SOC	B	42 mph	8°	0°	14 000	medium				283[a]
		SOC cross-wind [g]	B	42 mph	8°	+15°	14 000	coarse				309
		AoA effect	B	70 mph	6°	0°	11 100	coarse				282[a]
		AoA effect	B	70 mph	8°	0°	11 100	coarse				281[a]
	Exit	Cruise	B	70 mph	2°	0°	11 100	fine	311	312		
		Cruise	B	84 mph	2°	0°	13 250	fine	313 344	343		
		Cruise	A	84 mph	2°	0°	13 450	fine	347	346[h]		
		Cruise	C	84 mph	2°	0°	13 200	fine	348	350[e] 376[i]		
		TOC	B	70 mph	2°	0°	13 500	coarse	314	315		

		Condition	Plug	V_∞	α	β	RPM	Grid	Left	Right
Non-BLI (Podded)	Exit	Cruise	B	70 mph	2°	0°	11 550	fine	192[a]	197[a]
		Cruise	B	84 mph	2°	0°	13 700	fine	193[a] 200[a]	196[a, d]

[a] ESPs not temperature compensated
[b] noise in RPM and P_E
[c] could not control RPM at 5250
[d] double number of samples (20 instead of 10)
[e] tape left on fuse just upstream of inlets
[f] loose current signal wires from left motor
[g] no survey taken at $\beta = -15°$
[h] bias in θ_1 by one positive step ($+0.45°$)
[i] taken with pitch head driver on
(may cause interference in pressures)

Entry 2 – Wake Surveys

	Condition	Plug	V_∞	α	RPM	Left	Right
BLI (Integrated)	Cruise	B	84 mph	2°	13 250	321[d, f] 342[c]	325 340[c]
	Cruise	B	70 mph	2°	11 100	322[d, f] 341[c]	324 339[c]
	Cruise	A	84 mph	2°	13 450	332[c]	329[c]
	Cruise	A	70 mph	2°	11 250	331[c]	328[c]
	Cruise	C	84 mph	2°	13 200	336[c]	338[c]
	Cruise	C	70 mph	2°	11 150	335[c]	337[c]
	Cruise, left VT-HT	C	70 mph	2°	11 100	377[c]	
Non-BLI (Podded)	Cruise	B	84 mph	2°	13 700	207[a, e] 210[a, b, e]	219[a]
	Cruise	B	70 mph	2°	11 550	212[a, b]	
	Cruise	B	56 mph	2°	9 700	214[a]	
	Cruise	B	42 mph	2°	7 000	216[a]	
	Cruise	B	84 mph	6°	14 000	211[a, b]	
	Cruise	B	70 mph	6°	14 000	213[a, b]	
	Cruise	B	56 mph	6°	14 000	215[a]	
	Cruise	B	42 mph	6°	14 000	217[a]	

[a] ESPs not temperature compensated
[b] double number of circumpherential locations (400 instead of 200) and double number of samples (20 instead of 10)
[c] no indexing (no cup, rake off the model)
[d] no indexing cup; rake riding on plug induced changes in angle of attack as it rotated around
[e] possible rake slippage causing offset by 1-2 steps at 360° position
[f] survey was taken with rake guard on

Common Geometry

(units: inches)

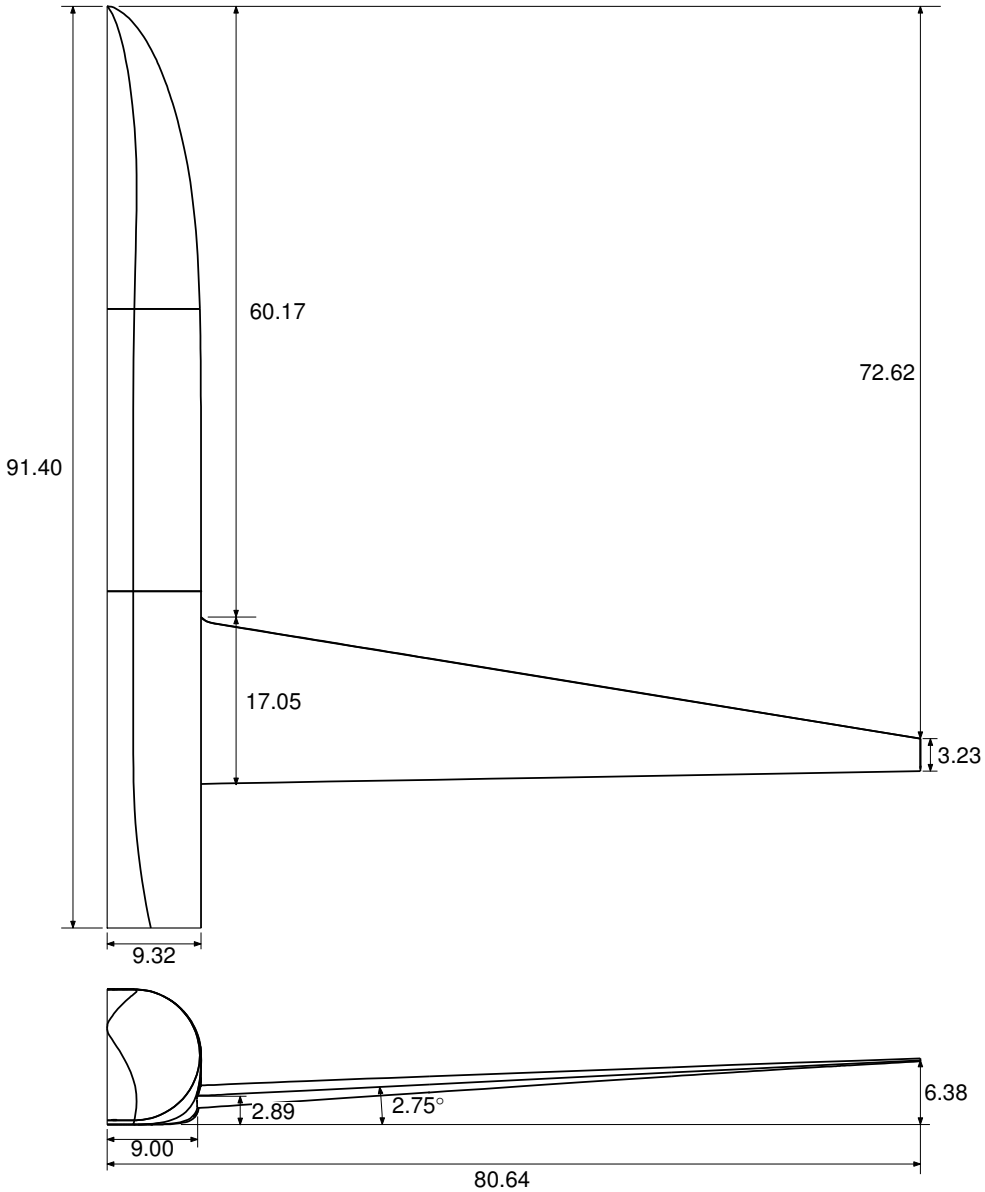

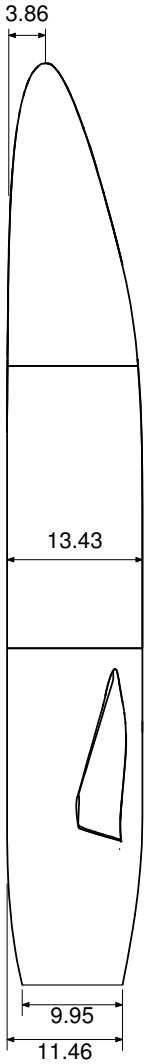

Unpowered Configuration

(units: inches)

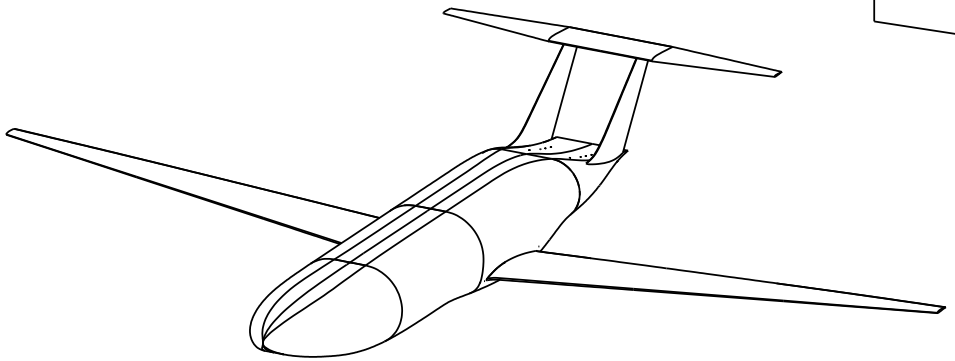

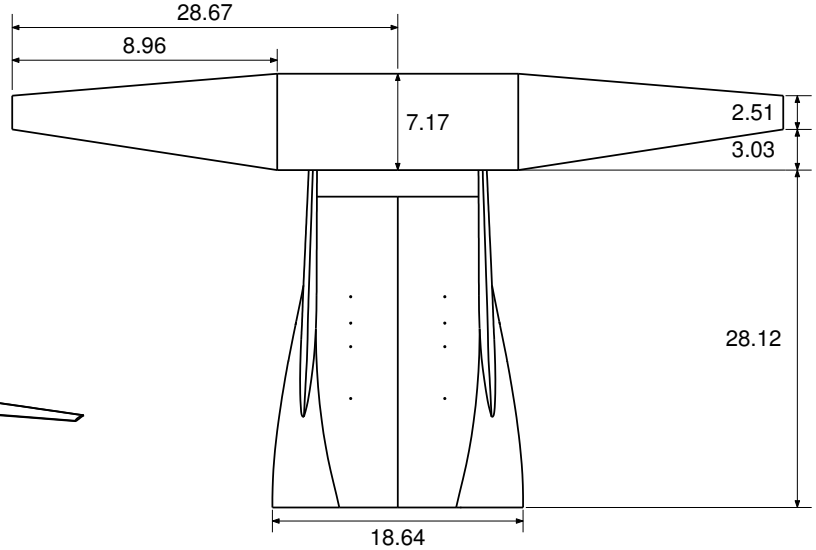

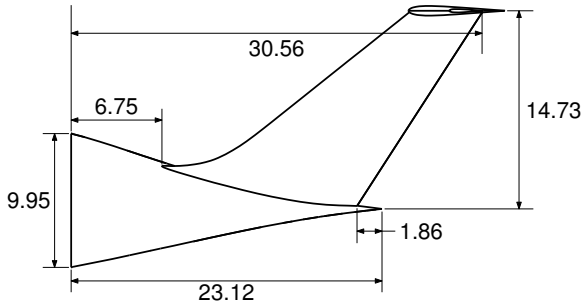

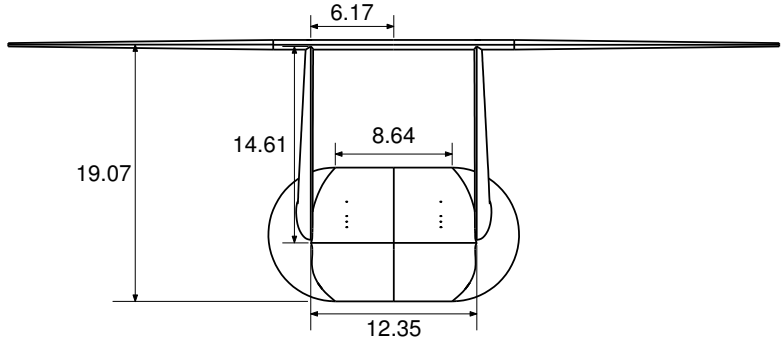

Non-BLI Configuration

(units: inches)

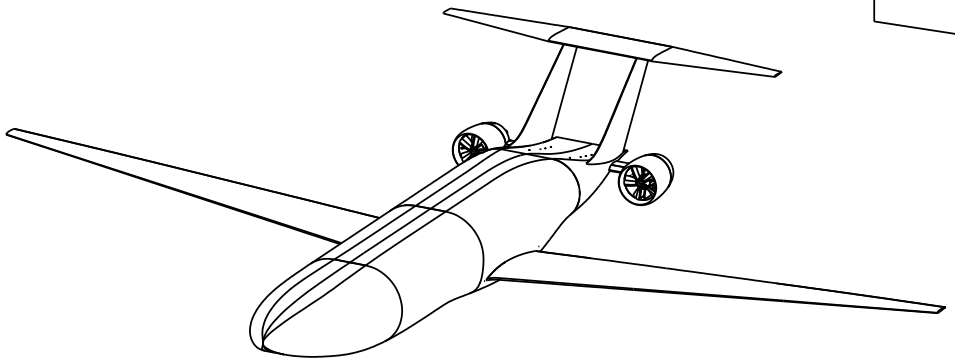

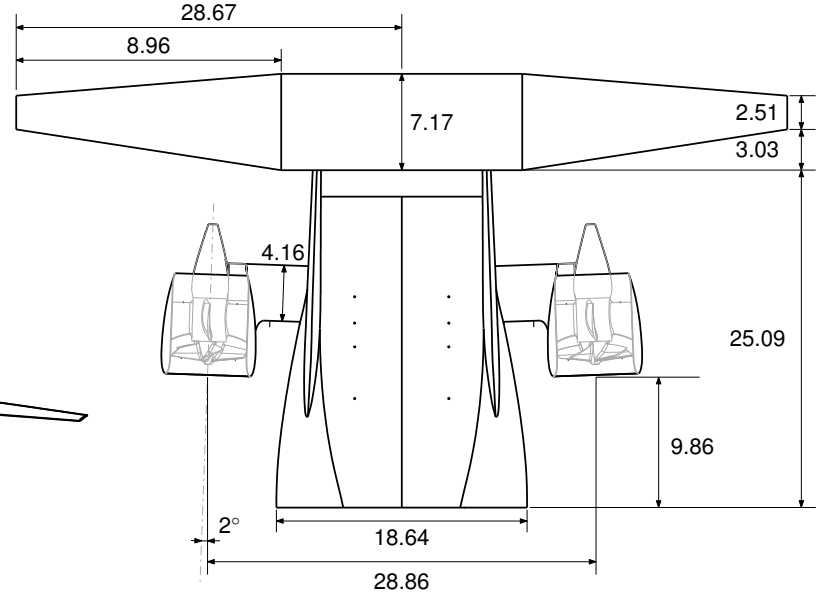

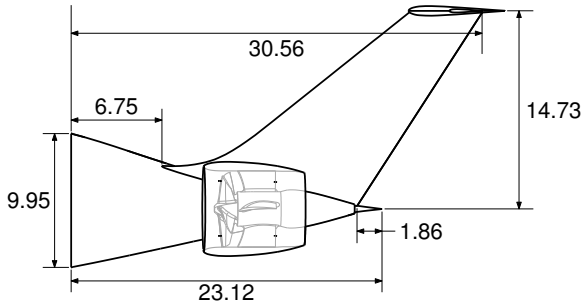

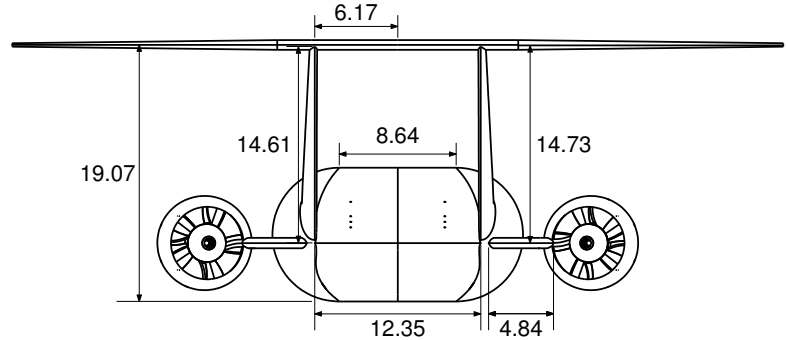

BLI Configuration

(units: inches)

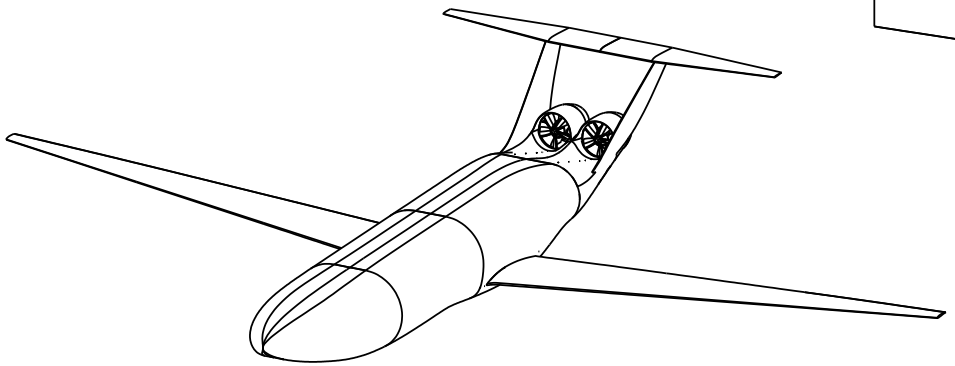

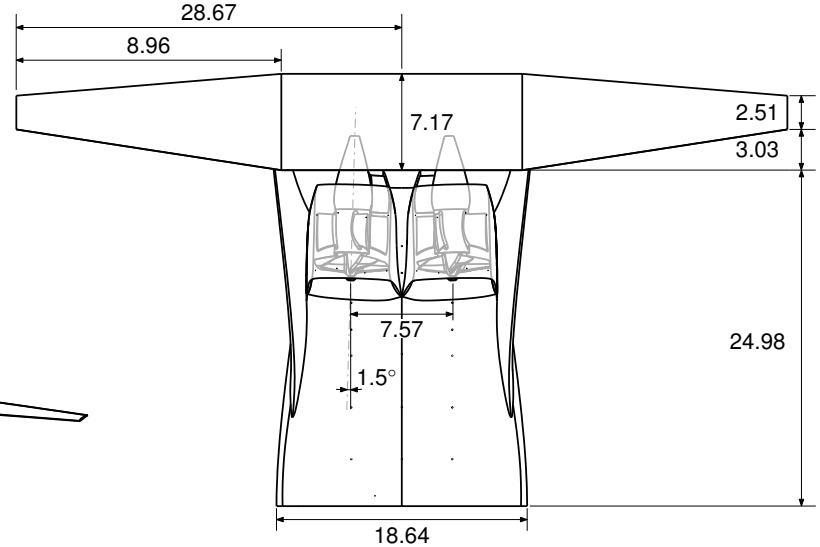

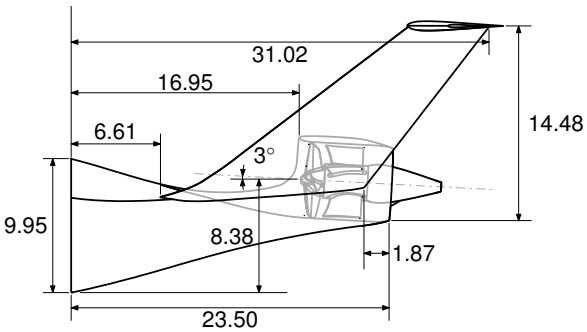

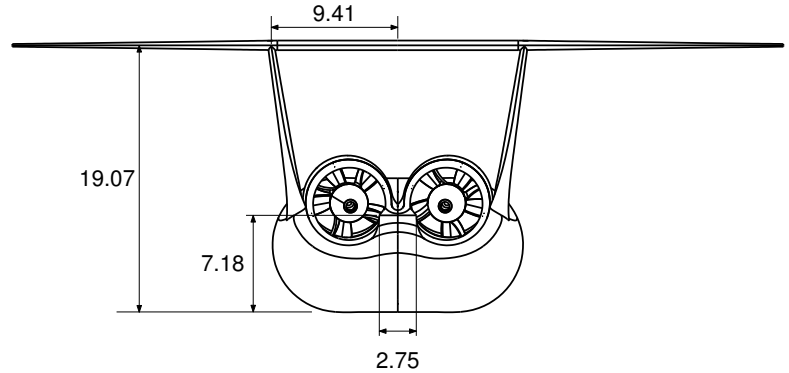

Non-BLI Propulsor

(units: inches)

Propulsor fan and stator: Aeronaut TF8000
Electric motor: Lehner 3040 series, 27 windings

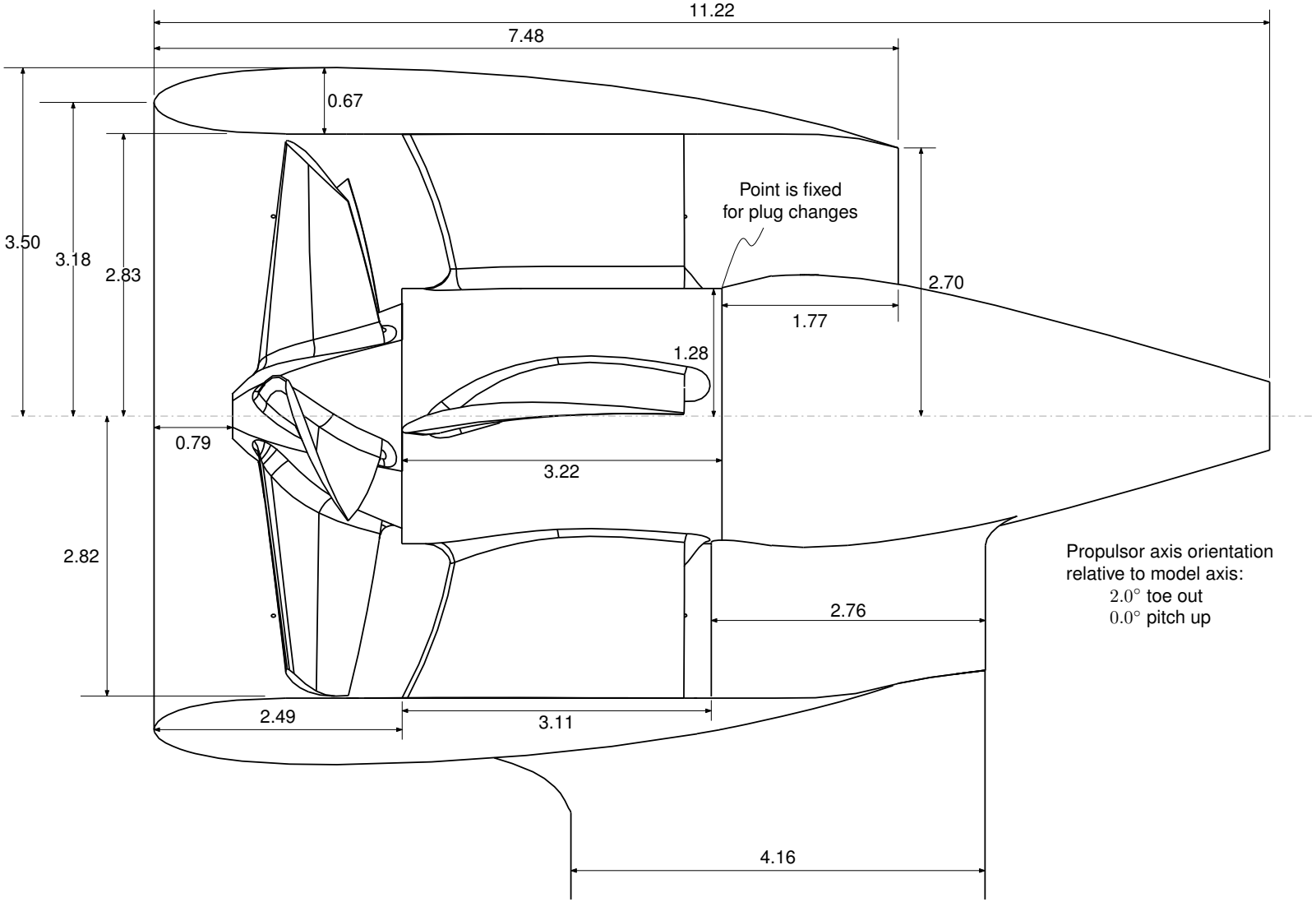

BLI Propulsor

(units: inches)

Propulsor fan and stator: Aeronaut TF8000
Electric motor: Lehner 3040 series, 27 windings

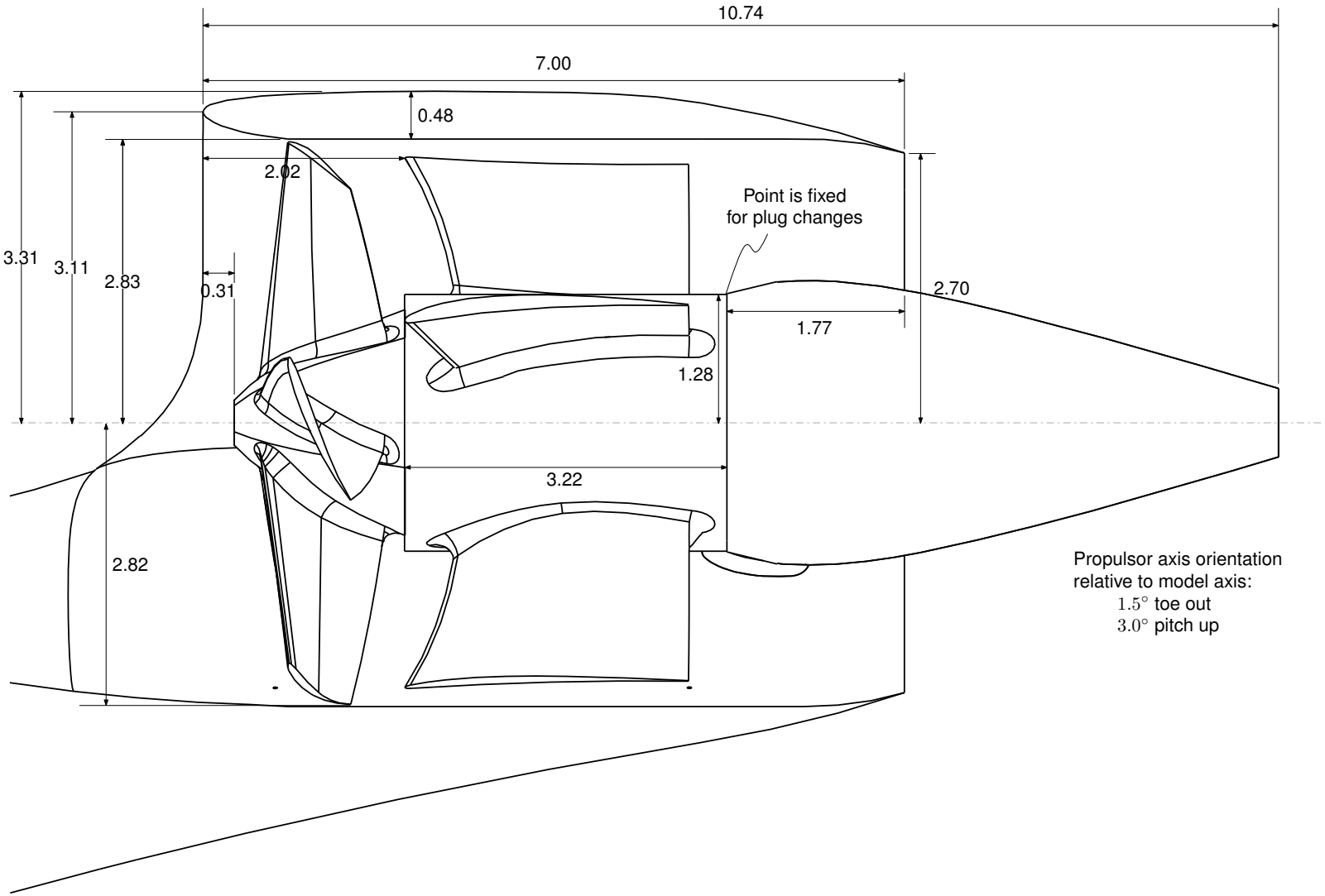

Propulsor Nozzle Plugs

(units: inches)

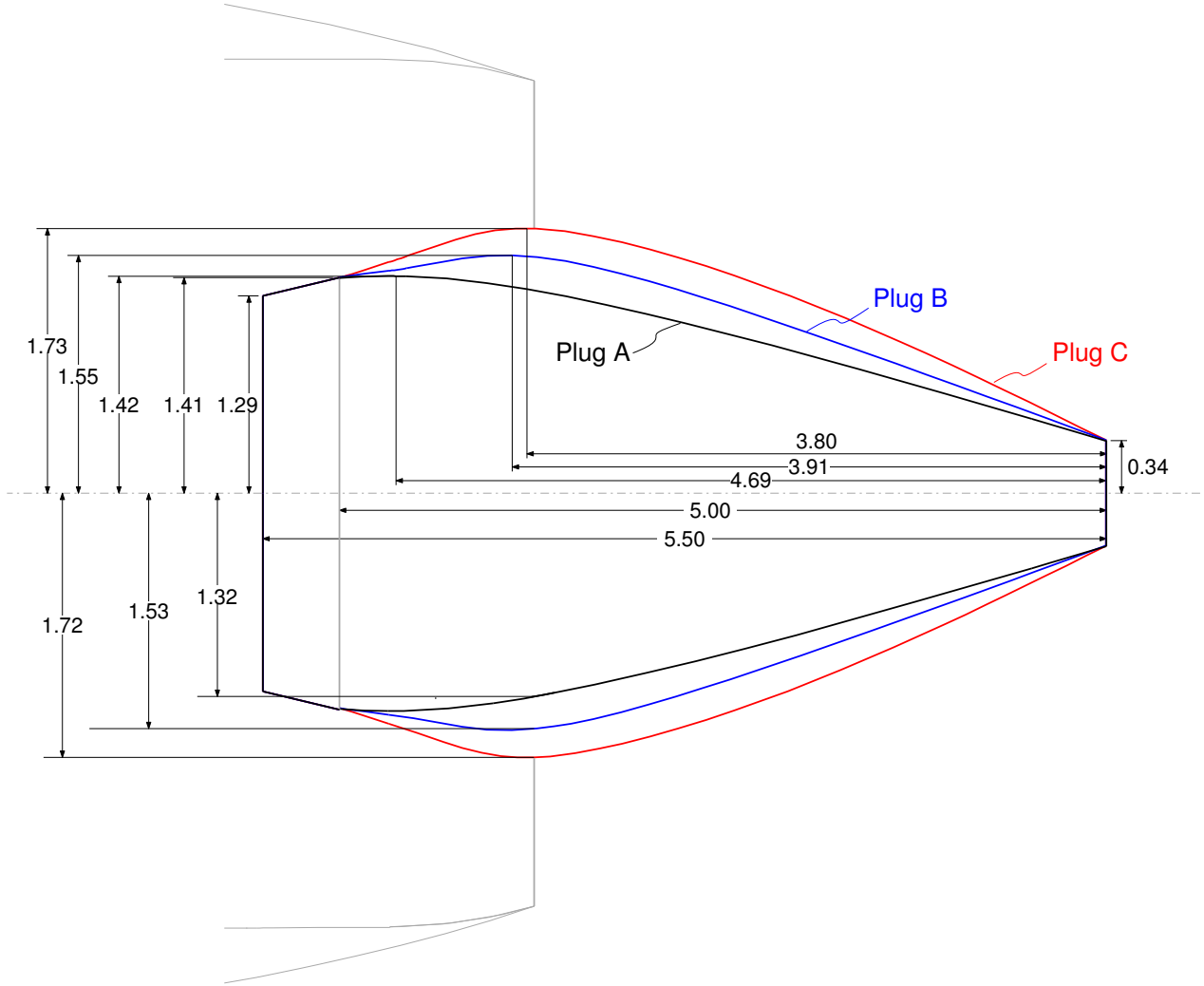

Wing Geometry and trip Locations

DA 00	chord	16.13 in
	twist	$2.0°$
	y	9.32 in
	s^+_{trip}	0.250 in
	s^-_{trip}	0.562 in
	h_{trip}	0.013 in
	w_{trip}	0.125 in
DA 02	chord	14.25 in
	twist	$2.0°$
	y	19.71 in
	s^+_{trip}	0.250 in
	s^-_{trip}	0.562 in
	h_{trip}	0.013 in
	w_{trip}	0.125 in
DA 03	chord	10.03 in
	twist	$1.5°$
	y	43.01 in
	s^+_{trip}	0.219 in
	s^-_{trip}	0.500 in
	h_{trip}	0.013 in
	w_{trip}	0.125 in
DA 04	chord	6.14 in
	twist	$0.8°$
	y	64.52 in
	s^+_{trip}	0.187 in
	s^-_{trip}	0.406 in
	h_{trip}	0.013 in
	w_{trip}	0.125 in
DA 05	chord	3.23 in
	twist	$0.5°$
	y	80.65 in
	s^+_{trip}	0.187 in
	s^-_{trip}	0.218 in
	h_{trip}	0.013 in
	w_{trip}	0.125 in

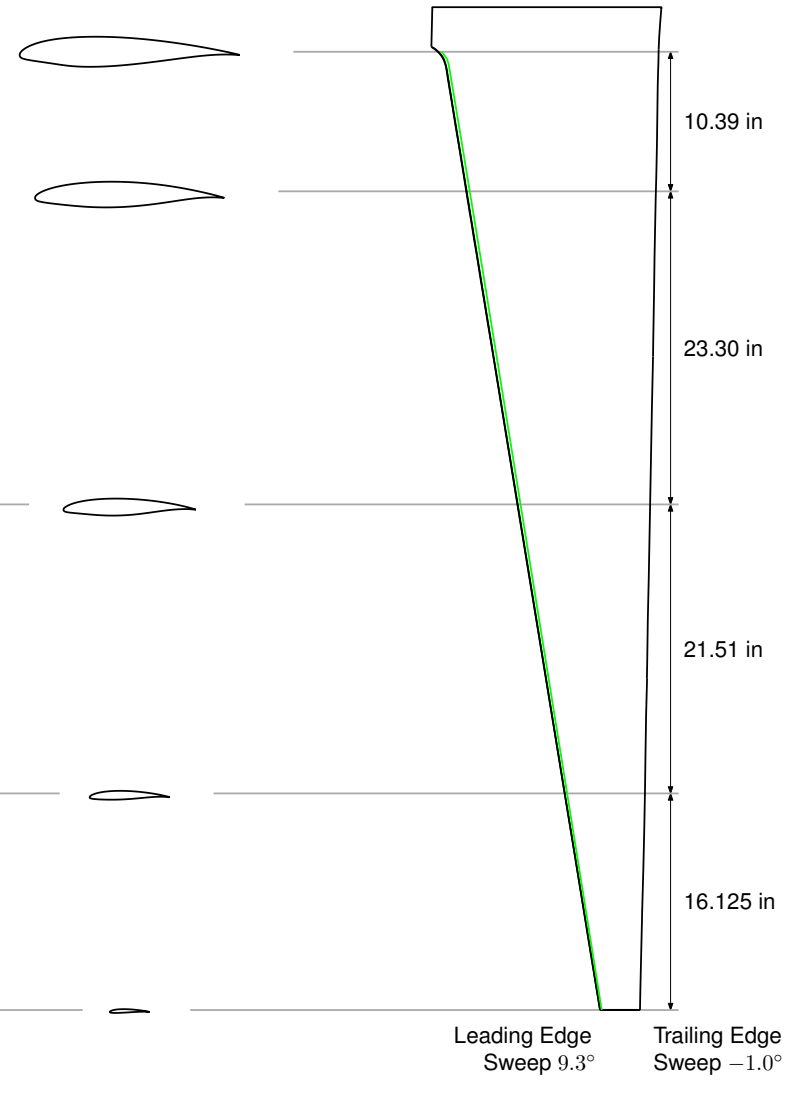

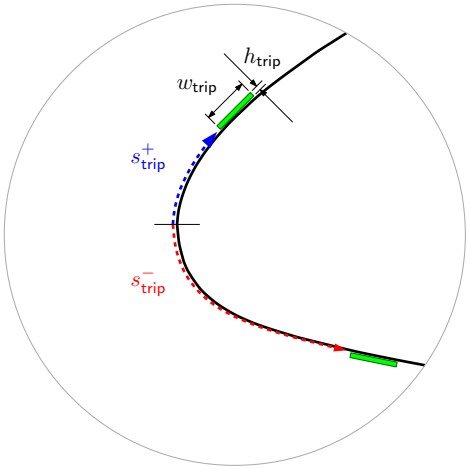

Trip Locations: Fuselage and Tail

(units: inches)

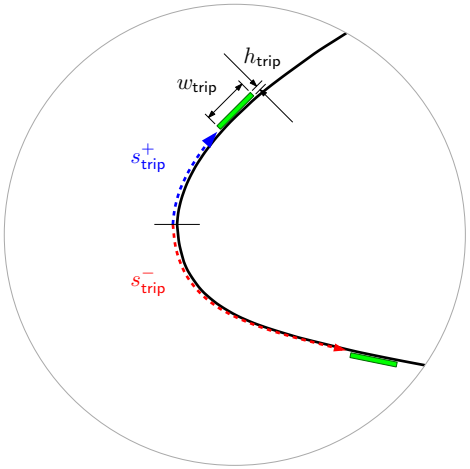

Horizontal Tail

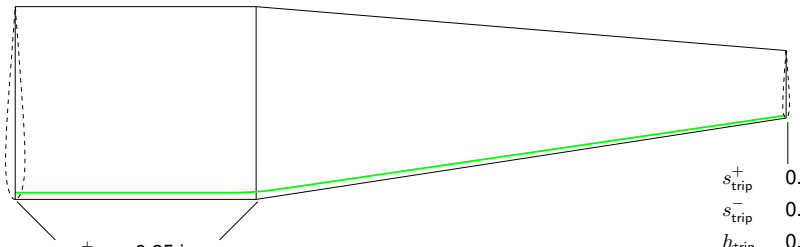

s^+_{trip}	0.25 in
s^-_{trip}	0.25 in
h_{trip}	0.013 in
w_{trip}	0.125 in

s^+_{trip}	0.125 in
s^-_{trip}	0.125 in
h_{trip}	0.013 in
w_{trip}	0.125 in

Non-BLI Vertical Tail

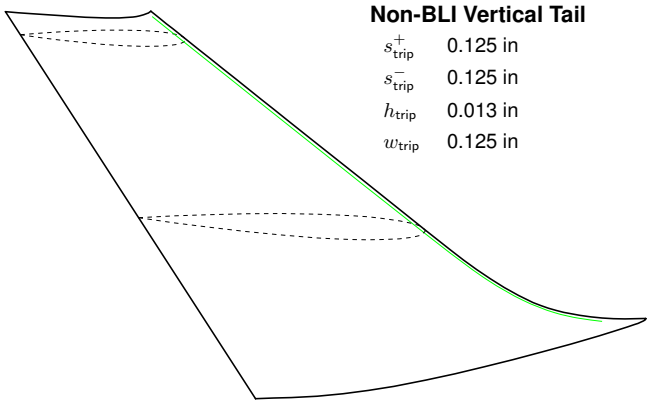

s^+_{trip}	0.125 in
s^-_{trip}	0.125 in
h_{trip}	0.013 in
w_{trip}	0.125 in

BLI Vertical Tail

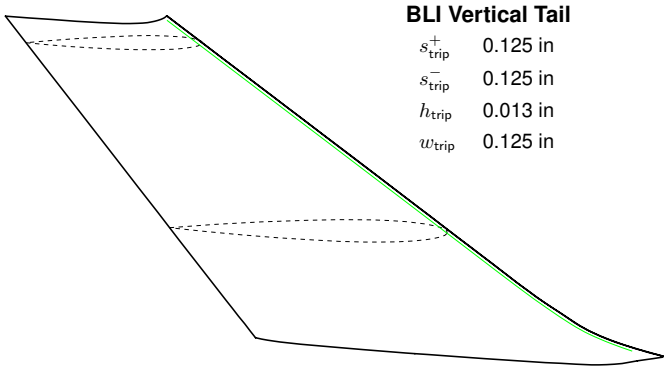

s^+_{trip}	0.125 in
s^-_{trip}	0.125 in
h_{trip}	0.013 in
w_{trip}	0.125 in

Fuselage Nose

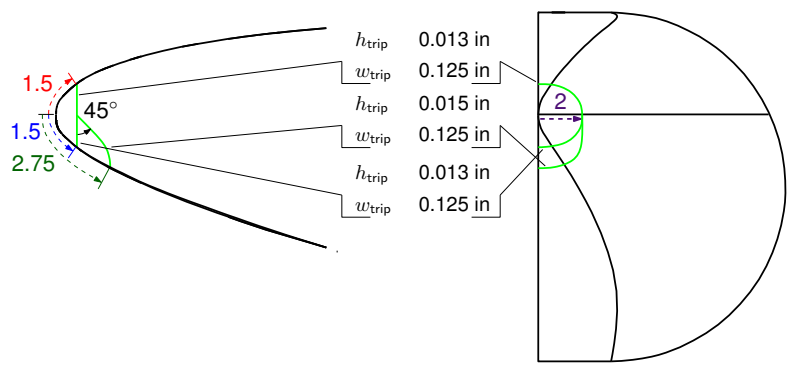

h_{trip}	0.013 in
w_{trip}	0.125 in
h_{trip}	0.015 in
w_{trip}	0.125 in
h_{trip}	0.013 in
w_{trip}	0.125 in

Trip Locations: Nacelles

(units: inches)

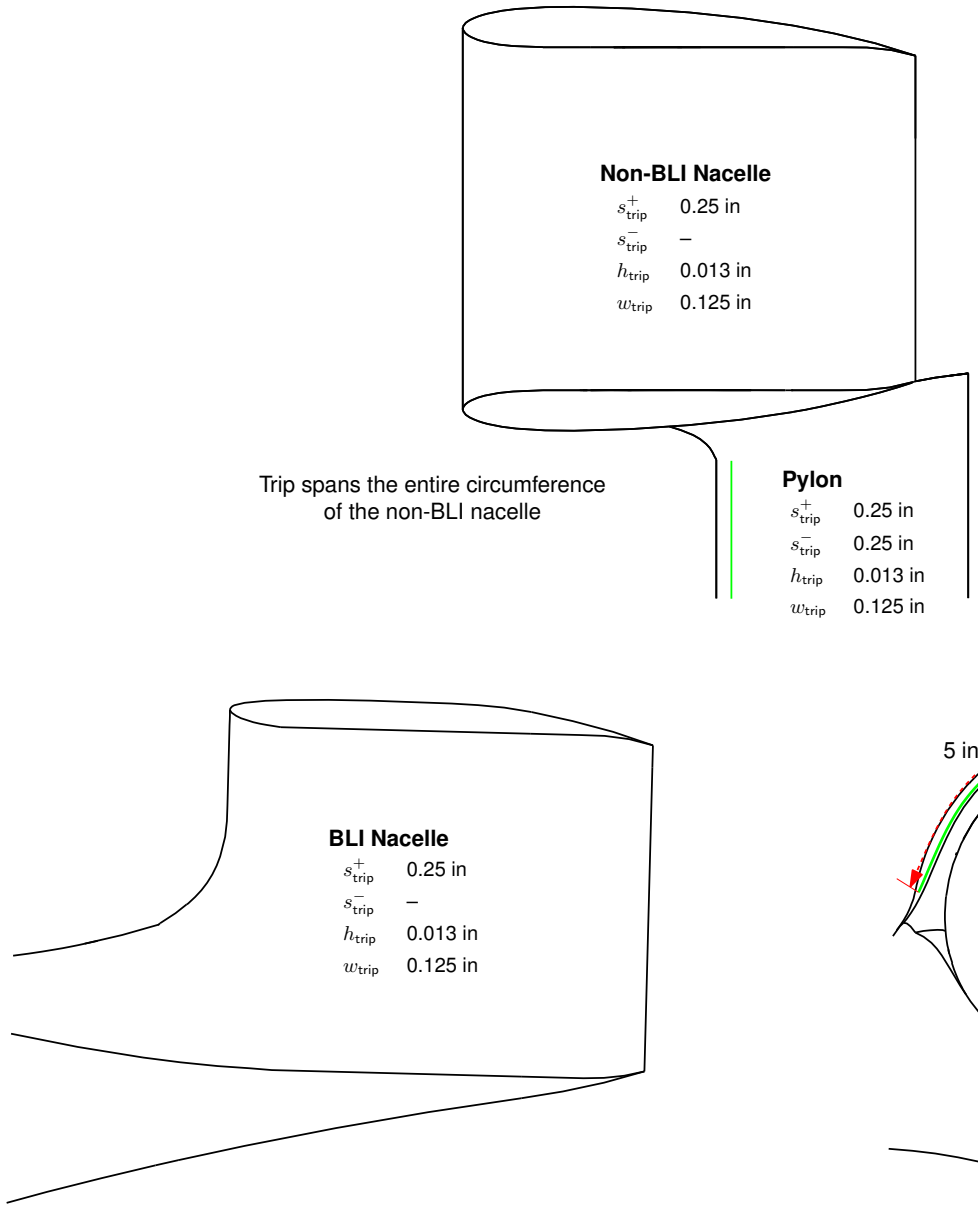

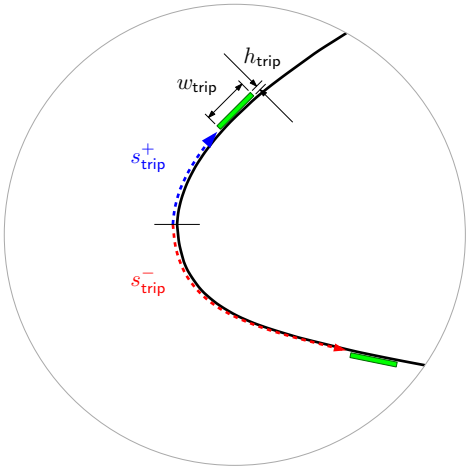

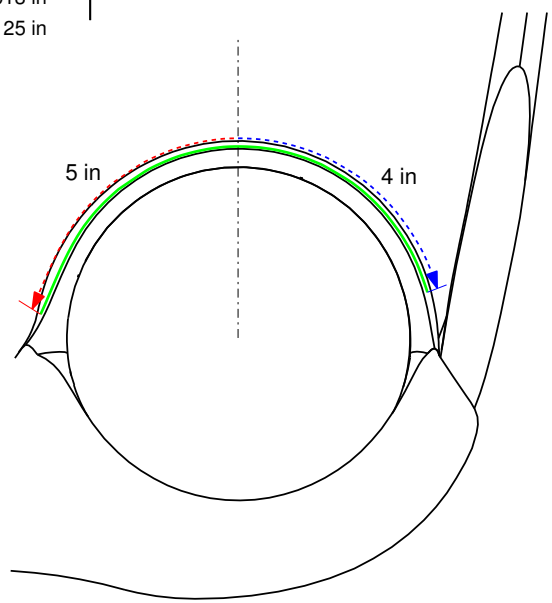

Instrumentation: Forces, Moments, Angle of Attack

(units: inches)

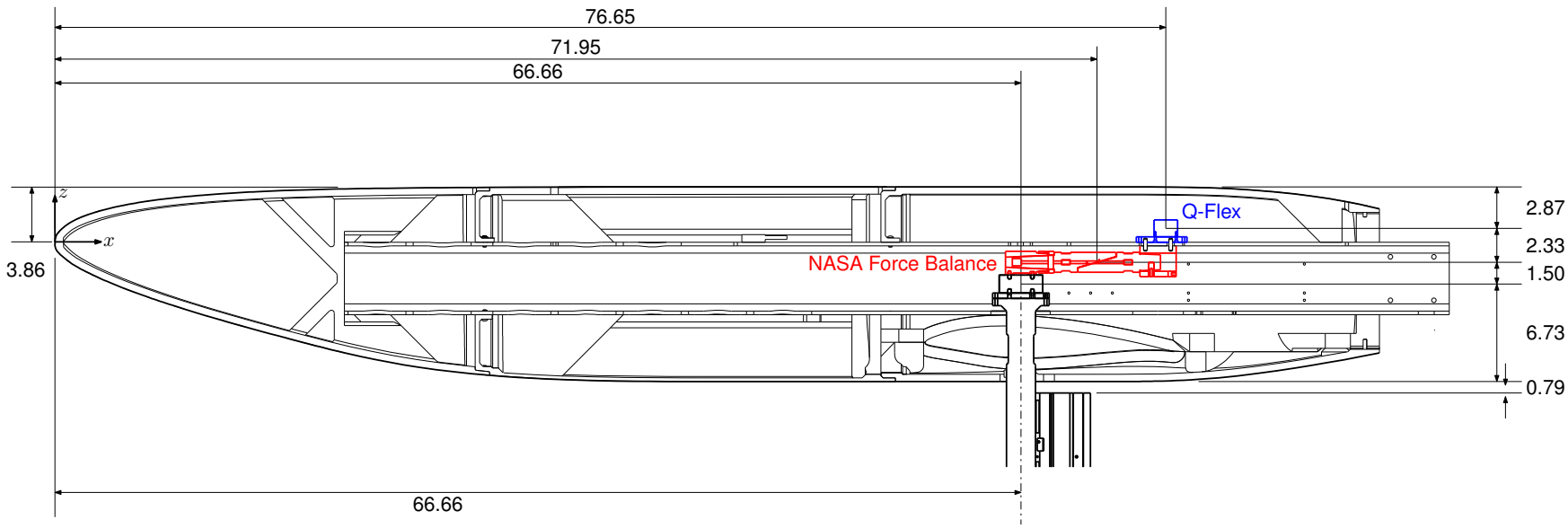

Model Positioning in Tunnel Test Section

(placement uncertainty: ± 1 in)

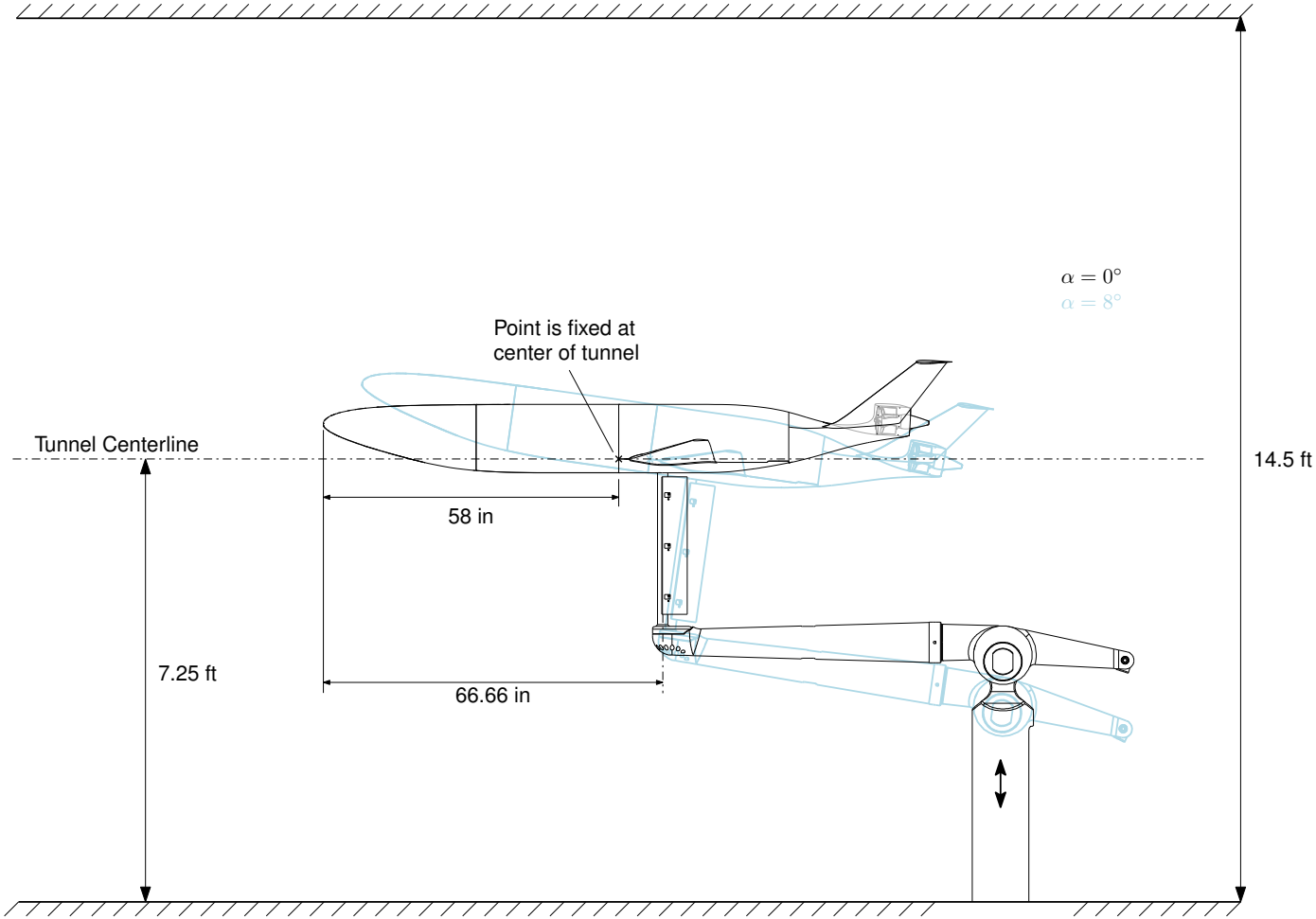

Moment Reference Center and Load Check Locations

(units: inches)

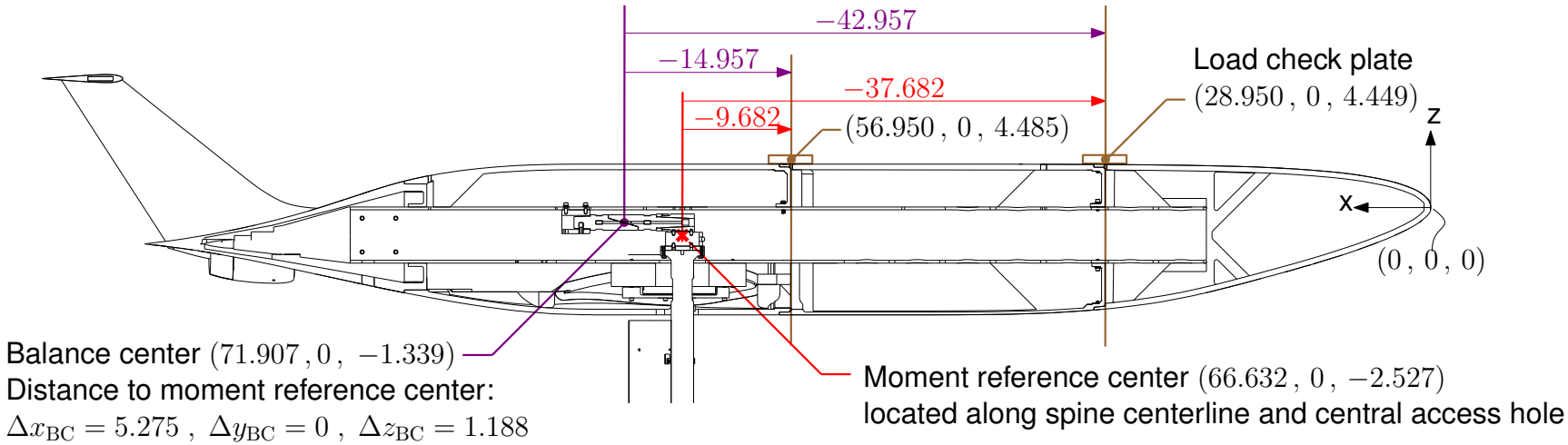

References

[1] E. M. Greitzer, P. Bonnefoy, E. De la Rosa Blanco, C. Dorbian, M. Drela, D. Hall, R. Hansman, J. Hileman, R. Liebeck, J. Lovergren, P. Mody, J. Pertuze, S. Sato, Z. Spakovszky, C. Tan, J. Hollman, J. Duda, N. Fitzgerald, J. Houghton, J. Kerrebrock, G. Kiwada, D. Kordonowy, J. Parrish, J. Tylko, and E. Wen, "N+3 aircraft concept designs and trade studies, final report," NASA CR 2010-216794, 2010.

[2] A. Uranga, M. Drela, E. M. Greitzer, N. A. Titchener, M. K. Lieu, N. M. Siu, A. C. Huang, G. M. Gatlin, and J. A. Hannon, "Preliminary experimental assessment of the boundary layer ingestion benefit for the D8 aircraft," AIAA 2014-0906, AIAA SciTech, 52nd Aerospace Sciences Meeting, 13–17 Jan 2014, National Harbor, MD, 2014.

[3] M. Drela, "Development of the D8 transport configuration," AIAA 2011-3970, 29th AIAA Applied Aerodynamics Conference, Honolulu, HI, 27–30 June 2011, 2011.

[4] A. Betz, *Introduction to the Theory of Flow Machines, First English Edition.* New York: Pergamon Press, 1966.

[5] L. Smith, "Wake ingestion propulsion benefit," *Journal of Propulsion and Power*, vol. 9, pp. 74–82, Jan–Feb 1993.

[6] M. Drela, "Power balance in aerodynamic flows," *AIAA Journal*, vol. 47, no. 7, pp. 1761–1771, 2009.

[7] J. Kerrebrock, *Aircraft Engines and Gas Turbines.* MIT Press, 1977.

[8] A. Grasch, "Design of a model propulsor for a boundary layer ingesting aircraft." M.S. Thesis. Massachusetts Institute of Technology, Dept. of Aeronautics and Astronautics. Available at `http://hdl.handle.net/1721.1/85778`, September 2013.

[9] G. L. Gentry Jr, P. F. Quinto, G. M. Gatlin, and Z. T. Applin, "The langley 14- by 22-foot subsonic tunnel: Description, flow characteristics, and guide for users," Technical Paper 3008, NASA, 1990.

[10] M. K. Lieu, "Quantification of the boundary layer ingestion benefit for the D8-series aircraft using a pressure rake system." M.S. Thesis. Massachusetts Institute of Technology, Dept. of Aeronautics and Astronautics. Available at `http://hdl.handle.net/1721.1/97264`, February 2015.

[11] M. Lieu, A. Uranga, M. Drela, and E. Greitzer, "Rapid flow surveys via rotating rake system and use in powered wind tunnel models," AIAA 2014-2801, AIAA Aviation, 30^{the} AIAA Aerodynamic Measurement Technology and Ground Testing Conference, 16–20 June 2014, Atlanta, GA, 2014.

[12] E. van Dam, "Inlet distortion characterization of the boundary layer ingesting D8 aircraft." M.S. Thesis. Delft University of Technology, Faculty of Aerospace Engineering, February 2015.

[13] N. Siu, "Evaluation of propulsor aerodynamic performance for powered aircraft wind tunnel experiments." M.S. Thesis. Massachusetts Institute of Technology, Dept. of Aeronautics and Astronautics. Available at `http://hdl.handle.net/1721.1/97265`, February 2015.

[14] N. Siu, N. Titchener, C. Casses, A. Huang, A. Uranga, M. Drela, and E. Greitzer, "Evaluating propulsor mechanical flow power in powered aircraft wind tunnel experiments," AIAA 2014-25661, AIAA Aviation, 32nd AIAA Applied Aerodynamic Conference, 16–20 June 2014, Atlanta, GA, 2014.

[15] C. Casses, "Aerodynamic benefits of boundary layer ingestion for the D8 double-bubble aircraft." M.S. Thesis. Massachusetts Institute of Technology, Dept. of Aeronautics and Astronautics. Available at `http://hdl.handle.net/1721.1/101494`, September 2015.

[16] R. A. Wahls, J. B. Adcock, D. P. Witkowski, and F. L. Wright, "A longitudinal aerodynamic data repeatability study for a commercial transport model test in the national transonic facility," TP 3522, NASA, 1995.

[17] S. Pandya, A. Huang, A. Espitia, and A. Uranga, "Computational assessment of the boundary layer ingesting nacelle design of the D8 aircraft," AIAA 2014-0907, AIAA SciTech, 52nd Aerospace Sciences Meeting, 13–17 Jan 2014, National Harbor, MD, 2014.

[18] P. G. Buning, D. C. Jespersen, T. H. Pulliam, G. H. Klopfer, W. M. Chan, J. P. Slotnick, S. E. Krist, and K. J. Renze, "OVERFLOW User's Manual," NASA, 2005.

[19] S. A. Pandya, "External Aerodynamics Simulations for the MIT D8 "Double-Bubble" Aircraft Design," ICCFD7-4304, 2012.

[20] W. M. Chan, R. J. Gomez, S. E. Rogers, and P. G. Buning, "Best Practices In Overset Grid Generation," AIAA Paper 2002-3191, 2002.

[21] W. M. Chan, "Developments in Strategies and Software Tools for Overset Structured Grid Generation and Connectivity," AIAA-2011-3051, 2011.

[22] W. M. Chan and J. L. Steger, "Enhancements of a Three-Dimensional Hyperbolic Grid Generation Scheme," *Appl. Math & Comp.*, vol. 51, pp. 181–205, 1992.

[23] T. H. Pulliam and D. S. Chausse, "A Diagonal Form of an Implicit Approximate Factorization Algorithm," *J. Comp. Phys.*, vol. 39, no. 2, pp. 347–363, 1981.

[24] F. R. Menter, "Two-Equation Eddy-Viscosity Turbulence Models for Engineering Applications," *AIAA Journal*, vol. 32, no. 8, pp. 1598–1605, 1994.

[25] M. Drela, "XFOIL: An analysis and design system for low Reynolds number airfoils," in *Low Reynolds Number Aerodynamics* (T. Mueller, ed.), Springer-Verlag, Jun 1989. Lecture Notes in Engineering, No. 54, `http://web.mit.edu/drela/Public/web/xfoil`.

[26] M. Drela and H. Youngren, "Athena Vortex Lattice," Sep 2004. `http://web.mit.edu/drela/Public/web/avl`.

[27] "Assessment of experimental uncertainty with applications to wind tunnel testing," AIAA Standards S-071A-1999, 1999.

[28] B. N. Taylor and C. E. Kuyatt, "Guidelines for evaluating and expressing the uncertainty of nist measurement results," Technical Note 1297, NIST, January 1993.

[29] H. W. Coleman and W. G. Steele, *Experimentation, Validation, and Uncertainty Analysis for Engineers*. Wiley, 3rd ed., 2009.

[30] J. D. Anderson, *Modern Compressible Flow.* McGraw-Hill, 3 ed., 2004.

[31] J. Hileman, J. Katz, J. Mantilla, , and G. Fleming, "Payload fuel energy efficiency as a metric for aviation environmental performance," 6th Internation Congress of the Aeronautical Sciences, 14–19 Sept 2008, Anchorage, AK, 2008.

[32] E. Gunn and C. Hall, "Aerodynamics of boundary layer ingesting fans," GT2014-26142, ASME Turbo Expo 2014, 16–20 Jun 2014, D usseldorf, Germany, 2014.

[33] R. Florea, D. Voytovych, G. Tillman, M. Stucky, A. Shabbir, and O. Sharma, "Aerodynamic analysis of a boundary-layer-ingesting distortion-tolerant fan," GT2013-94656, of ASME Turbo Expo 2013, 3–7 Jun 2013, San Antonio, TX, 2013.

[34] D. Hall, "Analysis of civil aircraft propulsors with boundary layer ingestion." Ph.D. Thesis. Massachusetts Institute of Technology, Dept. of Aeronautics and Astronautics. Available at `http://hdl.handle.net/1721.1/97353`, February 2015.

[35] D. K. Hall, A. C. Huang, A. Uranga, E. M. Greitzer, M. Drela, and S. Sato, "Boundary layer ingestion propulsion benefit for transport aircraft," *Journal of Propulsion and Power*, vol. 33, no. 5, pp. 1118–1129, 2017.

[36] A. Uranga, M. Drela, E. M. Greitzer, D. K. Hall, N. A. Titchener, M. K. Lieu, N. M. Siu, C. Casses, and A. C. Huang, "Boundary layer ingestion benefit of the D8 transport aircraft," *AIAA Journal*, vol. 55, no. 11, pp. 3693–3708, 2017.

[37] A. Uranga, M. Drela, D. K. Hall, and E. M. Greitzer, "Analysis of the aerodynamic benefit from boundary layer ingestion for transport aircraft," *AIAA Journal, in press*, 2018.

[38] W. Lord, G. Suciu, K. Hasel, and J. Chandler, "Engine architecture for high efficiency at small core size," AIAA 2015-0071, AIAA SciTech, 53nd Aerospace Sciences Meeting, 13–17 Jan 2014, Kissimmee, FL, 2015.

[39] A. DiOrio, "Small core axial compressors for high efficiency jet aircraft." M.S. Thesis. Massachusetts Institute of Technology, Dept. of Aeronautics and Astronautics. Available at `http://hdl.handle.net/1721.1/77107`, September 2012.

4 Task 2: High Efficiency, High Pressure Ratio Small Core Engines

This section presents the work and results of the Task 2. The content that follows was submitted as the Task 2 Final Report to NASA on 30 October 2014, and was prepared by W.K. Lord and G.L. Suciu from Pratt & Whitney, and by A.G. DiOrio, E.M. Greitzer, and C.S. Tan from MIT. Some of the material was also presented in References [38] and [39]. The technology road-map that was part of the report submitted to NASA is not included here since it contains restricted material.

Task 2 Abstract

This documents reports findings and conclusions concerning high-efficiency, high-pressure ratio, small core engine and compressor technology for advanced civil aircraft (2035 time frame). The work was carried out by an MIT-Pratt&Whitney team as part of the NASA/MIT N+3 Phase 2 contract. The report gives the background and motivation that sets small core technology--defined here as compressor corrected exit flow levels between roughly 1.5 and 3 lbm/s--on the critical path for advanced commercial engines to power a short/medium range subsonic transport in the 737 class. It then introduces the issues that need to be addressed for success in this regime, from both the compressor and the engine perspectives, and describes conceptual design studies that define the characteristics of such compressors and engines. This is done first in a generic sense and then more specifically for the D8, double bubble, boundary layer ingesting aircraft. The D8 propulsion system includes a novel engine architecture that not only enables lower non-dimensional tip clearance, and thus higher efficiency, than current configurations at these low corrected flows, but also meets the FAA '1 in 20' rule that applies to engine failure occurrence. Finally, the report presents a technology roadmap that calls out research and development issues needing to be faced to make these engines a reality.

4.1. Directions in Propulsion Technology

Two recent sources have given expositions of the history and the directions in civil aircraft propulsion technology (Epstein, 2014; Lord, 2014). These describe a quest for fuel burn that has led to decreases in fan pressure ratio, and thus lower exhaust jet velocity, enabling higher propulsive efficiency. In terms of engine configuration, the changes have meant increases in engine bypass ratio. Jet aircraft of the 1970s had engines with bypass ratios of 5. The bypass ratio has now grown to over 10 for engines that will enter service in 2015-2019 with a fuel burn decrease of more than 15 per cent compared to current engines. The longer term trend is to bypass ratios from 15 to 20 with even larger decreases in fuel burn.

The direction of engine configuration for commercial aircraft is portrayed in Figure 4.1. It can be stated succinctly: *big fans/small cores*. One major enabler for future bypass ratio growth is the geared turbofan architecture, which allows the low pressure compressor, and low pressure turbine, to turn at an RPM three or more times that of the fan. A second is the high-efficiency, high-pressure ratio core engine system, with higher work per unit mass flow compared to today's engines. This latter, in turn, is enabled by high turbine entry temperatures, which are required to make these pressure ratios useful. An excellent discussion of the evolution of core engine technology from a designer's perspective has been given by Koff (2004), who shows both the increases in core power per unit mass flow that have been achieved and the potential for improvements still to be realized.

4.1.1 Bypass Ratios, Efficiencies, And Core Sizes

As background for the subsequent discussion, Figure 4.2 presents information about the bypass ratios of current (2014) engines and next generation (N+1) engines as a function of the takeoff thrust. The new turbofans for both single aisle and twin aisle aircraft have bypass ratios larger than 10.

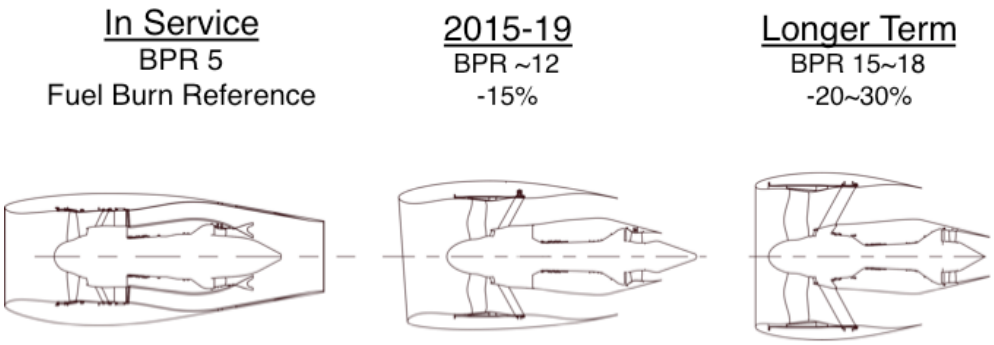

Figure 4.1. The commercial aviation propulsion trend towards big fans/small cores; bypass ratio numbers represent values for single aisle aircraft [Lord, 2014].

Figure 4.3 highlights aircraft engine performance achievements in terms of contours of overall efficiency, the ratio of thrust power to chemical energy (heating value) of the fuel. The vertical axis is the core thermal efficiency, defined as the ratio of mechanical work produced by the gas generator part of the core, to the heat input to the cycle; the latter is, to a close approximation, equal to the fuel chemical energy. The horizontal axis is the ratio of the thrust power, namely the power needed to propel the aircraft in steady level flight at the cruise speed (i.e., the product of thrust and flight speed), to the mechanical power supplied by the core, which is the product of propulsive times transmission efficiency. The overall efficiency targeted for the ultra high bypass ratio engines is considerably more than twice the original values of the initial turbojet values (on the chart at coordinates roughly 0.4, 0.4). Another aspect of Figure 4.3 is that the gain in propulsive times transmission efficiency is larger than the gain in thermal efficiency. In terms of the main influences, high overall pressure ratio is the driver for thermal efficiency and lower fan pressure ratio is the driver for increased propulsive efficiency.

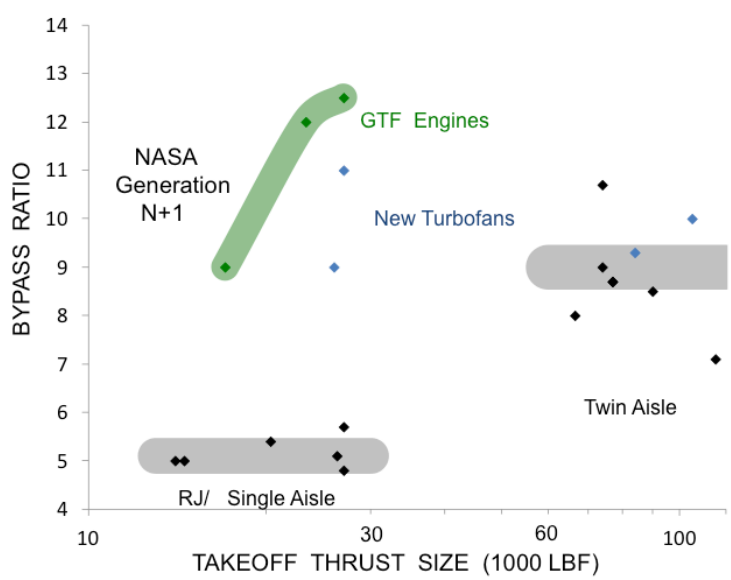

Figure 4.2. Bypass ratio vs. engine takeoff thrust size for 2014 production engines (best in class) and new engines, EIS 2015-2020 [Lord, 2014]

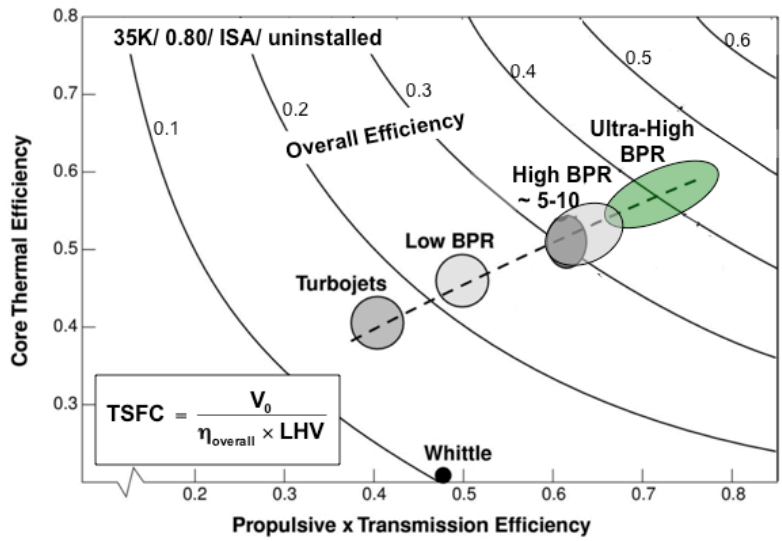

Figure 4.3. Core thermal efficiency, propulsive efficiency, and overall efficiency, for commercial aircraft engines [Epstein, 2014].

The trends in engine efficiencies and core size[1] are illustrated chronologically in Figure 4.4, which are curve fits to data. The figure includes trend lines for thermal efficiency and propulsive efficiency as well as the trends in normalized core size, versus year of introduction. The technology 'barriers' that have been surmounted to achieve these levels are well known and include higher pressure ratios (improved ability for off-design matching) improved materials, more effective turbine cooling schemes (both of which result in higher turbine entry temperatures), and better component efficiencies.

The inference from the information presented is of an inexorable industry trend of decreased core size. This is generic for aircraft of the 737 class, not only the D8, and it is thus useful to give further context to frame the small core issues and the research and technology needed.

[1] The quantity $\dot{m}\sqrt{T_t}/Ap_t$, the *flow parameter* (also referred to as *corrected flow per unit area*), with $\dot{m}$ mass flow, T_t stagnation temperature, A flow area, and p_t stagnation pressure, is a function of the Mach number and the gas properties. For air, therefore, it is approximately a function of Mach number only. This means the *corrected flow*, as defined below, can be written as [with $F(M)$ a known function of Mach number and θ and δ as nondimensional stagnation temperature and pressure, respectively]

$$\text{Corrected flow} = \frac{\dot{m}\sqrt{T_t/T_{t_{ref}}}}{p_t/p_{t_{ref}}} = \frac{\dot{m}\sqrt{\theta}}{\delta} = AF(M).$$

Assuming the compressor Mach number is roughly the same for different compressors, in order to meet the combustor inlet flow requirements, the corrected flow is thus a measure of compressor exit area and hence compressor size. For given compressor flow, increases in overall pressure ratio decrease the exit corrected flow and the compressor exit area.

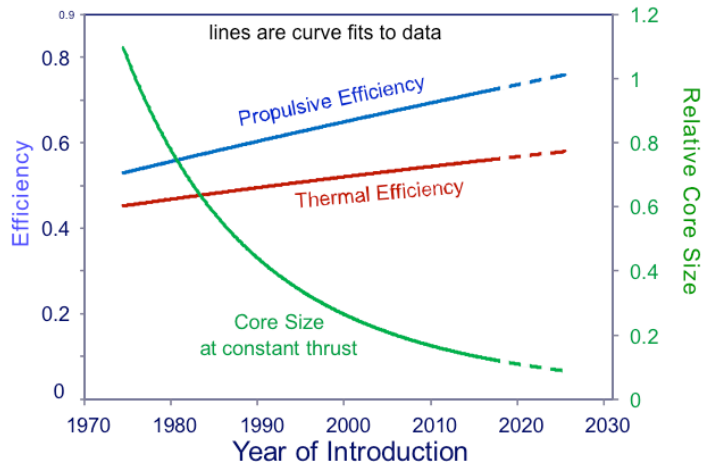

Figure 4.4. Chronology of thermal efficiency, propulsive efficiency, and core compressor size [Epstein, 2014].

4.1.2 The Aircraft Engine Parameter Space

As an introduction to the design spaces and the different constraints on the components, Figure 4.5 depicts engine parameters in terms of core size (corrected flow in lbm/s) and overall pressure ratio, OPR. Current (generation N) and near term (generation N+1) engines are shown. The design space for these engines is bracketed by architecture and by material and temperature limits primarily associated with the compression system. The architecture for large core engines, with core size larger than 3 lbm/s, is an all-axial compressor. For smaller engines, with core size less than 3 lbm/s, the engines have both axial and centrifugal compressors. As the design pressure ratio increases there is a corresponding increase in compressor exit temperature , T_{t_3} . The combination of high T_{t_3} and high rim speed becomes a limit on the overall pressure ratio due to material thermal or mechanical fatigue at the back end of the compression system, and this is typically more limiting for axial-centrifugal compressors due to higher rim speeds.

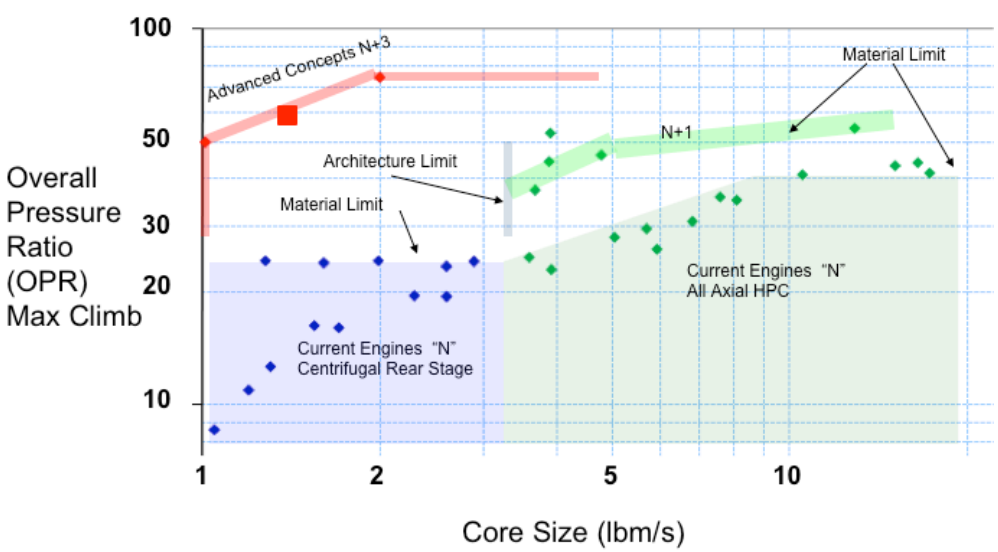

Figure 4.5. Aircraft engine parameters and limitations in terms of compressor exit corrected flow and overall pressure ratio (OPR) [Lord *et al.*, 2015].

An important feature of Figure 4.5 is the currently empty upper left hand corner of core engine design space at high overall pressure ratio and small core size. As we will see in more depth, the *thermodynamics of the core engine cycle is both straightforward and unforgiving*. Engine cycle computations say unambiguously that *the design of the N+3 engine wants to be located far into uncharted territory* that constitutes this upper left hand corner.

4.2. Small Core Engine Performance and the D8 Aircraft

The MIT N+3 Phase1 Aircraft Concept Design Study (Greitzer et al., 2010) identified the D8, double bubble vehicle configuration, with boundary-layer ingesting (BLI) propulsion mounted at the upper aft fuselage, as a promising concept with potential to meet the NASA goals for N+3 generation aircraft. Two key technology challenges were identified for further study and technology maturation in Phase 2: i) small high-efficiency core engines, the subject of this report and ii) propulsion-airframe integration including BLI, which has been the focus of the experiments carried out at the NASA Langley 14 x 22 foot Subsonic Wind Tunnel, as described by Uranga et al. (2014).

The double-bubble concept aircraft was sized for a 737-800 type mission. The D8.6 vehicle configuration is a twin-aisle double-bubble fuselage with two side-by-side engines, which are flush mounted at the upper aft fuselage within the 'pi tail'[2]. The technology advances envisioned by 2035 affect aerodynamics, materials, propulsion, and the vehicle configuration itself, and the estimated takeoff thrust size of the engines is only 15000 lbf.

The N+3 D8 propulsion system, designed for a mission optimized cruise thrust specific fuel consumption (TSFC), has high overall pressure ratio (OPR) with near zero levels of turbine cooling for high thermal efficiency, making use of advanced high-temperature materials. It has a low fan pressure ratio (FPR) propulsor with *boundary layer ingestion for high propulsive efficiency*. The reference current aircraft and engine technology level at "Generation N" for this program is the 737-800 and CFM56-7B24 combination. The reference level of TSFC is approximately 0.60 lbm/hr/lbf quoted at 35K ft/ 0.80 Mach/ ISA/ uninstalled.

4.2.1 Thermal Efficiency Trends

We now examine in more depth the two items that comprise the overall efficiency, thermal efficiency and propulsive efficiency. The *thermal efficiency* trend with OPR, at cruise conditions, Flight Mach number = 0.8, is presented in Figure 4.6. There is an ideal trend line shown for a thermodynamically ideal Brayton cycle with optimum turbine entry temperature, zero cooling flow, and 100% component efficiencies. There is a second trend line at lower efficiency that represents an uncooled cycle with 90% efficient components. Actual performance levels for three generations of engine technology are also indicated. The actual efficiencies are substantially lower than that for the ideal cycle due to non-ideal component efficiencies, turbine cooling, leakage, windage, etc. Both, however, follow a similar upward trend with OPR as the engine technology advances.

The actual thermal efficiency levels in Figure 4.6 do depend on engine thrust size, mainly due to the scale effect on component efficiencies, so the figure shows performance levels consistent

[2] The name comes from the similarity with the Greek letter π

with 25K lbf nominal thrust size for generation N and N+1. The generation N engines (CFM56, V2500) have cruise OPR about 30. The generation N+1 engines are here considered to be the new engines in the 24K-30K thrust size for the new and re-engined single-aisle aircraft that will enter service in 2015-2020 time frame. These have cruise OPR about 40. Generation N+3 is a small thrust size engine at cruise OPR ~ 50, with high efficiency components even at the small core size, with near zero turbine cooling, and with a thermal efficiency near 60%.

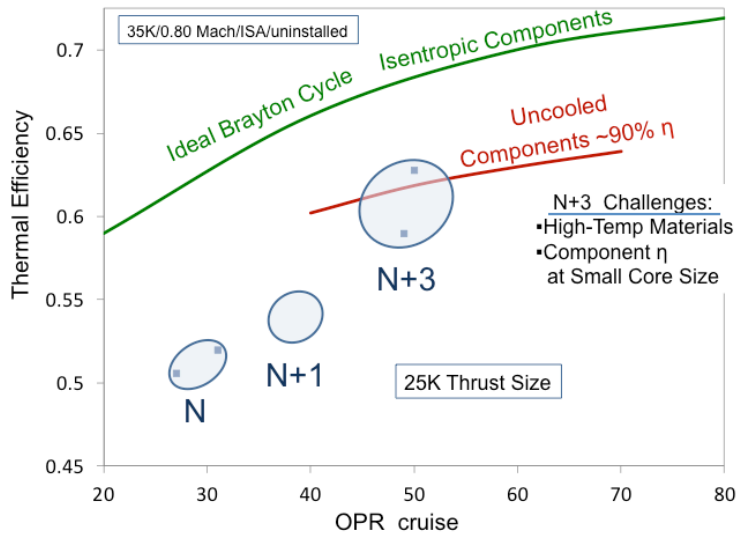

Figure 4.6. Thermal efficiency trends with overall cycle pressure ratio (OPR) [Lord *et al.*, 2015].

4.2.2 Propulsive Efficiency Trends

The *propulsive efficiency* as a function of specific thrust (thrust per unit engine mass flow) is given in Figure 4.7. We define propulsive efficiency here as propulsive power (net thrust x flight velocity) divided by input shaft power. The 'ideal podded' curve is for an isentropic propulsor in a podded installation. This curve is consistent with the familiar definition that propulsive efficiency $= 2/\left(1+V_j/V_0\right)$, where V_j is exhaust jet velocity and V_0 is flight velocity. The specific thrust, or thrust per unit mass flow, is $F/\dot{m}V_0 = V_j/V_0 - 1$.

A second curve is shown for an ideal propulsor with boundary layer ingestion. The figure is based on an assumed ingested drag equal to 15% of propulsor net thrust, and an ideal propulsor for which the pressure rise varies on each streamtube so that the exit profile has uniform jet velocity. The quantity K is a boundary layer shape parameter, defined as $K = \left(\theta^*/\theta\right) - 1$, where θ^* is the boundary layer kinetic energy thickness and θ is the momentum thickness. The boundary layer analysis used is similar to that presented originally by Smith (1993) and the uniform jet velocity corresponds to *wake recovery*, R, of unity in his analysis..

The indicated difference in propulsive efficiency between ideal podded and ideal BLI in the range of interest is roughly 5 percent. Actual performance levels for three generations of engine

technology are also indicated. There is an upward trend with decreasing specific thrust from generation N to N+1 at a slope that parallels the ideal podded curve, and an offset to a higher level for the N+3 engine, which incorporates BLI. Specific thrust is used here as the independent parameter rather than fan pressure ratio (FPR) because it is a well defined quantity even for the boundary layer ingestion case where there is nonuniform inlet stagnation pressure. The cruise FPR associated with generation N is 1.7. For generation N+1 it is in the range 1.4 to 1.5, and for generation N+3 it is in the range 1.3 to 1.4

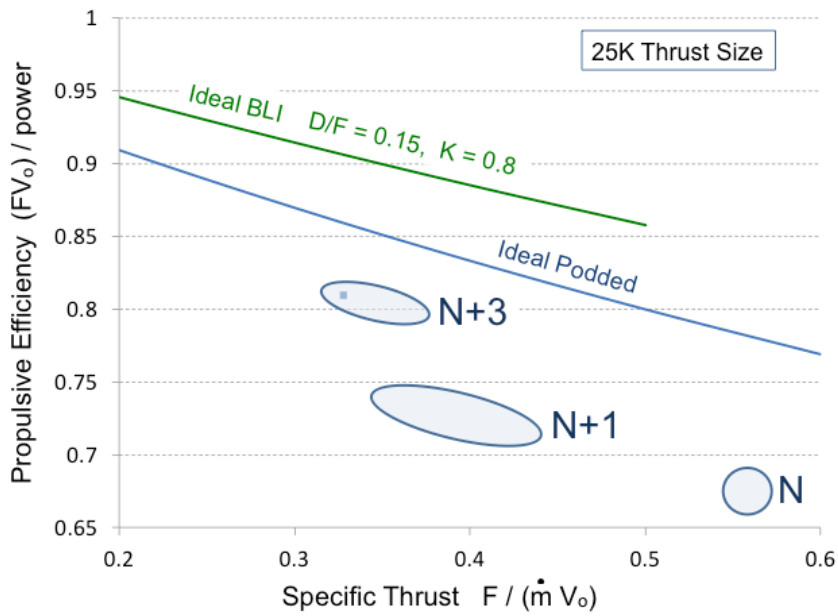

Figure 4.7: Propulsive efficiency as a function of specific thrust, $F/\dot{m}V_0$ [Lord *et al.*, 2015].

In terms of overall engine system performance, the improvement from generation N to N+1 has been quoted at a decrease of 15% in TSFC. The target improvement from generation N to generation N+3 is a decrease of 30% in TSFC, about half of the NASA N+3 fuel burn reduction goal of -60%. The improvement for N+3 relative to generation N splits out approximately as: flying slower 5% (N+3 cruise at 0.74 Mach); thermal efficiency 10%; propulsive efficiency 15%.

4.3. Small Core Engine Technology Challenges

There are a number of technology challenges associated with meeting the N+3 performance targets. For an engine core, the critical needs are high temperature materials and high OPR with high efficiency components, at small core size. The goal for high temperature-capable materials is common across all engine sizes. The desired engine attributes, however, namely a high OPR (and high turbine entry temperature) engine cycle with a low specific thrust propulsor in a small thrust range (less than 20K lbf, say) drive the engine design to a small core size, as illustrated for the N+3 engine in Figure 4.5.

As mentioned there are generic single aisle aircraft small core engine challenges as well as specific challenges presented by the D8 airframe. We discuss the former first. To start, it is useful to illustrate what core size means in terms of actual hardware. This is portrayed in Figure 4.8 in which a picture of the rear of a high-pressure compressor is used to highlight the dimensions of the exit stator. The outlines of the stator at a corrected flow of 5.7 lbm/s are given by the yellow lines, and the outlines for a corrected flow of 3.0 lbm/s by the red lines. There are challenges with blade geometry and with holding clearances, as well as decreased Reynolds number.

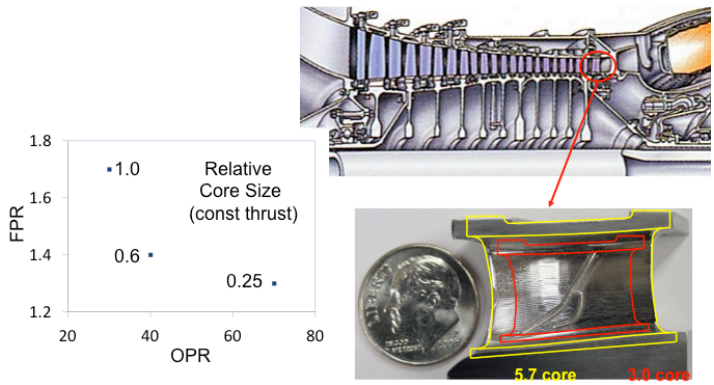

Figure 4.8: Core size high overall pressure ratio engines—yellow lines show 5.7 lbm/s core size, red lines show 3.0 core size [Lord, 2014].

4.3.1 Component Technology Issues

The challenges can be, at least conceptually, separated into issues having to do with *component technology*, issues having to do with *propulsion system-airframe integration*, and issues having to do with *engine architecture*. To introduce the first of these Figure 4.9 captures the current experience with small core compressors. The blue line gives a design system estimation of the change in efficiency with core size [Epstein, 2014]. Assessments of the unavoidable losses, as well as estimates of the effects of changes in the engine architecture to reduce non-dimensional tip clearance, imply, however, that that there is a potential to mitigate much of the 3% fall off seen, as given by the red line marked 'physics'. (These assessments are summarized in the later parts of this section.) It is by no means a foregone conclusion that total mitigation can be accomplished, but ideas for design changes have been brought forward which may open the route to doing this, and these are also described later in this document. The inference from the figure is that raising the performance to the red line is not against any physical laws, it is rather a case of, specifically, what must be done differently from current practice.

Of direct interest from an aircraft mission perspective is the fuel burn increase associated with compressor efficiency. DiOrio (2012) has examined this for a D8 mission; his estimate is shown in Figure 4.10. The figure gives the change in fuel burn (0.6% increase) for a 1% decrease in high compressor polytropic efficiency, calculated using the TASOPT (Drela, 2011) software.

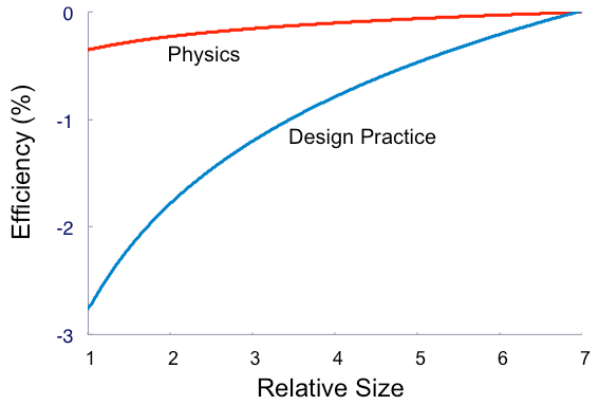

Figure 4.9: Component efficiency and core size trend [Epstein, 2014].

Two major sources of inefficiency in the compressors of small core engines, low Reynolds numbers and large tip clearance, were computationally assessed by DiOrio [2012]. Three different compressor configurations were examined to quantify the efficiency associated with each at flows down to 1.5 lbm/s, consistent with the D8 application. The impact of compressor size, blade geometry, tip clearance, and compressor configuration were assessed against a global metric, aircraft mission fuel burn. A summary of DiOrio's findings are given below.

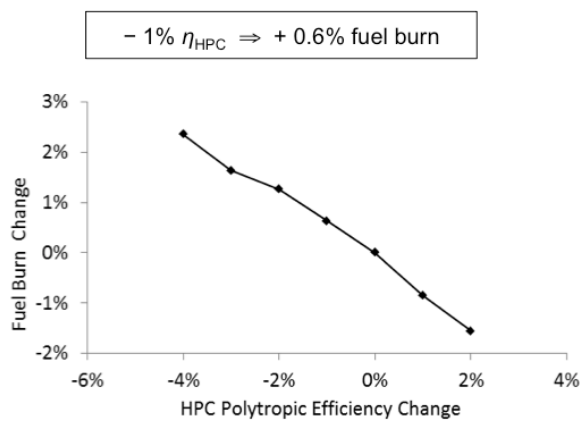

Figure 4.10: Effect on fuel burn of changes in high pressure compressor efficiency [DiOrio, 2012].

The three configurations examined are shown schematically in Figure 4.11. The first was a direct scaling to1.5 lbm/s exit corrected flow from current compressors for single-aisle civil transport aircraft. The last stage had hub-to-tip ratio of 0.93. This is referred to as *pure scale* in the figure. In the second configuration the minimum radius of the high pressure compressor was set at a value consistent with an existing small engine low-pressure spool shaft diameter. This is referred to as the *shaft limited* configuration. The mean radius for this configuration is larger than that from the pure scale configuration. The third configuration, referred to as *shaft removed,* did not have the constraint on inner (low-pressure spool) shaft diameter, so the minimum radius of the high pressure compressor could be pulled in, reducing the hub-to-tip radius ratio of the last stage

to 0.85. Blade size, Reynolds number, and tip clearance were all found to be dependent on configuration, with the shaft-limited configuration presenting the greatest challenge (lowest Reynolds numbers and largest tip clearances).

The lowest rotor Reynolds number estimated for the 1.5 lbm/s shaft limited compressor was 160,000. There was a 2.3% decrease in stage efficiency compared to operation at a Reynolds number of 10^6. Blade and vane geometry optimization were found to give a small mitigation of the effects of low Reynolds number in the shaft-limited configuration. For the compressor examined, the efficiency increase with the optimized blade was 0.2%. Blade optimization can have a larger impact at Reynolds numbers below 150,000, i.e., for core sizes below 1.5 lbm/s.

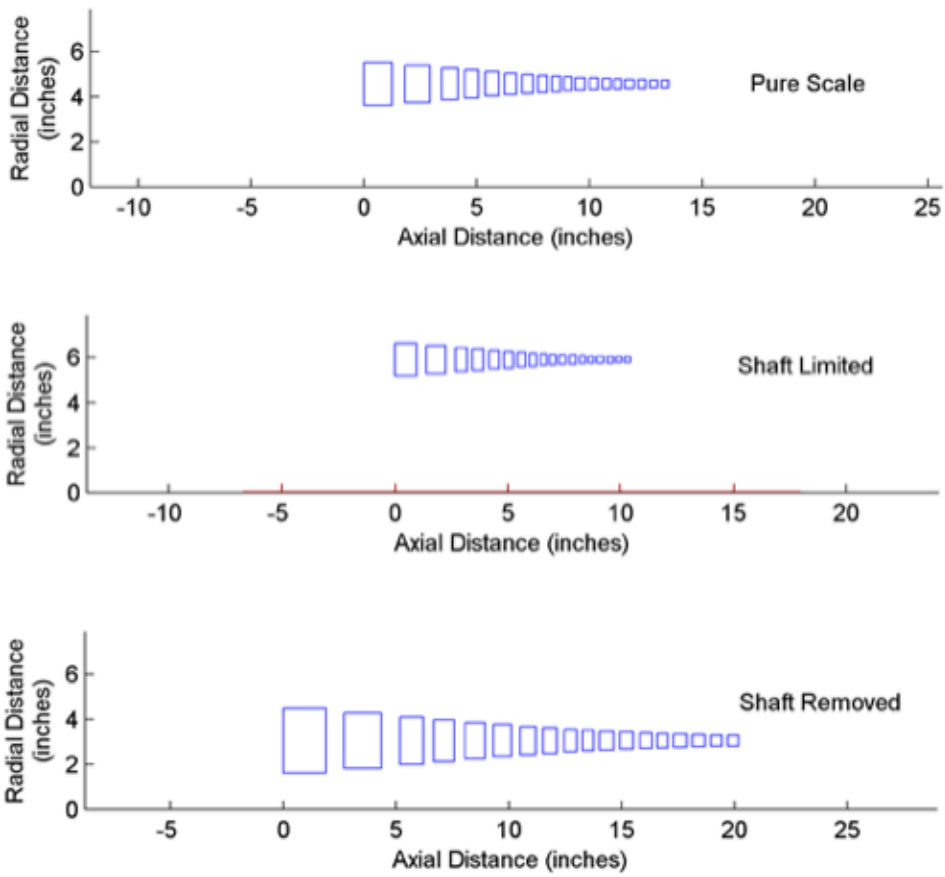

Figure 4.11: Core engine compressor configurations examined: Pure Scale –Compressor with a hub-to-tip ratio of 0.93 at the last stage photoscaled to a lower corrected flow; Shaft Limited –Assumes the minimum radius is set by the low-presssure compressor (LPC) shaft radius; Shaft removed–Eliminates the LPC shaft constraint, decreasing the allowable flow path inner radius [DiOrio, 2012].

To bound the examination of the effects of clearance, two limiting cases were defined. The first was *fixed clearance*, i.e., clearance held at a value representative of single-aisle aircraft engine high compressors. The second was based on the ability to *scale clearances with radius*. If clearances are fixed (i.e., the clearances do not scale with core size), the maximum tip clearance

in a 1.5 lbm/s HPC could be 4.5%, leading to a stage efficiency penalty of 7.0%. The fuel burn increases associated with small core compressor inefficiency were found to be between 0.4% and 3.4%, depending on compressor configuration and tip clearance scaling.

Decreasing the mean radius of a machine allows larger blades, so Reynolds numbers are increased and non-dimensional tip clearances are decreased, by pulling in the flow path. Reducing the rear stage hub-to-tip ratio from 0.93 to 0.85 allowed an increase in compressor polytropic efficiency of between 1.5% and 2.0% for a 1.5 lbm/s core.

Tip clearances were found to be the largest source of inefficiency in the small core compressors examined, regardless of configuration. There was approximately a 1.6% gain in efficiency for every 1% reduction in gap-to-span ratio. If physical tip clearances can be scaled, there is a 1.5 – 2.5% increase in efficiency for the compressor studied, compared to the situation in which the clearances do not scale. Results of the calculations of fuel burn are given in Figure 4.12, for a 'best case' and 'worst case' configuration.

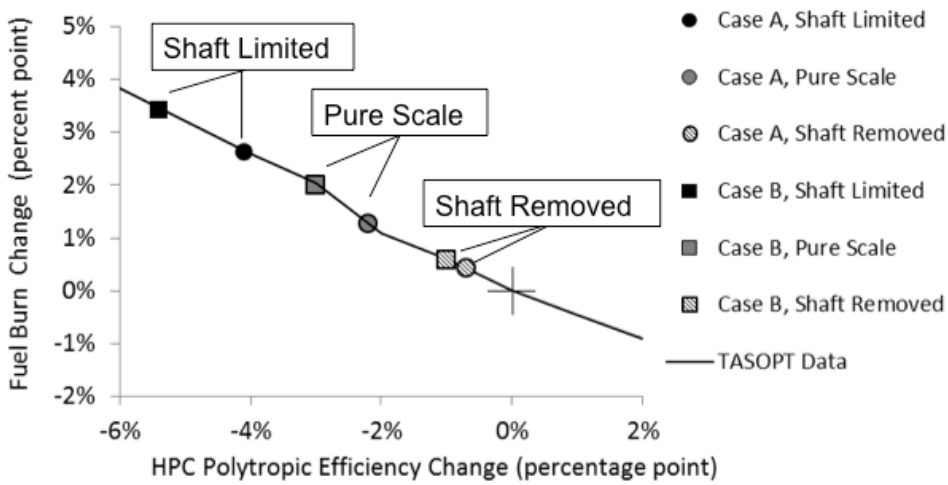

Figure 4.12: D8.6 Fuel burn impact of configuration—Case A: Best case scenario (blade optimized for low Reynolds number, clearances scale with compressor size, Case B: Worst case scenario (blade not optimized for low Reynolds number, fixed minimum clearance, physical clearances do not scale) [DiOrio, 2012].

4.3.2 Propulsion System Integration Issues

The second major challenge is associated with propulsion system-airframe integration. Figure 4.13 shows the consequence of 'business as usual' in going from the current single-aisle bypass ratio of 5 to the proposed value of 18, at constant thrust. While the figure may be tongue-in-cheek, the point is that step changes in the integration of the propulsion system and the airframe, or even a different type of aircraft, may be needed.

Figure 4.14 addresses the latter approach with the D8, double bubble aircraft (so-called because the cross section of the fuselage looks like two bubbles—see the three-view at the left of Figure 4.14) aircraft. The aircraft has engines mounted above the fuselage, between the two vertical members of the 'pi-tail' structure, with ample space for ultra high bypass engines. The engines

ingest the fuselage boundary layer, giving a propulsive efficiency benefit that yields lower fuel burn. The performance and integration aspects of this boundary layer ingesting aircraft are other main issues that this project addresses, through analysis, computation, and powered model tests at the 14 x 22 foot NASA Langley Subsonic Wind Tunnel (Uranga et al, 2014).

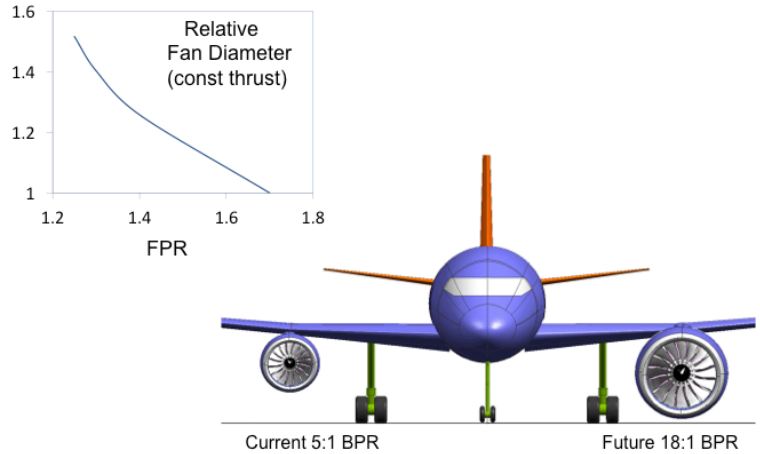

Figure 4.13: Aircraft installation challenge for flow low fan pressure ratio, high fan bypass ratio, turbofans [Lord, 2014]

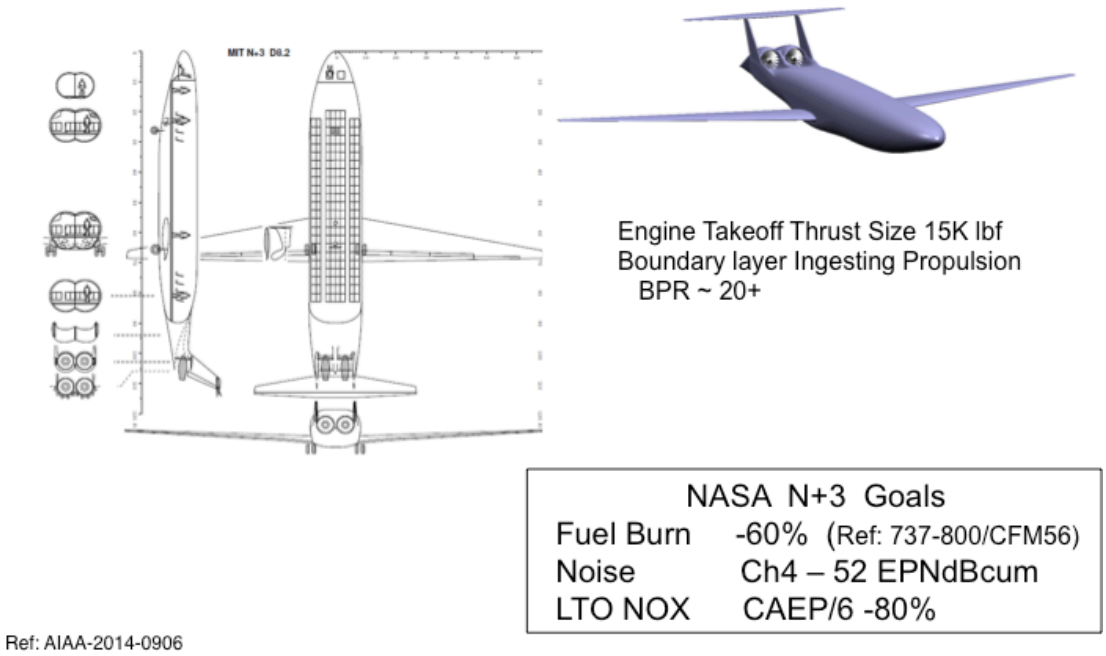

Figure 4.14: N+3 D8, double bubble configuration – 180 passengers, 2000 nautical mile range [Lord, 2014].

4.3.3 Engine Architecture Issues

The architecture challenge is surfaced in Figure 4.15, which shows a scale illustration of an 18:1 bypass geared turbofan. The design issues are flagged on the chart. The first two have already been mentioned: the low blade height at compressor exit, an inherent consequence of the

decrease in annulus height at high values of OPR, and the difficulty, perhaps the impossibility, of getting a fan shaft sized to drive the large fan through the center of the small core—the low pressure spool shaft goes through the inside of the high pressure spool shaft in current architectures. Solving this problem could be done with the alternative architecture shown on the right, which will be discussed in more depth below. Finally, the slender core is vulnerable to engine 'backbone bending' which can bow the cases, leading to increased running clearances, lower efficiency, or rubs.

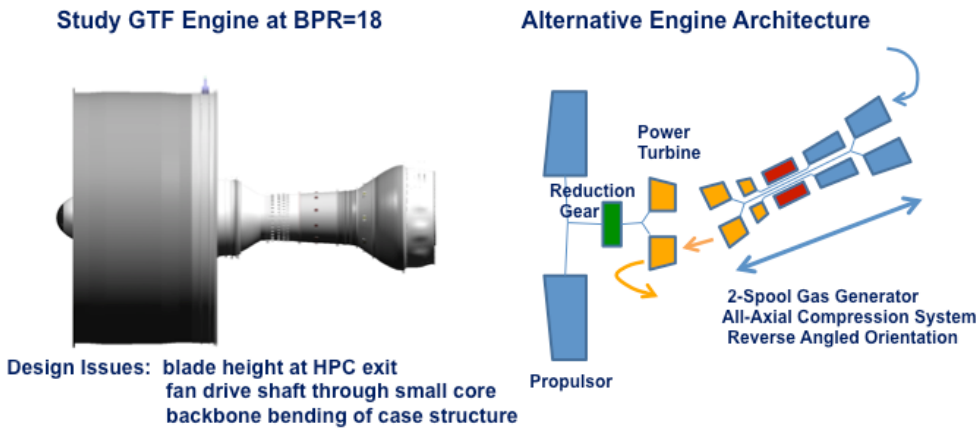

Figure 4.15: Engine architecture design issues for ultra high bypass ratio propulsors (and unconventional architecture) [Lord, 2014].

4.3.4 D8 Specific Challenges

Many of the technology difficulties associated with small core engines apply to the current tube-and-wing configurations as well as the D8, but there are specific challenges associated with the N+3 propulsor and propulsion-airframe integration. One is boundary layer ingestion and a second is the FAA 1-in-20 rule.

For the first of these, there is a benefit for boundary layer ingestion, but the nonuniform inflow conditions may give a penalty to cruise fan efficiency that would subtract from the ideal BLI benefit. Further, with high levels of inlet stagnation pressure distortion, the operability and stall margin of both the fan and core engine must be assessed over the complete range of engine operating conditions. Also associated with inlet distortion is unsteady loading of fan blades, unsteady blade stress, and high cycle fatigue that must be kept within design limits of the fan blade material. Some information on the level and form of the inlet distortion will be provided in the wind tunnel experiments, but this is an area for future work.

The second point is that the D8.6 aircraft with two closely spaced engines located within the pi tail faces a major challenge in the FAA '1-in-20 rule' (FAA, 1997). The 1-in-20 rule concerns engine installation design guidelines to prevent loss of aircraft in the unlikely event of an uncontained rotor failure in a turbomachinery component. The rule is illustrated on Figure 4.16 and the relevant excerpt from the FAA document is:

"Safety Analysis Objectives.

(3i) Single One-Third Disc Fragment. There is not more than a 1 in 20 chance of catastrophe resulting from the release of a single one-third disc fragment."

The implication for the N+3 vehicle configuration is that a turbine disk burst event in one engine should not cause shutdown of the other engine or damage the tail surfaces to the extent that there is loss of flight control. The next section describes an unconventional engine architecture to address the 1-in-20 rule.

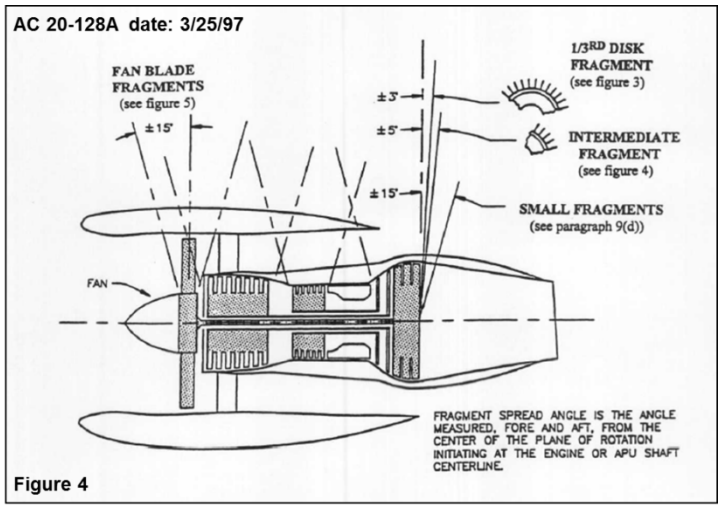

Figure 4.16: Description of 1-in-20 rule for engine fragments [FAA document, 1997].

4.4. Engine Architecture

4.4.1 Overall Features Of The Concept Engine

The new concept engine architecture is a high-OPR two-spool gas generator that is aerodynamically coupled to the power turbine and propulsor in a reverse offset arrangement. Patent applications have been filed for this invention. The concept engine, illustrated schematically on the right hand side of Figure 4.15, directly addresses the issues associated with the D8 design space.

The gas generator section is not mechanically coupled to the propulsor section of the engine, so the drive shaft connecting the power turbine to the fan does not pass through the core engine. This enables the disk bores and flowpath through the gas generator to be pulled inward to a smaller radius, allowing the mean flow path radius to decrease. This, in turn, creates a larger span height for a given flow area, in other words for a given compressor size[3].

[3] A strong driver of efficiency is the blade leakage flow, whose impact scales as clearance to span height. We thus wish to minimize this non-dimensional clearance metric. The flow area. A. is given by

$$A = \pi\left(r_0^2 - r_i^2\right) = \pi\left(r_0 + r_i\right)\left(r_0 - r_i\right) = 2\pi r_m h \,,$$

where r_0, r_i, and r_m are the outer radius, inner radius, and mean radius respectively and h is the span height, $r_0 - r_i$. For constant flow area, therefore, the span height is given by $h = A/\left(2\pi r_m\right)$, and shrinking the mean radius thus improves the non-dimensional clearance.

The thrust loads are transferred directly from the propulsor section of the engine to the airframe structure, with no significant loads or moments acting on the core. The backbone bending effect that occurs in conventional high-BPR turbofan engine installations is thus avoided. Elimination of a low spool drive shaft with pulled in flowpath combined with elimination of backbone bending to avoid deleterious impact on turbomachinery clearances enables consideration of an all-axial compressor at small core size (exit corrected flow in the 1 to 3 lbm/s range). Cycle design with an OPR of approximately 55 at maximum climb condition is within the compressor exit-rim speed mechanical design space of current axial compressor technology.

4.4.2 Initial Architecture Definition

An important aspect of the conceptual engine architecture is that each core can be oriented at an angle that will keep the adjacent core, and other vital components such as critical aircraft flight controls, out of the burst zone. This provides an effective means to address the 1-in-20 rule. Figure 4.17 defines the engine-to-engine relationship that permits a failure in any one of the two gas generators (which have the high kinetic energy components) while retaining full integrity in the remaining adjacent engine and its nacelle and nozzle. These latter are kept safe from the unlikely event of an uncontained rotor failure that would cause liberation of large rotor particles, intermediate fragments, and small fragments. The engine-to-engine 'burst zone' criteria that must be satisfied according to the FAA Advisory Circular are:

- For 1/3 disk fragments [+/- 3 degrees]
- For intermediate fragments [+/- 5 degrees]
- For small disk fragments [+/- 15 degrees].

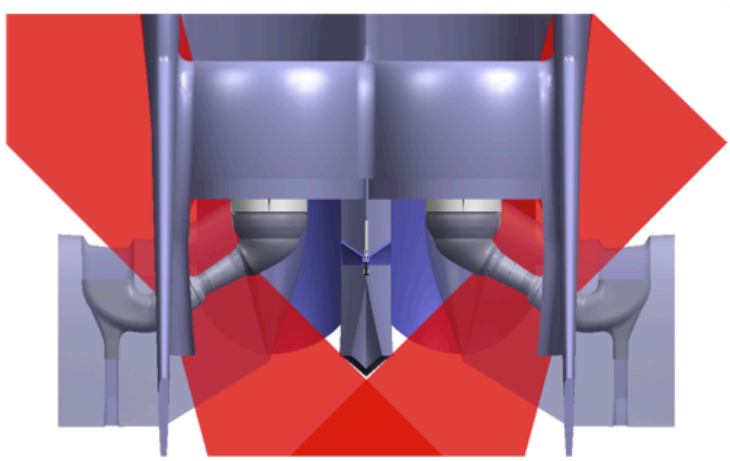

Figure 4.17: Engine-airframe integration to address the '1-in-20 rule' [Lord *et al.*, 2015].

Figure 4.18 illustrates the ability to position both gas generators, and their respective burst zones, away from critical aircraft components. The implication is that the criticality of flight capability is preserved, and the aircraft will be designed and sized to tolerate an acceptable level of "sacrificial" damage (as described below).

In the description of the engine architecture that has been created, we will recount the iterations in the design process to show not only 'the answer', but also the choices and decisions that have led to the proposed configuration. As an example, to realize the requirements in Figure 4.17, the gas generator flexibility was exercised to a level not common in conventional engine layout. Looking at a rear view, as in Figure 4.19, the gas generator was clocked an additional 30 degrees and the inlets rotated an equal amount.

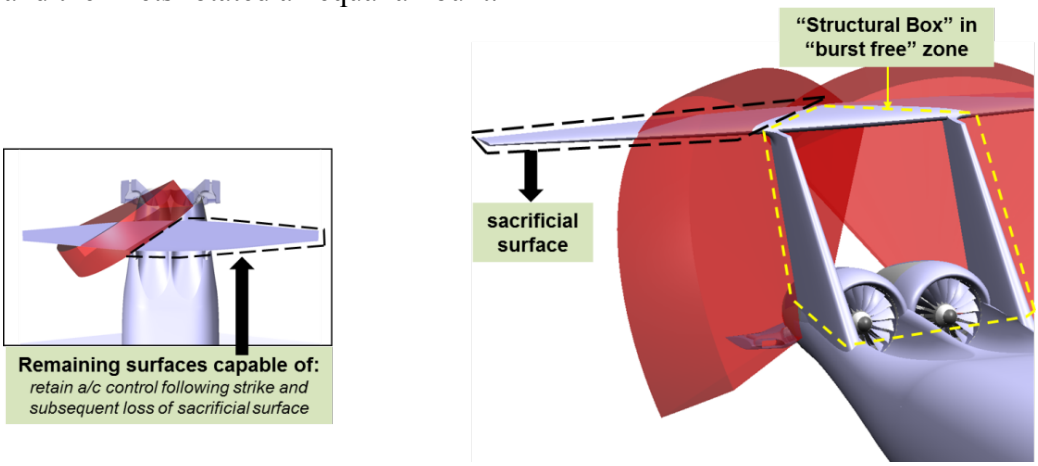

Figure 4.18: Burst free zones and sacrificial surfaces [Lord *et al.*, 2015].

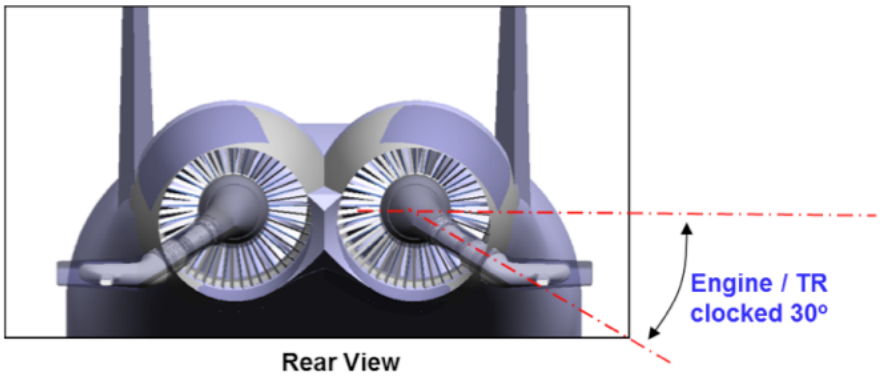

Figure 4.19: Rear view of nacelles showing engine clocking for adjustment of burst zone [Lord *et al.*, 2015].

The above views represent the initial concept architecture using the reverse angled core in the D8.6 twin engine installation. In this instantiation of the idea the length of the core is such that the core intake is an external inlet extending outboard of the vertical tail (Figure 4.20). The concept engine architecture also requires 180 (or nearly) degree turnaround ducts leading into the compressor intake and the power turbine exhaust. These ducts, which are sketched in Figure 4.21, must be designed with low Mach number flow to avoid excessive pressure losses.

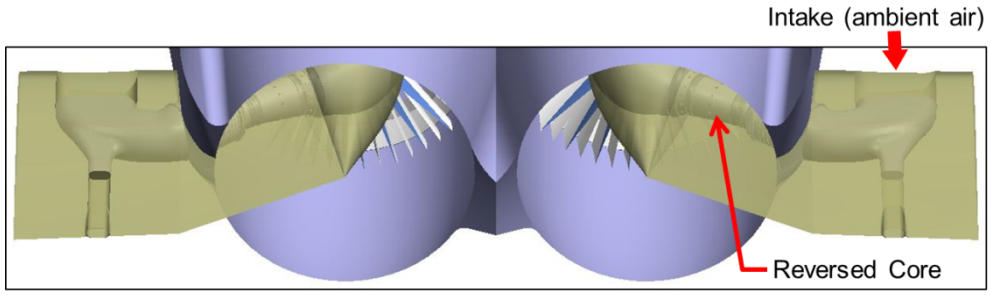

Figure 4.20: Core intake external to vertical tail [Lord *et al.*, 2015].

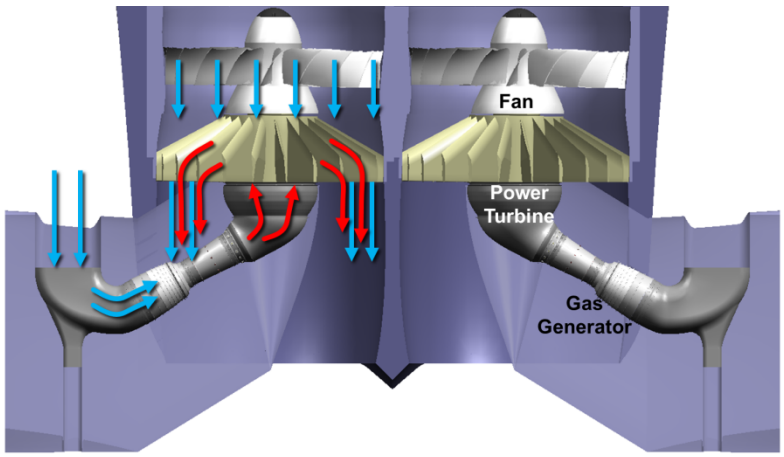

Figure 4.21: Turnaround ducts between core inlet and core gas generator [Lord *et al.*, 2015].

It is noted that there is precedent for a small aircraft gas turbine engine with a reverse core, the PT6, which has been in production at Pratt & Whitney Canda for 50 years. More than 50,000 of these engines delivered, as of 2013, for over 100 different applications. A sketch of the PT6 architecture is given in Figure 4.22.

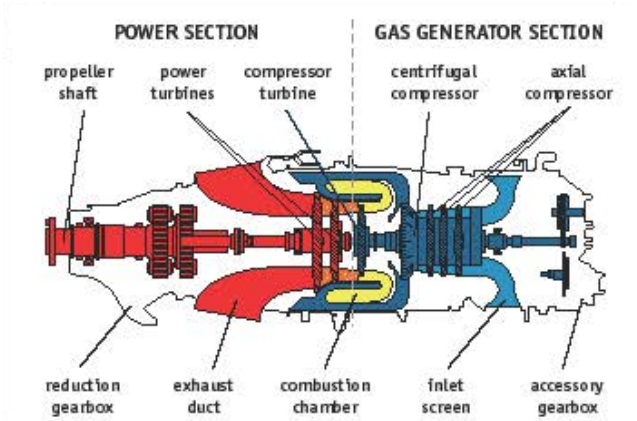

Figure 4.22: PT6 engine with a reverse core (and inlet behind the compressor) [http://www.turbokart.com/about_pt6.htm]

4.5. Thermodynamic Cycle Model

4.5.1 Initial Engine Cycle

Two thermodynamic cycle models were constructed for the N+3 engine. The thrust requirements specified by MIT were takeoff sea level, 0.19 Mach, 10400 lbf; max climb 44000 ft, 0.74 Mach, 2290 lbf; average cruise 45000 ft, 0.74 Mach, 1945 lbf.

The initial cycle was developed consistent with the cycle parameters of the Phase 1 engine design: cruise OPR = 50, FPR = 1.4 . The resultant fan size from the P&W analysis was a 62 inch diameter fan at a BPR of 18. The core flowpath was defined and the overall dimensions of the gas generator determined to be approximately 50 inch axial length and 20 inch max diameter. When installed relative to the fan in the reverse angled orientation, the compressor inlet projected outside the aft fuselage lines so the initial cycle model included an external air intake to the core, incorporating an inlet particle separator. A block diagram of the components, their connectivity, and a cycle summary is given in Figure 4.23.

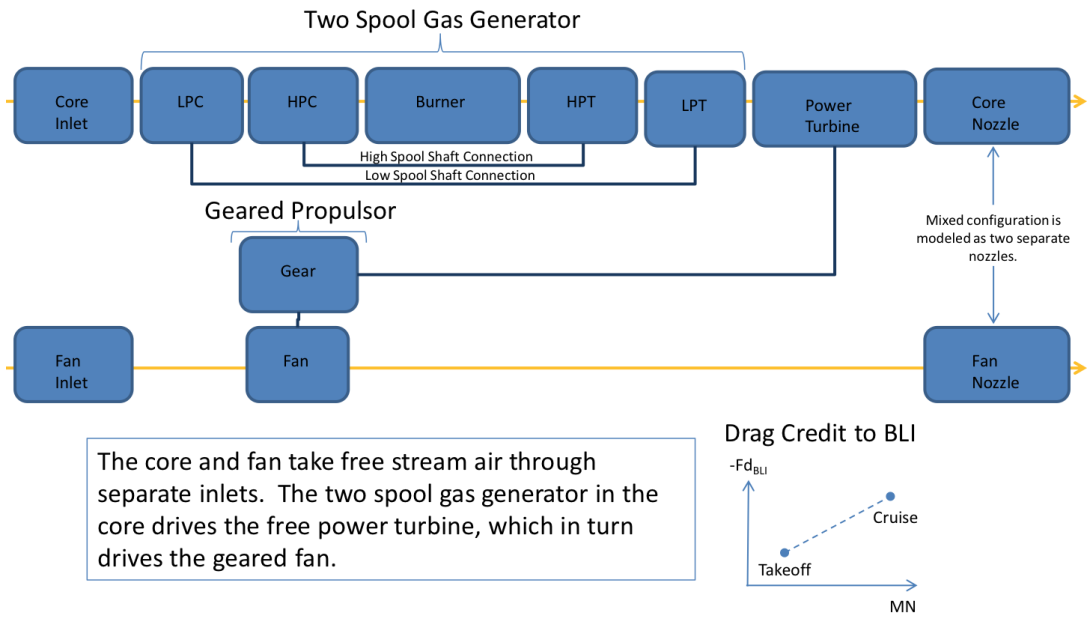

Figure 4.23: Initial D8 engine cycle description.

4.5.2 Second Generation Engine Cycle

Although the external inlets for the cores yielded a consistent cycle description, there was little enthusiasm within the team for having the inlets on the outside of the vertical tails. A second analysis of the engine cycle was subsequently undertaken with the objective of making the fan bigger and the core smaller so the core intake could be supplied from fan discharge with no need for an external core inlet. The FPR was reduced to 1.3, fan boost into the core was assumed, and turbine entry temperature increased by 250°F. The resulting engine, whose block diagram is given as Figure 4.24, has fan diameter 72 inch, core size 1.3 lbm/s, bypass ratio of 30,

core axial length 42 inch, and core diameter 16 inch. It is thus feasible to install this smaller core in the angled orientation behind the larger fan.

There are differences between the cycle models and the original MIT Phase 1 engine model that deserve comment. P&W assumed lower component efficiencies, particularly in the turbines and increased the level of secondary flow to 5% to account for leakage and cavity purge in the hot section. P&W cycle analyses also account for parasitic losses associated with windage, bearing compartments, etc. To be consistent with the reverse core configuration, a pressure loss for the turnaround duct into the compressor intake was assessed at 1% of local stagnation pressure. The loss estimated for the turnaround duct at the power turbine exhaust were 2% in stagnation pressure.

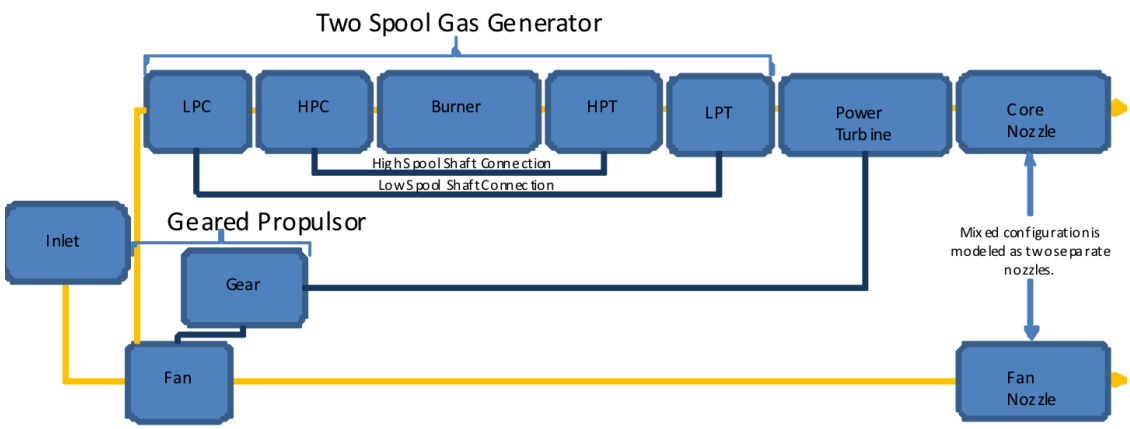

Figure 4.24: Second generation D8 engine cycle description.

Boundary layer ingestion was modeled in the cycle simulation by decreasing the ram drag by an amount equivalent to the ingested drag. The calculations used an ingested drag of 14% of aircraft drag at cruise, or equivalently 14% of engine net thrust. The modeling also incorporated a pressure loss from freestream to the front of the BLI engine inlet that represents a face averaged boundary layer stagnation pressure defect. This pressure loss was 4.5% in the original cycle analyis and 3.2% in the second generation version. The difference arises because the second pass model had a larger fan diameter so the same boundary layer loss is averaged over a larger inlet mass flow, the rest of which is at free-stream conditions.

The result of the P&W cycle analysis was a TSFC of 0.41 lbm/hr/lbf at 45000ft/ 0.74 Mach/ average cruise. This value is more than a 30% reduction from the generation N level. The TSFC is higher than the MIT Phase 1 result of 0.37, with the difference mainly attributable to the core engine modeling items mentioned, which reduce the cycle thermal efficiency. The TSFC numbers do not take into account any customer power extraction.

4.6. Engine Materials & Weight

Material selection is typically based on cycle temperature (compressor exit and turbine entry temperatures) and the associated mechanical speed of the respective spools. For the D8 aircraft engine, despite the high level of performance achieved there is no need to provide the high-pressure tubine with cooled cooling air (CCA) or similar cooling treatment for the back of

the high-pressure compressor. The emphasis is placed on reducing the levels of turbine cooling & leakage air (TCLA), meaning that we acknowledge a given level of cavity purge & leakage and rely on technology to eliminate blade & vane cooling. Ceramic metal composites (CMCs) and/or monolithic materials are seen as providing the capability to run uncooled blades & vanes. In addition, to address the reversed core, and to provide weight savings, we identified CMC as a likely material for the transition duct that connects the gas generator and the power turbine. Finally, the hot section will deploy Gamma-Ti rotor grade material.

The cold side of the engine is not affected by the cycle selection (elevated temperatures), but it is nevertheless exposed to unique aero-mechanical loads which require attention. The loads are introduced because the fan operating conditions include:

- Low fan pressure ratio (FPR) resulting in large swings in fan flow incidence angle at different operating modes. This is a situation in which flutter is often encountered.
- Inlet distortion caused by BLI ingestion

To deal with these conditions, we configured the fan rotor as a 3D woven and shrouded integrated bladed rotor (IBR). This would provide appropriate structural strength, as well as light weight, to handle the conditions described above. Also, the cold inlet ducts that lead to the gas generator will be of organic metal composite (OMC) material.

Table 4.1 gives a summary of bare engine weight and shows how the N+3 reversed core engine compares to a Gen 1 Geared Turbofan (GTF) engine of similar thrust class.

Table 4.1. Comparison of N+3 reverse core engine and reference engine (geared turbofan)

	Engine Comparison Data	
	N+3 Reverse Core	N+1 Reference
Thrust	15K	17K
Fan Dia	72”	56”
BPR	30	8.5
FPR_{CLIMB}	1.3	1.6
Bare Engine Wt	4,700 lbm	3,600 lbm

Note the 30 BPR (3.5 times the reference) and the 16 inch larger fan diameter (+ 28%) that differentiates the new engine concept. There is a difference in weight (at ‘Bare’ engine level) of approximately 1,100 lb. However, the D8 propulsion system installation does not utilize a conventional pylon, with the reversed core propulsor mounting directly on the fuselage frame. There is thus no need for the pylon structure, so there is a potential weight saving that can help offset the engine weight difference.

4.7. Propulsion-Airframe Mechanical Integration

The double-bubble aircraft is not a conventional podded engine application. As such, the first design activity was aimed at integrating the propulsor with the nacelle and the fuselage. This needed a distinctly different approach than from legacy tail mounted applications (i.e., DC-9 type

installations). The propulsor and its power turbine were designed as prime reliable and fully capable to coexist and operate side by side without concern as to the 1:20 rule which had to be addressed for the gas generator (see Section 4.3.4).

Figure 4.25 shows how the *nacelle* and the *propulsor* were integrated with the double-bubble aft fuselage. The majority of the nacelle surfaces are aerodynamically contoured and blended with the fuselage to define the aft extremity of the aircraft. Definition of the *thrust reverser* was then carried out, and this also defined the propulsor placement on the aft fuselage. Once the overall configuration was established, detailed attention was granted to the satisfying the 1:20 rule, and assuring full compatibility between the gas generator, the nacelle, the propulsor, and the fuselage.

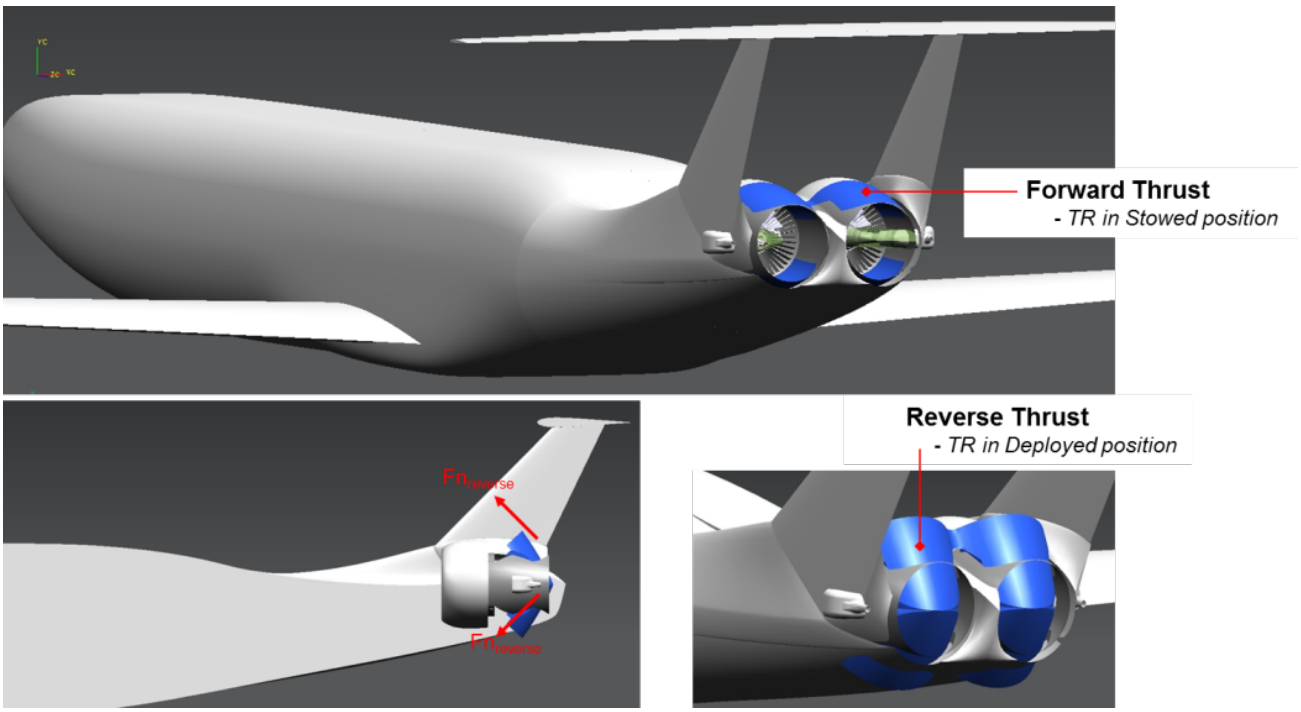

Figure 4.25: Integration of the nacelle and thrust reverser with the aft fuselage of the D8.

Figure 4.26 shows the thrust reverser in stowed and deployed position. The figure defines the first attempt to integrate a complete airplane with sized components, and thus to support the claim to a successful First Level Feasibility study. The systems that are integrated in this view include:

1) Functional *pivot thrust reverser*,
2) Ambient air *intakes for the gas generator*,
3) *Inlet particle separators,*
4) *Pi tail* empennage
5) Round *exhaust nozzles.*

During the second phase of design optimization, the goal was to integrate the external air inlets into the fan stream. Doing this would allow the cores to achieve benefits from: (i) pressure boost

available downstream of the fan blade, and (ii) cleaner source of air flow into the gas generator and not requiring the use of inlet particle separators. This prompted additional engine cycle iterations aimed at improving the relationship between the fan and core size, meaning a larger fan diameter and a smaller core size to facilitate integration of the gas generator air inlet into the fan stream.

Figure 4.27 is a sketch of the inlet ducting system resulting from the elimination of the ambient air inlets and their related inlet particle separators. This major change in the core flow stream duct system re-defines the relationship between the fan, the gas generator inlet duct, and the width of the fuselage. A comprehensive picture of the overall impact is given by comparing Figure 4.27 with the initial layout in Figure 4.21.

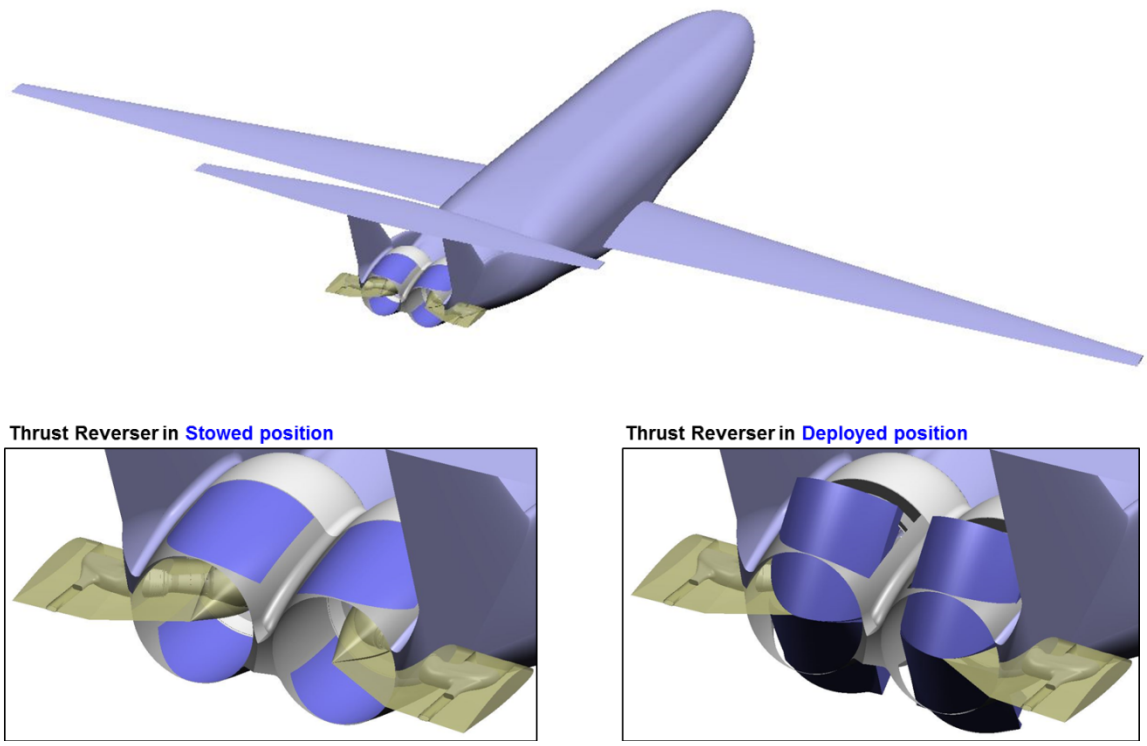

Figure 4.26: Integrated view of thrust reversers in stowed and deployed positions—initial engine configuration.

As might be expected, other features of the aircraft were altered during the integration process. The initial version of the airframe-propulsion system integration defined a fuselage width tapering down to meet the two propulsors originally sized at a 62 inch fan diameter. The second configuration featured a constant fuselage width that terminates into the aft empennage-fuselage housing the larger 72 inch diameter fans and the smaller core size gas generator. The gas generator was placed further back in the fuselage to satisfy the 1:20 rule without having to clock its orientation as in the first iteration.

Because the fan and gas generator inlet are located on the top of the fuselage in the second generation design, the possibility of foreign object damage (FOD) ingestion is greatly reduced compared to the initial design or to podded engines installed under wing or on the fuselage.

Figure 4.28 shows the fan inlet definition and the unique gas generator inlet. The latter is placed on a horizontal plane to the face of the fan to enable shielding from runway debris, as described, and to minimize direct BLI ingestion into the gas generator. The gas generator inlet duct is located at the leading edge of a horizontal bifurcation aerodynamic fairing that extends downstream to enclose the GG. Because there is flow ingested at the leading edge, the back pressure distortion on the fan due to the area blockage of the bifurcation is minimized. In our case, the entire inlet area directs air to the gas generator and in the process has the effect of entirely eliminating the legacy blockage.

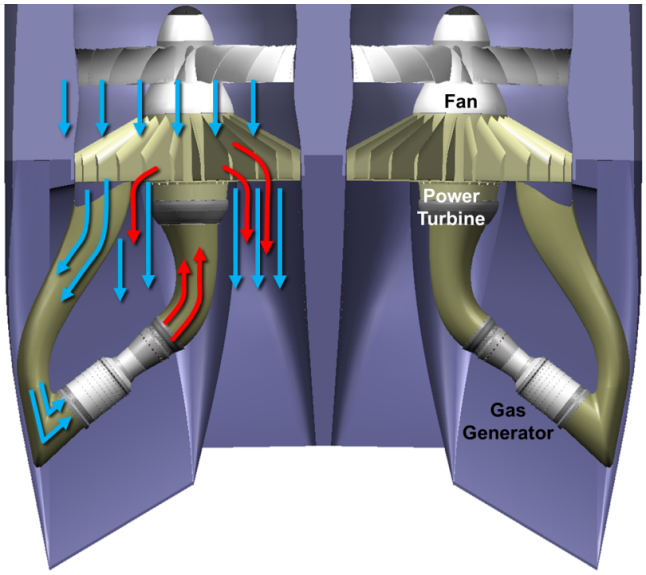

Figure 4.27: Sketch of engine configuration--fan, gas generator, power turbine, and connecting ducting [Lord *et al.*, 2015].

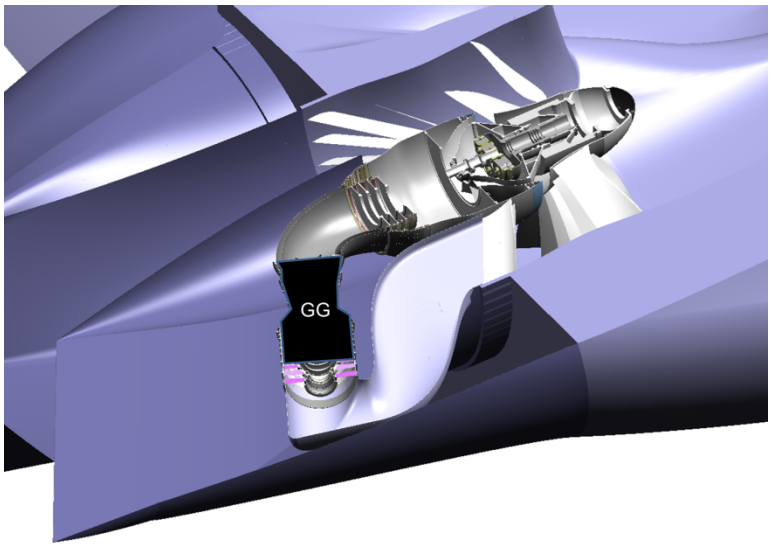

Figure 4.28: Sketch of gas generator and fan and fan inlet system [Lord *et al.*, 2015].

To mitigate possible separation in the area at the intersection of the two round exhaust nozzles (see Figure 4.26), Figure 4.29 shows our shaping of the exhaust nozzle, by blending from a rectangular fashion to the two round inlets. The wind tunnel and computational results for the configuration examined, have not (so far) indicated a separation problem in this area, although analysis is still underway, so it is an open question about the need for this refinement as the design evolves.

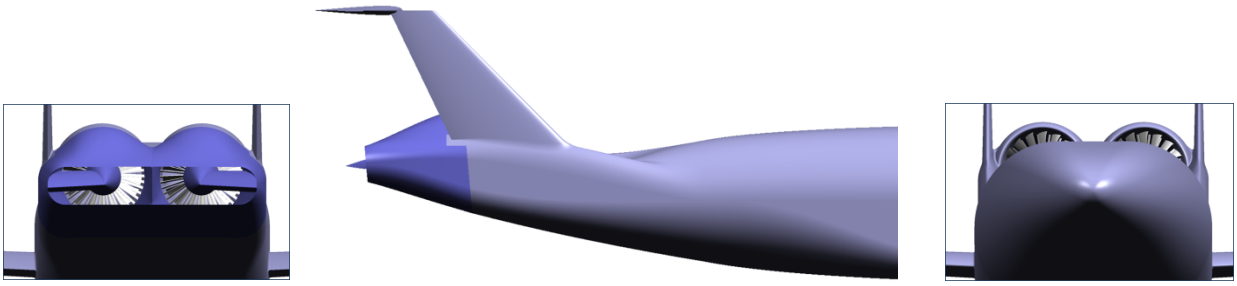

Figure 4.29: View of exhaust nozzle [Lord *et al.*, 2015].

In summary, we have carried out a comprehensive aircraft-propulsion system integration assessment that addresses all the first level challenges associated with the D8 airplane and its unconventional architecture. In this, we defined a new engine concept that complements the D8 airframe to achieve the NASA step change performance goals. Figure 4.30 gives a rendering of the final configuration.

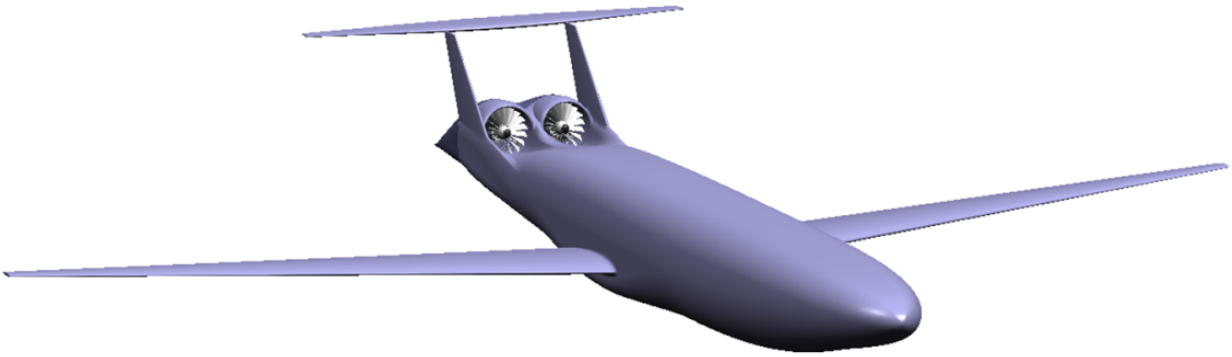

Figure 4.30: Rendering of the D8 aircraft and integrated propulsion system [Lord *et al.*, 2015].

Acknowledgments
This work was supported by NASA under Cooperative Agreement Number NNX11AB35A. We are very pleased to acknowledge the support. The authors would also like to acknowledge the contributions and suggestions of other N+3 team members and participants in the 'small core telecons': R. M. Chriss, N. A. Cumpsty, Y. Dong, A. H. Epstein, M. Drela, D. K. Hall, K. Hasel, M. D. Hathaway, M. L. Celestina, J. S. Sabnis, T. G. Tillman. Further, we wish to recognize the help and support for this project shown by the NASA Fixed Wing Project Management team. Finally, we are pleased to thank R. Courchesne-Sato for assistance in the preparation of this report.

References

Arend, D. J., Tillman, T. G., and O'Brien, W. F., *Generation after Next Propulsor Research: Robust Design for Embedded Engine Systems.* AIAA paper 2012-4041, AIAA/ASME/SAE/ASEE 48th Joint Propulsion Conference, 2012

DiOrio, A. G., "Small Core Axial Compressors for High Efficiency Jet Aircraft", MS Thesis, Department of Aeronautics and Astronautics, Masschusetts Institute of Technology, September 2012

Drela, M., "Design Drivers of Energy-Efficient Transport Aircraft", SAE Paper 2011-01-2495, 2011

Epstein, A. H., "Aeropropulsion for Commercial Aviation in the 21st Century and Research Developments Needed", *AIAA Journal* (AIAA Dryden Lecture in Research), 52, No. 5, May 2014, pp. 901-911

FAA Advisory Circular 20-128A "Design Considerations for Minimizing Hazards Caused by Uncontained Turbine Engine and Auxiliary Power Unit Rotor Failure", 25 March, 1997

Florea, R. V., Voytovych, D., Tillman, G., Stucky, M. Shabbir, A., Sharma, S., "Aerodynamic Analysis of a Boundary-Layer-Ingesting Dirtortion-Tolerant Fan", ASME Paper, GT2013-94656, Presented at SAME Turbo Expo 2013.

Greitzer, E. M.; Bonnefoy, P., A.; Blanco, E., De la Rosa; Dorbian, C., S.; Drela, M.; Hall, D., K.; Hansman, R., J.; Hileman, J., I.; Liebeck, R., H.; Lovegren, J.; Mody, P.; Pertuze, J.,A.; Sato, S.; Spakovszky, Z., S.; Tan, C., S.; Hollman, J., S.; Duda, J., E.; Fitzgerald, N.;Houghton, J.; Kerrebrock, J., L.; Kiwada, G., F.; Kordonowy, D.; Parrish, J., C.; Tylko, J.;Wen, E., A.; Lord, W., K.., *N+3 Aircraft Concept Design and Trade Studies Final Report* Contract NNX08AW63A, 31 March 2010.

Greitzer, E. M., Tan, C. S., Graf, M. B, *Internal Flow: Concepts and Applications*, Cambridge University Press, 2007.

Gunn, E. J., and Hall, C. A., Aerodynamics of Boundary Layer Ingesting Fans, ASME Paper GT2014-26142, presented at ASME Turbo Expo 2014.

https://janes.ihs.com/CustomPages/Janes/Home.aspx

Koff, B. L. "Gas Turbine Technology Evolution: A Designer's Perspective", *AIAA Journal of Propulsion and Power*, Vol. 20, No. 4, July-August, 2004.

Lord, W. K. "Propulsion Technology Direction", Presented at ICAO Meeting, *Fueling Aviation With Green Technology*, Montreal Canada, 9, 10 September 2014.

Norris, G., and Warwick, G., "Flush With Potential", *Aviation Week and Space Technology*, 30 September 2013.

Smith, L. H. , "Wake Ingestion Propulsion Benefit", *AIAA Journal of Propulsion and Power*, Vol 9, No 1, Jan-Feb 1993.

http://www.turbokart.com/about_pt6.htm (see also http://www.pwc.ca/en/engines/pt6a , http://en.wikipedia.org/wiki/Pratt_%26_Whitney_Canada_PT6)

Uranga, A., Drela, M., Greitzer, E. M, Titchener, N., Lieu, M. K., Siu, N. M., Huang, A. C., Gatlin, G. M., Hannon, J. A., "Preliminary Experimental Assessment of the Boundary Layer Ingestion Benefit for the D8 Aircraft", AIAA Paper 2014-0906, Presented at AIAA SciTech, 52nd Aerospace Sciences Meeting, 13 – 17 Jan 2014, National Harbor, MD.

A Student Theses Abstracts

This Appendix contains the title pages and abstracts of the graduate student theses that were completed under the Phase 2 project at MIT and that are most relevant to the work presented in this report.

Name	Thesis Reference	Degree			Time on N+3 Team
		Level	Year	Institution	
DiOrio, A.	[39]	M.S.	2012	MIT	Nov. 2010 – Aug. 2012
Hall, D.	[34]	Ph.D.	2015	MIT	Sept. 2008 – Jan. 2015
Lieu, M.	[10]	M.S.	2015	MIT	Mar. 2011 – Jan. 2015
Siu, N.	[13]	M.S.	2015	MIT	Mar. 2011 – Jan. 2015
Casses, C.	[15]	M.S.	2015	MIT	Sept. 2013 – Aug. 2015
van Dam, E.	[12]	M.S.	2015	TU Delft	Jan. 2014 – Dec. 2015

A.1 A. DiOrio, "Small Core Axial Compressors for High Efficiency Jet Aircraft", MIT M.S. 2012

Small Core Axial Compressors for High Efficiency Jet Aircraft

by

Austin Graf DiOrio

B.S. in Mechanical Engineering
Johns Hopkins University (2010)

Submitted to the Department of Aeronautics and Astronautics
in partial fulfillment of the requirements for the degree of

Master of Science

at the

MASSACHUSETTS INSTITUTE OF TECHNOLOGY

September 2012

Author .....
Department of Aeronautics and Astronautics
August 23, 2012

Certified by .....
Edward M. Greitzer
H.N. Slater Professor of Aeronautics and Astronautics
Thesis Supervisor

Certified by .....
Choon Sooi Tan
Senior Research Engineer
Thesis Supervisor

Accepted by .....
Eytan H. Modiano
Professor of Aeronautics and Astronautics
Chair, Graduate Program Committee

Small Core Axial Compressors for High Efficiency Jet Aircraft

by

Austin Graf DiOrio

Submitted to the Department of Aeronautics and Astronautics
on August 23, 2012, in partial fulfillment of the
requirements for the degree of
Master of Science

Abstract

This thesis quantifies mechanisms that limit efficiency in small core axial compressors, defined here as compressor exit corrected flow between 1.5 and 3.0 lbm/s. The first part of the thesis describes why a small engine core with high overall pressure ratio (OPR) is desirable for an efficient aircraft and shows that fuel burn can be reduced by up to 17% compared to current engines. The second part examines two specific effects: Reynolds number and tip clearance. At a core size of 1.5 lbm/s, Reynolds number may be as low as 160,000, resulting in reductions in stage efficiency up to 1.9% for blades designed for high Reynolds number flow. The calculations carried out indicate that blades optimized for this Reynolds number can increase stage efficiency by up to 1.6%. For small core compressors, non-dimensional tip clearances are increased, and it is estimated that tip clearances can be up to 4.5% clearance-to-span ratio at the last stage of a 1.5 lbm/s high pressure compressor. The efficiency penalty due to tip clearance is assessed computationally and a 1.6% decrease in polytropic efficiency is found for a 1% increase in gap-to-span ratio. At the above clearance, these efficiency penalties increase aircraft mission fuel burn by 3.4%, if current design guidelines are employed. This penalty, however, may be reduced to 0.4% if optimized blades and a smaller compressor radius than implied by geometric scaling, which allows reduced non-dimensional clearance, are implemented. Based on the results, it is suggested that experiments and computations should be directed at assessing: (i) the effects of clearance at values representative of these core sizes, and (ii) the effect of size on the ability to achieve a specific blade geometry and thus the impact on loss.

Thesis Supervisor: Edward M. Greitzer
Title: H.N. Slater Professor of Aeronautics and Astronautics

Thesis Supervisor: Choon Sooi Tan
Title: Senior Research Engineer

A.2 D. Hall, "Analysis of Civil Aircraft Propulsors with Boundary Layer Ingestion", MIT Ph.D. 2015

Analysis of Civil Aircraft Propulsors with Boundary Layer Ingestion

by

David Kenneth Hall

B.S.E., Duke University (2008)
S.M., Massachusetts Institute of Technology (2011)

Submitted to the Department of Aeronautics and Astronautics
in partial fulfillment of the requirements for the degree of

Doctor of Philosophy in Aeronautics and Astronautics

at the

MASSACHUSETTS INSTITUTE OF TECHNOLOGY

February 2015

Author .....
Department of Aeronautics and Astronautics
January 14, 2015

Certified by .....
Edward M. Greitzer
H.N. Slater Professor of Aeronautics and Astronautics
Thesis Committee Chair

Certified by .....
Choon Sooi Tan
Senior Research Engineer
Thesis Committee

Certified by .....
Mark Drela
Terry J. Kohler Professor of Fluid Dynamics
Thesis Committee

Certified by .....
Nicholas A. Cumpsty
Professor Emeritus, Imperial College
Thesis Committee

Accepted by .....
Paulo Lozano
Associate Professor of Aeronautics and Astronautics
Graduate Committee Chair

Analysis of Civil Aircraft Propulsors with Boundary Layer Ingestion

by

David Kenneth Hall

Submitted to the Department of Aeronautics and Astronautics
on January 14, 2015, in partial fulfillment of the
requirements for the degree of
Doctor of Philosophy in Aeronautics and Astronautics

Abstract

This thesis describes (i) guidelines for propulsor sizing, and (ii) strategies for fan turbomachinery conceptual design, for a boundary layer ingesting (BLI) propulsion system for advanced civil transport aircraft. For the former, configuration performance analysis shows BLI yields a reduction in mechanical power required to propel a given aircraft. For the latter, fan turbomachinery design attributes are identified to mitigate the impact of BLI inlet distortion on propulsor performance.

The propulsion system requirements are determined using a mechanical energy analysis, in which the performance of the airframe and propulsor are characterized in terms of sources and sinks of power. Using this framework, the propulsor can be sized based on the performance of the isolated airframe. Analysis of the power savings due to BLI (from reduction of viscous dissipation both in the aircraft wake and the propulsor jet) leads to scaling choices for the sizing of propulsor simulators for wind tunnel experiments to assess BLI benefit.

Fan stage distortion response is assessed computationally for a range of turbomachinery design parameters and for distortions characteristic of BLI. The numerical results show the importance of three-dimensional flow redistribution upstream of the fan, and indicate that, for the parameters examined, non-axisymmetric fan stators have the largest effect on decreasing blade row velocity distortions and thus mitigating losses due to flow non-uniformity.

Thesis Committee Chair: Edward M. Greitzer
Title: H.N. Slater Professor of Aeronautics and Astronautics

Thesis Committee: Choon Sooi Tan
Title: Senior Research Engineer

Thesis Committee: Mark Drela
Title: Terry J. Kohler Professor of Fluid Dynamics

Thesis Committee: Nicholas A. Cumpsty
Title: Professor Emeritus, Imperial College

A.3 M. Lieu, "Quantification of the Boundary Layer Ingestion Benefit for the D8-Series Aircraft Using a Pressure Rake System", MIT M.S. 2015

Quantification of the Boundary Layer Ingestion Benefit for the D8-Series Aircraft Using a Pressure Rake System

by

Michael K. Lieu

B.S., Aeronautics and Astronautics, Massachusetts Institute of Technology, 2011

Submitted to the Department of Aeronautics and Astronautics
in partial fulfillment of the requirements for the degree of

Master of Science in Aeronautics and Astronautics

at the

MASSACHUSETTS INSTITUTE OF TECHNOLOGY

February 2015

Author .....
Department of Aeronautics and Astronautics
January 15, 2015

Certified by .....
Edward M. Greitzer
H. N. Slater Professor of Aeronautics and Astronautics
Thesis Supervisor

Certified by .....
Mark Drela
Terry J. Kohler Professor of Fluid Dynamics
Thesis Supervisor

Certified by .....
Alejandra Uranga
Research Engineer, Department of Aeronautics and Astronautics
Thesis Supervisor

Accepted by .....
Paulo C. Lozano
Associate Professor of Aeronautics and Astronautics
Chair, Graduate Program Committee

Quantification of the Boundary Layer Ingestion Benefit for the D8-Series Aircraft Using a Pressure Rake System

by

Michael K. Lieu

Submitted to the Department of Aeronautics and Astronautics
on January 15, 2015, in partial fulfillment of the
requirements for the degree of
Master of Science in Aeronautics and Astronautics

Abstract

This thesis presents the results of experiments carried out at NASA Langley Research Center (LaRC) 14'×22' Subsonic Wind Tunnel to determine the aerodynamic boundary layer ingestion (BLI) benefit for the D8 aircraft advanced transport concept. The experiments involved a back-to-back comparison between two D8 aircraft configurations: a podded propulsion system (non-BLI) and a fuselage integrated propulsion system (BLI). The BLI benefit was evaluated from flow surveys upstream and downstream of the propulsor using a rotating rake system for the two configurations. The BLI benefit, defined as the mechanical flow power saving at cruise conditions (zero net streamwise force), from the BLI configuration relative to the non-BLI configuration, was found to be 8.2% ±0.8%. The experimental-computational approach and the sensitivity analysis of the estimated BLI benefit to uncertainties such as flow angles and instrumentation errors are described in the thesis. The benefits and drawbacks of the rotating rake measurement technique used in the D8-series powered model aircraft experiments are also discussed.

Thesis Supervisor: Edward M. Greitzer
Title: H. N. Slater Professor of Aeronautics and Astronautics

Thesis Supervisor: Mark Drela
Title: Terry J. Kohler Professor of Fluid Dynamics

Thesis Supervisor: Alejandra Uranga
Title: Research Engineer, Department of Aeronautics and Astronautics

A.4 N. Siu, "Evaluation of Propulsor Aerodynamic Performance for Powered Aircraft Wind Tunnel Experiments", MIT M.S. 2015

Evaluation of Propulsor Aerodynamic Performance for Powered Aircraft Wind Tunnel Experiments

by

Nina M. Siu

B.S., Massachusetts Institute of Technology, 2011

Submitted to the Department of Aeronautics and Astronautics
in partial fulfillment of the requirements for the degree of

Master of Science in Aeronautics and Astronautics

at the

MASSACHUSETTS INSTITUTE OF TECHNOLOGY

February 2015

Author .....
Department of Aeronautics and Astronautics
January 29, 2015

Certified by .....
Edward M. Greitzer
H. N. Slater Professor of Aeronautics and Astronautics
Thesis Supervisor

Certified by .....
Alejandra Uranga
Research Engineer, Department of Aeronautics and Astronautics
Thesis Supervisor

Accepted by .....
Paulo C. Lozano
Associate Professor of Aeronautics and Astronautics
Chair, Graduate Program Committee

Evaluation of Propulsor Aerodynamic Performance for Powered Aircraft Wind Tunnel Experiments

by

Nina M. Siu

Submitted to the Department of Aeronautics and Astronautics
on January 29, 2015, in partial fulfillment of the
requirements for the degree of
Master of Science in Aeronautics and Astronautics

Abstract

This thesis describes a methodology to convert electrical power measurements to propulsor mechanical flow power for a 1:11-scale, powered wind tunnel model of an advanced civil aircraft utilizing boundary layer ingestion (BLI); mechanical flow power is a surrogate for aircraft fuel burn. Back-to-back experiments of BLI and non-BLI aircraft configurations to assess the BLI benefit directly measured electrical power, and supporting experiments were performed in a 1×1 foot wind tunnel at the MIT Gas Turbine Laboratory to convert these measurements into mechanical flow power. The incoming flow conditions of the powered wind tunnel tests (Reynolds number and inlet distortion) were replicated. This propulsor characterization was found to convert the electrical power measurements to mechanical flow power with experimental uncertainty of roughly 1.6%.

Thesis Supervisor: Edward M. Greitzer
Title: H. N. Slater Professor of Aeronautics and Astronautics

Thesis Supervisor: Alejandra Uranga
Title: Research Engineer, Department of Aeronautics and Astronautics

A.5 E. van Dam, "Inlet Distortion Characterization of the Boundary Layer Ingesting D8 Aircraft", T U Delft M.S. 2015

Inlet Distortion Characterization of the Boundary Layer Ingesting D8 Aircraft

NASA N+3 Project

Master of Science Thesis

For obtaining the degree of Master of Science in Aerospace Engineering at Delft University of Technology

Elise van Dam

February 26, 2015

Faculty of Aerospace Engineering · Delft University of Technology

DELFT UNIVERSITY OF TECHNOLOGY
DEPARTMENT OF AERODYNAMICS

The undersigned hereby certify that they have read and recommend to the Faculty of Aerospace Engineering for acceptance the thesis entitled **"Inlet Distortion Characterization of the Boundary Layer Ingesting D8 Aircraft"** by **Elise van Dam** in fulfillment of the requirements for the degree of **Master of Science**.

Dated: February 26, 2015

Supervisors:

Prof.Dr.ir. G. Eitelberg

Dr. A.G. Rao

Prof.Dr.ir. L.L.M. Veldhuis

Dr. M.D. Pavel

Abstract

This thesis experimentally assesses the inflow towards the propulsors and the pressure distribution at the propulsor fan-face for the boundary layer ingesting D8 aircraft, and examines the dependence of the model, the propulsor and the flight condition on the inlet distortion. Use is made of mini-tuft flow visualization and five hole probe pressure surveys. The results are compared with CFD simulations. The experiments were performed at the most important mission points of the D8: cruise, descent, start of climb, and top of climb. CFD was only performed for cruise and top of climb. From the pressure distributions the distortion coefficient, DC(60), was calculated, the maximum variation in pressure over a specified circumferential segment (60°).

At cruise the DC(60) equaled ~ 0.3, compared to DC(60)$\sim$ 0.1-0.2 for conventional aircraft. The D8 model caused cross-flow to the propulsors, the flow is directed towards the sides of the model. Both fans rotate in the same direction, such that one propulsor has the flow in the direction of rotation, and the other has the flow opposite to the direction of rotation, causing an asymmetry between the left and right propulsor. The flight phase is characterized by α, the angle of attack, λ, the ratio of tip velocity over tunnel speed, and β, the yaw angle. It is found that at a high value of λ the pressure differences at the fan-face are reduces by engine suction, lowering the distortion and counter-acting the cross-flow. A low value of λ means a relative lower influence of the propulsor on the flow, such that the propulsor is not able to (fully) counter-act the cross-flow, resulting in a higher difference in DC(60) and power required between the left and right propulsor. Changing α mainly changes the location of the pressure distributions.

The results from experiments agree well with CFD, there is a 1% deviation in DC(60) at top of climb condition, and 6% at cruise. The pressure distributions look similar and the pressure coefficient values scale equally, from -0.8 to 0.

Further research should focus on the exact fan response on the distortion. The D8 used conventional engines, optimized for uniform inflow. Developing a BLI optimized engine could further increase the BLI benefit. The D8 model induced cross-flow, resulting in an asymmetry between the left and right engine. Eliminating this cross-flow by a change in model design could also decrease the distortion.

A.6 C. Casses, "Aerodynamic Benefits of Boundary Layer Ingestion for the D8 Double-Bubble Aircraft", MIT M.S. 2015

Aerodynamic Benefits of Boundary Layer Ingestion for the D8 Double-Bubble Aircraft

by

Cécile J. Casses

B. Eng., Ecole Centrale Paris, 2013

Submitted to the Department of Aeronautics and Astronautics
in partial fulfillment of the requirements for the degree of

Master of Science in Aeronautics and Astronautics

at the

MASSACHUSETTS INSTITUTE OF TECHNOLOGY

September 2015

Author .....
Department of Aeronautics and Astronautics
August 19, 2015

Certified by .....
Edward M. Greitzer
H. N. Slater Professor of Aeronautics and Astronautics
Thesis Supervisor

Certified by .....
Alejandra Uranga
Research Engineer, Department of Aeronautics and Astronautics
Thesis Supervisor

Accepted by .....
Paulo C. Lozano
Associate Professor of Aeronautics and Astronautics
Chair, Graduate Program Committee

Aerodynamic Benefits of Boundary Layer Ingestion for the D8 Double-Bubble Aircraft

by

Cécile Casses

Submitted to the Department of Aeronautics and Astronautics
on August 19, 2015, in partial fulfillment of the
requirements for the degree of
Master of Science in Aeronautics and Astronautics

Abstract

This thesis describes experimental assessments of the aerodynamic boundary layer ingestion (BLI) benefit of the D8 advanced civil aircraft design. Two independent methods were applied for 1:11 scale (4.1 m wingspan) powered aircraft model experiments in the NASA Langley 14x22-foot Subsonic Wind Tunnel. The metric used as a surrogate for fuel consumption was the input mechanical flow power, and the benefit was quantified by back-to-back comparison of non-BLI (podded) and BLI (integrated) configurations.

The first method (indirect) was the estimate of mechanical flow power based on the measured electrical power to the propulsors, plus supporting experiments to characterize the efficiencies of the fans and the electric motors that drive them, at the MIT Gas Turbine Laboratory. The second method (direct) was the direct integration of flowfield measurements, from five-hole probe surveys at the inlet and exit of the propulsors, which provided flow angles, velocity components, and pressure coefficients. Data were taken at different wind tunnel speeds, and conditions to determine overall performance dependence on non-dimensional power and angle of attack. At the simulated cruise point, the first method gave a measured aerodynamic BLI benefit of 7.9%±1.5% at 70 mph tunnel velocity, and 8.5%±1.5% at 84 mph, and the second method gave a measured benefit of 8.1%±3.3% at 70 mph, and 12.2%±3.4% at 84 mph. For the aircraft models examined, the aerodynamic benefit was found to come primarily from a decrease in the propulsor jet velocity (increase in propulsive efficiency) and thus a decreased jet dissipation, with the contribution from decreased wake and airframe dissipation being roughly an order of magnitude smaller.

Thesis Supervisor: Edward M. Greitzer
Title: H. N. Slater Professor of Aeronautics and Astronautics

Thesis Supervisor: Alejandra Uranga
Title: Research Engineer, Department of Aeronautics and Astronautics